

University of Louisville

ThinkIR: The University of Louisville's Institutional Repository

Electronic Theses and Dissertations

5-2015

Shape analysis of the human brain.

Matthew Joseph Nitzken 1987-
University of Louisville

Follow this and additional works at: <https://ir.library.louisville.edu/etd>



Part of the [Electrical and Computer Engineering Commons](#)

Recommended Citation

Nitzken, Matthew Joseph 1987-, "Shape analysis of the human brain." (2015). *Electronic Theses and Dissertations*. Paper 2067.

<https://doi.org/10.18297/etd/2067>

This Doctoral Dissertation is brought to you for free and open access by ThinkIR: The University of Louisville's Institutional Repository. It has been accepted for inclusion in Electronic Theses and Dissertations by an authorized administrator of ThinkIR: The University of Louisville's Institutional Repository. This title appears here courtesy of the author, who has retained all other copyrights. For more information, please contact thinkir@louisville.edu.

SHAPE ANALYSIS OF THE HUMAN BRAIN

By

Matthew Joseph Nitzken
B.S., University of Louisville, 2009
M.Eng., University of Louisville, 2010

A Dissertation
Submitted to the Faculty of the
J.B. Speed School of Engineering at the University of Louisville
in Partial Fulfillment of the Requirements
for the Degree of

Doctor of Philosophy in Electrical Engineering

Department of Electrical and Computer Engineering
University of Louisville
Louisville, Kentucky

May 2015

Copyright 2015 by Matthew Joseph Nitzken

ALL RIGHTS RESERVED

SHAPE ANALYSIS OF THE HUMAN BRAIN

By

Matthew Joseph Nitzken
B.S., University of Louisville, 2009
M.Eng., University of Louisville, 2010

A Dissertation Approved on

April 20, 2015

by the following Dissertation Committee

Dissertation Director
Dr. Ayman S. El-Baz, Ph.D.

Co-Director Dr. Tamer Inanc, Ph.D.

Dr. Manuel Casanova, M.D.

Dr. Olfa Nasraoui, Ph.D.

Dr. Jacek M. Zurada, Ph.D.

DEDICATION

Sometimes our light goes out but is blown into flame by another human being.

Each of us owes deepest thanks to those who have rekindled this light.

- Albert Schweitzer

This dissertation is dedicated to Edward W. Scharre,
and my parents, Joseph A. Nitzken and Katherine S. Nitzken.

ACKNOWLEDGMENTS

I want to give my deepest thanks to Dr. Ayman El-Baz for his hours of patience and assistance in helping me during my studies at the University of Louisville. Thanks to his generous knowledge and help during my time at U of L, I have been able to complete all of the tasks that I set out to finish. It has been a great honor to work with him.

I would like to extend my sincere thanks to all of my committee members, Dr. Tamer Inanc, Dr. Manuel Casanova, Dr. Olfa Nasraoui, and Dr. Jacek M. Zurada, who have been a tremendous help during my doctoral studies. I also would like to thank the Bioluminescence Laboratory, and all of its members, who I have worked with for many years, and who have helped me on occasions to numerous to count.

Finally I want to profusely thank my loved ones, family, and friends. They have provided me with inspiration and years of support during this degree program, and throughout life itself. I cannot thank them enough for giving me the opportunities to dream, allowing me to pursue the impossible, and then providing me the loving support to never give up. Above all, they are ultimately responsible for the work I present here, and all my future endeavors.

ABSTRACT

Shape Analysis of the Human Brain

Matthew Joseph Nitzken

April 20, 2015

Autism is a complex developmental disability that has dramatically increased in prevalence, having a decisive impact on the health and behavior of children. Methods used to detect and recommend therapies have been much debated in the medical community because of the subjective nature of diagnosing autism. In order to provide an alternative method for understanding autism, the current work has developed a 3-dimensional state-of-the-art shape based analysis of the human brain to aid in creating more accurate diagnostic assessments and guided risk analyses for individuals with neurological conditions, such as autism.

Methods: The aim of this work was to assess whether the shape of the human brain can be used as a reliable source of information for determining whether an individual will be diagnosed with autism. The study was conducted using multi-center databases of magnetic resonance images of the human brain. The subjects in the databases were analyzed using a series of algorithms consisting of bias correction, skull stripping, multi-label brain segmentation, 3-dimensional mesh construction, spherical harmonic decomposition, registration, and classification. The software algorithms were developed as an original contribution of this dissertation in collaboration with the BioImaging Laboratory at the University of Louisville Speed School of Engineering. The classification of each subject was used to construct diagnoses

and therapeutic risk assessments for each patient.

Results: A reliable metric for making neurological diagnoses and constructing therapeutic risk assessment for individuals has been identified. The metric was explored in populations of individuals having autism spectrum disorders, dyslexia, Alzheimers disease, and lung cancer.

Conclusion: Currently, the clinical applicability and benefits of the proposed software approach are being discussed by the broader community of doctors, therapists, and parents for use in improving current methods by which autism spectrum disorders are diagnosed and understood.

TABLE OF CONTENTS

DEDICATION	iii
ACKNOWLEDGMENTS	iv
ABSTRACT	v
1 INTRODUCTION	1
1.1 The Human Brain	1
1.2 Magnetic Resonance Imaging	5
2 DEFINING AUTISM	11
2.1 Introduction	11
2.2 History of Autism Spectrum Disorders	12
2.3 Neuropathology of Autism	14
2.4 Prevalence of Autism	18
2.5 Importance of Early Detection	20
2.6 Existing Methods for Detecting Autism	21
3 SURVEY OF SHAPE ANALYSIS	25
3.1 Introduction	25
3.2 Medial Axis and Skeletal Analysis	29
3.3 Geodesic Distances	34
3.4 Procrustes Analysis	39

3.5	Deformable Models	43
3.6	Spherical Harmonics	48
3.7	Morphometry	54
3.8	Additional Methods.....	58
3.8.1	Distance Mapping	59
3.8.2	Entropy-based Particle Systems	60
3.8.3	Graph Matching	60
3.8.4	Homologous Modeling	61
3.8.5	Laplace-Beltrami	62
3.8.6	Reeb Graph	63
3.8.7	Spectral Matching	64
3.8.8	Symmetry Analysis	65
3.8.9	Volumetric Analysis	66
3.9	Discussion.....	66
3.9.1	Research Challenges	66
3.9.2	Comparisons and Trends	68
3.10	Summary of Shape Analysis	70
4	SIGHT FRAMEWORK	71
4.1	Introduction.....	71
4.2	Skull Stripping	74
4.2.1	Bias Correction.....	74
4.2.2	BET Skull Stripping	75
4.2.3	Visual Appearance-Guided Iso-Surfaces	76
4.2.4	First-Order Visual Appearance ($P(\mathbf{g} \mathbf{m})$)	77
4.2.5	Second-Order Visual Appearance ($P(\mathbf{m})$)	79

4.2.6 Skull Stripping Results	81
4.3 Segmentation	83
4.3.1 Atlas Construction	84
4.3.2 Shape Probability Classification	88
4.3.3 Intensity Classification	91
4.3.4 Fusion of Shape and Intensity Classification	93
4.3.5 Spatial Refinement.....	94
4.3.6 Post-Processing.....	98
4.4 Mesh Generation.....	99
4.4.1 Pre-Processing.....	99
4.4.2 Delaunay Triangulated Meshing	104
4.4.3 Laplacian Smoothing	107
4.4.4 Spherical Deformation	108
4.5 SPHARM Analysis	113
4.5.1 SPHARM reconstruction error	115
4.5.2 Surface complexity	115
4.6 Registration	118
4.6.1 3D Volume Registration.....	118
4.6.2 Spherical Harmonics (SPHARM) Registration.....	121
4.7 Classification	126
4.7.1 Metric Computation	126
4.7.2 Brodmann Areas	128
4.7.3 List of the Brodmann Areas.....	129
4.7.4 Ray-casting and Area Delineation.....	137
4.7.5 Constructing a Simple Classifier	142
4.7.6 Brodmann Risk Analysis.....	150

5	RESULTS	156
5.1	Autism Spectrum Disorders	157
5.1.1	Kennedy Krieger Institute Results	158
5.1.2	University of California, Los Angeles Results	162
5.1.3	University of Michigan Results	166
5.1.4	NDAR Conturo Vanderbilt Results	172
5.1.5	Infant Brain Imaging Study Results	175
5.1.6	Risk Analysis Results	178
5.2	Other Applications	180
5.2.1	Dyslexia	180
5.2.2	Alzheimer's Disease	183
5.2.3	Lung Cancer	185
5.2.4	Summary	187
6	DISCUSSION	188
6.1	Recommendations	190
6.2	Limitations	191
6.3	Further Research	192
7	CONCLUSION	194
	REFERENCES	196
	APPENDICES	233
	CURRICULUM VITA	267

LIST OF TABLES

3.1 Medial axis shape analysis approaches	30
3.2 Geodesic distance shape analysis approaches	35
3.3 Procrustes shape analysis approaches	40
3.4 Deformable model shape analysis approaches.....	45
3.5 SPHARM shape analysis approaches	50
3.6 Morphometry-based shape analysis approaches	55
3.7 Additional shape analysis approaches	58
5.1 Autism KKI results.....	159
5.2 Autism UCLA results	163
5.3 Autism UM results.....	167
5.4 Autism Conturo results.....	173
5.5 Autism IBIS results	177
5.6 Dyslexia brain region results.....	183

LIST OF FIGURES

1.1	The human brain.....	2
1.2	Anatomy of the human brain	3
1.3	Artistic representation of brain hemispheres	4
1.4	Magnetic Resonance Imaging Scanner	6
1.5	Example MR images of the human brain	6
1.6	Example MRI Pulse sequences	8
1.7	Examples of MR imaging noise	9
2.1	Visual representation of the autism spectrum	12
2.2	The Diagnostic and Statistical Manual of Mental Disorders, Fifth Edition	14
2.3	The amygdala of the brain.....	17
2.4	CDC prevalence of autism	19
2.5	Change in prevalence of autism.....	19
2.6	The Wechsler Intelligence Scale for Children	22
2.7	Eye tracking applied to autism	23
3.1	3D brain mesh	26
3.2	First-order shape analysis using reflections	27
3.3	Gaussian curvatures in the second-order shape analysis	28
3.4	Medial axis of a 2D object.....	29

3.5	The medial axis in an object.....	32
3.6	Voronoi skeleton pruning scheme.....	33
3.7	Skeleton extraction from a corpus callosum.....	33
3.8	Visual representation of a simple geodesic distance.....	36
3.9	Illustration of geodesic distance on a synthetic surface.....	37
3.10	Example of geodesic distance in two-dimensional image.....	38
3.11	Procrustes prototypes for different brain structures.....	41
3.12	MRI image of the brain identified for Procrustes analysis.....	43
3.13	Illustration of a deformable model.....	44
3.14	Deformable model identifying the cortex.....	45
3.15	Qualitative segmentation performance of a deformable model.....	47
3.16	Decomposition of an object using SPHARM.....	51
3.17	SPHARM segmentation of hippocampus shapes.....	52
3.18	Use of the SPHARM distance correspondence to establish a mapping.....	52
3.19	Approximation of the 3D brain cortex shape for diagnosis.....	53
3.20	VBM morphometry of brain regions.....	56
3.21	Example of distance mapping.....	59
3.22	Illustration of graph matching between subjects.....	60
3.23	Explanation of homologous modeling.....	62
3.24	Illustration of a Reeb graph of a cranium.....	63
3.25	Human Brain Asymmetry.....	65
4.1	Application of bias correction to MRI scans.....	75
4.2	Results of BET algorithm.....	76
4.3	Iso surfaces overlaid on MRI scan.....	77
4.4	Visualization of LCDG with two dominant modes.....	78
4.5	3D binary MGRF neighborhood system.....	80

4.6	Results of skull stripping approach	82
4.7	Overview of brain segmentation models.....	83
4.8	Results of FSL BET, SUSAN, and FAST algorithms	85
4.9	Results of BrainSuite algorithms	86
4.10	Example MR atlases.....	86
4.11	Illustration of brain and non-brain shape probability maps	89
4.12	Visual representation of the shape probability classification.....	89
4.13	Segmentation result using the shape probability classification	90
4.14	Intensity classification histograms	91
4.15	Visual representation of the intensity classification	92
4.16	Segmentation result using the intensity classification.....	93
4.17	Segmentation result after combining shape, intensity, and spatial refinement	95
4.18	3D grayscale MGRF neighborhood	96
4.19	Final segmentation result.....	98
4.20	Segmented MRI scans	99
4.21	Segmented MRI scans with CSF removed	100
4.22	Segmented binary MRI scans.....	101
4.23	Segmented MRI scans following pre-processing	102
4.24	A 3D volumetric brain mesh	105
4.25	Detailed representation of Delaunay triangulations	106
4.26	Example of a condensed Wavefront OBJ file format	107
4.27	Result of Laplacian smoothing on a brain mesh.....	108
4.28	2D illustration of Attraction-Repulsion	109
4.29	Attraction-Repulsion center condition	109
4.30	Attraction-Repulsion neighbor condition	110
4.31	Unit sphere constructed from a brain mesh	112

4.32	An brain mesh and its SPHARM reconstruction.....	114
4.33	SPHARM error reconstruction curve.....	116
4.34	Surface complexity reconstruction curve	117
4.35	Overview of the 3D volumetric registration	119
4.36	Mutual information between two objects.....	120
4.37	Voxel overlap between two objects.....	121
4.38	Pre- and post-alignment MRI brain slices	121
4.39	Overview of the SPHARM registration	123
4.40	Original mesh and its SPHARM aligned counterpart	124
4.41	High contrast brain curvature	126
4.42	3D surface curvature	127
4.43	Brodmann areas of the brain	128
4.44	The traditional Point in Polygon problem.....	138
4.45	Ray-casting example	141
4.46	Ray-casting delineated Brodmann areas	142
4.47	A simple Bayes classifier	144
4.48	Functional Brodmann areas for speech.....	152
4.49	Functional Brodmann areas for music	153
5.1	Autism KKI performance	159
5.2	Autism UCLA performance	162
5.3	Autism UM performance	167
5.4	Autism Conturo performance.....	173
5.5	Autism IBIS performance	176
5.6	Brain region results for dyslexia	182
5.7	Brain change in Alzheimer's Disease	184

5.8 3D shape approximation of lung cancer nodules 186

LIST OF ALGORITHMS

1	Brain Extraction Approach.....	81
2	Sight Foundry	87
3	3D Flood-Fill	103
4	Attraction-Repulsion	111
5	Volumetric Registration	122
6	SPHARM Registration	125
7	Ray-Casting	140
8	NSIM Similarity Metric	145
9	Brodmann Area Reduction	148
10	Classification	151

CHAPTER 1

INTRODUCTION

1.1 The Human Brain

The human brain has 100 billion neurons, each neuron connected to ten thousand other neurons. Sitting on your shoulders is the most complicated object in the known universe.

- Michio Kaku

The human brain is one of the most complicated anatomical structures in the human body. Carpenters Human Anatomy defines the brain as weighing, on average, about 3lbs. or 1.5kg and having an average volume of 1130 cubic centimeters in females, and 1260 cubic centimeters in men [1]. In all humans, there is substantial variation amongst individuals, and the brain has many variations and changes even among the same species. Analyzing such a variable structure poses a significant challenge [2]. Figure 3.1 illustrates the complexity of the human brain when represented in a mesh format.

In research, computer-aided medical diagnostics call for the quantitative analysis of many structural parts of the brain, such as the cortex, ventricles, corpus callosum, hippocampus, brain stem, and gyrifications [1]. The brain has long been a topic of research, but modern day

shape analysis of the brain has only been possible due to the assistance of computers [3].

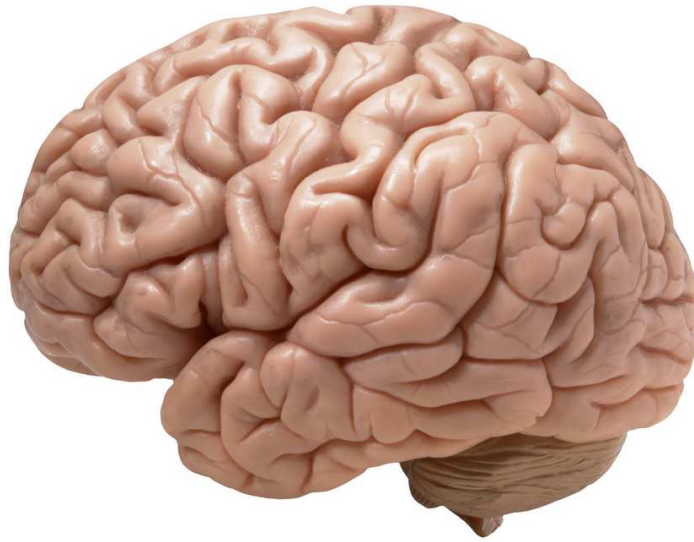


Figure 1.1: *The human brain.*

While the human brain has the same general structure as the brains of all other mammals, it has a distinctly more developed cortex [4, 5]. In terms of volume, large animals such as whales and elephants have brains that are larger in absolute size. However, when measurements are taken using the encephalization quotient, which compensates for the size of the body, the human brain is more than twice as large as the brain of a bottlenose dolphin, and over three times as large as the brain of a chimpanzee. Much of this complexity stems directly from the cerebral cortex, which is the most well known part of the brain. The anterior of the brain contains the frontal lobes, which are associated with executive functions, such as self-control, planning, reasoning, and abstract thought. The posterior of the brain, which is the portion of the cerebral cortex devoted to vision, is also greatly enlarged in humans [5].

The human cerebral cortex is a thick layer of neural tissue that covers most of the brain [1, 4, 5]. This layer is folded to increase the surface so that it can fit into the volume available. The pattern of folds is similar across individuals, although there are many small variations. The cortex is divided into four lobes, referred to as the frontal lobe, parietal lobe, temporal

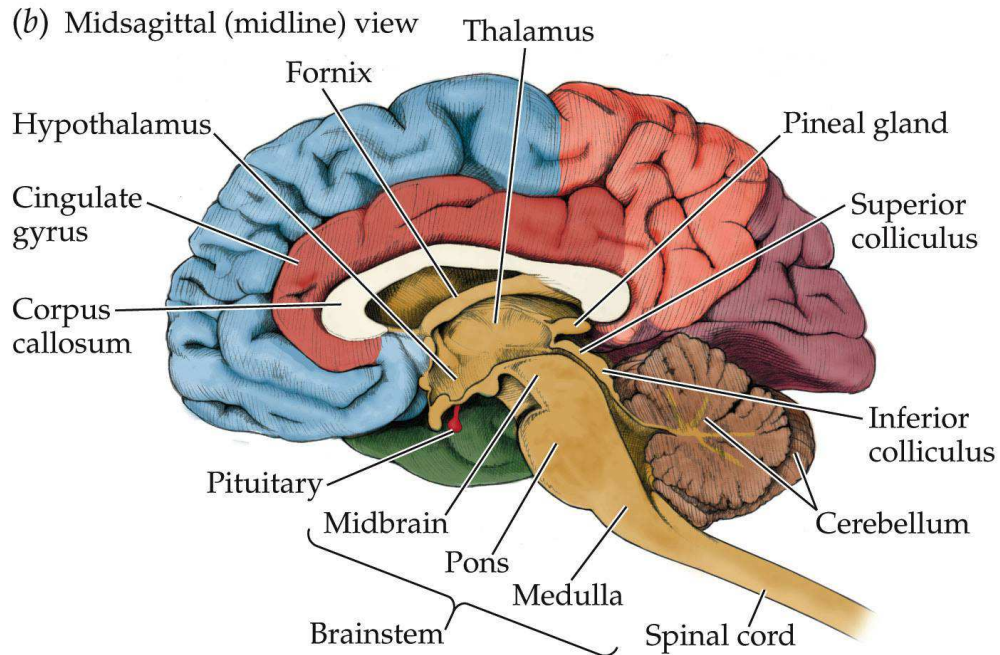


Figure 1.2: *Anatomy of the human brain. Courtesy Biological Psychology 6th Ed.*

lobe, and occipital lobe. (Some classification systems also include a limbic lobe and treat the insular cortex as a lobe.) Within each lobe are numerous cortical areas, each associated with a particular function such as vision, motor control, language, etc. The left and right sides of the cortex are broadly similar in shape, and most cortical areas are replicated on both sides. Some areas show strong lateralization, particularly areas involved in the processes of speech and language. In most people, the left hemisphere is the dominant hemisphere for language, with the right hemisphere playing a much lesser role. There are other functions, such as spatiotemporal reasoning, for which the right hemisphere is usually dominant. These differences play to the common notion that humans are left- or right-brained, although in reality this is regarded as myth.

Despite being protected by the thick bones of the skull, suspended in cerebrospinal fluid, and isolated from the bloodstream by the blood-brain barrier, the human brain is susceptible to damage and disease [1, 4, 5]. The most common forms of physical damage are from closed

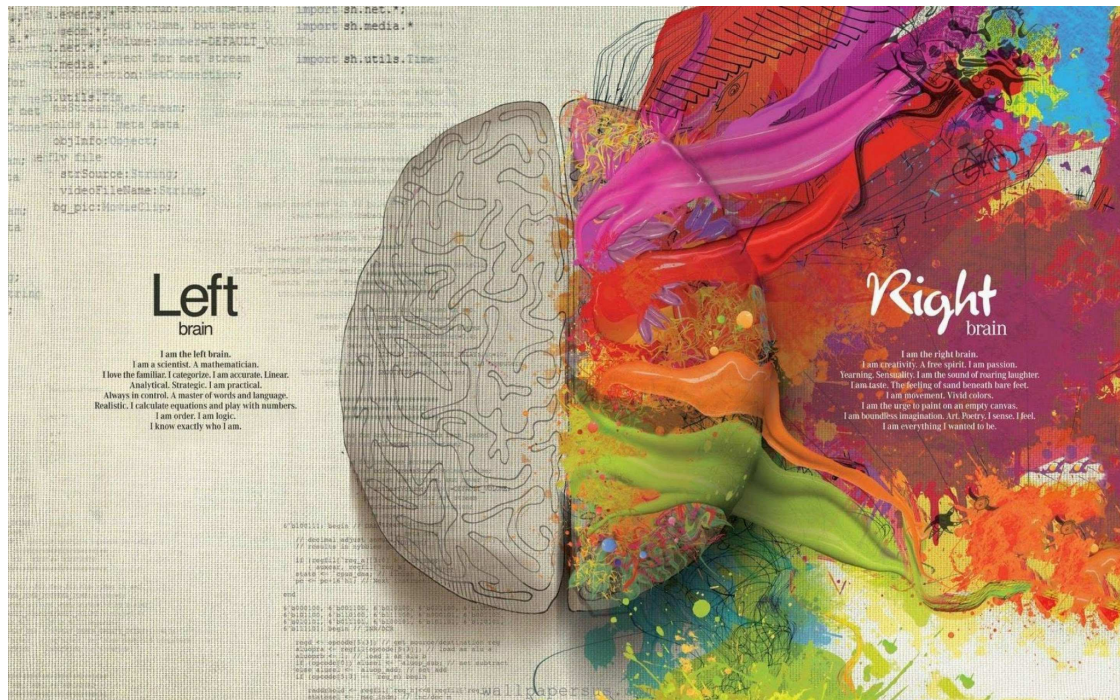


Figure 1.3: *Artistic representation of the left and right brain hemispheres. Courtesy Mercedes-Benz.*

head injuries such as a blow to the head, a stroke, or poisoning by a variety of chemicals that can act as neurotoxins. Infection of the brain, though serious, is rare due to the biological barriers which protect it. The human brain is also susceptible to degenerative disorders, such as Parkinson's disease, multiple sclerosis, and Alzheimer's disease. Several psychiatric conditions, such as schizophrenia and depression, are thought to be associated with brain dysfunctions, although the nature of such brain anomalies is not well understood.

Scientifically, the techniques used to study the human brain differ in important ways from those that are used to study the brains of other mammals. Invasive techniques, such as inserting electrodes into the brain, or disabling parts of the brain to examine the effect on behavior, are used with non-human species, but for ethical reasons, are not performed with humans. Humans are the only subjects who can respond to complex verbal instructions. It is often possible to use non-invasive techniques, such as functional neuroimaging or EEG

recording, more productively with humans than with non-humans. Some of the most important topics, such as language, can hardly be studied at all except in humans. Often, human and non-human studies form essential complements to each other. Individual brain cells (except where tissue samples are taken for biopsy for suspected brain tumors) can only be studied in non-humans; complex cognitive tasks can only be studied in humans. Combining the two sources of information to yield a complete functional understanding of the human brain is an ongoing challenge for researchers in neuroscience.

1.2 Magnetic Resonance Imaging

Magnetic Resonance Imaging (commonly referred to as MR Imaging or MRI) was first conceived in 1952, when Herman Carr, a graduate student at Harvard, proposed a one-dimensional MRI [6, 7, 8]. The usage of MRI in medicine did not really get started until Paul Lauterbur expanded the technique developed by Carr [9]. Lauterbur also had the added challenge of determining how to make a visual image from the MR signals. In 1974, Lauterbur published his first images, which showed the cross-section image of a living mouse. After this initial discovery, research resumed and techniques for both applying MRI to the human body and developing a greater understanding of k-space were patented. Lauterbur would go on to receive the Nobel Prize in 2003 for his contributions in the field of medicine.

In the 1980s, this work continued until the first full body MRI scanner was introduced at St. Bartholomews Hospital in London [8, 10]. GE Research in Schenectady, NY was the first company to take the technology to market and expand it to use high field-strength magnets which improved both the speed and resolution of the scanning. Today, MRI is used for many disorders because it is a significantly safer technique for the human body than using Computed-Tomography (CT) imaging. MRI is safer because it is based on magnetism instead of traditional X-Rays. Safety has become a primary reason that work in this area of research



Figure 1.4: *Magnetic Resonance Imaging Scanner.*

has opted to use MRI technology as the preferred scanning technology for the human brain.



Figure 1.5: *Example MR images of the human brain.*

Constructing MR images involves much mathematical calculation and research. Extensive literature has been published explaining this process, however, an overview will be provided [8, 11, 12]. An MRI scanner operates by generating a strong magnetic field that surrounds the object being imaged. In MR imaging, radio frequency (RF) signals are emitted to excite hydrogen atoms located in water-containing tissue of the body. The oscillating magnetic field creates a resonance in these particles. After being excited, the atoms in the body gradually relax back to their original state. It is this state of decay over time that is measured and used to create the image. The difference in water content between tissues produces different levels of contrast in the body. This decay and tissue contrast may be altered by using contrast agents, or by adjusting the parameters of the scanner, which are primarily the T1 and T2 weights. There are alternate methods used to create custom MRI scans.

The images acquired by an MRI are generated using specific pulse sequences [11, 12]. The MR pulse signals that make up these pulse sequences are electromotive forces that are induced in a coil by a rotating magnetic moment of nuclear spins. To create a clinically useable image, this pulse signal must be well above noise levels. These sequences are constructed to optimize the signal in a variety of different noise environments. This optimization is enabled by emitting different RF signal pulses at different time points. The combination of RF pulses places atoms inside of tissue into specific spins. Through the emission of multiple signals in a row, dramatically different images may be obtained.

The most common acquisitions are T1 and T2 weighted images. A T1-weighted image is a spin-lattice configuration and measures the tissue signal based on the repetition time of the originating signals (TR). This method produces optimal images within fatty tissue and is useful for acquiring images of the cerebral cortex and other similar organs. A T2-weighted image is referred to as a spin-spin acquisition and is based on the echo time (TE). The TE follows the TR in a pulse sequence, and occurs after an RF pulse has been emitted. The spin of the atoms decays faster in the second pulse of a T2-weighted image when compared

to a T1-weighted acquisition. T2-weighted imaging is useful in examining areas of the body with a high water content, such as the prostate, white matter of the brain, and edema, among others.

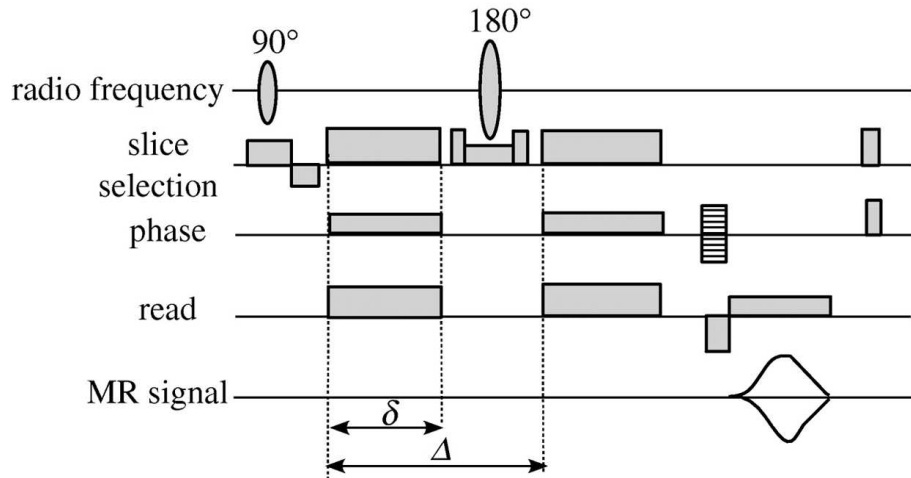


Figure 1.6: Example MRI Pulse sequences depicting where different signals are enabled and disabled.

MRI acquisition is not without flaw [8, 11, 13, 14, 15, 16]. The presence of movement in the subject or tissue being acquired, along with non-optimally selected acquisition parameters, can lead to data corruption and noise. The two primary sources of noise are: (i) noise that occurs during signal processing in the MR hardware; and (ii) noise originating from the patient or object being imaged. Noise occurring from hardware is a simpler problem to solve [17].

In the MR hardware receiver chain, noise may be generated from the preamplifier hardware and connections between the preamplifier and the RF receiver coil [15, 13]. The RF coil is a conductor, and therefore thermal noise is produced by the stochastic motion of the free electrons present in this coil. The stochastic motion of the RF coil causes ohmic based losses. This is amplified by the presence of the patient, which creates eddy current losses. Due to the close proximity of the hardware to the patient, patient originated eddy currents are inductively coupled to the RF coil. This problem can be easily solved by increasing the

conductivity of the receiver coils and the magnetic strength of the scanning hardware.

Patient based noise is a more difficult problem [15, 13, 14]. The conduction that is naturally present in the patient creates a large amount of noise. The human body naturally has a very large amount of resistance, and when placed into a circuit generates eddy currents (also referred to as patient loading). A large mass in the scanner creates both more loading and more noise. This noise is referred to as artifacts that appear in the MR images. Artifacts take several different forms, but the most common are inhomogeneities in neighboring voxels, bias, and ghosting.

Inhomogeneities occur in local areas of acquired images. Inhomogeneous voxels in the same tissue will have a narrow, but randomly distributed, range of values. Difficulties occur when tissues have similar distributions that overlap. An example is where voxel in the gray matter have intensity values between the limits of 90 and 120. A similar tissue, cerebro-spinal fluid may have values between 70 and 100. This can make delineation of the two different tissue types difficult.

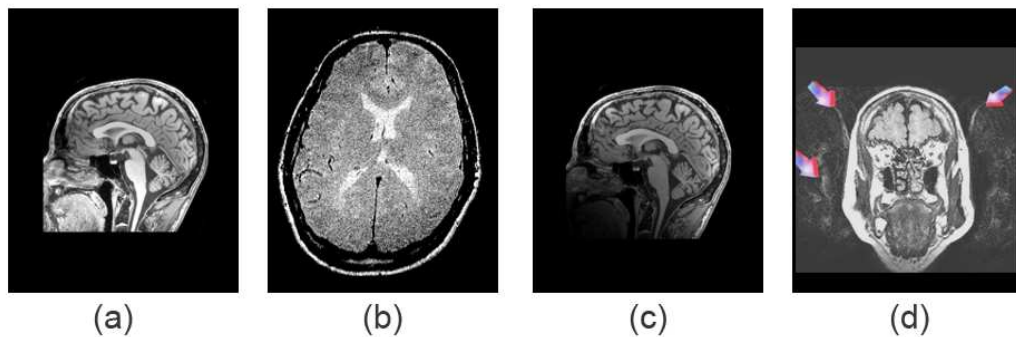


Figure 1.7: *Examples of MR imaging noise. (a) Noise-free image, (b) inhomogeneity noise, (c) bias noise, (d) ghosting noise.*

Bias and banding are errors where bands of dark or light voxels stretch throughout the image [15, 18]. A common example is where one hemisphere of the brain has correctly acquired values, while the other hemisphere gradually proceeds to darken as voxels move

toward the acquisition boundary. This creates a similar problem to inhomogeneous voxels. Tissues may have a wide range of values that heavily overlap one another.

Ghosting is a phenomenon that occurs from the magnetic nature of MR acquisitions. Ghosting is when an image is partially duplicated in the acquisition. These artifacts occur most commonly from patient movement combined with phase encoding. Phase encoding is the method in which MR signals are read and converted to images by sequentially scanning the patient. All errors that occur in MR imaging can be corrected using high-powered, properly configured scanners and carefully observing patients for movement. Errors can be accounted for using image processing algorithms, as discussed in Sections 4.2 and 4.4.2.

MRI scanning is a safe method and important for imaging work done on the brain, providing high resolution results for acquiring images of the brain. In Chapter 3, a detailed survey of brain analysis methods is presented. In nearly every approach MR imaging is the preferred modality. This understanding helps to illustrate the industry dominance of MRI in the field of brain imaging.

CHAPTER 2

DEFINING AUTISM

2.1 Introduction

But, I ask, what if autism isn't a processing error. What if it's a totally different operating system? What if I told you there was an app for that - and that app is our collective understanding?

- Marc Sirkin

Autism is a complex developmental disability that typically appears during the first three years of life. The condition results from a neurological disorder that affects the normal functioning of the brain, impacting development in the areas of social interaction and communication skills. Difficulties can be identified in both children and adults who have autism. The symptoms are identifiable in verbal and non-verbal communication, social interactions, and leisure or play activities. The classic form of autism involves a triad of impairments typically observed in the behaviors of social interaction, communication and language processes, and the existence of limited imagination. These behaviors are reflected in restricted, repetitive, and stereotyped patterns of behavior and activities [19].

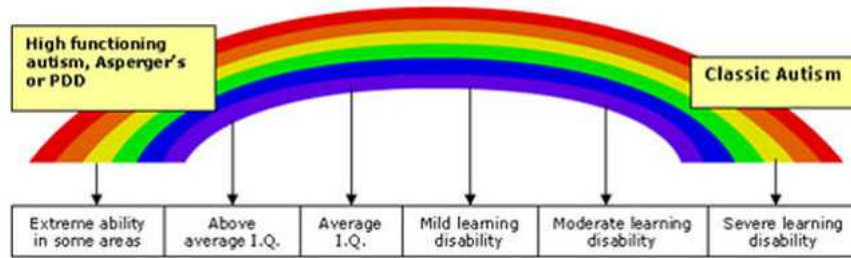


Figure 2.1: A visual representation of degrees of severity on the autism spectrum.

2.2 History of Autism Spectrum Disorders

In 1943, Leo Kanner, a psychiatrist at Johns Hopkins University, developed the diagnosis of autism. Leo Kanner was an Austrian psychiatrist and physician known for his work related to the field of autism. Kanner's work was the foundation of child and adolescent psychiatry in the U.S. and worldwide. His first textbook, *Child Psychiatry*, written in 1953, was the first English language textbook to focus on the psychiatric problems in children [20]. His seminal 1943 paper, "Autistic Disturbances of Affective Contact", with the work of Hans Asperger, established the modern study of autism [21]. By definition, autism spectrum disorder symptoms are manifested by 36 months of age. The symptoms are characterized by delayed and disordered language, impaired social interaction, abnormal responses to sensory stimuli, events, and objects, poor eye contact, an insistence on sameness, an unusual capacity for rote memory, repetitive and stereotypical behavior and a normal physical appearance.

Relatively few neuropathological studies have been performed on the brains of autistic subjects. Of those reported, abnormalities have been described in the cerebral cortex, the brainstem, the limbic system, and the cerebellum. Although, those individuals who have the disorder present with a specific set of core characteristics, each individual patient somewhat differs from another. It should not be surprising that the brains of these subjects should show a wide range of abnormalities. Understanding the central neurobiological profile of

this disorder requires delineation of the anatomic features, which are common to all cases, regardless of age, sex, and IQ. The results of systematic studies indicate that the anatomic features, consistently abnormal in all cases, include a reduced number of Purkinje cells in the cerebellum, small tightly packed neurons in the frontal cortex, and the medially placed nuclei of the amygdala [22, 23].

It is understood that the limbic system of the brain is important for learning and memory, and that the amygdala plays a role in emotion and behavior [24, 25, 26]. Research on the cerebellum indicates this structure is important as a modulator of a variety of brain functions having an impact on language processing, anticipatory and motor planning, mental imagery and timed sequencing. Defining the differences and similarities in brain anatomy in patients with autism, and correlating these observations with detailed clinical descriptions of the individual, may allow greater insight into the underlying neurobiology of this disorder.

The many patterns of abnormal behavior that cause diagnostic confusion include a pattern originally described by the Austrian psychiatrist, Hans Asperger [27]. The name he chose for this pattern was "autistic psychopathy", using the latter word in the technical sense of an abnormality of personality. This has led to a misunderstanding because of the tendency to equate psychopathy with sociopathic behavior. Asperger emphasized the stability of the clinical picture throughout childhood, adolescence, and at least into early adult life, apart from the increase in difficulty brought about by maturation. The primary characteristics of autism appear to be impervious to the effects of environment and education. Asperger considered the social prognosis to be good, meaning that most patients developed well enough to use their specialized skills to obtain employment. He also observed that some individuals had especially high levels of ability in special areas of interests and followed careers entering the fields of science and mathematics.

Autism emerged as a much more mainstream psychiatric condition with the release of the Diagnostic and Statistical Manual of Mental Disorders, Fourth Edition (DSM-IV) [28]. The

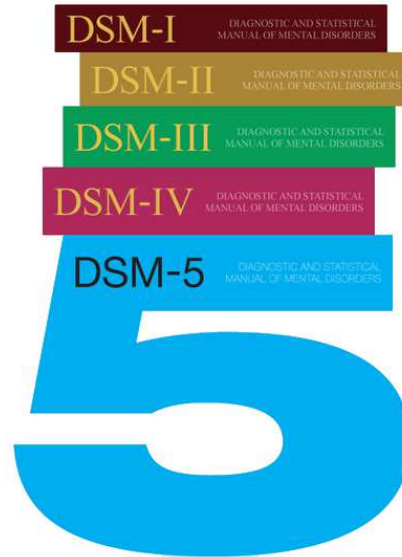


Figure 2.2: *The Diagnostic and Statistical Manual of Mental Disorders, Fifth Edition is the current gold standard for diagnoses, and made large changes to how autism is diagnosed.*

DSM-IV called for a specific set of criteria to be met and attempted to categorize autism into cases. With the continued rise in autism prevalence, and heavy scrutiny on the practices of diagnosis established by the DSM-IV, the DSM-V was released in 2013, replacing the categorization of autism with the term autism spectrum [29]. The condition of Asperger's Syndrome was also removed from autism spectrum disorder diagnosis.

2.3 Neuropathology of Autism Spectrum Disorders

Neuropathology is an important area of study for the purpose of learning how to create a diagnosis for autism spectrum disorders. The role of single-stranded micro deletions and epigenetic influences on brain development has dramatically altered our understanding of the etiology of autism spectrum disorders. Recent research has focused on the role of synapse

structure and its function as central to the development of autism and suggests possible targets for interventions. Brain connectivity has been one of the most popular areas of focus in medical imaging studies. Brain connectivity has served as the framework for conceptualizing autism spectrum disorders. Despite an increased awareness of autism, medical professionals and researchers have been quick to point out that autism is not at an epidemic level [30]. As of publication, there is no single or reliable group of causes that point toward the occurrence of autism. Studies have made efforts to tie the occurrence of autism spectrum disorders to a variety of variables including gastrointestinal issues [31, 32], environmental issues [33, 34, 35], and immunological issues [36]. However, no modern studies have been able to reliably reproduce results and concretely tie autism to any specific variable.

One of the most common myths in autism is that occurrence is directly tied to vaccinations, such as the MMR vaccination. A paper published by Andrew Wakefield in *The Lancet*, a renowned medical journal, made this claim in 1998 [37]. Researchers would go on to both disprove Wakefield's findings [38], and also prove that data presented in the work of Wakefield was fraudulent and artificially designed to push a personal agenda forward. Unfortunately, Wakefield's brash actions have created an ongoing debate surrounding autism spectrum disorders and vaccines that is still prevalent in the public's mind to this day [38]. It is important to realize that, to date, no valid studies have ever confirmed a link between any vaccine and autism spectrum disorders.

Studies into the structure of the brains of individuals with autism spectrum disorders have provided information that can help researchers better understand autism [39]. Studies, such as the infant sibling studies, are helping to identify the early markers of autism by defining the broader autism phenotype [40].

There are three sections of the human brain that are commonly implicated in autism spectrum disorders: the Grey Matter (GM), the White Matter (WM), and the Corpus Callosum (CC). Examination of these individual brain regions has demonstrated that a number of differences

exist between the neuropathology of individuals diagnosed with autism spectrum disorders and individuals diagnosed as neuro-typical. These examinations of the individual brain regions further indicate that there is a difference in connectivity resulting in a higher level of complexity in brain connections for individuals diagnosed with autism spectrum disorders [41].

The GM is found within the brain cortex. The GM contains nerve cells responsible for routing sensory and motor stimuli to inter-neurons located in the central nervous system. In individuals diagnosed with autism spectrum disorders, Abel et al. [42] identified a decrease in the quantity of GM in the brain cortex for individuals diagnosed with autism relative to a group of control individuals. Locations where this decrease is most prevalent include the right paracingulate sulcus and the left inferior frontal gyrus. Conversely, an increase in the quantity of GM was observed in the amygdala, periamygdaloid cortex, middle temporal gyrus, inferior temporal gyrus, and parts of the cerebellum.

Boddaert et al. found significant decreases in the concentration of GM in the superior temporal sulcus when comparing children having autism spectrum disorder to those without [43]. Children who fell within the autism spectrum also demonstrated a decrease in the concentration of white matter concentration in locations such as the right temporal pole and the cerebellum. Herbert et al. applied a similar voxel-based-morphometry (VBM) approach to a group of male individuals between the ages of 7 and 11 years [44]. The study by Herbert, demonstrated a substantially larger volume of white matter in the brains of individuals who fell within the autism spectrum. Herbert noted that the increase in overall volume was accompanied by a decrease in the cerebral cortex, hippocampus, and amygdala.

Other research has shown both different and contradicting findings. Egaas et al. [45], Schumann et al. [46], and Elnakib et al. [47] all implicated the corpus callosum in the development of autism. The corpus callosum is the largest single fiber bundle in the brain, being responsible for connecting the two hemispheres of the brain. When measured using different techniques, these studies all agreed in findings of a reduced size of the corpus callosum. A



Figure 2.3: *The amygdala of the brain is a small area located near the front interior of the brain. It can be seen in this 3D model highlighted in red.*

study by Schumann et al. contradicted the work of Herbert et al. by finding an increase in the size of the amygdala. While the findings of each of these studies is not wrong, and no articles have been redacted, the substantial contradiction between the findings of studies is indicative of the broad variability of patients who fall within the autism spectrum. The classification holds so many diverse types of patients, that there is great variability in the neuropathology of autism.

The cerebellum plays a role in the coordination of attention and motor control. Therefore, the cerebellum has also been proposed to play a role in autism spectrum disorders. Cerebellum mal-development has been a consistent finding in children who are unable to adjust their mental focus of attention to follow rapidly changing verbal, gestural, postural, tactile, and facial cues [48]. These cues signal the need for mental changes necessary when people are around groups of humans allowing them to process streams of social information. These cues allow an individual to alter their "spotlight of attention" from one source of information (e.g., auditory) to another (e.g., visual) in a fluid manner. This process of moving a source of atten-

tion involves disengaging ones attention from one source and then subsequently moving and reengaging it on another. Medically, this is the process of cognitively applying an inhibition to one source, and an making an enhancement to the new source. When a human selectively chooses to adjust the focus of their attention, the nervous system must quickly and accurately alter the pattern of neural responsiveness to sensory signals. This allows an individual to enhance the neural response to certain stimuli (e.g., vocalizations and gestures), and inhibit neural response to other stimuli [49, 50].

2.4 Prevalence of Autism

Since its discovery in 1975, the reported incidence of autism spectrum disorders has increased dramatically. Initially, it was believed that only one in 5000 individuals fell within the autism spectrum. As of 2014, this number has skyrocketed to include one out of every 68 children in the United States [51]. The Centers for Disease Control have identified that one in 42 boys and one in 189 girls are listed in the official autism prevalence reports by gender. Federal agencies and researchers have begun working on methods to acquire improved prevalence rates for autism spectrum disorders [52]. While the actual causes of autism spectrum disorders are unknown at this time, the rise in prevalence is most strongly believed to come from an increase in public awareness in the general population [53].

Initially, there were three classification of autism including autism spectrum disorders (ASD), Asperger's syndrome (AS) and pervasive developmental disorder (PDD). This classification has been simplified to the term autism spectrum. Asperger's syndrome is no longer classified as an autism spectrum disorder, however its removal does not contribute to a decrease in the overall prevalence of autism [54, 55]. This compression of a wide range of disorders into a single spectrum has contributed to difficulties in identifying and defining autism. The changing definition of autism has led to difficulties in accurately estimating the preva-

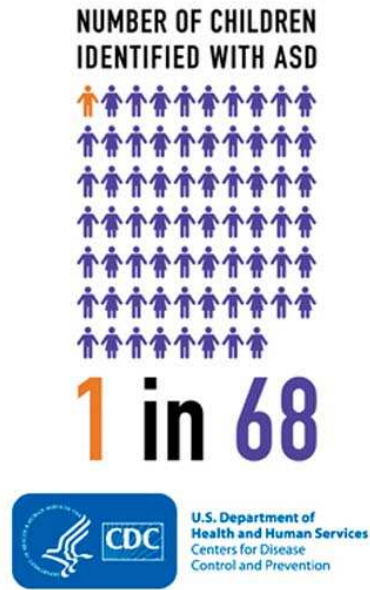


Figure 2.4: In 2014, 1 in 68 children are diagnosed with an autism spectrum disorder.

lence.

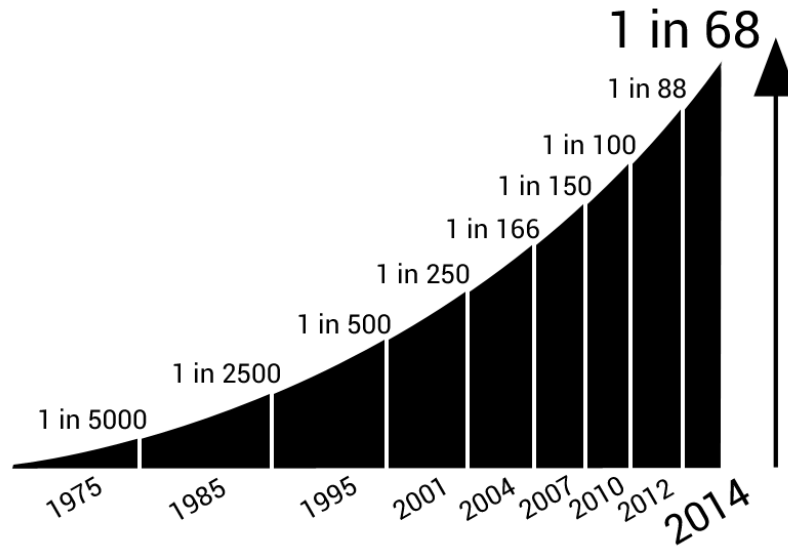


Figure 2.5: The prevalence of autism has unfortunately risen greatly since 1975.

2.5 Importance of Early Detection

Treatment for autism spectrum disorders is most effective when intervention is begun before the age of three years old [56]. Early intervention is over 400% more effective than intervention that begins at a later stage in life. Having the appropriate interventions can allow a child to integrate more easily with neurotypical children (sometimes referred to as mainstreaming) and achieve their maximum potential.

Early intervention is only possible when paired with early detection. At present, early detection of autism is difficult to achieve. Early detection is a key aspect of minimizing negative effects of autism on an individual. The primary reasons that it is difficult to detect autism at an early stage include: a wide variation in patient symptoms; slow identification and appearance of social and language deficits and delays; and the need for observable peer interactions, which often do not occur regularly before preschool. Parents often do not realize that their child has autism if there is not frequent opportunity to socialize with peers. It is equally unlikely that parents will notice the early signs of autism if the child is capable of meeting motor milestones, even if they exhibit language and developmental difficulties.

There is concrete evidence that points to large gaps of precious treatment time between the age of the child at the parents' first concern, the age of the first evaluation, and the age of a definitive diagnosis [57]. Parents typically become concerned between the ages of 15 and 22 months (earlier for children who also have intellectual disabilities). Children are often not seen by a specialist until 20 to 27 months at the earliest [41]. There is often further delay between the first visit to a specialist and the patient receiving a definitive diagnosis. Research confirms that this delay in diagnosis causes additional distress to parents and wastes valuable intervention time. This occurrence can be routinely observed in clinical visits with doctors and therapists in diagnostic and treatment facilities. The existence of this extreme delay has been confirmed by meeting with parents in specialized schools and support groups. The

importance of early detection and the difficulty in making treatment decisions indicates that the field of autism spectrum disorders need state-of-the-art technology for detection of autism in young children.

2.6 Existing Methods for Detecting Autism

The current gold standards of screening children include procedures that are difficult to validate and are subjective in nature. Pediatric evaluations rarely identify autism before the age of three [58]. The most common screening exams are the DSM-V [29], Autism Diagnostic Observations Schedule (ADOS) [59], and Autism Diagnostic Interview Revised (ADI-R) [60]. These exams can only be administered to children two years of age and older. While there has been progress in developing infant rating scales, these scales are not commonly used in clinical practice [61]. Most of these screening exams are accompanied by an IQ exam of the child, such as the Wechsler Intelligence Scale for Children (WISC) [62]. A diagnosis involves individual examinations from child psychiatrists, behavioral and occupational therapists, and speech language pathologists. The child may also be given an evaluation by a neurologist. A diagnostic session will generally last for one to two hours. During this time the child will undergo a battery of evaluations. All of the above mentioned exams, and other tests used but unlisted, provide subjective evaluations.

Current diagnostic exams are not capable of taking into consideration the disposition of the child on the day of the exam, or the impact of the length of the exam may have on the outcome. Parents have confirmed that they often leave the testing sites in a state of frustration and anxiety that their child may have not performed optimally during the evaluation. Discussions with professionals in the field have established there is a great deal of stress and difficulty with the current diagnostic methods. Due to the high prevalence of autism and the long wait times to receive a clinical evaluation for autism, it is not possible for parents to repeat

tests in order to wait for a "better day" for their child.



Figure 2.6: *The Wechsler Intelligence Scale for Children (WISC) is one of many tested administered to children. Assessments are made by determining, on a scale, how well the test administrator feels the child performed.*

Another method of early detection is the Modified Checklist for Autism in Toddlers (M-CHAT) [41]. The M-CHAT is another subjective screening tool that is much more simple to administer than the gold standard examinations. This test is used to help refer a child for early intervention services. The M-CHAT is ideally administered during the ages of 18 to 24 months. In this exam, parents complete the items listed on the checklist independently or by a scheduled interview. Meeting the criteria of the M-CHAT suggests the risk of ASD and indicates a potentially positive diagnosis for autism. M-CHAT administrators can request a follow up parent interview after the screening process. Unlike gold standard methods, the M-CHAT is an advisory screening tool, and cannot be used to make a formal diagnosis.

Researchers at Yale University have studied groups of two year old individuals diagnosed with autism [63, 64]. Researchers compared findings between children diagnosed with autism and children with developmental disabilities other than autism. The Yale program of research

focuses on mechanisms of socialization and their disruption in autism spectrum disorders. This work includes a close collaboration with Warren Jones in the development of novel techniques to quantify social processes using eye-tracking technologies [65]. The goal of using eye tracking is to visualize and measure the ontogeny of social engagement. New data analysis strategies have been used with children, adolescents, and adults who have autism spectrum disorders. These strategies reveal abnormalities of visual scanning behaviors when viewing naturalistic social approaches and situations. In the trials, a child would observe an actor alternating between the activities of talking and performing a pat-a-cake activity in a video. In this study, only children with autism showed a preference for the audio-visual synchronicity activities. Typically developing children were interested in the actor's engagement with the audience, regardless of the activity. Additional efforts have also focused on the use of eye tracking to distinguish early signs of autism [66, 67, 68]. This work has focused on how eye-tracking studies may help to distinguish early markers of autism through displaying social and video excerpts. Additional comparisons have been made between the usage of real footage versus cartoon animations.



Figure 2.7: *Results comparing neurotypical and autism spectrum eye tracking results.*

While there are many testing possibilities for detecting autism in children, the existing methods are not effective. When considering the DSM-V, ADOS, and ADI-R it is evident that a much quicker method needs to be developed to assist physicians, clinicians, and parents

in detecting autism in their children. Medical imaging, discussed in Chapter 3, shows great promise in providing quicker methods to make an accurate diagnosis.

CHAPTER 3

SURVEY OF SHAPE ANALYSIS METHODS

3.1 Introduction

*Everything we do, every thought we've ever had, is produced by the human brain.
But exactly how it operates remains one of the biggest unsolved mysteries, and
it seems the more we probe its secrets, the more surprises we find.*

- Neil deGrasse Tyson

The history of shape analysis techniques requires an inclusive survey of the applications prior methods that have been used. Methods of shape analysis for the human brain include techniques such as medial axis and skeletal analysis, geodesic distances, Procrustes analysis, deformable models, SPHARM, deformation-based morphometry, symmetry-based analysis, Laplace-Beltrami operators, and homologous modeling, among other techniques.

In 1979, Lande [70] proposed to analyze the shape of the brain by measuring the brain volume. While the volumetric analysis of brain scans, arguably, does not yield sound discriminatory features, it was a key starting point for shape analysis related to the brain. Later, Desimone et al. [71] and Martin et al. [72] proposed two more elaborate shape analysis frameworks. The first framework examined color, shape, and texture of the cortex on 2D

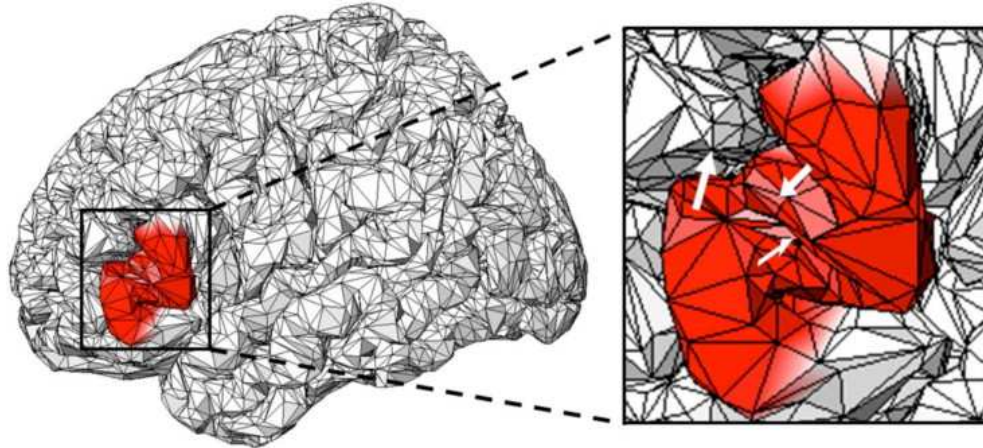


Figure 3.1: *3D mesh brain representation (the expanded section details its complexity and variability due to multiple different structures and gyrifications. Courtesy of Barras et al [69]*

scans of the brain. The second framework performed a more advanced analysis, by examining pre-generated mesh models of the brain ventricles. To more accurately represent the brain, the meshes were decomposed using eigen-vectors, that were obtained in a way similar to conventional Principal Component Analysis (PCA). These early frameworks for examining the shapes of brain constructs did not produce reliable descriptors of brain-related health or behavioral disorders, such as e.g. autism and Alzheimer's disorder. However, these frameworks inspired extensive subsequent research that helped to push the current field of brain shape analysis into the forefront of research and development for computer-assisted medical diagnostics.

Shape analysis applies to digital geometric models of surfaces and volumes of objects-of-interest to detect similarities or differences between the objects [73]. Typically, shape analysis is fully automated and is closely paired with some kind of object segmentation. Segmented objects are represented in a variety of digital formats including volumes, point clouds, and meshes. Most typically, the outer boundary (or surface) of an object, or a manifold representing this object, is examined. Henri Poincare [74] defines a manifold as the level set of a continuously differentiable function between Euclidean spaces that satisfies the non-

degeneracy hypothesis of the implicit function theorem. In a simplified version, the manifold can be thought of as an object with no holes or discontinuities.

Surface analysis, formally called surface interrogation, and computer-aided design systems explicitly examine intrinsic and extrinsic geometric properties of the surfaces found on objects and manifolds, including visual pleasantness, technical smoothness, and geometric constraints [75]. Surface analysis is used to detect surface imperfections, analyze shapes, or visualize different forms.

Shape analysis techniques can be primarily classified into first- and second-order types, each of the types contains large numbers of congruency-based, intrinsic, and graph based shape descriptors [75]. The first-order methods typically rely on surface normal vectors, inflections, and other intrinsic descriptors, obtained by the Laplace-Beltrami analysis. This method is considered the more popular geodesic path. Some congruency methods fall into this category, such as the shape distribution and symmetry analysis.

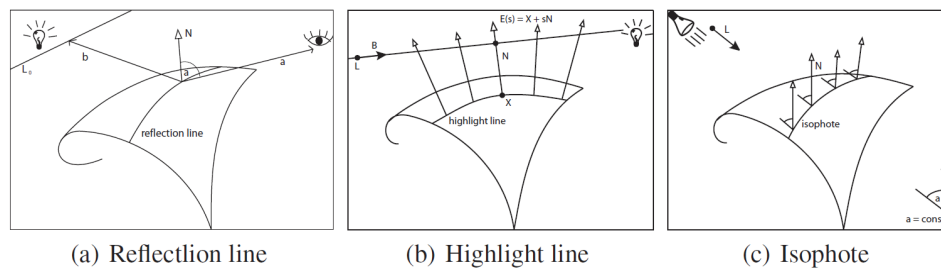


Figure 3.2: *1st-order shape analysis using reflections: examples of characteristics as seen in [75].*

Second-order analysis is based on the surface curvature and second derivatives. Typical descriptors are produced by moment analysis, spherical harmonics, and Procrustes analysis being invariant with respect to congruency and medial axis, skeletal, and Reeb graph analysis. These techniques heavily rely on the curvature. Importantly, many second-order analysis methods incorporate first-order techniques.

Both categories of shape analysis depend critically on shape interrogation, or the extrac-

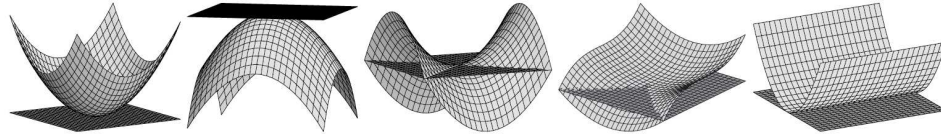


Figure 3.3: *Gaussian curvatures in the second-order shape analysis: from left to right, the convex, concave, saddle-shaped, parabolic point, and parabolic point region Gaussian curves as seen in [75].*

tion of structural characteristics of a shape from its geometric model [75], and re-meshing, i.e. repartitioning of primitive components to fit best the original shape. Most commonly, vertex-vertex or face-vertex methods are used to construct the meshes. The vertex-vertex method deals with a point cloud, where the points relate to critical junctures in an object, while the face-vertex method exploits faces that interconnect vertices in a specific and controlled manner [76]. A widely known example of the latter is Delaunay triangulation, in which every face is a triangle and the final mesh comprises a large number of interconnected triangular faces. While re-meshing helps to preserve the original shape of the object, it can also enhance some features of the shape. A primitive (such as e.g. a triangle that minimally characterizes the shape) can be applied repeatedly in a local region to fit any such feature.

Some of the most popular shape analysis techniques for application to the human brain are detailed and compared below. These include (i) the medial axis and skeletal analysis, which is commonly used for surface (2D) and volume (3D) reconstruction in complex models; (ii) geodesic distances to compare different brains by using intrinsic and graph based analysis; (iii) Procrustes analysis to provide accurate and quick statistical evaluation of shapes in rigid objects; (iv) deformable models evolving to fit boundaries of complex objects; (v) more recent 3D surface approximation with spherical harmonics to analyze the brain shape; (vi) morphometry based techniques to accurately analyze the volume of objects; (vii) and alternative and lesser used techniques.

3.2 Medial Axis and Skeletal Analysis

Medial axes of complex 2D/3D graphical models are widely used for surface reconstruction and dimensionality reduction. A medial axis, or a skeleton of an object, is defined as the set of internal points with over one closest point on the object's surface (see Figure 3.4). It is represented by a polygon or a similar simple construction of concatenated arcs and parabolas that follow the would-be determined centerline of the object. The medial axis and skeletal graphs facilitate indexing, matching, segmenting, or associating objects with one another. Medial axis analysis has a wide range of uses, that can be used in many anatomical applications outside of the brain, such as e.g. virtual colonoscopies.

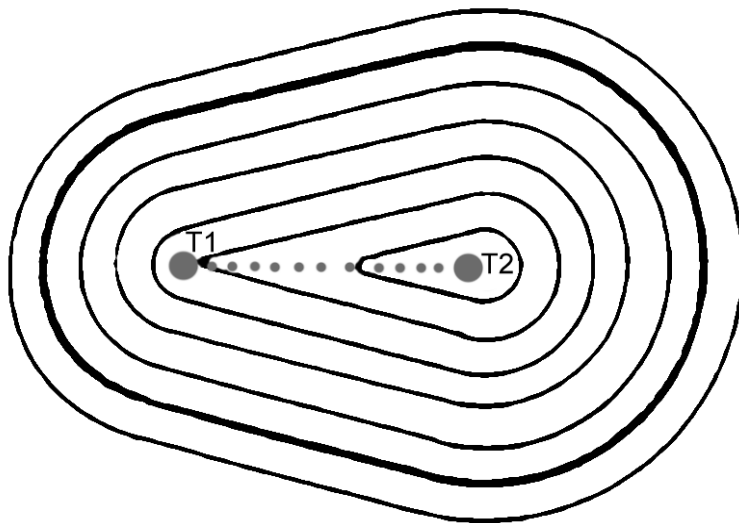


Figure 3.4: *Medial axis of a 2D object: the outer black line shows the boundary of the object and the central dark line connecting the points T1 and T2. Inner isolines indicate the same distances from the boundary [77].*

The notion of a skeleton of a 2D or 3D shape was first introduced by Blum et al [78, 79]. A skeleton begins by placing a primitive shape inside an object, such as a ball. The primitive is then inflated until reaching the object's surface, and this process is repeated until the object is filled with the maximum-size primitives. Connected centers of the primitives form the skeleton

that represents geometric properties of the object's interior, such as bends and elongations, and reveals the geometric structure, or constituent parts of the object, providing information about the object's position, orientation, and size.

Table 3.1: Automated (A) or semi-automated (SA) medial axis analysis: ground truth (GT) from clinician (C) or non-clinician (N) experts; dimensionality (Dim) and sizes (#) of experimental image databases.

Publication	Year	Mode	Dim	#	GT
Naf et al [80]	1996	A	3D	n/a	N
Golland et al [81]	1999	A	2D	66	C
Pizer et al [82]	1999	SA	2D	20	C
Golland et al [83]	2001	A	3D	30	C
Styner et al [84]	2001	A	3D	20	C
Gorcowski et al [85]	2007	A	3D	70	C
Elnakib et al [47]	2011	A	3D	34	C
Paniagua et al [86]	2013	A	3D	90	C

Table 3.1 indexes applications of skeletons for human brain analysis, starting with the novel proposal by Naf et al [80]. Naf classified various organs, including the brain, after characterizing their structure in 3D images with Voronoi diagrams and skeletons. Excepting [82], all the methods in Table 3.1 were used for the purposes of medical diagnostics or classification.

Golland et al [81] analyzed skeletons of the corpus callosum in 2D images to classify cases of schizophrenia. The initial skeletons were refined using snakes, or active contours, which evolved from different randomly chosen starting points. Then the curvature angles and the width of the skeleton were assigned discriminatory features. The angles were calculated between each set of adjacent points along the sampled medial axis, and the width was defined as the radial distance from the medial axis point to the surface boundary. Sampling more points of the skeleton provided finer details, but also increased the length of analysis time. The approach was tested on clinical datasets for normal and schizophrenic patients. A relatively high accuracy (70% in the best case) was obtained for identifying schizophrenia in patients

by the use of statistical shape analysis of the corpus callosum and hippocampus [83] (the accuracy of employing a linear classifier in determining schizophrenic patients on the training data proved consistently higher than the one using cross validation).

As noted in [81, 83], the main advantages and drawbacks of skeletons relates to their compact and intuitive shape representation that can be used for segmentation, tracking, and object recognition, including their high sensitivity to noise in the object's boundary, respectively. The complex and spatially variant structure of the brain leads to a large amount of noise along the typical shape boundary. To overcome this challenge, Golland proposed using general prior knowledge shapes, segmented training samples, and fixed topology skeletons [81, 83]. The significant benefit of such skeletons is they can be adjusted to each current object of similar shape and optimized for accuracy.

Pizer et al [82] proposed another method of quantifying object shapes in 2D images that were used in a variety of applications, including different brain structures. The skeletons were used to register brain shapes and compare the brain ventricles and brain stem. These structures could then be quantitatively described using a combination of medial axes and distance analysis.

Golland's works [81, 83] dealt primarily with the corpus callosum of the shape that typically featured no extending appendages. Contrastingly, Pizer's medial axis analysis was focused on the brain ventricles, the shapes of which (and their skeletons) often have one or more appendages. The skeletal appendages extend outward to include additional information about the more complex shapes. In Pizer's case, the medial axis analysis was modified to incorporate intersection points where multiple skeletons could be fused together, as e.g. in Figure 3.5. The resulting more complex skeletons proved to be useful for solving various problems, including segmentation and image registration [82]. Both Pizer's and Golland's approaches can be easily extended from 2D to 3D objects, at the expense of increased computational time due to the calculation of 3D distances.

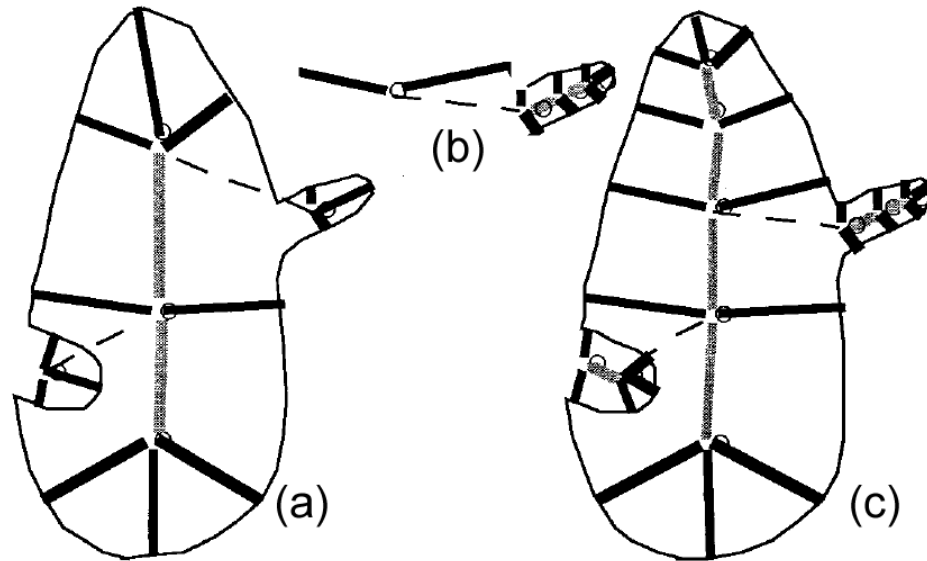


Figure 3.5: Shown is a visual representation of Pizer's [82] medial axis approach. Due to the complexity of the shape, it is initialized with three skeletons (a). These are then individually examined (b) to create a composite skeleton of the parent figure (c).

Styner and Gerig [84] expanded Pizer's concepts and analyzed the brain ventricles in 3D images using Voronoi skeletons and PCA to obtain discriminatory features of shape changes and locality. Spherical harmonics were used to analyze similarities between the skeletons and compare twin ventricles. Similar to Pizer's implementation, Styner and Gerig's skeletons contain many detailed branches and intersections to represent the shape of the object. To reduce the effect of the noise in the outer object's boundary of the shape, the shape was smoothed by using PCA to include only dominant characteristics of shapes. After this initial simplification, the Voronoi skeleton was constructed using standard medial axis computation. Then PCA was used once again to "prune" smaller and less important branches of the skeleton.

Gorcowski et al [85] used skeletons to analyze the shapes and poses of five brain structures in order to classify autism. The mean classification accuracy using poses, shapes, and a combination of poses and shapes was 56%, 60%, and 64%, respectively, for an image

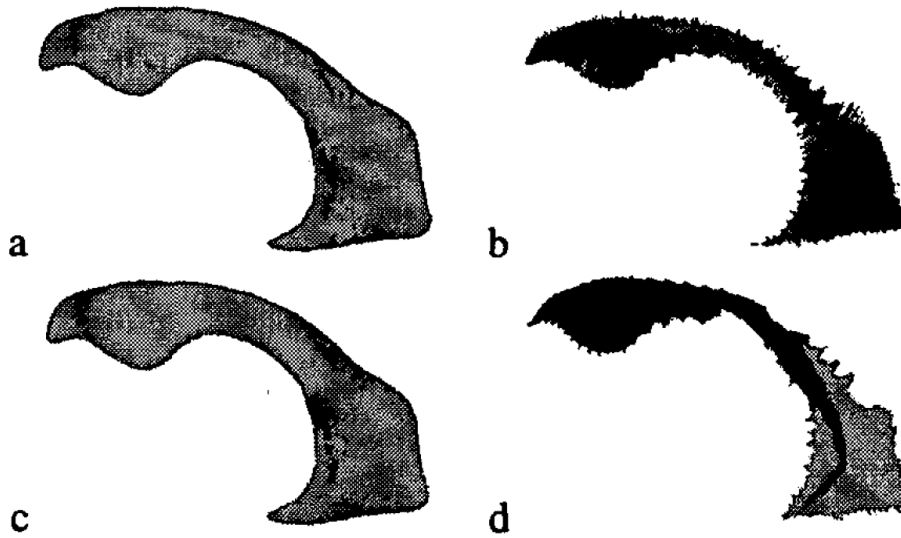


Figure 3.6: *The Voronoi skeleton pruning scheme designed by Styner and Gerig [84] and applied to lateral ventricles of the brain: the original boundary (a); the Voronoi skeleton before pruning (b); the reconstructed boundary (c) after the pruning, and the Voronoi skeleton after the pruning (d).*

database of 46 autistic and 24 control subjects. Although the combined features provided better results, the overall classification rate was rather low.

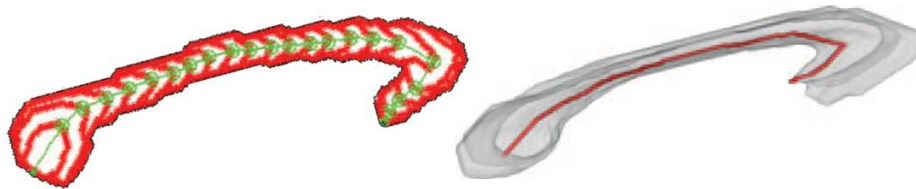


Figure 3.7: *Elnakib et al [47] skeleton extraction method showing the centerline extraction method on the left and the final extracted centerline on the right.*

Elnakib et al [47] obtained notably better classification accuracy, using a method shown in Figure 3.7, for autistic and control subjects by analyzing the corpus callosum centerline: the study correctly classified 94% autistic and 88% control subjects at the 85% confidence level, 94% autistic and 82% control subjects at the 90% confidence level, and 82% autistic and 76.5% control subjects at the 95% confidence level for the database of 17 autistic and

17 normal subjects. Elnakib et al. further extended their centerline extraction implementations [87, 88, 89, 90] to examine more aspects of the corpus callosum and its 3D centerline as applied to autism and dyslexia. This work was also explored by Casanova et al. [91, 92] and El-Baz et al [93].

Paniagua et al [86] used Spherical Harmonics (SPHARM) to calculate the mean latitude axis of ventricles in neonates. While this is not a full medial axis computation, it can be computed in a straightforward manner when using SPHARM. Paniagua introduced a fusion of the medial axis technique with SPHARM analysis to achieve a diagnostic classification in neonatal subjects. This method is consistent with the modern trend of combining techniques for better accuracy.

In total, medial axis and skeletal analysis are important shape analysis techniques for examining basic locations and shapes of structural parts of the brain. The main advantage of this method is that it creates simple representations of objects along with similarity measures and accurate descriptions for very complex shapes. These are useful in applications such as object classification and matching in medical diagnostics, providing clearer understanding of object structure and construction. The limited use of the object's surface is the major drawback of the skeletal analysis that significantly decreases the usefulness of the medial axes and skeletons in applications dealing with the surface characteristics and/or small variations in shapes.

3.3 Geodesic Distances

Of primary interest in the analysis of the brain is the ability to make detailed comparisons of different brains. This process often requires some form of non-rigid registration of the two surfaces of interest, or surface matching. A popular approach to shape analysis is the use of geodesic distances. Geodesic distances can serve as an important geometric mea-

surement of the brain and can help to provide a means of understanding complex shapes. Geodesic distances can serve to deliver a wealth of information about the surface geometry of a shape [75]. One of the first uses of geodesic distances, as applied to the brain, was by Griffin [94] in 1994. Griffin proposed the use of geodesic distance to characterize the cortical shape of the brain. This was later expanded by Khaneja [95] who used geodesic distance to examine the curvature of sulci in the brain.

Geodesic distance is a combination of intrinsic and graph-based analysis. Geodesic distance is defined as the length of the graph of a geodesic between two vertices within an object [96]. The distance is the shortest path between two points that can be found in a curved space (such as the surface of a sphere) and has a wide array of practical uses. If you have ever boarded a plane to travel between continents there is a strong likelihood that you have traveled on a geodesic path, because these are the shortest distances between two points. In the sulci of the brain, geodesic paths that connect two points in a single sulcus will often follow the curvature of the sulcus [97]. The detection of geodesic paths is a technique that is heavily utilized with surface meshes for common graphics operations such as mesh segmentation, watermarking, editing, and smoothing [75].

Table 3.2: Automated (A) or semi-automated (SA) geodesic distance analysis: ground truth (GT) from clinician (C) or non-clinician (N) experts; dimensionality (Dim) and sizes (#) of experimental image databases.

Publication	Year	Mode	Dim	#	GT
Wang et al [97]	2003	A	3D	n/a	N
Pastore et al [98]	2005	SA	2D	200	N
Huang et al [99]	2006	A	3D	36	C
Mio et al [100]	2007	A	3D	14	C
Butman et al [101]	2008	SA	3D	12	C
Hua et al [102]	2008	A	3D	20	N
Liang et al [103]	2008	A	3D	34	C
Joshi et al [104]	2012	A	3D	12	N

Table 3.2 lists applications of geodesic distance to the human brain analysis. Early ap-

plication methods by Wang et al [97] analyze the individual sulci of the brain. No methods that are primarily based on geodesic distance analysis have been used solely for medical diagnostics or classification.

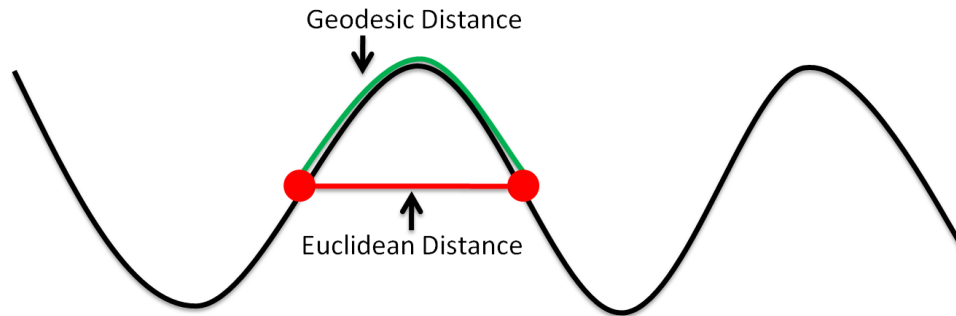


Figure 3.8: A visual representation of a simple geodesic distance. The two points on the curve (shown as red circles) are connected by Euclidean (red straight line) and geodesic (green curved line) distances. Note: the geodesic distance follows the arc of the curve.

Geodesic distance can be defined in a number of ways, however, the most common calculations are for the Gaussian curvature and the mean surface curvature of an object. These metrics allow features of the brain, such as the gyrus and sulcus, to be easily calculated by examining each point. Information about the convex and concave areas of the sulci can be determined by examining the sign of the Gaussian curvature to determine if the value is greater than or less than the mean surface curvature.

Once points of interest have been determined, the geodesic distance can be computed using a number of different methods [105, 106, 107]. One of the most popular, is the Fast Marching Method proposed by Kimmel and Sethian [107]. This method has gained wide acceptance due to the speed of the calculations, and its easy applicability to a vast array of applications, including two- and three-dimensional structures. An example of the result of the Fast Marching Method is illustrated on a synthetic surface in Figure 3.9.

Wang et al [97] proposed the use of geodesic distance analysis to analyze the sulci and gyral fissures of the brain for matching brains. Locations were classified and compared be-

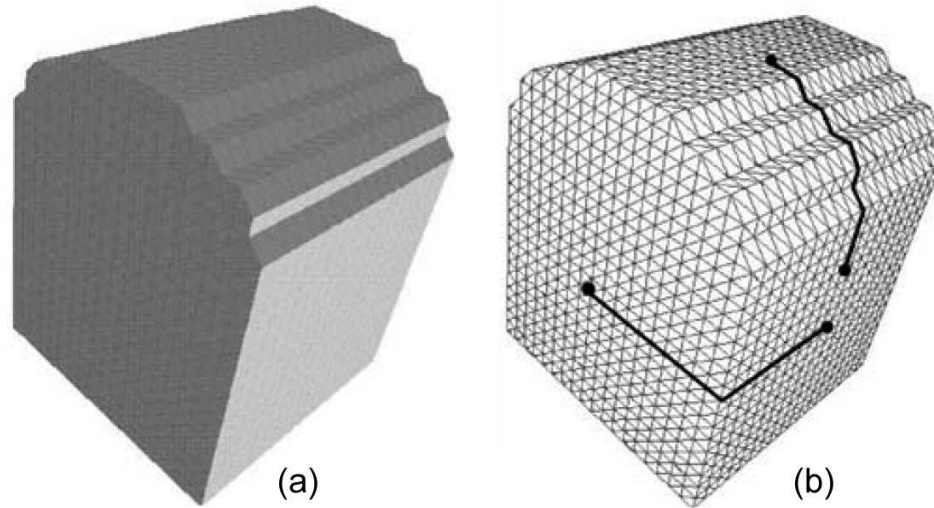


Figure 3.9: *Illustration showing the calculated geodesic distance between two points on a synthetic surface. (a) The original synthetic surface. (b) The synthetic surface overlaid with geodesic distances between four example points, calculated using the Fast Marching Method [107, 97]*

tween subjects. Areas where the sulci and gyri were similar could then be detected in the brain. Their results showed that surface correspondences could be found between brains, and that the fissures could be consistently identified across brains. Pastore et al [98] used geodesic distances to improve the segmentation accuracy (Figure 3.10) of the sulci and gyri in the brain. They found that geodesic distances proved to be a precise, efficient, and versatile method for segmenting the external boundary of the brain because the gyrifications of the brain have large curvatures and this feature is carried over into the MRI images.

Huang et al [99] proposed a brain extraction method for comparison of contours using geodesic distances. Results from this method showed that geodesic distances could aid in making extractions consistent across data sets, and the proposed method achieved a tight brain mask around the brain cortex. Mio et al [100] used geodesic distances to compare brains by comparing the decomposed geodesic curvature of each brain. Their work illustrated how geodesic distance could be successfully used to quantify morphological similarity and



Figure 3.10: Example of a geodesic distance calculation between two points (p and q) on the boundary of a 2D MRI scan [98]. The area has been zoomed and binarized so that the curvature can be clearly seen.

differences, and to identify particular regions where shape similarity and divergence were the most pronounced.

Butman et al [101] identified the brain ventricles and computed the volume of hydrocephalus in subjects using geodesic distance. Similar to the results of Huang, Butman showed that segmentation results were robust throughout data sets and were able to classify the hydrocephalus.

Hua et al [102] combined geodesic distances with vector image diffusion, a method of examining intrinsic geometric characteristics (e.g. mean curvatures) using a multi-scale diffusion and scale space, to match brains of different subjects. This method was shown to be superior to anisotropic diffusion and SIFT curvature matching algorithms for finding stable keypoints. Liang et al [103] approximated the curved cingulum bundle using Diffusion Tensor Imaging (DTI) tractography and geodesic distances. Although there were many limitations, a significant reduction in fractional anisotropy values, within specific anatomical regions, was detected when using geodesic distances.

Joshi et al [104] analyzed the sulcal curvature in the cortex of the human brain using geodesic curvature. They concluded that geodesic curvature showed promising prospects for analyzing the sulcal curvature in case of small temporal lobe lesions. In literature and application, geodesic distances are most often used to examine the curvatures of locations of

the brain and to locate key points that can be identified due to their curved nature. Geodesic distances have proven to be a useful shape analysis tool in segmentation, registration, and analysis. Geodesic distances are unique in that they incorporate aspects of first- and second-order analysis.

Geodesic distances have a large number of applications, but the primary advantages are applications in segmentation and the identification of locations in the shapes of brains. This method provides an excellent metric for examining curvature and localized areas of objects, and can provide many discriminatory metrics for classification. The major drawbacks of geodesic distances are a generally localized nature, and the difficulty of examining large and complex objects that have numerous inflections in their curvature. Three-dimensional analysis of shapes, such as the cortex and white matter of the brain, prove more challenging for geodesic analysis.

3.4 Procrustes Analysis

Procrustes analysis is a statistical form of congruent shape analysis that primarily focuses on the distributions of sets of shapes. It is interesting to note, that Procrustes was a rogue and bandit who was the son of Poseidon in ancient Greek mythology [108]. He was known for either stretching people or cutting off their limbs to force them to fit within a statically sized iron bed. The process of Procrustes analysis, thereby, refers to shape analysis in which properties such as translation, rotation and scaling are removed so that the shape can be fit into a common reference frame. The process is inherently congruent. Procrustes analysis is most commonly performed by superimposing shapes on top of one another, and then applying uniform properties so that geometric transformation of the objects are removed and the shapes can be compared. Procrustes analysis has also served an important role in shape warping, especially as applied to the brain [109].

Table 3.3: Automated (A) or semi-automated (SA) Procrustes analysis: ground truth (GT) from clinician (C) or non-clinician (N) experts; dimensionality (Dim) and sizes (#) of experimental image databases.

Publication	Year	Mode	Dim	#	GT
Duta et al [110]	1999	A	2D	28	C
Penin et al [111]	2002	SA	3D	N/A	N
Bienvenu et al [112]	2011	A	3D	144	N

Table 3.3 exemplifies applications of Procrustes analysis to brain analysis. This method begins with the early application by Duta et al [110], which analyzes the properties of skull structure. Bienvenu et al [112] used Procrustes analysis primarily for medical diagnostics or classification.

Nicolae Duta et al [110] proposed a method for the basis of Procrustes analysis in 2D shape models for use in medical image analysis. Duta defines the main reasons for the use of Procrustes analysis as a convenient way to compute the difference in a prototype (average shape) from a set of simultaneously aligned shapes. Once the point correspondences are found, there exists an analytical or exact solution to calculate the alignment problem.

Mathematically, Procrustes analysis seeks a solution to the following problem: Assume a given a set of m shape instances where $S_k = (x_i^k, y_i^k)_{i=1 \dots n_k}^{k=1 \dots m}$ that is represented by a set of landmarks or boundary points. This set is partitioned into a set of clusters, and for each shape cluster a mean shape, or prototype, must be computed. The set of prototypes can then be used for segmentation or the calculation of other metrics. One such metric is a Procrustes residual, which is defined as a deviation in landmarks on a specific object from the consensus of a group, or the prototypes. Duta illustrated the usage of Procrustes analysis for the segmentation of objects and registration of different objects following segmentation. Duta also introduced algorithms for global and local similarity measures using Procrustes analysis.

Penin et al [111] proposed a method for the study of the skull of humans and brains as



Figure 3.11: *Example of Procrustes prototypes by Penin et al [111] for different brain structures. The dark points are the landmarks in each prototype. The landmark points are connected for clarity. The small dots surrounding each main landmark point are the different landmark locations of the shapes used to construct the final prototype.*

compared to other primates through the use of tri-dimensional Procrustes analysis. In this study, twenty-nine key features were identified as common landmarks between the different skulls. The shapes of the features were defined as Procrustes residuals. A Procrustes residual is a deviation in a landmark from the consensus of a group. One downside, noted by Penin, was that in Procrustes analysis the size and shape are calculated as independent vectors when using traditional shape theory, meaning that normalization of objects is often required during pre-processing.

Bienvenu et al [112] proposed a similar method for examining endocranial variations. Bienvenu found that Procrustes analysis was more favorable for examining the skull, because it has less variability than the cortical surface itself, and is therefore less subjective to the noise introduced by the large differences found in the cortex. Similar to Penin, Bienvenu selected specific landmarks commonly found on the endocranial surface and generated a prototype. This prototype was then used to examine the differences between the males and females of different species. It was found that Procrustes analysis was capable of determining not only

the gender, but also the species due to the large variation in the landmarks of the prototypes.

In a follow up to his previous work, Duta examined the automated construction of shape models using Procrustes analysis [113]. This study determined that the major advantage of Procrustes analysis, as applied to the brain, was that Procrustes analysis provided a reliable method of classifying and segmenting anatomical structures in relatively rigid objects including the ventricles and corpus callosum of the brain (Figure 3.12).

Procrustes analysis struggles with more complex structures of the brain, specifically the gray and white matter. Procrustes analysis therefore provides an accurate and fast method of analysis for objects that do not have significant variation. This limits applicability to only specific cases. However it is a useful measure for examining the shape of the brain and its more rigid structures.

One of the more direct problems related to Procrustes analysis, is the method of selecting landmarks on the brain. Due to the variability in sulci and notable landmarks of the brain, there may be an impact on the resulting analysis. Furthermore, the selection of landmarks could introduce a bias into the analysis. If landmarks are not appropriately located, areas may either be over or under-compensated, adding an additional degree of complication to this form of analysis. It is likely one of the driving reasons that this methodology has only seen a moderate amount of modern adoption.

Procrustes analysis, while useful, does not provide as in-depth an analysis of complex objects as some other methods. Discussion of deformable models and spherical harmonics will illustrate examples of the more popular techniques for identifying mathematical differences between three-dimensional shapes that the human eye is unlikely to be able to classify.

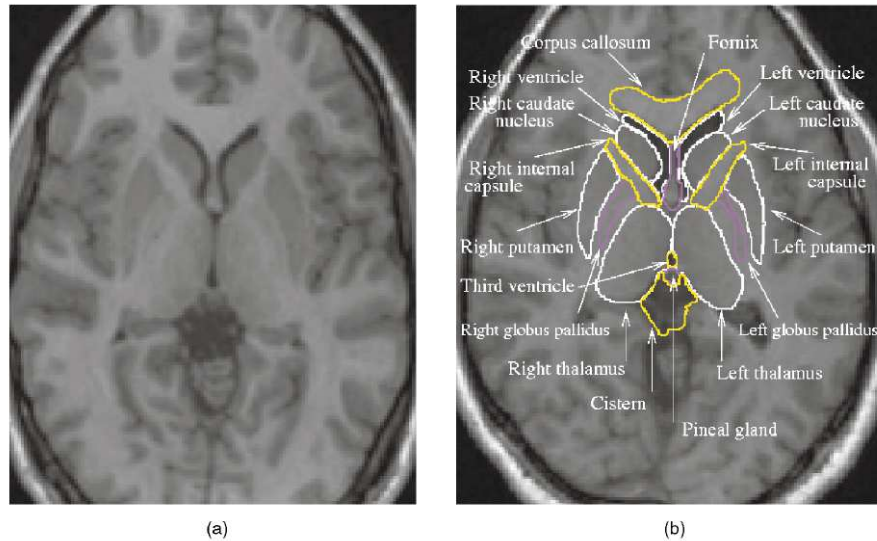


Figure 3.12: *Magnetic resonance image (a) of the human brain. Neuroanatomic structures of the brain are highlights by a neuroanatomist (b). Structures shown in yellow are accurately classified by Procrustes analysis. Image courtesy of Duta et al [113].*

3.5 Deformable Models

Deformable models, known as active surfaces, are a model-based technique that combines geometry, physics, and approximation theories in order to offer a unique and powerful approach to image analysis [114]. Deformable models have proven useful in a variety of brain applications, including segmentation, shape representation, matching, and motion tracking. Unlike more rigid methods of analysis, deformable models are capable of accommodating for significant variability in shapes (Figure 3.13), like those found in the brain, over time and a variety of different individuals. While deformable models were originally used in the field of computer vision, their application to the analysis of complex medical objects, such as the brain, was quickly realized by the scientific community. In their two-dimensional (2D) forms, deformable models are often referred to as active contours or snakes [115, 116].

Deformable models have mathematical foundations found in geometry, physics, and

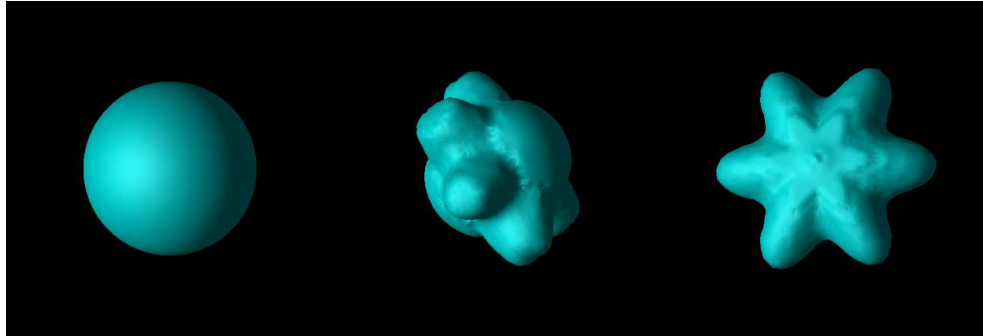


Figure 3.13: *Illustration of a 3D deformable model as it contracts on a star-like object [116]. Three frames of progression are shown starting at the left with the original spherical model. The model gradually deforms around the object until it has converged on the star in the center.*

shape approximation theory [114, 115, 116]. Geometry is used to represent an object's shape, and deformable models commonly make use of complex geometric representations, such as splines, that offer flexibility and many degrees of freedom. The use of physics is applied to impose constraints, controlling how that shape can vary, with respect to properties such as space and time. The name "deformable models" is closely associated with the incorporation of this elasticity theory, albeit at a physical level. Therefore, deformable models are most commonly constructed inside a Lagrangian dynamics setting able to respond naturally to constraints and applied forces. As a model deforms in the Lagrangian setting, the deformation energy will give rise to internal elastic forces. Potential energy functions for the external model are defined so that the model deforms to fit the data. Through the combination of these two energies, deformable models can be used for many situations. Some of the most common shape analysis applications of deformable models are in the areas of segmentation and volume analysis, along with shape matching and registration.

Table 3.4 exemplifies applications of deformable model to human brain analysis. It includes methods starting with the early application by Davatzikos et al [117] which was used to identify the central sulci and interhemispheric fissures in the brain. No methods that are primarily based on deformable model analysis have been used primarily for medical diagnostics

Table 3.4: Automated (A) or semi-automated (SA) deformable model analysis: ground truth (GT) from clinician (C) or non-clinician (N) experts; dimensionality (Dim) and sizes (#) of experimental image databases.

Publication	Year	Mode	Dim	#	GT
Davatzikos et al [117]	1996	SA	3D	6	N
Dale et al [118]	1999	A	3D	100	C
Smith [119]	2002	A	3D	45	C
Zhuang et al [120]	2006	A	3D	49	C
Joshi et al [121]	2007	A	3D	6	N
Tu et al [122]	2007	A	3D	28	C
Huang et al [123]	2009	A	3D	36	C
Liu et al [124]	2009	A	3D	38	N
Li et al [125]	2011	A	3D	5	N
Hashioka et al [126]	2012	SA	3D	14	C

or classification.

Davatzikos et al [117] proposed one of the earliest methods for analyzing the cortical surface of the brain using deformable models. They used deformable models to identify similar landmarks for alignment on different brains. Their results showed that deformable models could be used to register two different brains with one another, in order to select cortical and subcortical landmarks on the brain cortex.

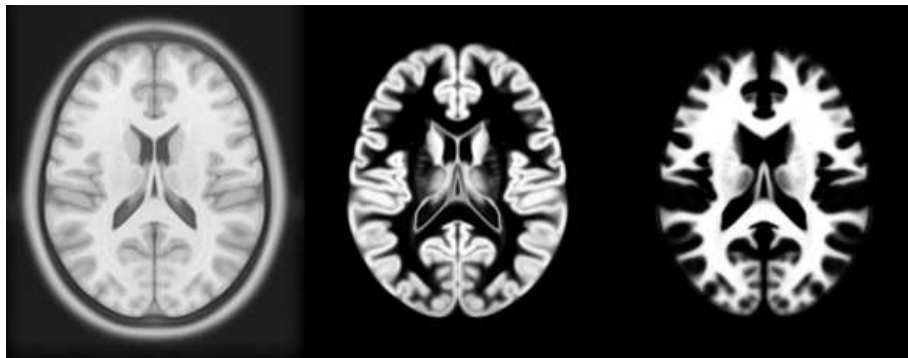


Figure 3.14: Segmentation results of the brain showing the gray matter and white matter are shown here. The goal illustrated in this figure is to analyze the volume, the deformable model proves useful in isolating the voxels that belong to the brain. After identifying the desired portion of the brain with a deformable model, calculating the volume becomes a trivial task [118].

Dale et al [118] used a simplified deformable model to segment the cortex of the brain (similar to Figure 3.14). The algorithm proved to be a robust method of identifying the cortex of the brain with an average accuracy of 96% across a wide variety of subjects. In 2002, Stephen Smith [119] introduced the Brain Extraction Tool (BET). An intensity model was used to initialize the surface model, which was later refined to extract the brain. It was shown to be a fast and accurate method of extraction, having a mean percentage error of about 7% over 45 data sets. Zhuang et al [120] used a model-based level set to perform skull stripping on pediatric and youth brains. The approach showed good accuracy using the DICE metrics with notable improvements over the BET proposed several years before by Smith [119].

Joshi et al [121] used deformable models to register sulci along with a coregistration of brain volume data. Results showed a statistical improvement over the AIR [127, 128] and HAMMER [129, 130] methods. Tu et al [122] used deformable models to aid in segmenting specific locations found in the brain. The discriminative model they developed played a major role in obtaining clear segmentations. Additionally, the segmentation could be further improved by adjusting the smoothness of the model and constraining the shape with a global shape model.

Huang et al [123] proposed the use of deformable models to segment the cortex, gray matter, and CSF of the human brain. They showed promising results when the data was analyzed using the DICE metric. They concluded that deformable models led to improved segmentation accuracy and robustness when applied using a hybrid approach against, as opposed to using only geometric or statistical features. On real clinical MRI data sets, the hybrid approach demonstrated an improved accuracy over other state-of-the-art approaches.

Liu et al [124] suggested a deformable model that was driven by radial basis functions to be used for automated extraction of the brain. This model proved to be an accurate and fast technique, having a similar accuracy to the BET proposed by Smith [119]. Li et al [125] proposed an alternative method for the automated extraction of the brain using a deformable

model. Their method was an extension of the human brain extraction tool and was found to more reliably extract brains through the inclusion of a deformable model. Hashioka et al [126] proposed a method that utilized Active Contour Modeling (ACM), also commonly referred to as “snakes”, for the extraction of the cortex in neonatal children. The results showed a Sensitivity of 98.5% with a false positive ratio of 13.8%. While their results were largely successful when an optimal head contour was present, they noted that a non-optimal contour performed less robustly.

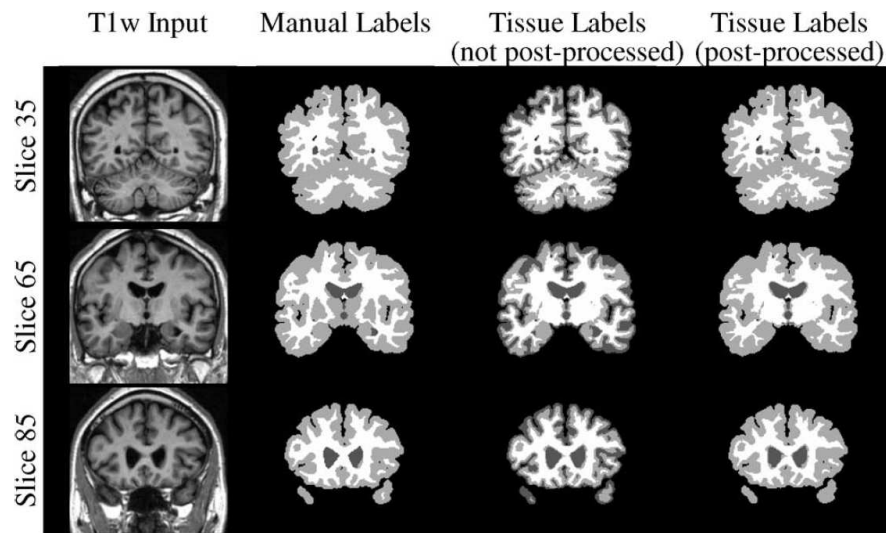


Figure 3.15: *Qualitative segmentation performance of a deformable model for labeling tissues in the brain in T1- and T2-weighted MRI images. Looking at the phantom and final labeled data, the high level of accuracy that deformable models possess for labeling locations in the brain can be seen [123].*

While deformable models may not be in the forefront of diagnosis classifications, they have become an integral element of shape analysis. These models excel in the area of shape segmentation. Deformable models are also very adaptable at isolating complex regions of shapes for further analysis. Deformable models provide useful and accurate ways to identify and segment locations in the brain which is a critical step in analyzing its shape. The major drawback of using deformable model analysis is that it does not often provide many metrics

for directly examining the brain for the purpose of classifying or matching.

3.6 Spherical Harmonics

Dealing with the orientation of the brain and aligning two brain objects with one another to compare differences in shape can prove challenging and time consuming. Spherical Harmonics (SPHARM), a popular method of shape analysis, can be used to improve alignment accuracy and speed. Spherical harmonic analysis [131, 132] considers 3D surface data as a linear combination of specific basis functions. Additionally, SPHARM provides a rotation invariant common coordinate system in which shapes can be analyzed. The main goal of SPHARM is to decompose a 3D object into concentric, or unit, spheres. This process discards the orientation information that primarily accompanies a 3D shape representation of an object. The result is a shape descriptor that is descriptive and invariant to orientation.

One of the major advantages of using spherical harmonics analysis of the entire brain is the ability to identify differences in the shape of different structures. The volume changes in the brain include intuitive features that can be used to describe illness, disorders, and atrophy. The area that SPHARM seeks to address is the structural changes inherent to the surface of the brain. The use of SPHARM applied to brain analysis was first proposed by Gerig et al [131] for the analysis of the lateral ventricles of the brain. SPHARM was originally developed as a technique for model-based segmentation and data storage, however its applications have grown in recent years. One important factor of SPHARM analysis, is that it relies primarily on the surface of a shape and manifold properties. Therefore, only manifold shapes (e.g. shapes without volumetric holes or disconnects in their surfaces) can be accurately analyzed.

SPHARM is a global-based shape analysis technique that is hierarchical in nature. Any shape can be parameterized by a set of basis functions, and these basis functions are the referred to as spherical harmonics. Spherical Harmonics was first discovered by Simon de

Laplace in 1782, although it would take several centuries before they were applied to the shape analysis of the brain. SPHARM is based on Laplace's equation, and it involves a mathematical solution regarding the angular components of the equation.

Spherical harmonic basis functions Y_l^m , $-l \leq m \leq l$ of degree l and m are defined on $\theta \in [0; \pi] \times \phi \in [0; 2\pi]$ by the following definitions [131]:

$$Y_l^m(\theta, \phi) = \sqrt{\frac{2l+1}{4\pi} \frac{(l-m)!}{(l+m)!}} P_l^m(\cos \theta) e^{im\phi} \quad (3.1)$$

$$Y_l^{-m}(\theta, \phi) = (-1)^m Y_l^{m*}(\theta, \phi)$$

where Y_l^{m*} denotes the complex conjugate of Y_l^m . P_l^m describes the associated Legendre polynomials given as

$$P_l^m(\omega) = \frac{(-1)^m}{2^l l!} (1 - \omega^2)^{\frac{m}{2}} \frac{d^{m+l}}{d\omega^{m+l}} (\omega^2 - 1)^l \quad (3.2)$$

The surface is decomposed from Cartesian coordinate functions and is represented as $v(\theta, \phi) = (x(\theta, \phi), y(\theta, \phi), z(\theta, \phi))^T$. To express a surface using spherical harmonics the following equation is used:

$$v(\theta, \phi) = \sum_{l=0}^{\infty} \sum_{m=-l}^l c_l^m Y_l^m(\theta, \phi) \quad (3.3)$$

where the coefficients c_l^m are three-dimensional vectors that are typically obtained through solving a least-squares problem for the points. These basis functions allow for a hierarchical description of the surface of a shape. The more coefficients used in the reconstruction, the more detail is present in the final constructed shape.

Table 3.4 lists applications of SPHARM to human brain analysis. The table includes methods starting with the early application by Keleman [133], along with notable applications, e.g. Gerig et al [131], which have shown SPHARM as a potential method for classifying neurolog-

Table 3.5: Automated (A) or semi-automated (SA) spherical harmonic analysis: ground truth (GT) from clinician (C) or non-clinician (N) experts; dimensionality (Dim) and sizes (#) of experimental image databases.

Publication	Year	Mode	Dim	#	GT
Keleman et al [133]	1999	A	3D	21	N
Gerig et al [131]	2001	A	3D	20	C
Chung et al [132]	2007	A	3D	28	C
Uthama et al [134]	2007	A	3D	40	C
Abdallah et al [135]	2008	A	3D	18	C
Chung et al [136]	2008	A	3D	28	C
Uthama et al [137]	2008	A	3D	20	C
Esmaeil-Zadeh et al [138]	2010	A	3D	95	N
Nitzken et al [139]	2011	A	3D	45	C
Nitzken et al [140]	2011	A	3D	30	C
Geng et al [141]	2011	A	3D	5	N
Kim et al [142]	2011	A	3D	n/a	C
Paniagua et al [86]	2013	A	3D	90	C
Hosseinbor et al [143]	2013	A	3D	69	C

ical disorders. SPHARM has been widely applied as a method for potential diagnosis.

Brechbhlér et al [144] demonstrated the usage of SPHARM as a method for parameterizing closed surfaces of 3-dimensional objects. In 1999 Keleman [133] demonstrated an ability of SPHARM to analyze shape deformations in neuro-radiological data. Keleman used training data to compute SPHARM representations of the brain which were then simplified using PCA and applied to the process of segment a cortex. Their results showed that SPHARM was a promising technique for improving standard brain segmentations because of the included 3D forces offered by SPHARM.

Gerig et al [131] proposed one of the most significant applications of SPHARM. It was used to analyze the volume similarity between twin brains and demonstrated that SPHARM shape measures reveal new information in addition to size measurements. They proposed that this information might become relevant for an improved understanding of the structural differences, not only in normal populations, but also in comparisons between healthy controls and autistic patients. An example of the deformation of an object is shown in Figure 3.16.

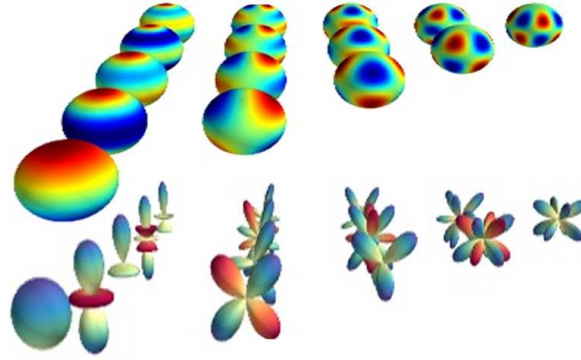


Figure 3.16: *Decomposition of an object, as described by Gerig et al [131]. In the upper section of the image the spherical harmonics are plotted overlaid on top of a unit sphere, and below the polar plot of the unit spheres are images shown to provide more detailed understanding of the actual information contained within each sphere.*

Styner and Gerig [145] later proposed a framework package based on SPHARM analysis entitled SPHARM-PDM, which could be used for analysis in a multitude of brain structures. This SPHARM-PDM package has been used for examining various brain structures, including work by Kim et al [142] on the hippocampus, and by Paniagua et al [86] (previously mentioned) on the lateral ventricles in neonates.

Chung et al [132] proposed a method to analyze the computed SPHARM coefficients to identify autism in subjects. While the SPHARM coefficients did not generate reliable results, their work showed the ability to accurately and efficiently encode neurological information using a weighted-SPHARM. Chung et al [136] continued their application to explore statistically significant differences between autistic and control subjects using the coefficients. While their work showed some areas of statistical difference, the detected locations were largely random. This work did show that weighted-SPHARM provides better smoothing in cortical applications than other comparative methods.

Uthama et al [134] proposed the analysis of the ventricle geometry using SPHARM between Parkinson's Disease (PD) and control patients. They showed that a statistically signifi-

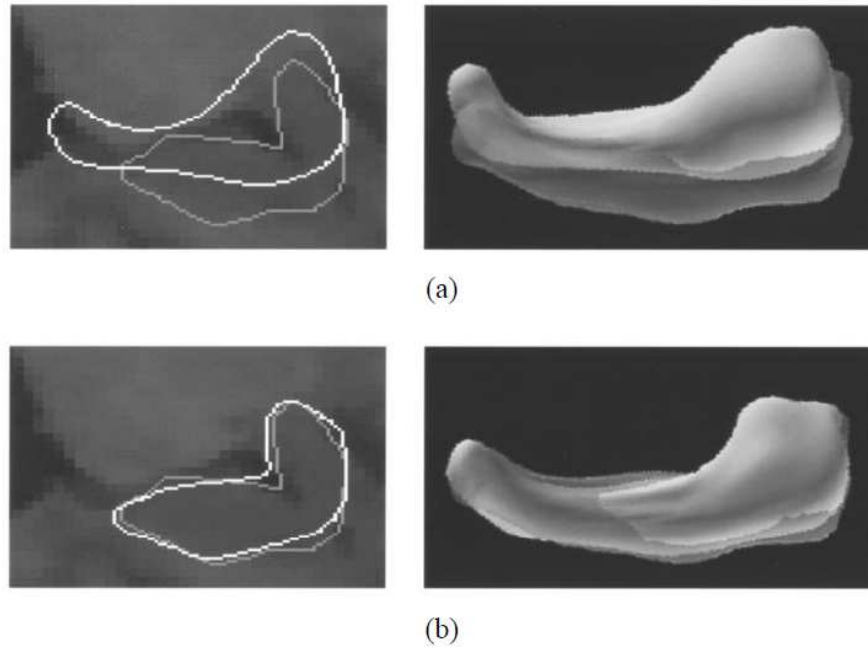


Figure 3.17: Keleman's use of SPHARM to segment two different hippocampus shapes [133]. On the left side the two-dimensional segmentation is shown, while the corresponding three-dimensional SPHARM segmentation is shown at right for the hippocampi a and b.

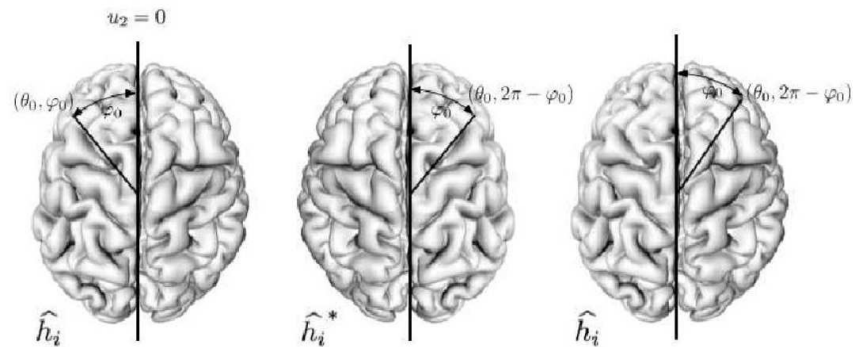


Figure 3.18: Chung's [132] use of the SPHARM distance correspondence to establish a mapping from the left hemisphere to the right hemisphere using a least-squares method.

cant comparison ($p < 0.05$) of controls and PD subjects could be performed using SPHARM. Uthama was able to detect subtle changes in synthetic and clinical brain ventricle data. Additionally, Uthama et al [137] proposed the use of SPHARM to perform fMRI spatial analysis.

This work demonstrated differences in the way PD patients and healthy controls respond to an increased task demand. The analysis illustrated that the inability to respond to a task demand was reflected in the failure of PD subjects to increase basal ganglia output, and a reliance on cerebellar and cortical activity to enable successful performance.

Abdallah et al [135] applied a parameterization to 3D meshes, and then used SPHARM application to improve shape detection of the ventricles. Results showed that a parameterization of a shape followed by SPHARM analysis can lead to improve comparisons and better shape descriptors.

Esmaeil-Zadeh et al [138] used SPHARM to analyze the hippocampus to classify subjects as either normal or epileptic. Their results showed that in an optimum case, a 90.32% rate of classification of left and right anterior temporal lobes could be achieved when validated using the leave-one-out method.

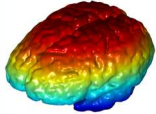
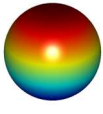
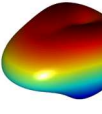
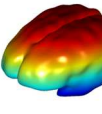
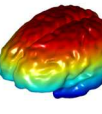
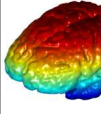
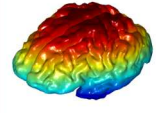
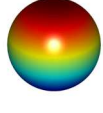
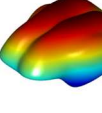
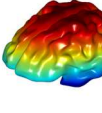
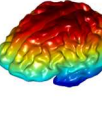
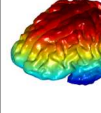
	Original mesh	1 SH	5 SHs	20 SHs	40 SHs	60 SHs
Autistic						
Control						

Figure 3.19: Method proposed by Nitzken [139] for the approximation of the 3D brain cortex shape for autistic (A) and normal subjects (C).

Nitzken et al [139, 146] proposed an alternative use of SPHARM by using the reconstruction error to classify autism (Figure 3.19). Using this error, classification accuracies, within a test population, of 100% could be achieved and illustrates a potentially effective way of classifying autism in subjects. Nitzken et al [140, 147] later expanded this theory to the classification of dyslexia. A variation was further used to examine changes related to aging in the

human brain [148].

Geng et al [141] demonstrated the use of SPHARM coefficients to perform nonrigid registration of brain white matter and fiber tracts. This method performed better than standard second order registration methods, although this could also be attributed to the use of higher order method inherent to SPHARM. Overall, it was found that SPHARM provided a notable improvement. In 2013, Hosseinbor et al [143] proposed a further expansion of SPHARM to a 4-dimensional representation of subcortical structures. This new 4D SPHARM is entitled HyperSPHARM and is intended to serve as a method of tracking changes over time. This allows SPHARM to directly compete with applications typically reserved for methods such as Voxel- and Deformation-Based Morphometry.

SPHARM is one of the most beneficial methods of shape analysis for providing meaningful global analyses of objects. SPHARM excels in brain analysis areas that involve large surfaces, such as the cortex and white matter. The major drawbacks to SPHARM analysis are that it can be difficult to localize the SPHARM analysis to understand select locations. It also struggles with applications such as segmentation and automated identification of objects in two-dimensional images. SPHARM's greatest strength comes in its ability to distinguish between shapes and its applications such as clinical diagnosis classification.

3.7 Voxel- and Deformation-Based Morphometry

Voxel based morphometry (VBM) is another technique for examining the entire brain [149, 150]. Table 3.6 lists applications of Morphometry-based techniques as applied to human brain analysis. VBM is a technique wherein brains between subjects are generally warped, aligned, and normalized in order to remove large differences between the brains. Volume is then compared across each brain on a voxel by voxel basis. In VBM, smoothed values of the voxels or an averaging of a voxel and its neighbors are typically used. The primary

usage for VBM, is the detection of differences and similarities for images between two populations or shapes [151]. Deformation-based morphometry (DBM) is a similar form of statistical analysis to VBM. However, instead of measuring the changes between voxels, the process uses changes on the deformation fields. The most common variant of DBM in brain shape analysis is Tensor-based morphometry (TBM), which is based on the Jacobian determinants. While DBM, and more specifically TBM, are able to detect more subtle changes between brains, the morphometries introduce a significantly higher degree of computational complexity when compared to VBM. In these incidences, the warping often involves highly non-linear algorithms. Both VBM and TBM are commonly used for calculating cortical thickness measurements as well.

Table 3.6: Automated (A) or semi-automated (SA) voxel- and deformation-based morphometry analysis: ground truth (GT) from clinician (C) or non-clinician (N) experts; dimensionality (Dim) and sizes (#) of experimental image databases.

Publication	Year	Mode	Dim	#	GT
Chung et al [152]	2002	A	3D	28	C
Leow et al [153]	2006	A	3D	17	C
Lepore et al [154]	2007	A	3D	30	C
Afzali et al [151]	2010	A	3D	31	C
Wang et al [155]	2012	A	3D	2	C
Yang et al [156]	2012	A	3D	60	C
Fletcher et al [157]	2013	A	3D	285	C
Shi et al [158]	2013	A	3D	35	C

In 2001, Ashburner et al [159] made a case for VBM in response to criticism posed in Dr. Bookstein’s article “Voxel-Based Morphometry Should Not Be Used with Imperfectly Registered Images” [149]. He explained that VBM was a method originally intended to explore cortical thickness that benefits from not being affected by volume changes, the major weakness of volumetric analysis. While acknowledging the partial volume effect as a potential issue, Ashburner detailed how modern normalization techniques allow for high-resolution image alignments and warping. He discussed that the use of VBM is not subject to the issues

of landmark selection as found in other analysis methods like Procrustes analysis. In summary, VBM is a useful and reliable method for examining the volume of the brain and its sub-components, while avoiding the traditional pitfalls associated with volumetric measurements.

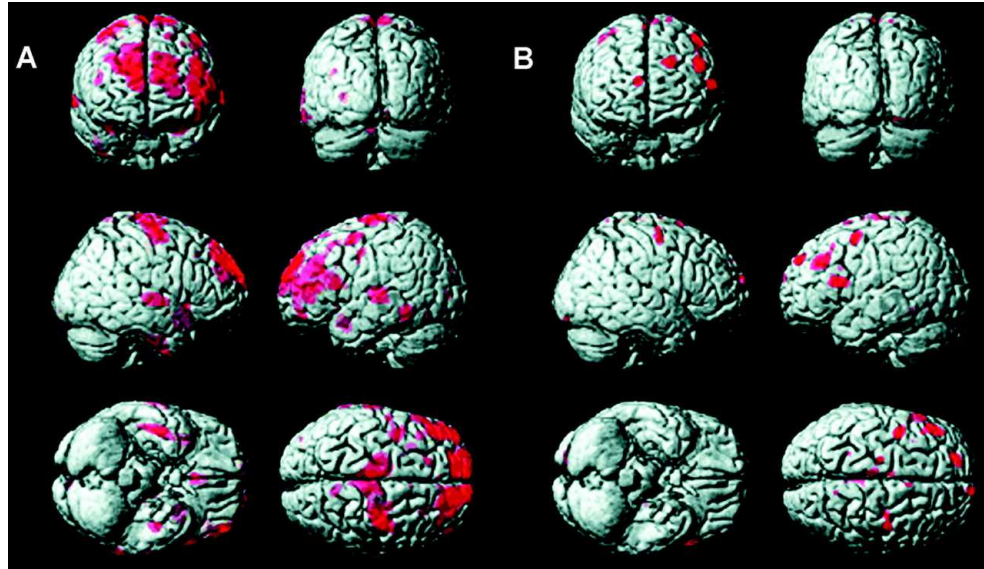


Figure 3.20: *Voxel based morphometry used to analyze size differences in localized regions of the brain.*

Afzali et al [151] explored the differences between using VBM and the tractography of diffusion tensor MRIs for patients who have epilepsy. Compared to the tractography methods, VBM showed a consistently accurate performance in analyzing the volume of the hippocampus and frontal lobe of the brain. Afzali discussed the downside of partial volume effects and increased statistical analysis complexity for VBM. However, he noted that with modern computing power the second fact becomes increasingly less significant. It is also important to understand, modern techniques have greatly reduced partial volume effects.

Chung et al [152] introduced a Tensor-based model for analyzing the brain surface in 2002. Chung applied a diffusion smoothing operator based on a standard Laplace-Beltrami operator to the tensors of the cortex and brain stem to determine local differences. The

approach demonstrated that TBM could detect localized regions of difference on the brain shapes of two clinical groups. Wang et al [155] applied a multivariate TBM to the lateral vents and the hippocampus. Wang demonstrated a straightforward framework for performing TBM operations on sub-components of the brain to be used by other researchers.

Lepore et al [154] applied a generalized TBM method to individuals with HIV/AIDS to examine differences between the corpus callosum and brain surfaces. Lepore also explored the use of multivariate tensors, and discussed how increasing the number of parameters for these tensors could improve the multivariate statistics. Lepore commented how TBM is useful in both registration and statistical analysis, illustrating the multiple use cases for many brain analysis applications.

Leow et al [153] proposed using TBM to identify changes in the brains of aging subjects. Leow's results showed that in Alzheimer's patients, there were reliable brain shape changes in the tensors relative to baseline controls over time. Leow also illustrated several methods for correcting distortion in TBM techniques. Fletcher et al [157] combined TBM and boundary-based methods to track longitudinal brain changes in subjects. This method was compared to those that do not involve boundary detection, and demonstrated how the inclusion of boundary parameters helped to correct for noise at the tissue boundaries. It also helped remove bias-correction, which may occur from warping algorithms, and added only minimal performance degradation. Fletcher, like Leow, also explored the proposition of using TBM to detect Alzheimer's in patients. Yang et al [156] also used VBM for the application of Alzheimer's. Yang studied the changes of VBM measurements in patients over a three year period. The study showed that atrophy clusters in the brain could be detected in patients who had been diagnosed with Alzheimer's.

Shi et al [158] used TBM to examine the effects of prematurity in the brains of newborns. Different from other methods, Shi registered the surface fluid of the brain instead of the cortex, and applied a TBM approach to this surface fluid. The statistical analysis showed common

clusters of significant difference between the brains of subjects. Shi also showed that the TBM approach was sensitive enough to measure the primarily smooth surface of the surface fluid and discern small but meaningful differences.

3.8 Additional Methods of Shape Analysis

Table 3.7: Automated (A) or semi-automated (SA) additional methods of shape analysis: ground truth (GT) from clinician (C) or non-clinician (N) experts; dimensionality (Dim) and sizes (#) of experimental image databases.

Method	Publication	Year	Mode	Dim	#	GT
Distance Mapping	He et al [160]	2007	SA	2D	10	N
Distance Mapping	El-Baz et al [161]	2007	A	3D	30	C
Entropy-based Particles	Cates et al [162]	2009	A	3D	56	C
Graph Matching	Geraud et al [163]	1995	SA	2D	n/a	N
Graph Matching	Yang et al [164]	2007	A	3D	120	N
Graph Matching	Long et al [165]	2012	SA	2D	60	C
Homologous Model	Yamaguchi et al [166]	2009	A	3D	4	N
Homologous Model	Yamaguchi et al [167]	2010	A	3D	11	N
Laplace-Beltrami	Angenent et al [168]	1999	A	3D	1	C
Laplace-Beltrami	Lai et al [169]	2011	A	2D	32	N
Laplace-Beltrami	Shishegar et al [170]	2011	A	3D	78	C
Laplace-Beltrami	Germanaud et al [171]	2012	A	3D	151	N
Reeb Analysis	Makram et al [172]	2008	A	3D	12	C
Reeb Analysis	Shi et al [173]	2011	A	3D	200	C
Spectral Matching	Lombaert et al [174]	2011	A	3D	36	N
Spectral Matching	Lombaert et al [175]	2013	A	3D	12	N
Symmetry-based	Prima et al [176]	2002	A	3D	250	C
Symmetry-based	Gefen et al [177]	2004	A	2D	232	N
Symmetry-based	Liu et al [178]	2007	A	2D	3	N
Symmetry-based	Feng et al [179]	2008	A	2D	1	N
Symmetry-based	Fournier et al [180]	2011	A	3D	37	N
Volume Analysis	Herman et al [181]	1988	A	3D	n/a	N
Volume Analysis	Wagenknecht et al [182]	2008	A	3D	n/a	N

Table 3.7 details additional applications of shape analysis. The table includes additional

methods such as graph-matching, symmetry-based analysis, Laplace-Beltrami analysis, and volumetric analysis. Many different methods have been applied as potential methods for diagnosis or classification.

3.8.1 Distance Mapping

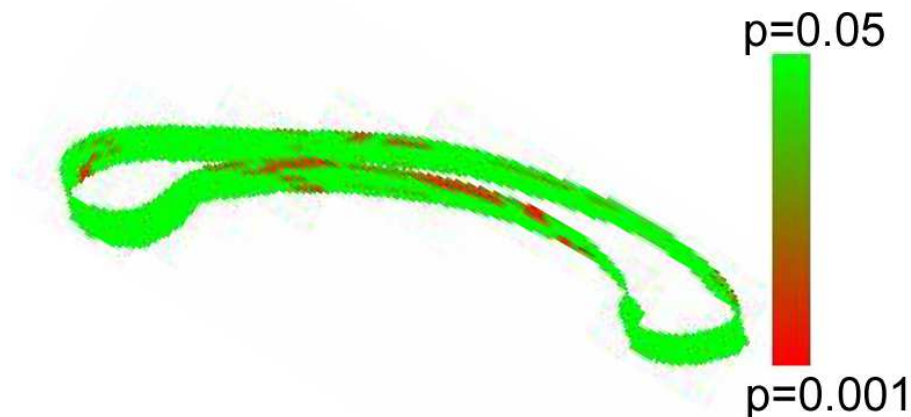


Figure 3.21: Method proposed by He et al [160] using distance mapping to examine areas of significant difference along the outer edge of the corpus callosum.

Distance mapping is a technique that has similarities to geodesic distance and medial axis analysis. It differs, in that more generalized distance metrics and locations are often computed and examined. He et al [160] proposed a method of brain analysis using distance mapping (Figure 3.21). They examined the statistical differences in distances at the border of a segmented corpus callosum in autistic patients. They hypothesized that a statistical mean difference between segmented images could be discovered, however the conclusion was that no meaningful statistical difference in shape between subjects could be found using the proposed method.

El-Baz et al. [161] proposed an alternative distance mapping technique based on the Fast Marching Method. They used this technique to approximate the thickness of the white mat-

ter in autistic patients. They expanded their work to improve the accuracy and explore the technique for different brain abnormalities [183, 184, 185, 186, 187, 188, 189].

3.8.2 Entropy-based Particle Systems

Cates et al [162] introduced a novel approach to brain shape analysis using an entropy-based system. Points are modeled on the surface of the brain as particles. These particles are then optimized and negative energy is measured to create a distribution of each unique shape. The technique is useful in both two- and three-dimensional analysis. The computational efficiency of the approach is based on the number of particles used. Cates applied the approach to the examination of the hippocampus. The advantages to the technique showed results consistent with many other techniques, while requiring a minimum amount of parameter tuning. Due to this fact it could be easily adapted to brain curvature.

3.8.3 Graph Matching

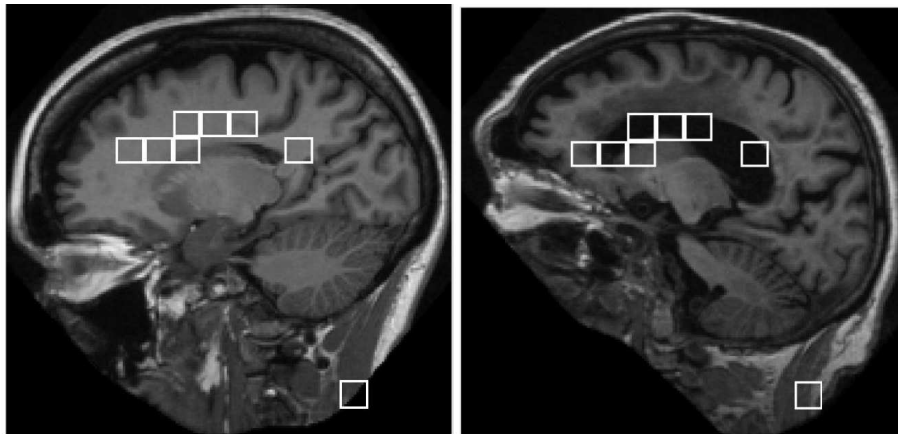


Figure 3.22: Method proposed by Long et al [165]. Showing areas that have been discriminated using a graph matching technique in two subjects.

Graph matching techniques involve converting more complex information into a more simplified graph-based representation. Similarities in the graphs are then used to identify, segment, and analyze the more complex information. Geraud et al [163] proposed a method of graph matching analysis. They utilized a Markovian relaxation on a watershed based adjacency graph to improve segmentation of neighboring structures of the brain. The results showed a good initial approach to the application of graph matching in the area of segmentation and identification.

Yang et al [164] proposed that two graph matching techniques could be used to constrain a search neighborhood and genetic algorithms can be used to optimize sulci labeling. They were able to achieve satisfactory identification rates for finding sulci using the proposed graph matching strategy.

Long et al [165] suggested that the brain shape could be decomposed to a graph by subdividing the images into a tree structure containing various properties of the specific brain. By manually selecting important locations for placing the subdivision structures, the brain could be successfully classified for cognitive impairment due to Alzheimer's disease.

3.8.4 Homologous Modeling

Homologous modeling is a mesh based technique, in which items having the same number of analysis points in the same locations on two different models can be examined. The technique has been applied to many different applications, but due to implementation complexity is rarely applied to the the whole brain. However, it may also be appropriate for the analysis of other discrete brain structures (e.g. corpus callosum, amygdala, or hippocampus).

Yamaguchi et al [166] demonstrated a method based on a homologous model to calculate a sulcal-distribution index for brains to identify brain fissures (Figure 3.23). Yamaguchi found a mean displacement of $1.3 \pm 0.7mm$ in the brain fissures. Their results suggested that a

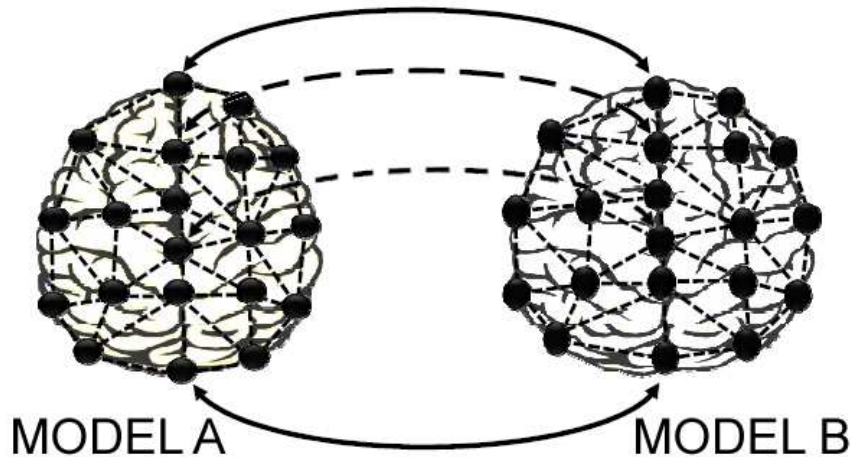


Figure 3.23: Method proposed by Yamaguchi et al [166] illustrating the concept of homologous modeling on two brains.

homologous model could be used to correspond the sulci and gyri effectively among the evaluated brains. Yamaguchi et al [167] proposed a later method to statistically quantify the brain shape using a homologous model. The work examined changes in the frontal and occipital lobes between male and female subjects. A significant difference ($p < 0.05$) was detected in the sample population.

3.8.5 Laplace-Beltrami

Laplace-Beltrami methods comprise any methods that rely heavily on the Laplace-Beltrami operator. The Laplace-Beltrami operator of a smooth function f on a Riemannian manifold M and is defined as $\Delta f = \text{div}(\text{grad} f)$, where div and grad are the divergence and gradient operators of the manifold M [170]. This technique is most commonly used in smoothing applications or curvature analysis.

Angenent et al [168] was the first researcher to propose brain analysis using a Laplace-Beltrami model. Angenent hypothesized that a brain could be flattened by using a Laplace-

Beltrami operator on the brain surface. The technique was shown to be an efficient method of flattening the brain.

Lai et al [169] used Laplace-Beltrami nodal curves and geodesic curve evolutions to segment to the corpus callosum. In small data tests, the method appeared to show robust positive results.

Shishegar et al [170] analyzed the first 20 eigenvalues of the Laplace-Beltrami spectrum to classify epilepsy. In the best testing results, Shishegar achieved a 91.9% true positive rate and a 33.3% false positive rate using out of normal range classifiers and cross-validation, illustrating that while there were difficulties, it was a promising method.

Germanaud et al [171] computed the eigenfunctions of the Laplace-Beltrami operator to decompose meshes for left and right handed subjects. Germanaud was able to detect shallow folds and rare deep folds in the brain, which lead to the quantification and classification of brains using the Spangy method.

3.8.6 Reeb Graph

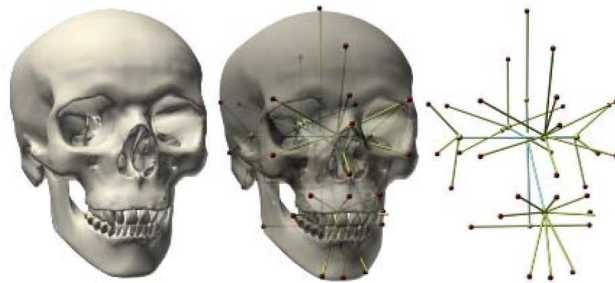


Figure 3.24: *Illustration of a Reeb graph of a cranium by Makram et al [172].*

A Reeb graph describes the connectivity of the level sets of an object [190]. Visually, a constructed Reeb graph looks similar to a medial axis skeleton. Makram et al [172] suggested

a method of using Reeb graph analysis to drive an elastic registration model for the detection of maxilla malformations. The results of detection were deemed satisfactory to a clinician, but actual values were not reported. The method illustrated the potential for Reeb graph analysis as a registration framework.

Shi et al [173] used reeb graph analysis to isolate, extract, and reconstruct enhanced brain surfaces. The system was able to process cortical surfaces with the accuracy of freesurfer, but at a lower computational cost.

3.8.7 Spectral Matching

Spectral correspondence as a way to examine the shapes of objects was first pioneered by Reuter [191, 192] in 2005, and was later expanded by Rustamov [193]. Spectral correspondence was combined with Laplace-Beltrami operators by Rustamov. In 2011, Lombaert et al [174] proposed a method of spectral correspondence that was applied to brain shapes. They used an eigendecomposition to match brain surfaces between subjects. Initially, the spectra are computed for each brain. These spectra are then sorted and aligned. The result allows point locations between two brains to be quickly matched. The method is primarily applicable to brain registration. Lombaert et al [175] proposed an extension of this work for corresponding features on the surface of the brain, entitled FOCUSR. Surface features of each brain were used to drive the alignment. The primary advantage of FOCUSR over competing techniques is the speed required to match the brains to one another. The spectral matching technique required only 208 seconds to achieve the same accuracy as FreeSurfer, a commercial brain analysis tool, which required several hours.

3.8.8 Symmetry Analysis

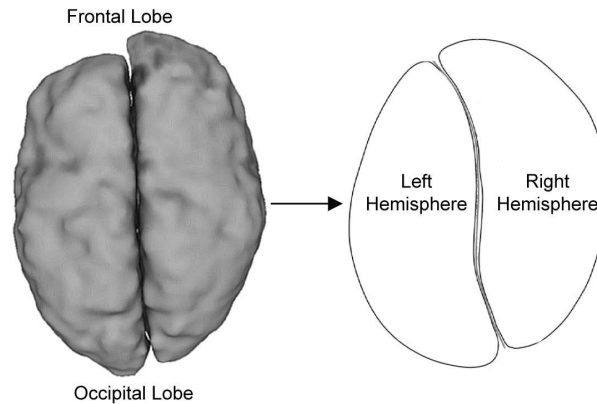


Figure 3.25: As shown by Fournier et al [180], the human brain has a slight asymmetry if test subjects are right or left-handed.

Symmetry based techniques exploit the fact that the human brain is largely symmetric along the sagittal plane, and use this information to make observations. Prima et al [176] proposed an early method of symmetry-based brain analysis. Prima analyzed brain symmetry to automatically compute the mid-sagittal plane and obtain sub-voxel accuracy in computing, reorienting, and re-centering 3D images in an efficient manner.

Gefen et al [177] aligned individual brain images along symmetry lines to create more accurate 3D models. Gefen concluded that some regions yielded better restoration in 3D models than other regions, but overall the alignment results were accurate and consistent.

Liu et al [178] examined the topic of multi-modality brain registration by aligning the symmetry planes of objects using affine transformations. Liu surmised that the test objects were successfully matched and the symmetry planes were accurately computed.

Feng et al [179] used the symmetry properties of the brain to improve brain segmentation algorithms. Feng's algorithm, while effective at determining bilateral symmetry, was limited by only being applicable to 2D images.

Fournier et al [180] examined the asymmetries in brains of humans and chimpanzees and compared left and right handed individuals to search for a difference (Figure 3.25). Fournier was able to recover typical global asymmetry patterns, and hypothesized that future symmetry-based analysis could provide an automated way of comparing individuals.

3.8.9 Volumetric Analysis

Volumetric techniques measure the volume of an object. Herman et al [181] proposed a method based on volumetric analysis to use gradient-based boundary tracking to examine the volume between control and Alzheimer's patients. Herman concluded that the gradient-based methods are superior to standard thresholding methods, but did not provide a detailed summary of the diagnostic results.

Wagenknecht et al [182] used a 3D Live-wire approach to extract volumes of interest from a brain for comparison or identification. An average miscalculation rate of less than 0.0039 was reported, and the proposed method demonstrated robust accuracy for extracting volumes of interest and calculating various properties for them.

3.9 Discussion

3.9.1 Research Challenges

The brain has long been a topic of research, but utilizing shape analysis with the help of computers enables researchers to examine its shape and texture. There are several major challenges facing shape analysis methods relating to the brain or other complex medical structures. The brain is a complex and very diverse organ. Unlike more rigid and well defined objects, that may be easily represented by geometric shapes, the brain suffers from large

irregular variabilities. The lack of overall consistency in the brain requires specific techniques that analyze it to be flexible, and must be adaptable to changes in contrast, shape, varying degrees of noise, and abnormality. This illustrates why techniques that rely on pre-determined templates or shape models may suffer in relevance to brain applications. This problem of consistency and complexity in the structure is the primary issue that leads to many of the challenges. These challenges can be summarized as follows:

- Due to the size and complexity of the brain and other medical objects, mesh based approaches often require a significantly large number of nodes or points of reference to perform an accurate surface or shape analysis. Even with modern computing, the complexity of the brain still poses a computational efficiency challenge.
- Medial axis and other skeleton-based analysis may require a large amount of branches and complex paths to accurately represent all of the distinct locations in the human brain.
- The known shape analysis and diagnostic techniques for the brain largely rely on the accuracy of brain segmentation and ability to properly determine structures in the brain. Even with the combination and fusion of modern techniques (e.g. active contours, deformable models, SPHARM, and geodesic distances), identification and segmentation accuracies still suffer significant errors when applied to large sets of data.
- Computer aided diagnostic systems have difficulty in accurately classifying neurological diseases based on shape metrics over the past decades. This is largely due to the lack of consistency found across different subjects, but is also due to the difficulty in properly registering and aligning brains so that like areas can be examined.

3.9.2 Comparisons and Trends

While there is a high degree of merit in all applications of shape analysis to the brain, some techniques are more suited to specific applications than others. There are four generalized applications of shape analysis techniques with the brain: examination of individual sulci and their curvatures on the brain, examination of the entire human brain and white matter as a whole, registration of brain shapes amongst subjects, and examination of the sub-components of the brain (e.g. corpus callosum, ventricles, hippocampus). Due to the wide variety of shapes and curvatures in the human brain, many techniques can be used with an array of different brain applications. However, it should be noted that most of the techniques are more commonly used in one or two areas.

Geodesic distances, medial axis, skeletal analysis, and Laplace-Beltrami methods are the most common methods used for examination of the individual sulci and brain curvature, with geodesic distances between the most prevalent of the modern applications. SPHARM, voxel- and tensor-based morphometry, volume analysis, symmetry-based modeling and deformable models are the most common applications for analysis of the brain and white matter. However, SPHARM is generally reserved for mesh-based applications, and deformable models are often preferred for registration and segmentation applications. While having some uses in whole brain shape analysis, Procrustes analysis, homologous modeling, graph matching, and symmetry-based modeling are most commonly used for brain registration and segmentation applications. Voxel- and Tensor-based morphometry, medial axis, skeletal analysis, SPHARM, and distance mapping are the most preferable methods for examination of sub-components of the brain, and while typically not always used exclusively, geodesic distances are often combined with these methods. Voxel- and Tensor-based morphometry and SPHARM also have significant applications in brain shape registration. It should be specifically noted, that deformable models have a high degree of applicability to all of the mentioned

analysis methods, and are often combined with or frequently used in many forms of brain shape analysis.

Longitudinal studies and those examining comparisons between populations tend to most commonly use SPHARM or morphometry based approaches, because these approaches often take factors of data alignment into account. Geodesic distances can also contribute to longitudinal studies. Deformable models, medial axis, and geodesic distance analysis are good methodologies for examining subcortical structures or regions in the brain along with intricate details about specific anatomy. Cortical thickness studies are most suited for morphometry or distance-based techniques, because these provide the most straightforward approaches for measurement studies. In summary, some methods are more suited to specific applications, however, unique studies may need to explore a combination of techniques and approaches due to the abnormality of the brain shape.

To address the aforementioned challenges, recent trends in shape analysis of the brain involve the following aspects:

- Many of the methods discussed were initially applicable to 2-dimensional analysis, but in recent years nearly all methods have evolved for use with 3-dimensional applications.
- In the past five years, deformable model methods [123, 124, 125] have seen an increase in usage and have taken the place of many segmentation processes, leading to an improved accuracy in brain segmentation. These advances will, undoubtedly, help to push forward new and improved shape analysis techniques.
- More complex techniques such as SPHARM, started by Gerig et al [131], have been further developed by others [135, 138, 136, 139, 140] in recent years. These methods have shown great promise by advancing the field of analysis on the cortex and white matter, including analysis of sub-components of the brain. These methods have illustrated the potential for parameter invariant applications that solve many of the difficult

alignment and registration errors that are often associated with the brain.

- In modern methods, automation has become increasingly important and semi-automated and manual methods has decreased. The reduction of human interaction has resulted in an increase in the accuracy of newer techniques.
- Methods such as medial axis analysis [47] and geodesic distances [104] are more frequently combined with other techniques, leading to more accurate segmentation, registration and classification of the human brain and its various subcomponents, including, the ventricles and corpus callosum.

3.10 Summary of Shape Analysis Methods

This survey details the numerous methods for solving the complex problem of brain shape analysis. Early techniques, which suffered from lower accuracies, slow computation times, and significant user input, have given rise to complicated modern techniques that offer greater degrees of automation and improved accuracy. Going forward, methods such as SPHARM, deformation-based morphometry, and deformable models will likely become the dominant modes for use in brain shape analysis. Geodesic distances, medial axis, and Laplace-Beltrami operations, among others, will be methods used to support and enhance these improved modes of analyzing brain shape. An amalgamation of techniques opens new opportunities for researchers and engineers to develop more advanced analysis methods. Exciting new opportunities, such as HyperSPHARM and 4-dimensional analysis techniques, offer a look into future understanding of where modern techniques and amalgamations may be headed. In conclusion, the future of the field of shape analysis for the brain is evolving rapidly, and new techniques will develop and emerge as technology continues to progress.

CHAPTER 4

THE SIGHT FRAMEWORK

If you're trying to achieve, there will be roadblocks. I've had them; everybody has had them. But obstacles don't have to stop you. If you run into a wall, don't turn around and give up. Figure out how to climb it, go through it, or work around it.

- Michael Jordan

The culmination of the work of this dissertation, initiated in 2008, is a software package entitled the Sight framework. This dissertation is designed to provide an informative and detailed explanation of this software. Sight is a diagnostic software that can provide insight and deeper understanding of the unique structure of brain matter and its functions. Sight is a software engine fully capable of analyzing the shape of the human brain, and has been used with a variety of other organs to detect medical anomalies.

4.1 Introduction

The first incarnation of the framework began in 2008, at Speed School of Engineering at the University of Louisville. This early stage program, based on the analysis of a single brain, required a lengthy 24 hours to process. The implementation was low resolution, and the

accuracy only showed moderate promise. The software would evolve over the next seven years until it became the Sight framework, and was capable of providing a high-definition neurological classification and risk analysis in only minutes.

An important aspect of Sight, is the reuse of code in a multitude of locations within the program. The reuse of code, specifically the registration algorithms, helps to make the program more efficient, faster, and simpler to maintain. To make the software description understandable, the general methodology will be described, then followed by an explanation of the registration algorithms. The registration algorithms are utilized throughout the other stages of processing.

The methodology is structured in the following format:

1. Skull stripping and bias correction
2. Segmentation and atlas generation
3. Mesh Generation, pre-processing, and mesh manipulation
4. Spherical Harmonics (SPHARM) processing and SPHARM derived metrics
5. Volumetric and SPHARM Registration
6. Classification, Brodmann area analysis and delineation, metric computations and metric reductions

The principle contributions of this dissertation in the field of medical imaging include the following, among others:

- Development and implementation of a complete, functioning framework for diagnosing conditions.
- Constructing of a new pipeline for quickly creating brain atlases for segmentation approaches.

- Algorithms for constructing volumetric manifolds, volume and mesh registration, mesh deformations, and polar mesh-based ray-casting, among others.
- Development of a new classifier for neurological disorders.
- Proposing and implementing the use of brain regions, and using these local regions as important shape characteristics for classification and understanding of the brain.
- Creating new shape metrics for examining the brain.

4.2 Skull Stripping

The first step of the Sight framework is the removal of the skull from the MRI scans. A hybrid skull stripping approach is used to remove the skull prior to segmentation. The technique is a modified version of an approach constructed by colleagues Al Ansary et al. The approach is used to accurately extract brain tissue from infant MR brain images. The framework integrates both stochastic and geometric approaches and comprises four basic steps: (i) bias correction, (ii) skull stripping, (iii) iso-surfaces generation, and (iv) final brain extraction using visual appearance features of the MR brain images. Details of the proposed approach are outlined in the following sections.

4.2.1 Bias Correction

Bias field noise, also referred to as illumination non-uniformity, is a form of noise found in brain that severely limits the accuracy of many existing brain extraction approaches. To accurately extract a brain from a set of MRI scans, it is necessary to account for this inhomogeneity in an image. A 3-dimensional Generalized Gauss-Markov random field (GGMRF) model [194] is applied, after brain intensity normalization, using a nonparametric approach proposed in work by Tustion et al [195]. This GGMRF model reduces noise effects and removes inconsistencies, by accounting for the 3D spatially homogeneous pair-wise interactions between the gray levels of the MRI data. The gray level values $q \in \mathbf{Q} = \{0, \dots, Q - 1\}$ are considered as samples from a 3D GGMRF model [194] of measurements using a voxel 26-neighborhood. The continuity of q values of each brain MR scan is amplified by using their maximum A posteriori (MAP) estimates [194] and voxel-wise stochastic relaxation (iterative conditional mode (ICM) [196]):

$$\hat{q}_s = \arg \min_{\tilde{q}_s} \left[|q_s - \tilde{q}_s|^\alpha + \rho^\alpha \lambda^\beta \sum_{r \in \mathcal{V}_s} \eta_{s,r} |\tilde{q}_s - q_r|^\beta \right] \quad (4.1)$$

where q_s and \tilde{q}_s are the original gray level values and their expected estimates, respectively, at the observed 3D location, $s = (x, y, z)$; \mathcal{V}_s is the 26-neighborhood system; $\eta_{s,r}$ is the GGMRF potential, and ρ and λ are scaling factors. The parameter $\beta \in [1.01, 2.0]$ controls the level of smoothing (e.g., $\beta = 2$ for smooth vs. $\beta = 1.01$ for relatively abrupt edges). The parameter $\alpha \in \{1, 2\}$ determines the Gaussian, $\alpha = 2$, or Laplace, $\alpha = 1$, prior distribution of the estimator.

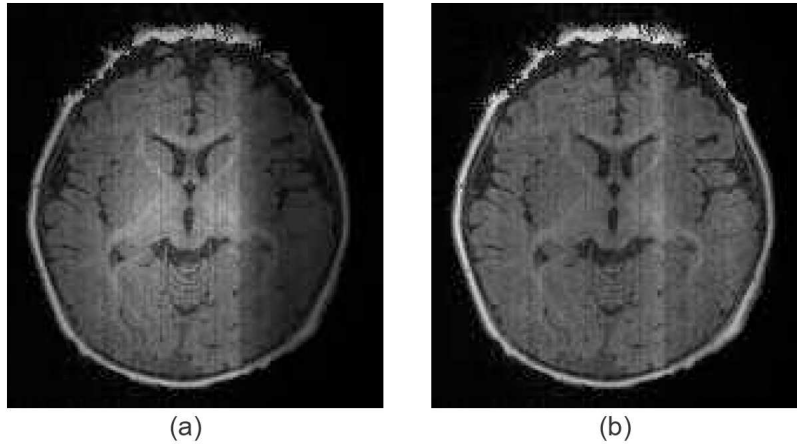


Figure 4.1: A sample MRI scan (a) before and (b) after bias correction.

4.2.2 BET Skull Stripping

The second step of the skull stripping framework removes voxels that are not part of the brain from the MR images. The Brain Extraction Tool (BET) algorithm [197, 198, 199], a deformable model-based approach, removes these voxels from brain MRIs. BET functions best when set run using a low BET factor of below 0.45. While BET extraction of the brain provides a solid first step, it often fails to remove all voxels that are not a part of the brain. For clinical

applications, such as cortical thickness measurement and techniques which examine the surface of the brain, inaccurate skull stripping results in an over- or under-estimation of the quantity of tissue.

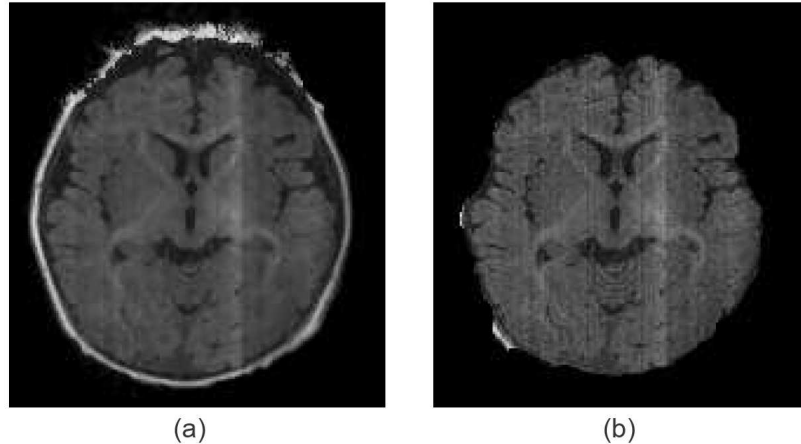


Figure 4.2: Results of applying the BET algorithm to a bias corrected MRI scan.

4.2.3 Visual Appearance-Guided Iso-Surfaces

To obtain more accurate brain extraction results, an additional processing step, based on the geometric features of the brain, accounts for the skull stripping errors not corrected by BET. Since non-brain tissues are brighter than brain tissue, this step exploits the visual appearance features of the MR brain data. An evolving iso-surface-based approach removes the voxels that do not contain brain information that remain after being processed with BET. This iso-surface approach is guided by the visual appearance features of the MR data. First, a set of nested, tangent surfaces (i.e., iso-surfaces) are generated by the fast marching level set (FMLS) approach [200], using the extracted brain from the BET step. In order to accurately classify MRI voxels as brain or non-brain, it is important to accurately model MR data visual appearance. To achieve this goal, a joint Markov-Gibbs random field (MGRF) model is used

and described below.

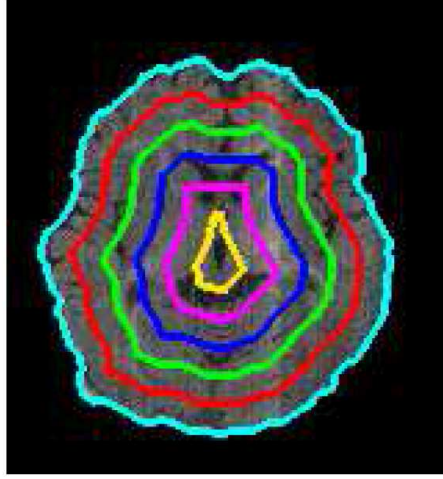


Figure 4.3: Representation of computed iso surfaces overlaid on an MRI scan after the application of the BET algorithm.

Let $\mathbf{Q} = \{0, \dots, Q - 1\}$ and $\mathbf{L} = \{\text{“brain”}, \text{“non-brain”}\}$ denote sets of gray levels q and region labels L , respectively. Let \mathbf{R} denote a 3D arithmetic lattice supporting a given grayscale image $\mathbf{g} : \mathbf{R} \rightarrow \mathbf{Q}$ to be segmented and its goal region map $\mathbf{m} : \mathbf{R} \rightarrow \mathbf{L}$. The 3D T1-weighted MR images, \mathbf{g} , and its map, \mathbf{m} , are described with the following joint probability model:

$$P(\mathbf{g}, \mathbf{m}) = P(\mathbf{g}|\mathbf{m})P(\mathbf{m}) \quad (4.2)$$

where $P(\mathbf{m})$ is an unconditional probability distribution of maps, and $P(\mathbf{g}|\mathbf{m})$ is a conditional distribution of the images given the map. The ultimate goal is to accurately estimate $P(\mathbf{g}|\mathbf{m})$ and $P(\mathbf{m})$, which are described next.

4.2.4 First-Order Visual Appearance ($P(\mathbf{g}|\mathbf{m})$)

To accurately approximate the marginal probability distributions of the voxel that do not belong to the brain, the empirical gray level distribution of the brain data is precisely approximated

with a linear combination of discrete Gaussians (LCDG) containing positive and negative components [201]. The LCDG restores brain and non-brain transitions more accurately than a conventional mixture of only positive Gaussians. The LCDG yields a better initial map, m , formed by voxel-wise classification of the grayscale image values. Next the LCDG is explained in more detail, and the process is outlined in Figure 4.4.

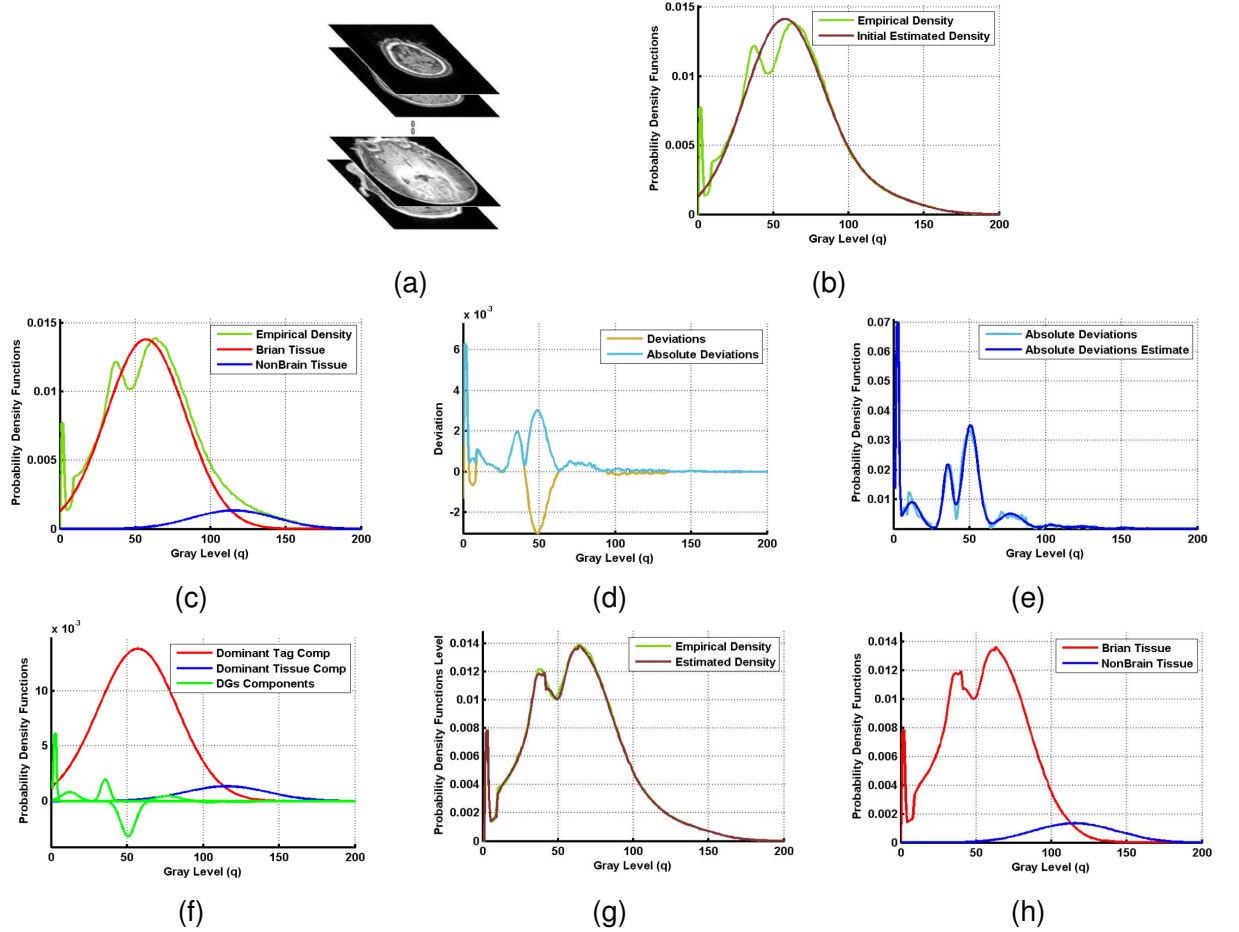


Figure 4.4: Typical set of MR brain images (a); and estimated density (b) using only two dominant Gaussian components (c), deviation between empirical and estimated densities (d), estimated density of absolute deviation (e), LCDG components (f), final estimated density (g), and the final estimated marginal density for each class (h).

Let $\Psi_{\theta} = (\psi(q|\theta) : q \in \mathbf{Q})$ define a discrete Gaussian (DG). A Discrete Gaussian (DG) ($\Psi_{\theta} = (\psi(q|\theta) : q \in \mathbf{Q})$) with $\theta = (\mu, \sigma^2)$ is defined as $\psi(q|\theta) = \Phi_{\theta}(q+0.5) - \Phi_{\theta}(q-0.5)$

for $q = 1, \dots, Q - 2$, $\psi(0|\theta) = \Phi_\theta(0.5)$, and $\psi(Q - 1|\theta) = 1 - \Phi_\theta(Q - 1.5)$ where $\Phi_\theta(q)$ is the cumulative Gaussian function with the mean μ and the variance σ^2). Integrating $\theta = (\mu, \sigma)$ over a continuous 1D Gaussian density with mean μ and variance σ^2 over successive gray level intervals [201].

The LCDG with two dominant positive DGs and $M_p \geq 2$ positive and $M_n \geq 0$ negative subordinate DGs is defined as [201]:

$$P_{\mathbf{w}, \Theta}(q) = \sum_{i=1}^{M_p} w_{p:i} \psi(q|\theta_{p:i}) - \sum_{j=1}^{M_n} w_{n:j} \psi(q|\theta_{n:j}) \quad (4.3)$$

where all the weights $\mathbf{w} = [w_{p:i}, w_{n:j}]$ are non-negative and meet an obvious constraint $\sum_{i=1}^{M_p} w_{p:i} - \sum_{j=1}^{M_n} w_{n:j} = 1$. All the LCDG parameters, including the numbers of DGs, are estimated from the mixed empirical distribution to be modeled, using the modified expectation-maximization (EM)-based algorithm introduced in [202].

4.2.5 Second-Order Visual Appearance ($P(\mathbf{m})$)

To overcome the effects of noise and to ensure segmentation homogeneity, the spatial interactions between the region labels of a brain map, m , are examined using the Potts MGRF model. This model is constructed using the 26-neighbors nearest to the target voxel (as shown in Figure(4.5(a))and analytical bi-valued Gibbs potentials (as shown in Figure(4.5(b)) Only the coincidence of the labels is considered. The MGRF model is defined by El-Baz et al [203] in Eq. 4.4 as:

$$P(\mathbf{m}) \propto \exp \sum_{(x,y,z) \in \mathbf{R}} \sum_{(\xi, \zeta, \kappa) \in \mathbf{V}_s} \mathbf{V}(m_{x,y,z}, m_{x+\xi, y+\zeta, z+\kappa}) \quad (4.4)$$

where \mathbf{V} is the bi-value Gibbs potential, that depends on whether the nearest pair of labels

are equal or not:

$$V = \begin{cases} V(\lambda, \lambda') = V_{\text{eq}} & \text{if } \lambda = \lambda' \\ V(\lambda, \lambda') = V_{\text{ne}} & \text{if } \lambda \neq \lambda' \end{cases} \quad (4.5)$$

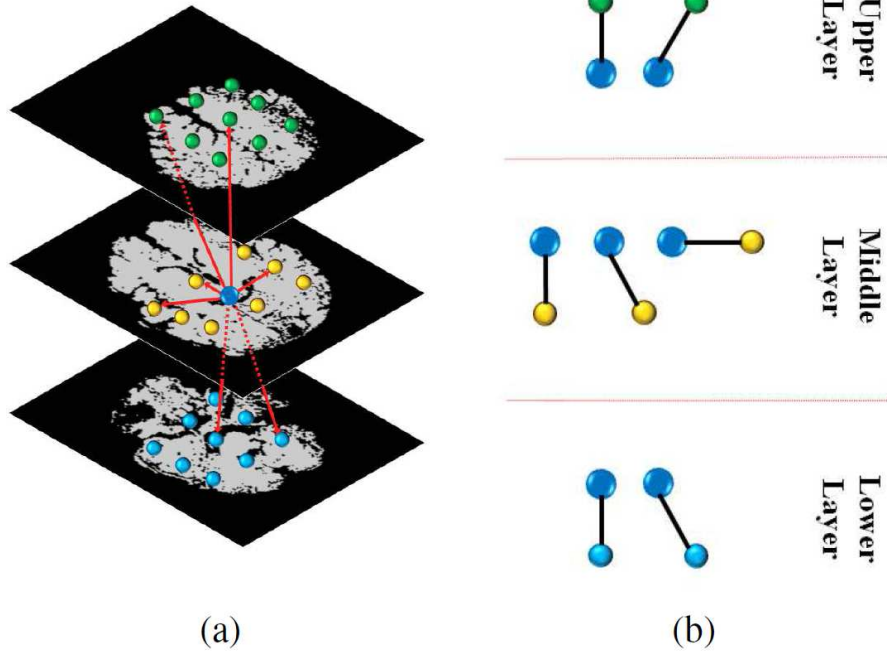


Figure 4.5: A graphical illustration for the 3D neighborhood system (a) and a sample of the different pair-wise cliques for the 2nd-order MGRF (b).

Let $f_{a,\text{eq}}(\mathbf{m})$ denote the relative frequency of the equal label pairs in the equivalent voxel pairs $\{((x, y, z), (x + \xi, y + \zeta, z + \kappa)) : (x, y, z), (x + \xi, y + \zeta, z + \kappa) \in \mathbf{R}; (\xi, \zeta, \kappa) \in \mathbf{v}_s\}$. The initial \mathbf{m} results in approximate analytical maximum likelihood potential estimates [203]:

$$V_{\text{eq}} = -V_{\text{ne}} \approx 2f_{\text{eq}}(\mathbf{m}) - 1 \quad (4.6)$$

that allow for computing the voxel-wise probabilities $p_{x,y,z}(m_{x,y,z} = \lambda)$ of each label $\lambda \in \mathbf{L}$. In

total, Algorithm 1 summarizes the basic steps of the proposed brain extraction framework.

Algorithm 1 Brain Extraction Approach

INPUTS:*MRI Volume***OUTPUTS:***MRI Volume with Skull Removed*

while Bias Correction of MR brain data is needed **do**

Brain intensity normalization [195].

GGMRF edge preservation [194].

end while

1. Strip the skull using the Open Source BET Platform [197, 198, 199].

2. Estimate the LCDG models for brain and non-brain tissues.

3. Form an initial \mathbf{m} by voxel-wise classification using LCDG models.

4. Estimate analytically the Gibbs potentials for the pair-wise MGRF model of \mathbf{m} to identify the MGRF probability.

5. Calculate the distance map inside the binary mask obtained from BET using FMLS [200].

6. Generate a set of N iso-surfaces using the distance map.

while $j \leq N$ **do**

a. Select the j^{th} iso-surface and classify its voxels using a Bayes classifier.

b. Are all the voxels on the selected iso-surfaces classified only as brain tissue?

if no then

continue

else

break

end if

end while

7. Apply connected component analysis to obtain the final results.

4.2.6 Skull Stripping Results

The application of the skull stripping framework successfully removes the skull and scalp tissue from a set of MR brain images. The bias is removed so that the images are suitable for segmentation. Results of the framework can be seen in Figure 4.6.

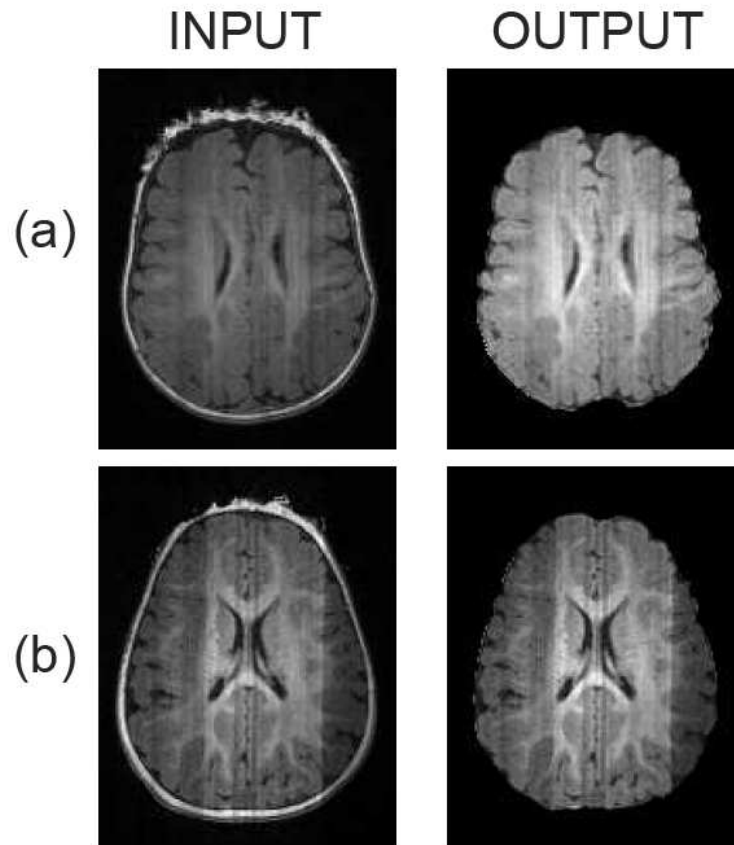


Figure 4.6: *Skull stripping results for two different subjects showing a reliable brain extraction using the proposed framework.*

4.3 Segmentation

Segmentation of the brain is the accurate delineation of brain tissue into a select number of classes. For shape analysis of the brain, it is necessary to understand where the gray matter (GM), white matter (WM), and cerebro-spinal fluid (CSF) are located in the brain. The following modified segmentation approach was developed to meet this need. Segmentation follows skull stripping in the Sight framework.

The proposed segmentation framework is broken into five distinct steps: (i) atlas-guided shape probability classification; (ii) shape-seeded intensity classification; (iii) intensity and shape fusion; (iv) spatial refinement; (v) post-processing.

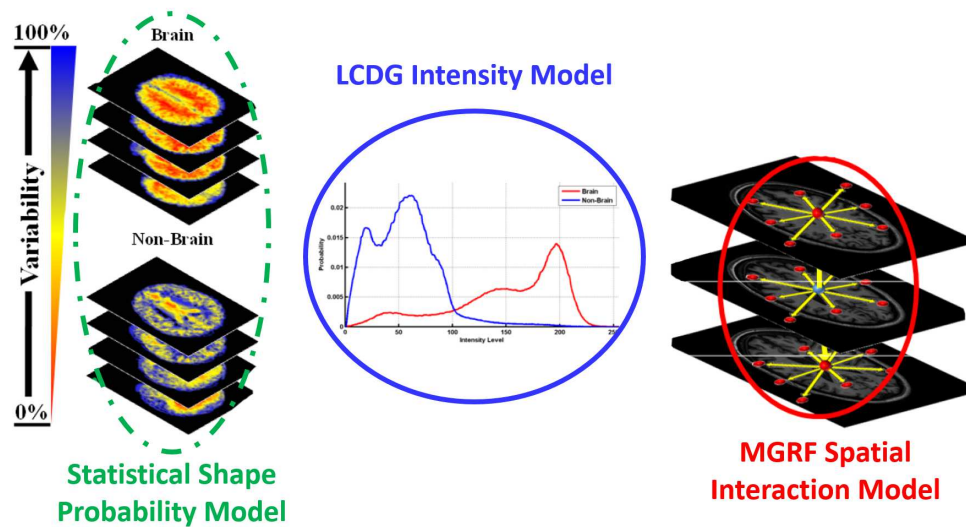


Figure 4.7: The three primary models used in brain segmentation are the atlas-guided shape probability classification, shape-seeded intensity classification, and spatial refinement.

4.3.1 Atlas Construction

Before explaining the segmentation approach, it is necessary to understand how an atlas is constructed. Atlases are used to guide the shape probability classification. The Sight Foundry platform was designed to quickly and easily construct a set of atlases with a minimal amount of user interaction. This process, combines elements of FSL [197, 198, 199] and BrainSuite [204, 205, 206, 207, 208, 209] platforms.

The skull is stripped from a new atlas subject using the FSL BET algorithm [197, 198, 199]. The subject is then processed through the FSL SUSAN algorithm [197, 198, 199]. SUSAN is a noise reduction algorithm that uses nonlinear filtering to reduce noise in an image. SUSAN also preserves the underlying structure of the image by averaging a voxel with local voxels which have similar intensities. This creates a uniform version of the brain MRI scan. The brain that has been processed using BET and SUSAN is passed through the FSL FAST algorithm [197, 198, 199]. FAST (FMRIBs Automated Segmentation Tool) is a software algorithm that segments a 3D image of the brain into different tissue types (Grey Matter, White Matter, and CSF). FAST corrects for spatial intensity variations (also known as bias field or RF inhomogeneities). The underlying method of FAST, is based on a hidden Markov random field model and an associated Expectation-Maximization algorithm. The whole process is fully automated, robust, and reliable, compared to most finite mixture model-based methods, which are sensitive to noise. The FSL processing steps are done inside a Linux Virtual Machine running Linux Mint, using FSL v5.0. There is no user input required in any of the FSL procedures.

The new atlas subject is simultaneously analyzed using the BrainSuite package. The subject is processed using the standard BrainSuite pipeline to construct a cerebrum label. The BrainSuite skull stripping (BSE) algorithm is used to remove the skull from the MRI scans [204, 206, 207]. This procedure removes voxels containing skull and scalp information

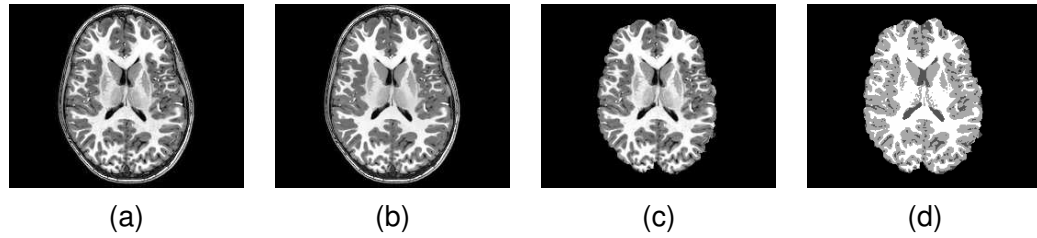


Figure 4.8: Results of applying the FSL application to a MR brain scan. Shown is an example of the (a) original MR image, (b) SUSAN processed MR image, (c) BET skull stripped MR image, and (d) FAST segmented MR image.

from the MRI scans by utilizing a combination of anisotropic diffusion filtering, Marr-Hildreth edge detection, and a sequence of morphology operators. A non-uniformity correction is applied to the volume following the process of skull stripping. The non-uniformity correction adjusts for shading artifacts and bias field inconsistencies. The tissue is classified in the extracted brain using a partial volume measurement model. This model combines a spatial prior that models the largely contiguous nature of major brain tissue types. A cerebrum labeling mask is constructed by computing an AIR nonlinear registration that aligns a multi-subject atlas average brain volume to the new atlas subject brain volume [204, 208, 209]. The labels are transferred for the different brain regions from the atlas space to the individual subject space. The BrainSuite software runs on the Microsoft Windows operating system. No user input is required to operate the BrainSuite pipeline.

A fusion of the information produced from these two approaches is used to create a new brain atlas. The three atlases created by the FSL software (raw skull stripped volume, SUSAN skull stripped volume, and tissue labeled volume) and the cerebrum labeling mask created using the BrainSuite software are loaded in to the Sight Foundry platform. Negative values in these four image volumes, resulting from scanner acquisition errors, are removed. The remaining image volume values are normalized between the integers of 0 and 255. The volumes are then scaled, based on scanner acquisition parameters, so that the voxels in each volume are of size $1mm \times 1mm \times 1mm$. A mask of the T1-weighted MR information is

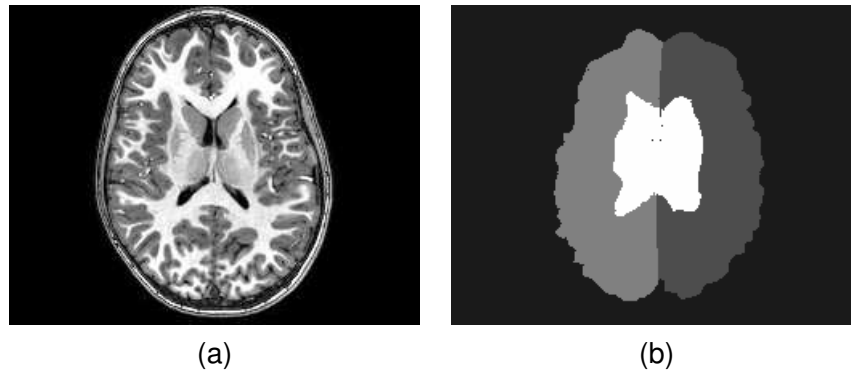


Figure 4.9: Results of applying the BrainSuite application to a MR brain scan. Shown is an example of the (a) original MR image and the (b) cerebral cortex mask of the MR image.

created from the skull stripped mask. The background (area that contains no useful data) is given a value of 0. The cerebral mask is used to identify the location of the brain stem and the cerebellum in the new atlas brain. These locations are assigned a label of 1. Finally the CSF, GM, and WM, are each given labels of 2-4, respectively using the labels determined by FAST.

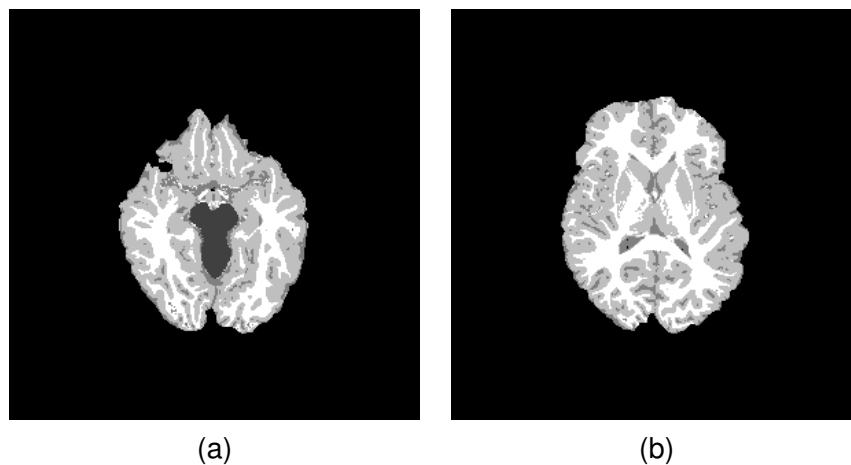


Figure 4.10: Two example MR atlas images. In (a) the four labels, including the brain stem label, are visible. In (b) labels in the cortex of the brain atlas are visible.

Each new atlas is saved containing two pieces of information. The atlas contains the original bias-corrected and normalized grayscale information. The atlas also contains the

corresponding labeled atlas mask. The atlases are then aligned using a non-linear registration to an atlas designated as the master atlas. The entire Sight Foundry approach is detailed in Algorithm 2.

When constructing a new set of segmentation atlases, seven to thirteen brains are used. Each of these atlases is constructed using the above described approach. These brains are used to establish the probabilistic shape prior that guides the shape probability classification.

Algorithm 2 Sight Foundry

INPUTS:

bet ← FSL BET(volume)
fast ← FSL FAST(volume)
susan ← FSL SUSAN(volume)
bse ← BRAINSUITE BSE(volume)
hemi ← BRAINSUITE REGION(volume)

OUTPUTS:

originalAtlas
susanAtlas

for all volumes **do**
 RESCALEVOLUME(volume)
 REMOVEDNEGATIVEVALUES(volume)
end for
hemi ← ISOLATECORTEX(*hemi*)
for all volumes **do**
 volume ← LOGICAL(*hemi*) .* volume
end for
tm ← VOLUMEREGISTER(atlas,*hemi*)
for all volumes **do**
 volume ← AFFINETRANSFORM(volume,*tm*)
end for
for *originalAtlas* **do**
 t1 ← volume
 label ← *fast*
end for
for *susanAtlas* **do**
 t1 ← *susan*
 label ← *fast*
end for

4.3.2 Shape Probability Classification

The segmentation process begins by using a guided shape probability classification. This means shape segmentation is guided by a set of previously aligned atlases that incorporate the local intensity data of each Atlas. Following skull stripping, a nonlinear registration between the target subject and the master Atlas is computed and stored. The original target subject with this transformation matrix and the corresponding data is loaded into the memory of the computer. The shape probability classification helps to improve the overall segmentation accuracy, because the expected shapes of each brain label are constrained with a probabilistic shape prior. The shape prior is a spatially variant independent random field of region labels on a volume map, m , defined as:

$$P_{\text{sp}}(\mathbf{m}) = \prod_{(x,y,z) \in R} p_{\text{sp}:x,y,z}(m_{x,y,z}) \quad (4.7)$$

$p_{\text{sp}:x,y,z}(l)$ is the voxel-wise empirical probabilities of the co-aligned atlases constructed in the previous step. Ten co-aligned atlases are used to create the probabilistic shape prior.

To perform the shape probability segmentation, each voxel in the target data space (the image volume being segmented) is transposed using the nonlinear registration to the Atlas space. In the atlas space, a small window is taken around the location of the transposed voxel. Within this window, intensities and labels of the corresponding probabilistic shape prior values are collected.

A location that contains a tissue label will always be a nonzero value. A check is performed to determine if nonzero labels are located within this window. If there are no labels with nonzero values found, the window is enlarged by a small marginal value. When the window has enlarged to the a degree that nonzero labels are detected, the absolute difference between the target voxel value and the nonzero labels are computed. This difference is com-

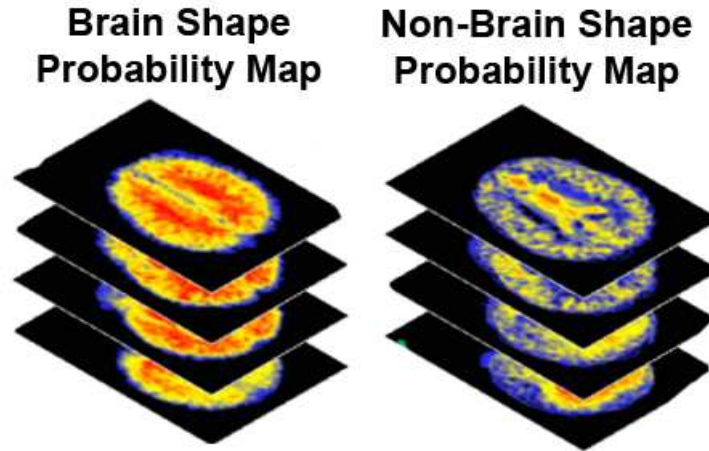


Figure 4.11: *Illustration of brain and non-brain shape probability maps. The registered shape probability maps are used to construct the shape probability classification.*

puted between the grayscale intensity of the target voxel and the grayscale intensity values for nonzero labels. The difference is computed for all nonzero labels. Labels that have differences within a specified threshold are accepted as matches to the target voxel. If no labels are detected within the specified threshold then the threshold is increased.

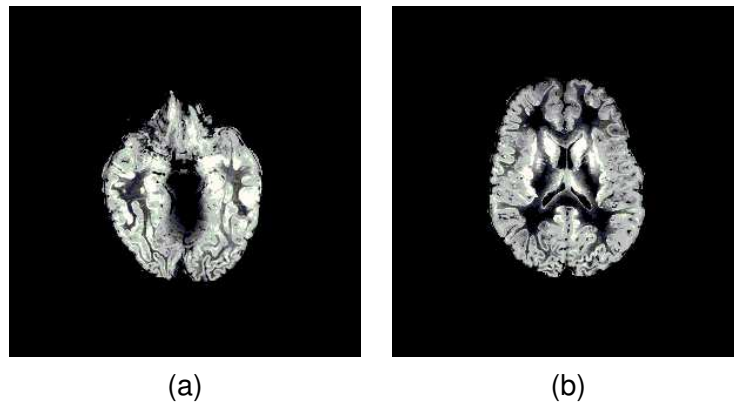


Figure 4.12: *Visual representation of the shape probability classification for the gray matter of the brain at two locations in an MR brain scan.*

Once the window contains more than one nonzero label that is within the difference threshold, the algorithm will classify the target voxel. The number of occurrences of each label within

the window with an acceptable difference threshold is determined. This creates a histogram of the number of occurrences of each label related to the target voxel. The label that occurs most frequently is selected. The lower label is selected in the case of two occurrences having an equivalent value in the histogram. Voxels with lower labels are considered of lesser importance than higher labels because voxels are assigned classes of: (i) brain stem; (ii) CSF; (iii) GM; and (iv) WM. In later steps of the Sight framework, only the gray matter and white matter are considered. It is preferable to assign an incorrect voxel a value that will later eliminate it from processing rather than to include it as an erroneous part of the brain volume. Each voxel in the target volume is iterated through the use of this procedure.

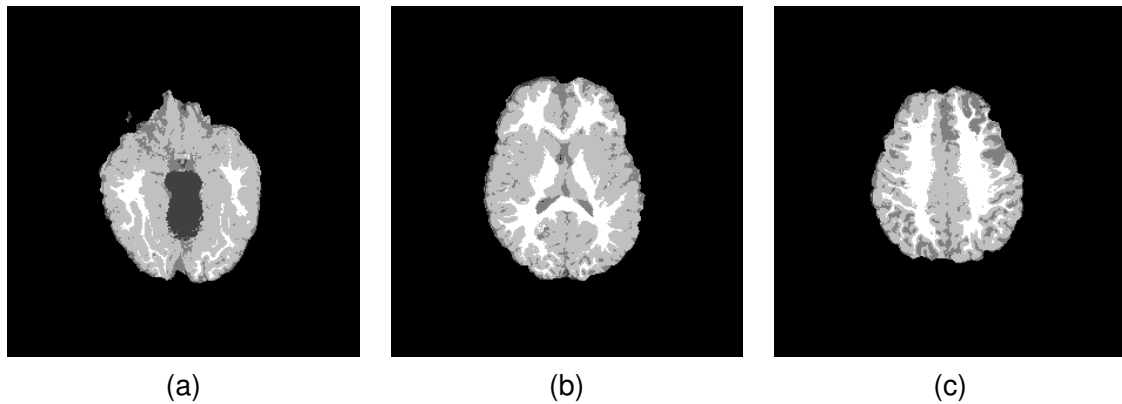


Figure 4.13: *Segmentation result using the shape probability classification depicted at three different locations in an MR brain scan. The final result of the shape probability contains smooth labels.*

The shape classification is limited by a maximum number of steps. The window size and threshold can each increase a maximum of three times. If acceptable values are not found within this limited search space then the target voxel is marked as a zero value and is removed from further classification.

4.3.3 Intensity Classification

While shape probability segmentation provides a good starting point, the end result is often too smooth and blurry to be useful as a stand alone segmentation model. It is necessary to implement a complementary intensity model into the segmentation platform. This intensity model is seeded with the shape probability model to increase initial accuracy and improve refinement speed.

To accurately approximate the marginal probability distributions of the brain and non-brain tissue, the empirical gray level distribution of brain data is precisely approximated with a linear combination of discrete Gaussians (LCDG) having both positive and negative components [201]. The LCDG restores brain and non-brain transitions more accurately than a conventional mixture of only positive Gaussians. This process yields a better initial map, m , formed by voxel-wise classification of the image gray values.

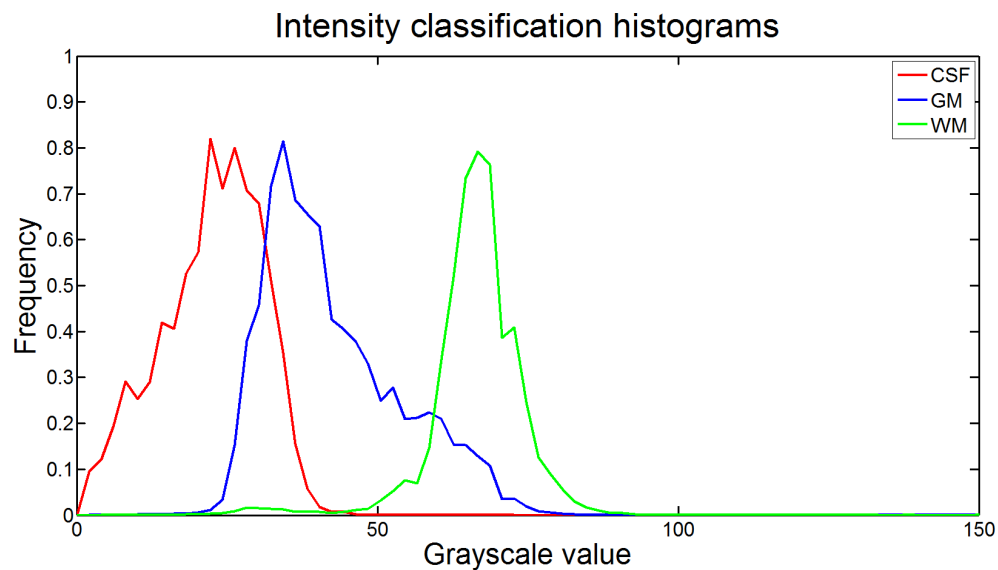


Figure 4.14: Intensity classification histograms for the CSF, GM, and WM of the brain.

The marginal intensity distribution of the MR images has three dominant modes that are seeded using the shape model: one mode for non-brain tissues (CSF), one for the grey

matter (GM), and one mode for the white matter (WM). The fourth class, the brain stem, is not included in the intensity model because the brain stem is formed from CSF, GM, and WM tissue. Because the brain stem includes all types of brain tissue, its inclusion introduces a large amount of noise in the intensity model as the dominant modes of the brain stem overlap with the modes of the brain proper.

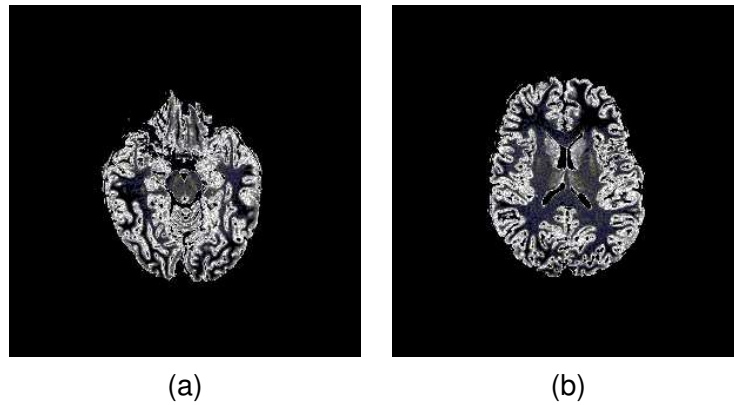


Figure 4.15: *Visual representation of the intensity classification for the gray matter of the brain at two locations in an MR brain scan.*

The basic steps of building the LCDG model are as follows. First, the marginal empirical probability distribution of the input grey level images for each class as determined by the shape model is collected. The shape data is used to create initial masks of tissue that falls under each dominant mode. The average starting value of each mode is determined by the collection of intensities found within each of these masks. Establishing the starting values using this process ensures that regions remain appropriately separated and are centered within their respective intensity ranges. The obtained empirical distribution is approximated with a mixture of three positive DGs relating to each dominant mode. The deviations between the empirical and the estimated distributions are approximated with alternating "subordinate" components of the LCDG. The obtained positive and negative subordinate mixtures are added to the dominant mixture to yield the final mixed LCDG model. This LCDG model is partitioned into three LCDG-submodels (one per class) by associating the subordinate DGs

with the dominant terms. This association is made so that the misclassification rate is minimized [201].

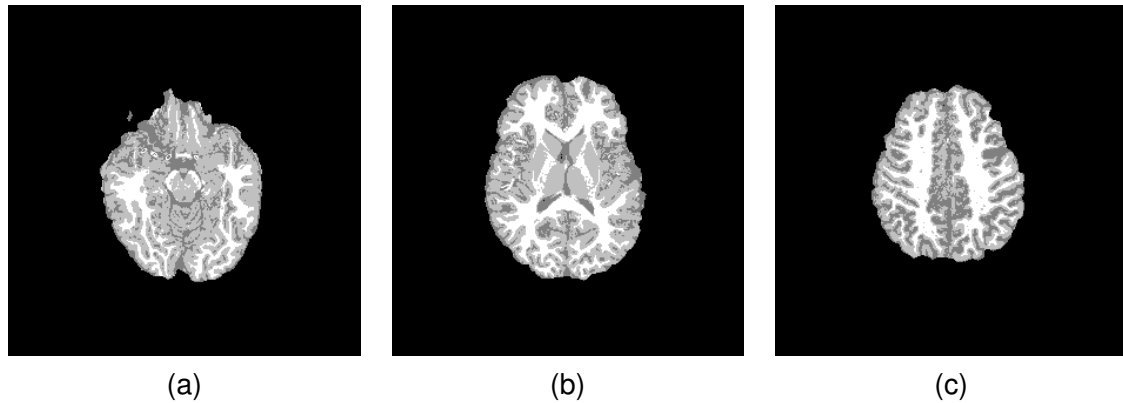


Figure 4.16: *Segmentation result using the intensity classification depicted at three different locations in an MR brain scan. The final result of the intensity classification contains sharp labels.*

Using the final LCDG refined histogram for each label, the target volume is segmented using the intensity. For each grayscale voxel in the target volume, the class with the highest probability of occurrence, based on intensity, is determined. By seeding the intensity model with the shape probability classification, the accuracy of the intensity model is greatly improved. This results in a more accurate segmentation of the brain tissue than using traditional seeding methods which start each dominant mode at evenly distributed random values.

4.3.4 Fusion of Shape and Intensity Classification

The shape probability classification is combined with the intensity model classification. For each label the probabilities of both shape and intensity are added together to form a single probability of each label occurring at a given voxel. The shape and intensity probabilities provide an equal contribution in determining the single probability. The voxels being segmented are then iterated through the algorithm. At each voxel, the label with the highest probability is

selected. There is an exception made when a voxel has a probability of belonging to the brain stem. Voxels only have a probability of belonging to the brain stem in the shape probability classification model. If the probability that a voxel belongs to the brain stem is greater than 50% the voxel is designated as belonging to the brain stem.

4.3.5 Spatial Refinement

Spatial refinement is performed on the volume after it has been segmented using the shape and intensity models. Spatial refinement is used to improve the shape and intensity segmentation. MGRFs are Markov random fields that occur on rectangular lattices with Gibbs probability distributions. MGRFs have been widely used in image modeling since the 1980s [210, 211, 212, 213, 214]. Most MGRF models assume that conditional signal dependencies are translation-invariant, and a lesser number of models assume a form of limited rotational invariance. Commonly, rotational invariance assumes that the same conditional dependencies occur between voxel pairs located at the angular rotation steps of 45° or 90° . To account for sizable local geometric deviations between relevant areas of an image volume, the spatial refinement used in the Sight framework uses a set of MR images of the brain, g . The framework models these images using a generalized translation- and rotation-invariant second-order MGRF. This descriptive MGRF model assumes a certain number, N , of embedded characteristic central-symmetric neighborhoods \mathbf{n}_v ; $v = 1, \dots, N$, in (\mathbf{R}) of each voxel $\mathbf{r} = (x, y, t)$ within the volume. The neighborhood (\mathbf{n}_v) of the voxel \mathbf{r} consists of the voxels \mathbf{r}' , located at distances $d(\mathbf{r}, \mathbf{r}')$ from an indexed semi-open interval $[d_{v:\min}, d_{v:\max})$, such that $d_{v-1:\max} = d_{v:\min}$ for $v = 2, \dots, N$. The distances are measured by the L2 norms of the coordinate offsets $\mathbf{o} = \mathbf{r}' - \mathbf{r}$.

The purpose of using an MGRF is to construct a smoothing algorithm that intelligently preserves the raw information. The MGRF functions by minimizing the energy in a specific

location so optimally the grayscale value at any location is selected. One primary difference of the MGRF proposed in this work is the implementation of a dynamically resizable window. The window is based on grayscale labels, as opposed to binary labels. This allows the approach to navigate difficult grayscale data applications in the brain.

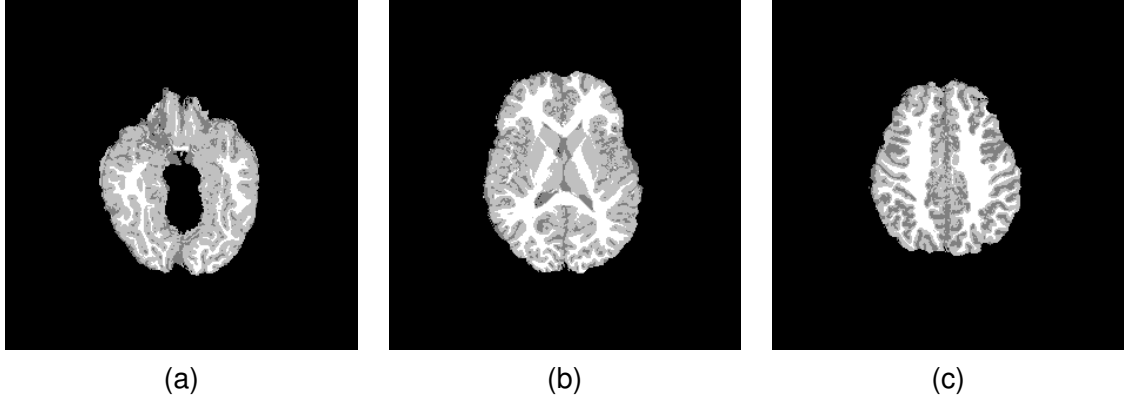


Figure 4.17: Segmentation result after fusing the shape probability and intensity classifications and applying spatial refinement. Results are depicted at three different locations in an MR brain scan. Inhomogeneities are corrected by applying the spatial processing.

The brain is a 3-dimensional structure and is composed of a stack of images. This MGRF implementation treats the data as a 3D entity. Typically MGRF approaches have used 2D slices. This adjustment allows information from neighboring slices to be taken into consideration. Each index, v , in this model, specifies a family of the neighboring voxel pairs, $\mathbf{C}_v = \{\mathbf{c}_v = (\mathbf{r}, \mathbf{r}') : \mathbf{r}' - \mathbf{r} \in \mathbf{n}_v; \mathbf{r}, \mathbf{r}' \in \mathbf{R}\}$. These families are considered as second-order cliques of the neighborhood graph. The nodes of the cliques contain the nearby voxels. The result is the construction of a nested spherical neighborhood system for the MGRF model.

Cliques from each family \mathbf{C}_v support their own real-valued Gibbs potential $V_v(g(\mathbf{r}), g(\mathbf{r}'))$, which quantifies this particular pairwise voxel interaction. To account for possible local brightness changes, affecting signal offsets, the potential depends on the absolute intra-clique signal difference: $\Delta = |q - q'| \in \mathbf{D} = \{0, 1, \dots, Q - 1\}$ where $q = g(\mathbf{r})$ and $q' = g(\mathbf{r}')$. For brevity, the potentials are represented below column vectors, $\mathbf{V}_v = [V_v(\Delta) : \Delta \in \mathbf{D}]$. The

characteristic cliques to be taken into account in the MGRF are stratified into N families, $\{\mathbf{C}_v : v = 1, \dots, N\}$. The potentials \mathbf{V}_v and their embedded non-intersecting distance intervals are defined as: $d_{1:\min} < d_{1:\max} \leq d_{2:\min} < \dots \leq d_{N:\min} < d_{N:\max}$.

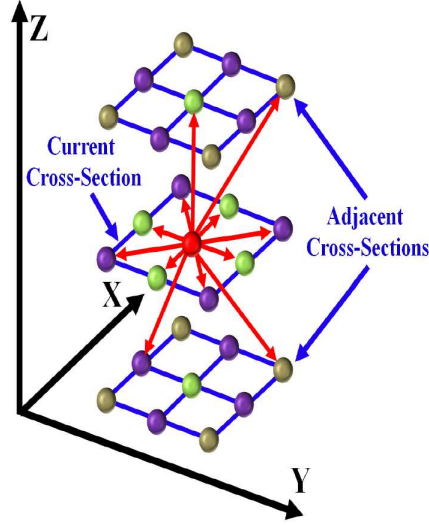


Figure 4.18: Illustration of the 3D spatial neighborhood system.

This type of MGRF has the Gibbs probability distribution [215]:

$$P(\mathbf{g}) = \frac{1}{Z_V} \exp(|\mathbf{R}| \mathbf{V}^T \mathbf{F}(\mathbf{g})) \equiv \frac{1}{Z_V} \exp(|\mathbf{R}| (\mathbf{V}_{\text{vox}}^T \mathbf{F}_{\text{vox}}(\mathbf{g}) + \sum_{v=1}^N \rho_v \mathbf{V}_v^T \mathbf{F}_v(\mathbf{g}))) \quad (4.8)$$

where T indicates the transposition. Z_V is the normalizing factor (the partition function) depending on the first- and second order potentials. $\mathbf{V} = [\mathbf{V}_{\text{vox}}; \mathbf{V}_v : v = 1, \dots, N]$ is the column vector of these potentials for the clique families $\{\mathbf{C}_v : v = 1, \dots, N\}$. $\rho_v = \frac{|\mathbf{C}_v|}{|\mathbf{R}|}$ is the relative size of the clique family with respect to the lattice cardinality $|\mathbf{R}| = XYT$, i.e., the relative number of cliques in the family \mathbf{C}_v . The column vector $\mathbf{F}(\mathbf{g}) = [\mathbf{F}_{\text{vox}}(\mathbf{g}); \rho_v \mathbf{F}_v(\mathbf{g}) : v = 1, \dots, N]$ contains relative empirical probabilities $f_{\text{vox}}(q|\mathbf{g})$ and $f_v(\Delta|\mathbf{g})$ of signals $q \in \mathbf{Q}$ in the voxels and absolute signal differences $\Delta \in \mathbf{D}$ in the cliques from the family \mathbf{C}_v over the image \mathbf{g} ,

respectively:

$$\begin{aligned}
\mathbf{F}_{\text{vox}}(\mathbf{g}) &= \left[f_{\text{vox}}(q|\mathbf{g}) = \frac{|\mathbf{R}_q(\mathbf{g})|}{|\mathbf{R}|}; q \in \mathbf{Q} \right]; \\
\mathbf{F}_v(\mathbf{g}) &= \left[f_v(\Delta|\mathbf{g}) = \frac{|\mathbf{C}_{v:\Delta}(\mathbf{g})|}{|\mathbf{C}_v|}; \Delta \in \mathbf{D} \right]; \\
\sum_{q \in \mathbf{Q}} f_{\text{vox}}(q|\mathbf{g}) &= 1; \quad \sum_{\Delta \in \mathbf{D}} f_v(\Delta|\mathbf{g}) = 1;
\end{aligned} \tag{4.9}$$

where the sublattice $\mathbf{R}_q(\mathbf{g})$ contains all the voxels \mathbf{r} , such that $g(\mathbf{r}) = q$, and the subfamily $\mathbf{C}_{v:\Delta}(\mathbf{g})$ contains all the pairwise cliques $\mathbf{c}_v = (\mathbf{r}, \mathbf{r}')$ of this family, such that $|g(\mathbf{r}) - g(\mathbf{r}')| = \Delta$.

Analytical first approximations of the maximum likelihood estimates of the potentials are defined as follows [215]:

$$\begin{aligned}
V_{\text{vox}}(q) &= \lambda (f(q|\mathbf{g}) - f_{\text{irf:vox}}(q)); q \in \mathbf{Q}; \\
V_v(\Delta) &= \lambda (f_v(\Delta|\mathbf{g}) - f_{\text{irf:dif}}(\Delta)); \Delta \in \mathbf{D}; \\
v &= 1, \dots, N
\end{aligned} \tag{4.10}$$

where the scaling factor λ is also analytical and $f_{\text{irf:vox}}(q) = \frac{1}{Q}$ and $f_{\text{irf:dif}}(\Delta)$ are the probabilities of the voxel signal q and inter-voxel signal difference Δ , respectively, for an independent random field of equiprobable signals:

$$f_{\text{irf:dif}}(\Delta) = \begin{cases} \frac{1}{Q} & \text{if } \Delta = 0 \\ \frac{2(Q-\Delta)}{Q^2} & \text{otherwise} \end{cases} \tag{4.11}$$

The factor λ can be omitted (i.e. set to $\lambda = 1$) if only relative interaction energies are computed for the clique families.

While the approach is an iterative process it is applied only one time in the Sight framework. The approach can be modified to refine a variety of image types, including Tagged MR Images of the heart to measure stress and strain.

4.3.6 Post-Processing

After the shape, intensity, and spatial processing are completed, a cleaning algorithm is applied to the final segmentation. A flood-fill algorithm is applied to a negative mask of the brain stem. This process fills possible holes that may have been misclassified as brain tissue within the region of the brain stem. The corrected negative mask is used to update the brain stem labels in the final segmentation.

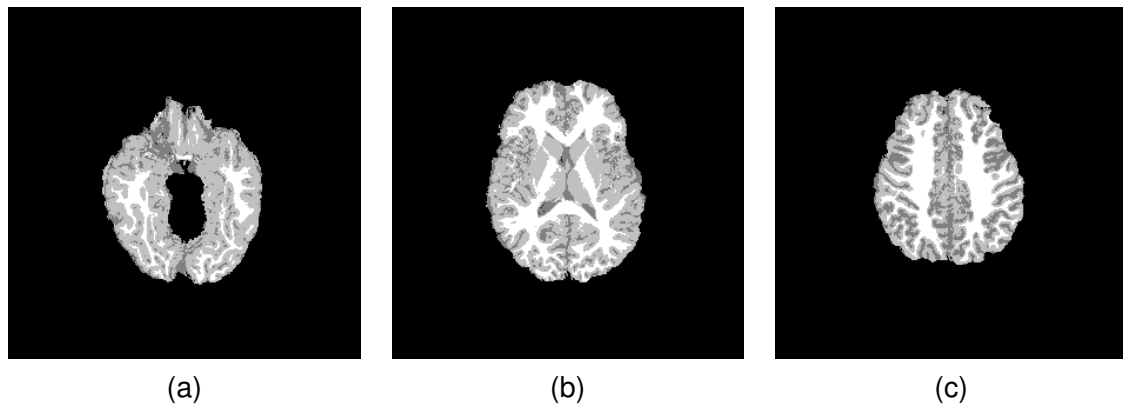


Figure 4.19: *Final segmentation result. Results are depicted at three different locations in an MR brain scan. The final result has the brain stem and cerebellum removed and contains sharp and accurate labels throughout the cerebral cortex.*

A binary mask is constructed from the CSF, GM, and WM labels. A four directional connectivity analysis is performed in both two and three dimensions to remove regions of the brain that are ancillary voxels to the brain proper. This removes erroneous areas found near the edges, top and bottom of the brain. This corrected binary mask is used to extract the brain from the labeled segmentation. The final labeled segmentation is saved as a series of images that will be used to construct a mesh of the brain.

4.4 Mesh Generation

4.4.1 Pre-Processing

Following segmentation, pre-processing procedures must ensure that the quality of the segmented images are acceptable for creating a mesh manifold. Preprocessing procedures are required to create a volumetric manifold from the segmented images. This volumetric manifold is required to create a mesh manifold [216, 217]. By definition, a manifold is a topological space that resembles a Euclidean space, or a space that encompasses a three-dimensional Euclidean plane [218, 219]. A mesh manifold is an object that contains no holes. This means that for every edge (a connection between two points or nodes), each edge is incident to only one or two faces and that all of the faces surrounding any node form a closed or an open fan. This condition is a principal requirement for utilizing Spherical Harmonics. 3D Spherical Harmonic analysis can only be performed on a mesh manifold.

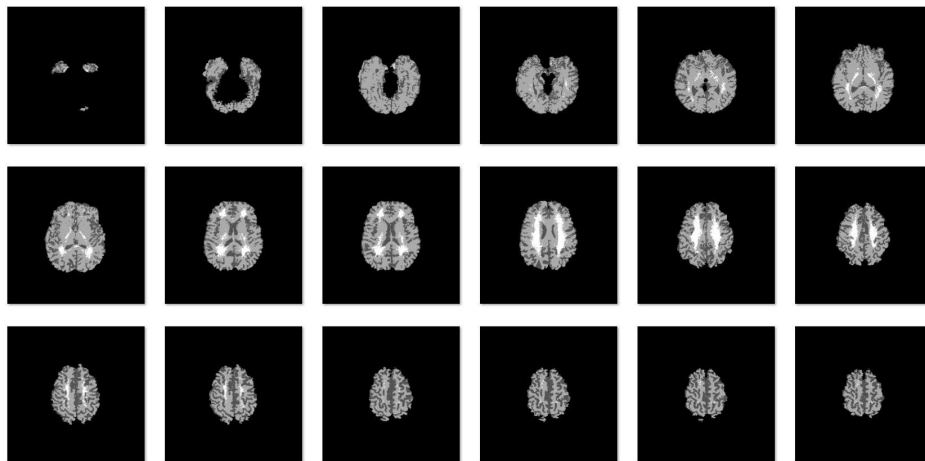


Figure 4.20: A set of raw segmented MRI scans containing CSF, GM, and WM tissue.

Segmented MRI scans by default do not meet the condition of a volumetric manifold. The following procedure is applied to an MRI volume to create a volume manifold: (i) removal of

all non-brain voxels; (ii) construction of the binary representation of the brain; (iii) removal of non-connected shapes; (iv) 2D and 3D flood-filling of the images; (v) rigid registration to a mesh alignment atlas.

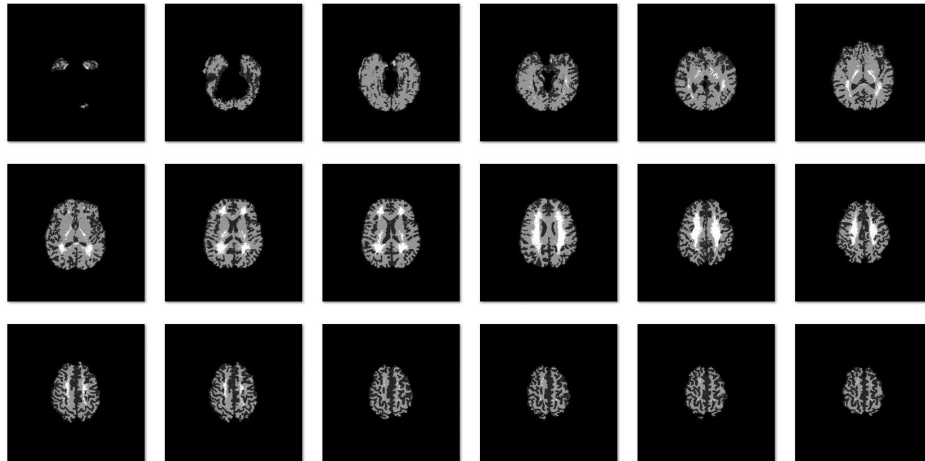


Figure 4.21: *The CSF has been removed from the images in Figure 4.20.*

The first procedure removes all non-brain voxels from the target volume. This step is accomplished by eliminating all voxels that do not have a label representing the white or gray matter of the brain. In step two, these labels are then combined into a single label. The brain labels are then converted to a binary format. A binary representation consists of only numbers 1 and 0, where 1 represents the brain, and 0 represents nothing. After removing labels that do not contain brain information, erroneous disconnected shapes may be present in the volume. These disconnected shapes are not part of the brain proper.

The removal of disconnected shapes is done in a specific sequence. First, in each slice of the MRI scan, the number of connected objects and size of each object is computed. This computation is done using a 2D connected-component region growing labeling method [220]. Any objects that have a size below a specific threshold are removed. The threshold is defined using empirical testing. This removal threshold is defined as less than 30 voxels. When constructing a mesh of a brain, faces that comprise fewer than 30 voxels result in spiked or

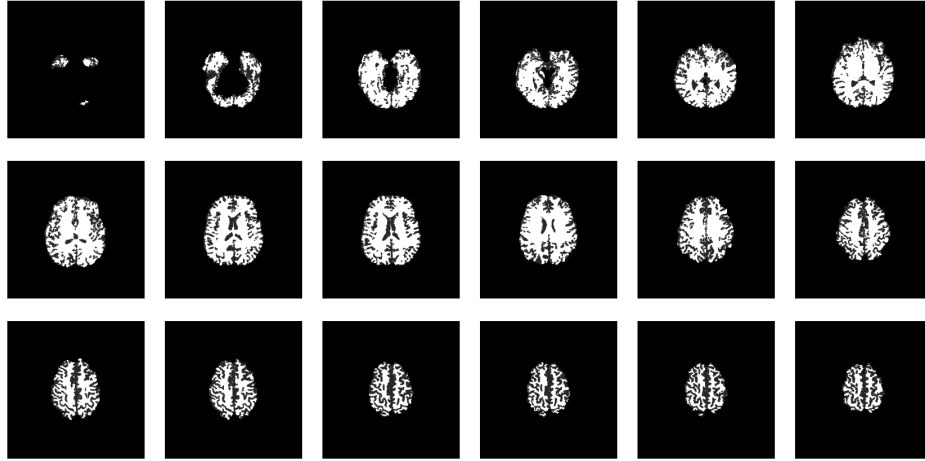


Figure 4.22: *The images in Figure 4.21 having been converted to a binary representation.*

pointed areas on the surface of the mesh. Connected areas of fewer than 30 voxels are not common in the brain, and only occur in locations at the extreme top and bottom image slices of the brain. The reason for this occurrence, is that the CSF and GM have very similar values in these locations, and they are often misclassified voxels. Therefore, removing these extreme peaks from the data is beneficial to ensure the integrity of the volume.

After the 2D disconnected shapes are removed, a 3D connectivity analysis is performed. Each connected object and its corresponding size is computed using connected component labeling. In this analysis only the largest connected object is retained in the volume. Any other objects are discarded. The end result of this process, is that a mask of the cerebral cortex remains in the volume

After removing all disconnected objects, a two stage flood-fill process is used to remove voxels holes in the mask of the cerebral cortex. The 2D flood fill algorithm works by detecting the outer boundaries of the binary image in each slice and filling in all contained voxels. The 3D flood-fill algorithm is more complex , because it accounts for a more difficult problem. In a 3D brain mask, there are locations inside the mask with large holes. These holes are not seen as 2D holes when using a simple flood- fill algorithm. More accurately, these occurrences can

be thought of as voids that are detected in areas such as the ventricles of the brain (fluid filled locations found near the center of the brain in each hemisphere). The holes are removed from the volume using a custom algorithm. To remove these holes, each individual pixel containing no information is examined in the 3-dimensional volume. At each pixel, a ray is extended in the $\pm X$ and $\pm Y$ directions until it reaches a non-zero value or the edge of the volume. If the ray touches a voxel in all of the $\pm X$ and $\pm Y$ directions, it is marked as a possible hole and is examined in a second iteration. In the second iteration, a ray is extended in the $\pm Z$ direction for a distance of 5% of the volume size or until the edge of the volume is reached. If non-zero values are detected in both the $\pm Z$ directions, the hole is denoted as a void that must be filled. The entire process repeats until no holes are detected in the image. In practice, only three passes are required to accomplish this goal. The process is detailed in Algorithm 3.

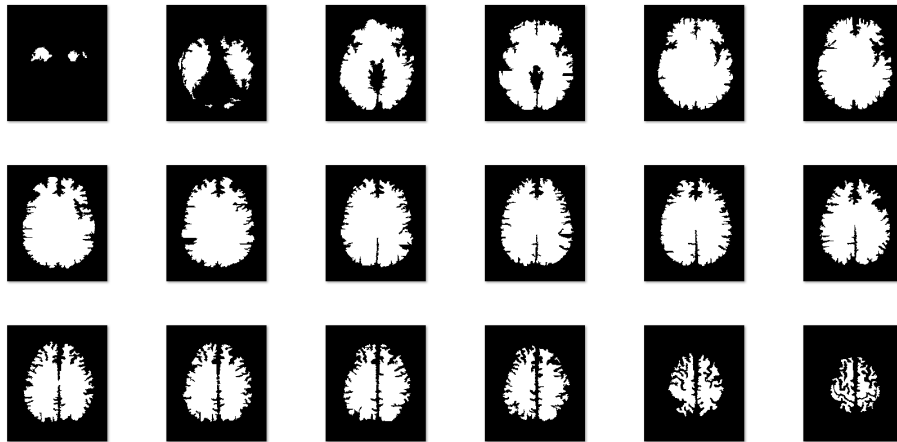


Figure 4.23: Results after application of the cleaning algorithms on the binary images in Figure 4.22.

The result of performing these pre-processing steps is a product containing the true manifold volume mask of the brain. The last step performs a rigid registration of the brain using an algorithm developed for this purpose. A rigid registration is used to preserve the integrity of the brain shape, so only translation and rotation are applied. The registration technique, which is used for multiple applications, is discussed in complete detail in section 4.6.1.

Algorithm 3 3D Flood-Fill

INPUTS:*Volume containing holes***OUTPUTS:***Volume without holes*

```

change ← true
while change do
  change ← false % assume no changes
  for all voxels do
    if voxel == 0 || voxel == boundary then
      continue
    end if
    track ← true
    for all directions do % check directions
      if track then
        track ← false
        for all voxelT in + direction do
          if voxelT == 1 then % found object boundary
            track ← true
          end if
        end for
      end if
      if track then
        track ← false
        for all voxelT in - direction do
          if voxelT == 1 then % found object boundary
            track ← true
          end if
        end for
      end if
    end for
    if track then
      voxel ← 1 % fill the hole
      change ← true
    end if
  end for
end while

```

4.4.2 Delaunay Triangulated Meshing

Once the 3-dimensional manifold volume is properly constructed a mesh is generated. The mesh generation is performed using a modified version of the TETGEN algorithm initially constructed for the iso2mesh Matlab based mesh generation system, written by Qianqian Fang and David Boas [221, 222]. This system is built on the CGAL Delaunay Triangulation mesh engine [223]. CGAL is the open source Computer Geometry Algorithms Libra, that offers algorithms utilized for performing geometric manipulations of data. The CGAL Delaunay triangulation method functions by creating a circumscribing sphere of each cell, sequentially placing triangulations within this sphere. No vertices of any triangulation are placed within the center of the circumscribing sphere. These triangulations are uniquely defined, except in degenerate cases, where the five points are co-spherical. If this situation occurs, the triangulations are recomputed in a circumscribing sphere. This method produces a non-rigid mesh generation, and points are not constrained to contain a specific number of neighbor nodes. This means that the number of neighbors is bound at a minimum of three nodes. A properly formed triangular node must have a minimum of three faces, a restriction reached using the examined node and a minimum of three neighbors. It is important to note that this process has no maximum number of neighbors. Repeated application has determined that it is unconventional for triangulations to have over seven neighbors.

When constructing a mesh, several additional rules must be considered. A mesh must have 50,000 nodes during construction. Due to the the differences in the unique shape of meshes, the number of nodes that may occur in any area changes dynamically. This causes the number of face changes to alter dynamically based on the positioning of the nodes. It is critical that there must be a consistent number of nodes present so that meshes can be aligned with one another using a 1-1 node ratio. In previous work, the node count was restricted to 12,500 nodes due to processing and computational time. Advances made to the

smoothing and spherical deformation algorithms have rendered the total computational time irrelevant, and the decision to use 50,000 nodes is based on the decision that this number creates an accurate representation of the brain. While it is possible to add additional nodes, this often leads to an over-saturation of nodes resulting in a negligible accuracy improvement at the expense of additional time.

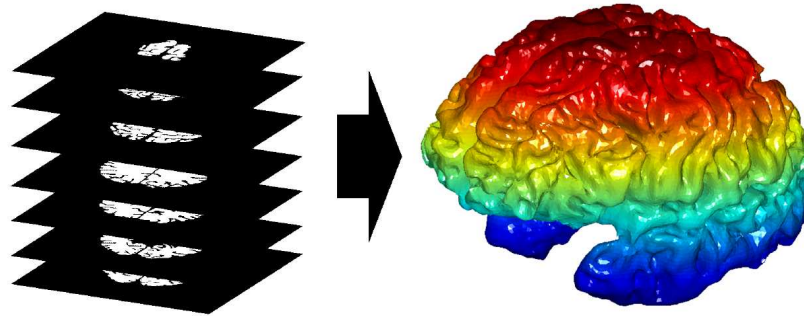


Figure 4.24: A 3D volumetric mesh constructed from a set of processed images.

The data received from the mesh generation becomes a collection of nodes and triangulations [223]. The nodes matrix is of size $3 \times N$, and the triangulations matrix is of size $4 \times T$, where N is the maximum allowable number of nodes and T varies based on the positions used by the mesh engine and the triangulations created between points. The fourth column in the triangulation matrix, represents the presence of face connectivity at this point. This column is discarded to create a traditional $3 \times T$ representation of mesh triangulations. In a restricted mesh manifold all face connectivities are valid.

Once the initial mesh is created, it becomes necessary to reposition it in 3-dimensional space and resize the mesh to appropriate proportions. Resizing is only necessary if the data is not uniformly scaled. The centroid of the mesh is calculated in the X , Y , and Z directions. Using the coordinates of the centroid, the mesh is repositioned, so it is centered on the origin in 3-dimensional Cartesian space ($x = 0$, $y = 0$, $z = 0$). To appropriately resize a mesh, its original image slice acquisition scaling was used. The images were repositioned according

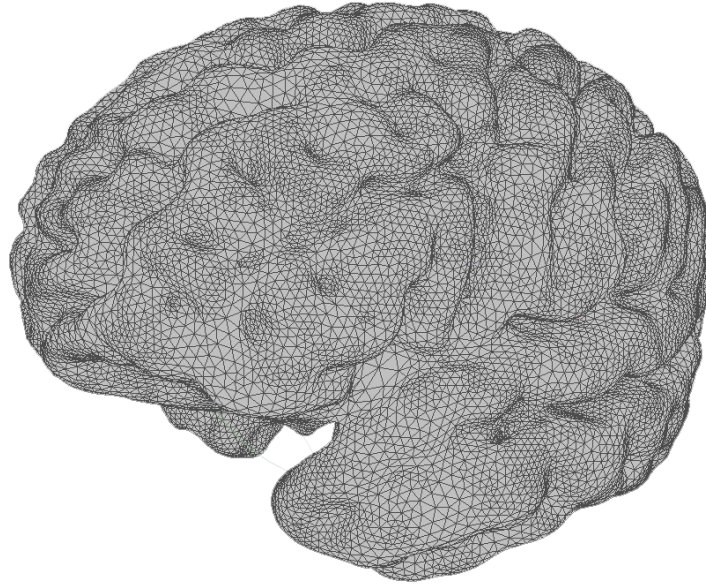


Figure 4.25: *Detailed representation of the Delaunay triangulations on the surface of the constructed brain mesh.*

to the X , Y , and Z magnification parameters.

The final mesh is stored as a Wavefront OBJ, developed by Wavefront Technologies [224]. The standardized Wavefront OBJ is the most universal format of choice in a majority of commercial mesh applications. The Wavefront OBJ format can be read by nearly all modern commercial and open-source applications that perform mesh analyses. This allows for potential integration of the Sight framework with third-party software. The use of this format also ensures that mesh objects constructed using the proposed framework are useable, regardless of changes made to the mesh computation algorithms. Custom algorithms were constructed to efficiently save and load meshes in the Sight framework.

```

1 #####
2 #
3 # OBJ File Generated by Sight
4 #
5 #####
6 # Object C:\mesh_original.obj
7 #
8 # Vertices: 50000
9 # Faces: 100028
10 #
11 #####
12 vn 0.509214 -0.183036 -0.840951
13 v -62.703628 -9.894772 32.941709
14 vn -0.004199 0.389533 0.921003
15 v -6.811038 -43.400631 -56.254838
16 vn 0.192854 0.785432 0.588135
17 v 57.364928 -10.894431 44.949070
18 # 50000 vertices, 50000 vertices normals
19
20 f 26977//26977 26970//26970 48332//48332
21 f 26977//26977 48332//48332 26978//26978
22 f 8678//8678 11824//11824 11822//11822
23 f 19415//19415 19416//19416 17840//17840
24 f 18106//18106 8336//8336 18098//18098
25 # 100028 faces, 0 coords texture
26
27 # End of File

```

Figure 4.26: Example of a condensed Wavefront OBJ file format containing sample data from a Delaunay triangulated mesh.

4.4.3 Laplacian Smoothing

Before beginning a spherical deformation, a Laplacian smoothing operation is performed on a mesh to create a more suitable starting point for constructing a spherical shape [225, 226, 227, 228]. The equation for smoothing a node on a mesh is defined as:

$$\bar{x}_i = \frac{1}{N} \sum_{j=1}^N \bar{x}_j \quad (4.12)$$

where N is the number of vertices that are adjacent to node i , x_i is the updated position for node i , and $i \in M$, where M is the set of nodes in a mesh [225].

Before beginning a spherical deformation a subject is smoothed $N_{initsmooth}$ number of times where $N_{initsmooth} = \frac{\text{Number of Nodes}}{100}$. This results in the algorithm performing 500 smoothing operations on a 50,000 node mesh. In each analysis of the brain, this value remains

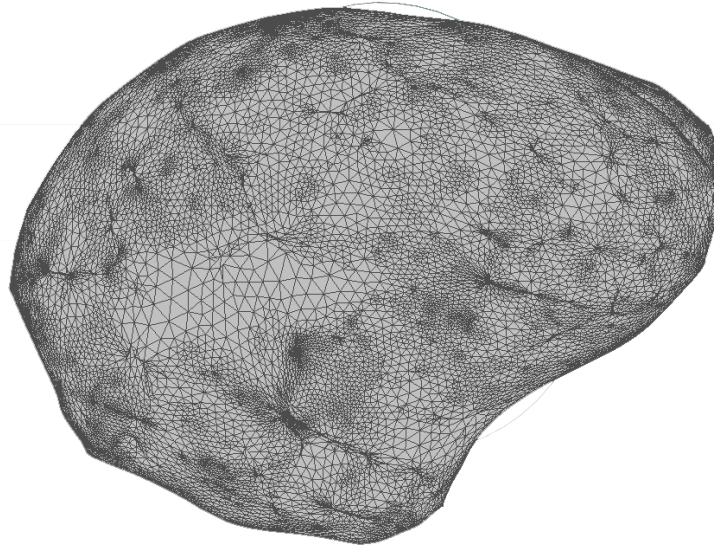


Figure 4.27: *Result of applying 500 iterations of Laplacian smoothing to the mesh in Figure 4.25.*

constant. However, when examining other organs that are smaller or larger, the number of smoothing operations is altered dynamically.

4.4.4 Spherical Deformation

Spherical Harmonic (SPHARM) analysis [3, 229, 230] considers a set of 3D surface data as a linear combination of specific basis functions. SPHARM plays a critical role in the reconstruction and understanding of brain meshes. Before being able to perform SPHARM calculations, it is necessary to create the base or 0th harmonic of the SPHARM sequence. To construct this base harmonic, the brain mesh manifold is deformed into a unit sphere. This unit sphere deformation is accomplished by using the "Attraction-Repulsion" mapping approach.

This approach deforms the original mesh manifold into a unit sphere mesh that meets the following conditions: (i) the unit distance of each node from the brain cortex center as shown in Figure 4.29, and (ii) an equal distance of each node from all of its nearest neighbors

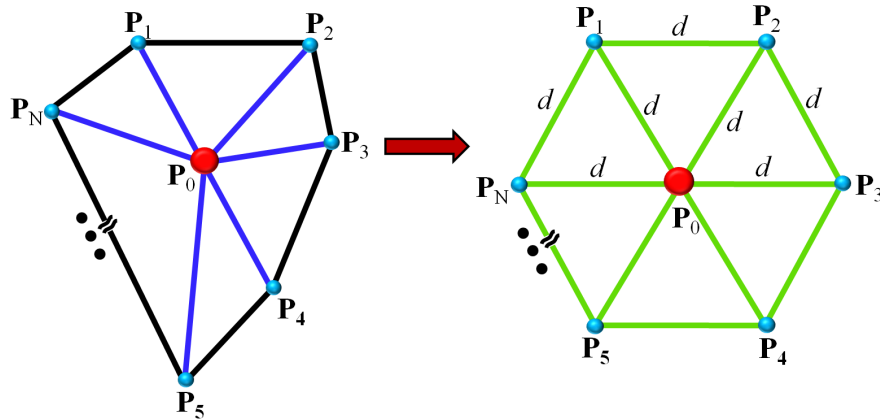


Figure 4.28: 2D illustration of Attraction-Repulsion neighbor node rearrangement: (a) initial vs. (b) final equidistant locations in all the directions.

as shown in Figure 4.30. The Attraction-Repulsion approach has changed algorithmically, in addition to improvements in speed and accuracy, from its original incarnation proposed in 2010.

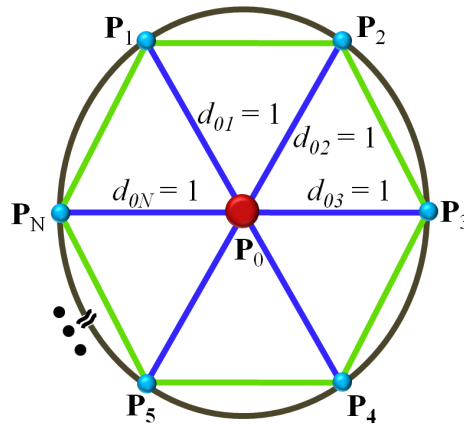


Figure 4.29: 2D illustration of the neighbors showing a unit distance from one neighbor to another.

To detail the Attraction-Repulsion Algorithm (see its summary in Algorithm 4), let τ denote the iteration index, I be the total number of the mesh nodes (in all the experiments below $I = 50,000$ nodes), and $\mathbf{P}_{\tau,i}$ be the Cartesian coordinates of the surface node i at iteration τ ; $i = 1, \dots, I$. Let J be the number of the neighbors for a mesh node (see e.g., Figure 4.30)

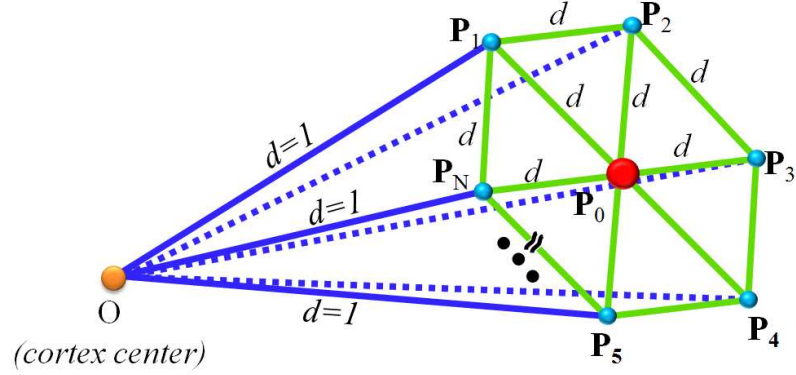


Figure 4.30: 3D illustration of the unit distance from all surface nodes to the center of the brain cortex.

and $d_{\tau,ij}$ denote the Euclidean distance between the surface nodes i and j at iteration τ (as shown in Figure 4.30(b)), where $i = 1, \dots, I$ and $j = 1, \dots, J$. Let $\Delta_{\tau,ji} = \mathbf{P}_{\tau,j} - \mathbf{P}_{\tau,i}$ denote the displacement between the nodes j and i at iteration τ . Let $C_{A,1}$, $C_{A,2}$, C_R be the attraction and repulsion constants, respectively, that control the displacement of each surface node.

The initial attraction step of the proposed mapping centers each node \mathbf{P}_i ; $i = 1, \dots, I$, with respect to its neighbors by adjusting iteratively its location:

$$\mathbf{P}'_{\tau,i} = \mathbf{P}_{\tau,i} + C_{A,1} \sum_{j=1; j \neq i}^J \Delta_{\tau,ji} d_{\tau,ji}^2 + C_{A,2} \frac{\Delta_{\tau,ji}}{d_{\tau,ji}} \quad (4.13)$$

where the factor $C_{A,2}$ keeps the tightly packed nodes from collision and pushes the adjusted nodes away from their neighbors, if a certain neighbor is much closer than the others.

The subsequent repulsion step inflates the entire mesh. The nodes are pushed outward so that they become evenly spaced. The nodes are then back-projected onto the unit sphere along rays initiating at the center of the sphere. To ensure that the unshifted nodes do not collide with previously altered nodes, the locations of each node \mathbf{P}_i ; $i = 1, \dots, I$, are updated before the back-projection is applied:

Algorithm 4 Attraction-Repulsion**INPUTS:***Brain Cortex Delaunay Mesh***OUTPUTS:***Unit Sphere Delaunay Mesh*

Smooth the mesh using Laplacian filtering.

Initialize the mapping of the smoothed mesh to the unit sphere.

 $iter \leftarrow 0$ **while** changes in nodes **do** **for all** nodes **do** **Attraction:** Update node using Eq. (4.13) **Repulsion:** Update node using Eq. (4.14) **end for** LAPLACIANSMOOTH(mesh, $n/(1000 * 2)$) % *smooth mesh n times* **if** iter > InitialIters **then** BACKPROJECT(mesh) % *back-project nodes onto unit sphere* **end if** $iter \leftarrow iter + 1$ **end while**

$$\mathbf{P}_{\tau+1,i}^{\circ} = \mathbf{P}'_{\tau,i} + \frac{C_R}{2I} \sum_{j=1; j \neq i}^I \left(\frac{\Delta\tau_{,ji}}{|\Delta\tau_{,ji}|^2} \right) \quad (4.14)$$

where a repulsion constant C_R controls the displacement of each surface node and establishes a balance between processing time and accuracy (e.g., a smaller C_R value guarantees that the node faces will not become crossed during the iterations at the expense of increased processing time). Appropriate values for C_R are between 0.4 and 0.6.

Adding Laplacian smoothing and an unrestricted initial deformation greatly improves the accuracy for creating a unit sphere mesh. An unrestricted deformation is one that applies the algorithm and omits the back-projection calculations. This allows the mesh manifold to expand in an unrestricted manner. The end result, is that the algorithm performs in the same way as filling a balloon with high pressure water. Initially, the shape of the balloon grows chaotically, and then the deformations slows to a more controlled spherical shape. This pro-

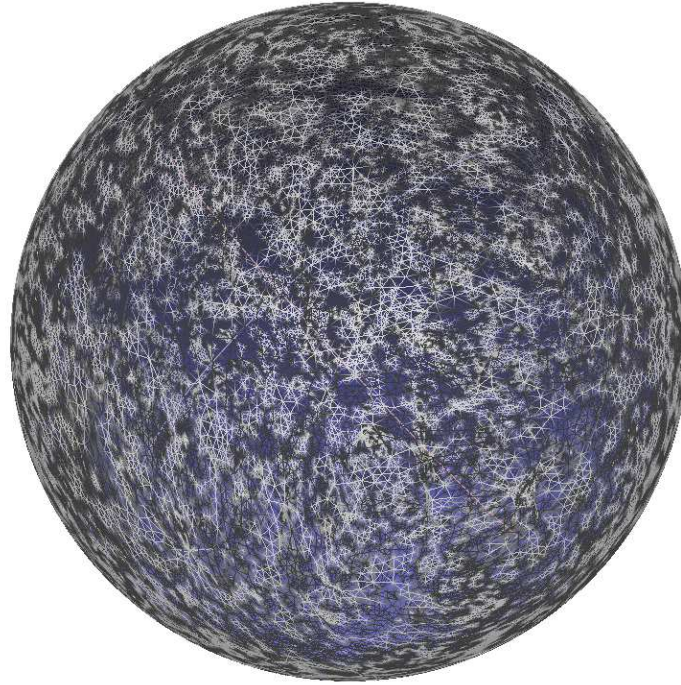


Figure 4.31: *Unit sphere constructed using the Attraction-Repulsion algorithm for the mesh in Figure 4.25.*

cess allows even a complex shape like the brain to be deformed into a unit sphere accurately and quickly. Processing speed is also a factor, therefore the algorithm has been optimized to complete spherical deformation of a 50,000 node mesh in under 300 seconds, or five minutes. This computational speed makes this algorithm one of the fastest spherical deformation algorithms. Performance on a smaller mesh, such as those used to represent other organs can be completed in a much shorter time frame.

4.5 Spherical harmonics (SPHARM) shape analysis

A weighted-SPHARM analysis [3, 229, 230] is used to reconstruct the brain and to derive metrics for classification. Once the brain mesh manifold has been mapped to the unit sphere, using the Attraction-Repulsion algorithm, the mesh is approximated by a linear combination of spherical harmonics. An approximation of an object using SPHARM, breaks the object into a string of linear harmonics where different degrees of information are stored in each harmonic. These linear harmonics are generated by solving an isotropic heat equation for the cortex surface on the base harmonic (the 0th harmonic, which is the unit sphere previously constructed) [3, 230]. The lower-order harmonics represent the basic root information of the shape. Higher-order harmonics contain information related to the fine details of the shape. For a visual reference, consider the SPHARM reconstruction of mesh in the image of a dragon fruit. The lower order harmonics would reconstruct the general shape information altering the the mesh to look similar to a mango. The higher-order harmonics would reconstruct the pointed structures on the surface of the dragon fruit. When applied to the brain, the sulci and curvature of the brain can be thought of as the spikes on the dragon fruit.

Let $\mathcal{S} : \mathbf{M} \rightarrow \mathbf{U}$ denote the mapping of a cortical mesh \mathbf{M} to the unit sphere \mathbf{U} . Each node $\mathbf{P} = (x, y, z) \in \mathbf{M}$ mapped to the spherical position $\mathbf{u} = S(\mathbf{P})$ is represented by the spherical coordinates $\mathbf{u} = (\sin \theta \cos \varphi, \sin \theta \sin \varphi, \cos \theta)$ where $\theta \in [0, \pi]$ and $\varphi \in [0, 2\pi)$ are the polar and azimuth angles, respectively. The SH $Y_{\alpha\beta}$ of degree α and order β is defined as [231]:

$$Y_{\alpha\beta} = \begin{cases} c_{\alpha\beta} G_{\alpha}^{|\beta|} \cos \theta \sin(|\beta|\varphi) & -\alpha \leq \beta \leq -1 \\ \frac{c_{\alpha\beta}}{\sqrt{2}} G_{\alpha}^{|\beta|} \cos \theta & \beta = 0 \\ c_{\alpha\beta} G_{\alpha}^{|\beta|} \cos \theta \cos(|\beta|\varphi) & 1 \leq \beta \leq \alpha \end{cases} \quad (4.15)$$

where $c_{\alpha\beta} = \left(\frac{2\alpha+1}{2\pi} \frac{(\alpha-|\beta|)!}{(\alpha+|\beta|)!} \right)^{\frac{1}{2}}$ and $G_{\alpha}^{|\beta|}$ is the associated Legendre polynomial of degree α and order β . For the fixed α , the polynomials G_{α}^{β} are orthogonal over the range $[-1, 1]$. As shown in [231], the Legendre polynomials are an effective means of calculating SHs, and this is the main motivation behind their use in this work.

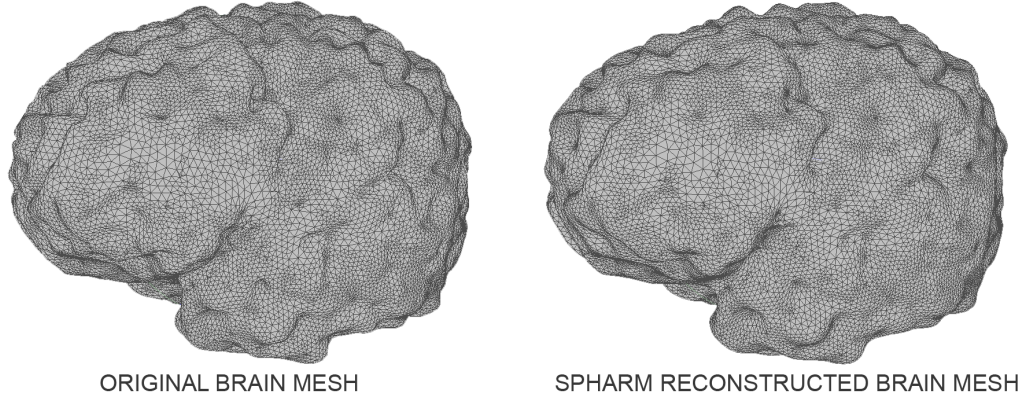


Figure 4.32: An original brain mesh and its SPHARM reconstruction using 80 harmonics. The two meshes are nearly identical to one another.

The brain cortex is reconstructed from the SPHARMs of Eq. (4.15). Using traditional SPHARM expansion, a standard least-square fitting model does not accurately approximate the 3D shape of the brain cortex. This can result in shape details being lost. To circumvent this problem, the iterative residual fitting model by Chung and Shen [230] is applied to the SPHARM expansions to accurately approximate the 3D gyrifications for brain cortices.

To perform a quantitative analysis of the brain shape, two techniques are used in measuring the complexity of the cerebral cortex: SPHARM reconstruction error and surface complexity.

4.5.1 SPHARM reconstruction error

As discussed in Section 4.6.2, SPHARM provides an optimum environment for aligning nodes between two meshes. Nodes maintain a static angular location in spherical coordinate space. These static angular locations remain constant throughout the entire reconstruction of an object. This allows for the deviation between a node in the reconstructed shape object when compared with its counterpart node in the original shape object. This deviation can be measured using a distance metric. The Euclidean distance is used to determine the amount of error between the reconstructed node location and its original location. The cumulative error for the entire shape can be determined for each set of harmonics. This cumulative error map is used to generate a reconstruction error curve that is unique to each subject, as shown in Figure 4.33. This reconstruction curve can be further simplified to a single reconstruction error metric. The reconstruction error is defined as the cumulative area under the reconstruction error curve. The reconstruction error can serve as a robust metric for the examining the complexity of the surface of an object, e.g. the cerebral cortex.

4.5.2 Surface complexity

The surface complexity is a metric for examining the complexity of the cerebral cortex using the SPHARM coefficients. For a unit sphere f , having a SPHARM expansion as shown in Eq. (4.15), the surface complexity, $S(f)$, is defined as:

$$\begin{aligned} S(f) &= \sum_{L=0}^{\infty} \varepsilon_L^2 \\ &= \sum_{L=0}^{\infty} LB_L^2 \end{aligned} \tag{4.16}$$

where L is the number of harmonics, and b are the previously calculated SPHARM coefficients. The squared residual ε_L^2 is defined as:

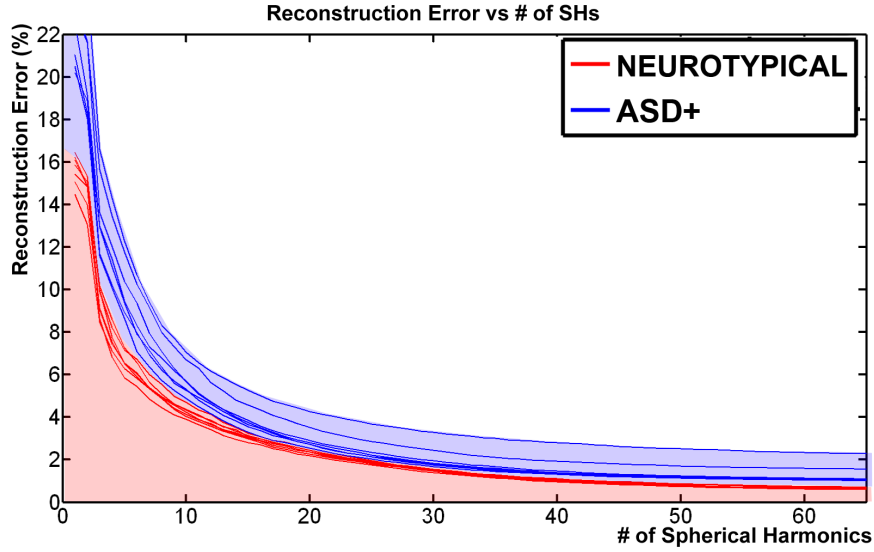


Figure 4.33: A sample SPHARM error reconstruction curve illustrating ASD+ and neurotypical subjects.

$$\begin{aligned}
 \varepsilon_L^2 &= \|f - f_L\|^2 \\
 &= \left\| \sum_{l=L+1}^{\infty} \sum_{m=-l}^l b_{lm} Y_l^m \right\|^2 \\
 &= \sum_{l=L+1}^{\infty} \sum_{m=-l}^l |b_{lm}|^2 \\
 &= \sum_{l=L+1}^{\infty} B_l^2
 \end{aligned} \tag{4.17}$$

For use in 3-dimensional SPHARM analysis there are three sets of coefficients for each direction, X , Y , and Z . The surface complexity is expanded from Eq. 4.17 to be defined as:

$$S(f) = \frac{\sum_{L=0}^{\infty} L(B_{L,x}^2 + B_{L,y}^2 + B_{L,z}^2)}{\|f_x\|^2 + \|f_y\|^2 + \|f_z\|^2} \tag{4.18}$$

The surface complexity computation generates a unique curve for each subject similar to the SPHARM reconstruction error curves, as shown in Figure 4.34. An advantage of this calculation is that it relies solely on computations from the coefficients. This makes the calculation a self contained metric representing the average degree of SPHARM expansion. The surface complexity is a convergent metric. The surface complexity is a unique metric for examining

the cerebral cortex.

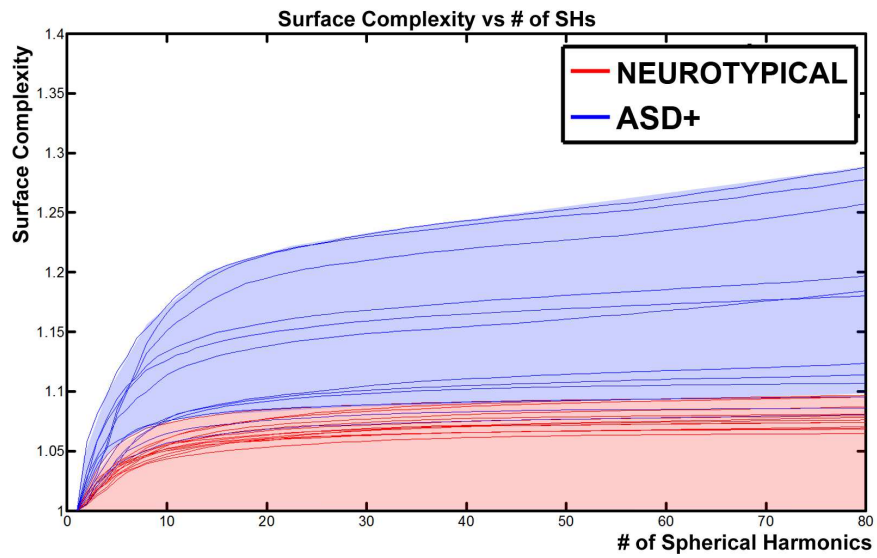


Figure 4.34: A sample surface complexity reconstruction curve illustrating ASD+ and neurotypical subjects.

4.6 Registration and Alignment

Two distinct registration approaches are used in the Sight framework. The first approach, is a volumetric rigid/non-rigid registration, used to manipulate and align volumetric meshes with atlases for segmentation. The second approach, is a SPHARM based mesh registration, used to position nodes belonging to different meshes along the same angular locations in a spherical coordinate system. This enables uniformly labeled regions to be quickly extracted and analyzed.

4.6.1 3D Volume Registration

In order to accurately examine the brain surface, the target brain volumes are aligned to a reference volume using geometric transformations. These geometric transformations may be either rigid or nonrigid Euclidean movements. The most favorable alignment is selected using an unconstrained optimization of a nonlinear fitness function. The fitness function combines two weighed terms depending on relative (X,Y,Z) -translations and rotations (denoted below θ) of a target 3D volume in regards to a reference [232].

Rigid registration involves registering two objects without altering or distorting the shape of either object, while nonrigid registration disregards object alterations and distortions [233, 234]. Translation, the process of moving a volume in space, and rotation, the process of spinning a volume, are rigid transformations. Scaling, the process of resizing a volume, and shearing, the process of skewing a volume, are nonrigid transformations and result in brain shape distortions. Scaling and shearing are therefore excluded from rigid registrations, but are utilized in nonrigid registrations. The proposed registration framework does not support the concept of warping. Empirical testing on brain registrations has demonstrated that warping offers a minor advantage in accuracy in exchange for a significant increase in

computation time.

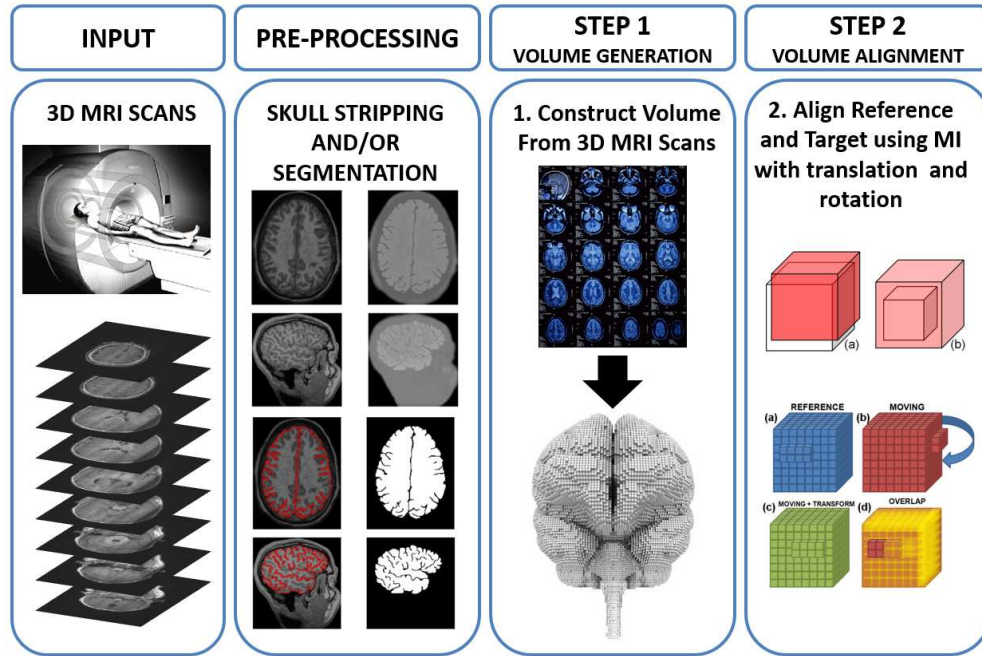


Figure 4.35: Overview of the 3D volumetric registration approach detailing each step in the framework.

The fitness function is composed of two terms that evaluate the alignment. These terms are relative 3D mutual information (MI) and voxel overlap between the volumes. MI (see, e.g. [235]) is computed between distance maps for a reference and target volume. The target volume is the data that is being aligned to the reference volume. Each distance map is computed using the Multi-Stencils Fast Marching Method [236]. The relative 3D MI is as follows:

$$E_{mi}(\theta) = \frac{M_{tar}(\theta)}{M_{max}} \quad (4.19)$$

where $M_{tar}(\theta)$ is the MI between the transformed target and the reference, and M_{max} is the MI between the reference and itself.

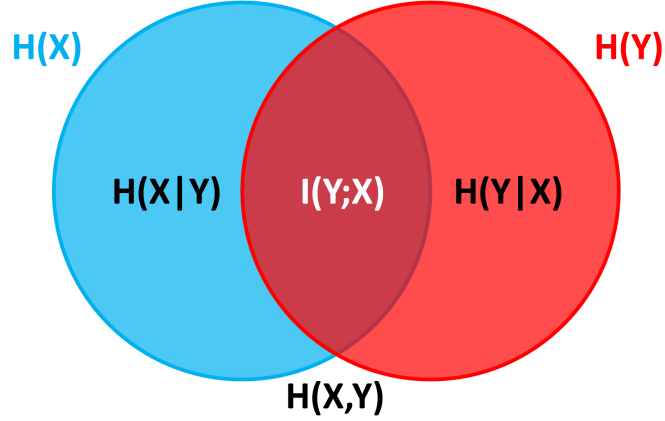


Figure 4.36: A visual representation of the mutual information between two objects.

The relative voxel overlap is calculated as

$$E_{\text{voxel}}(\theta) = 1 - \frac{\sum_{(i,j,k)=(1,1,1)}^{(I,J,K)} |V_{\text{tar}}(i, j, k; \theta) - V_{\text{ref}}(i, j, k)|}{\sum_{(i,j,k)=(1,1,1)}^{(I,J,K)} V_{\text{ref}}(i, j, k)} \quad (4.20)$$

where $V_{\text{ref}}(i, j, k)$ and $V_{\text{tar}}(i, j, k; \theta)$ denote binary voxel values indicating the presence (1) or absence (0) of the reference and transformed target volumes, respectively, within their common 3D voxel space of the size $I \times J \times K$. The weighted fitness function $F_{\text{fit}}(\theta)$ to be maximized is then:

$$F_{\text{fit}}(\theta) = w_{\text{mi}} E_{\text{mi}}(\theta) + w_{\text{voxel}} E_{\text{voxel}}(\theta) \quad (4.21)$$

where w_{mi} and w_{voxel} are pre-selected fixed weights (in our experiments, $w_{\text{mi}} = w_{\text{voxel}} = 0.5$ assuming equal contributions of both the terms).

The unconstrained nonlinear maximization of this function searches for translation-rotation parameters, $\theta^* = \arg \max_{\theta} F_{\text{fit}}(\theta)$, aligning it closely to the reference volume. An iterative block-coordinate descent optimization was used to circumvent the complicated and time-consuming simultaneous optimization of the six translation-rotation parameters. The block-coordinate optimization toggles between the function of translation, rotation, scaling,

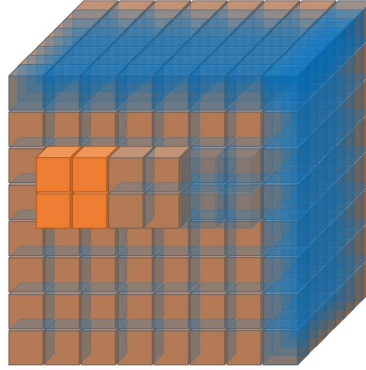


Figure 4.37: A visual representation of the voxel overlap between an orange and a blue object. Non-matching voxels can be seen at the front of the two objects.

and shearing. The cycles are repeated until convergence is reached. Convergence is reached when no further changes of the parameters θ^* are found. The algorithm is detailed in Algorithm 5.

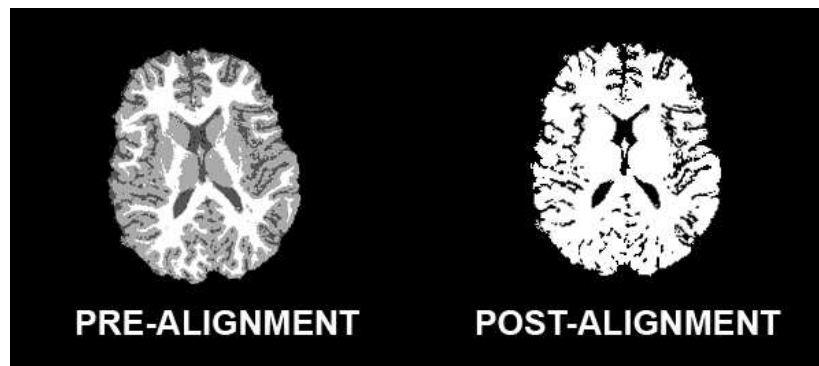


Figure 4.38: Pre- and post-alignment views of a MRI brain slice. In a properly oriented scanner the changes are minimal to the volume. Uncorrected, these small changes introduce errors when comparing multiple volumes.

4.6.2 Spherical Harmonics (SPHARM) Registration

Mesh registration is required to examine differences between individual nodes in different meshes. SPHARM is used to simplify the difficulty of a mesh surface registration. SPHARM

Algorithm 5 Volumetric Registration

INPUTS: R = Reference volume T = Target volume (*volume being aligned*)**OUTPUTS:** T = Target volume (*aligned*)REMOVEVOXELPADDING(R)REMOVEVOXELPADDING(T) $MI \leftarrow$ MUTUALINFORMATION(R, T) $VO \leftarrow$ VOXELOVERLAP(R, T)fitness $\leftarrow (MI + VO) * 0.5$ **while** fitness < THRESHOLD **do** GRADIENTDESCENTOPTIMIZATION(< *Translate* >, R, T) **if nonrigid then** GRADIENTDESCENTOPTIMIZATION(< *Scale* >, R, T) $MI \leftarrow$ MUTUALINFORMATION(R, T) **end if** GRADIENTDESCENTOPTIMIZATION(< *Rotate* >, R, T) **if nonrigid then** GRADIENTDESCENTOPTIMIZATION(< *Shear* >, R, T) **end if** $MI \leftarrow$ MUTUALINFORMATION(R, T) $VO \leftarrow$ VOXELOVERLAP(R, T) fitness $\leftarrow (MI + VO) * 0.5$ **end while**APPLYVOXELPADDING(R)APPLYVOXELPADDING(T)

can be used as an alternative to complicated and lengthy point-to-point correspondence algorithms, where correspondences are established manually or found using analytical search algorithms [237].

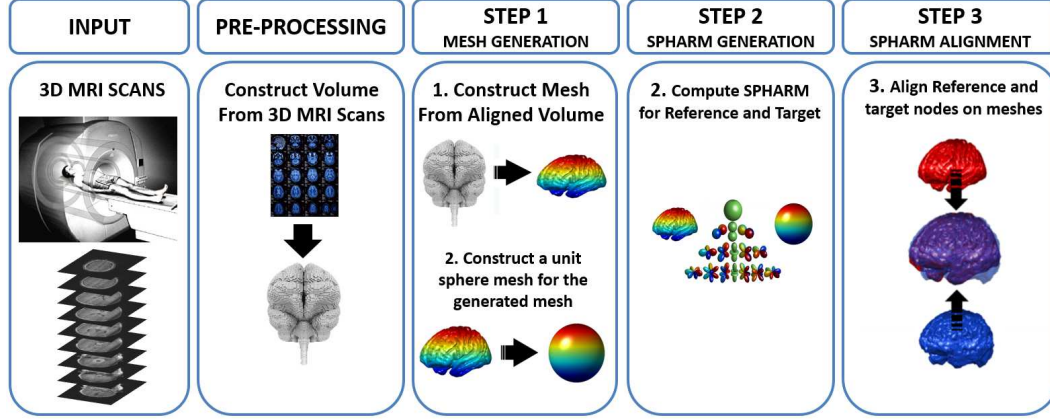


Figure 4.39: Overview of the SPHARM registration approach detailing each step in the framework.

Let Ω denote a pair of polar and azimuthal spherical angles related to a 3D point on the cortical surface supported by the unit sphere. The target, T , and reference, R , meshes consist each of n nodes: $T = \{\mathbf{t}(\Omega_i) : i = 1, \dots, n\}$ and $R = \{\mathbf{r}(\Omega'_i) : i = 1, \dots, n\}$, where $\mathbf{t}(\Omega_i) = [x_t(\Omega_i), y_t(\Omega_i), z_t(\Omega_i)](\Omega_i)$ and $\mathbf{r}(\Omega'_i) = [x_r(\Omega'_i), y_r(\Omega'_i), z_r(\Omega'_i)](\Omega'_i)$ denote the 3D (x, y, z) -coordinates of the mesh nodes. These target and reference nodes relate to their own, and generally unrelated, spherical angles $\{\Omega_i : i = 1, \dots, n\}$ and $\{\Omega'_i : i = 1, \dots, n\}$, respectively.

The SPHARMs, $Y_{lm}(\Omega)$, of degree l ; $l = 0, 1, \dots, k$, and order m ; $-l \leq m \leq l$, form a set of the orthonormal functions on the sphere [3]. The orthonormality holds with respect to the inner product, $\langle f, \varphi \rangle$, of the arbitrary functions, $f(\Omega)$ and $\varphi(\Omega)$, supported by the sphere.

Weighted k -degree SPHARM approximations, T_{ap} and R_{ap} , of the target and reference surfaces, respectively are defined as follows [229]:

$$\mathbf{t}_{\text{ap}}(\Omega) = \sum_{l=0}^k \sum_{m=-l}^l w_l \mathbf{b}_{lm} Y_{lm}(\Omega); \quad \mathbf{r}_{\text{ap}}(\Omega) = \sum_{l=0}^k \sum_{m=-l}^l w_l \mathbf{b}'_{lm} Y_{lm}(\Omega) \quad (4.22)$$

where a smoothing degree-dependent weight, $w_l = e^{-(l+1)\sigma}$; $\sigma > 0$, is selected empirically to reduce Gibbs ringing artifacts in these approximate surfaces and the vectorial SPHARM coefficients, $\mathbf{b}_{lm} = [\langle x_t, Y_{lm} \rangle, \langle y_t, Y_{lm} \rangle, \langle z_t, Y_{lm} \rangle]$ and $\mathbf{b}'_{lm} = [\langle x'_t, Y_{lm} \rangle, \langle y'_t, Y_{lm} \rangle, \langle z'_t, Y_{lm} \rangle]$ are computed on the basis of the target, T , and reference, R , mesh nodes and SPHARM functions $Y_{lm}(\Omega)$.

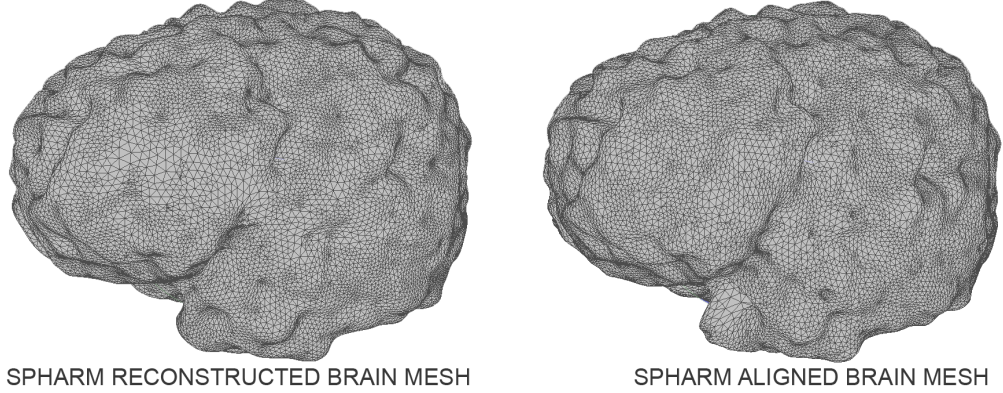


Figure 4.40: A view of an original mesh and its SPHARM aligned counterpart. Brain shape information is not lost during the mesh registration.

The approximations of Equation (4.22) map the target mesh to the reference mesh. This approximation can be used for exploring sulcal and gyral folding patterns [238]. The mapping preserves the target shape and curvature, as it relates to the reference nodes, by interpolating between the neighboring mapped target nodes. The algorithm is detailed in Algorithm 6.

Algorithm 6 SPHARM Registration

INPUTS: R = Reference mesh T = Target mesh (*mesh being aligned*)**OUTPUTS:** T = Target mesh (*aligned*)GENERATEHARMONICS(R)GENERATEHARMONICS(T)displace \leftarrow ZEROS(SIZE(T .NODES))**for all** harmonics **do** **for all** dimensions **do** $Y \leftarrow$ HORZCAT(real(R .coeff(harmonic, dim), imag(R .coeff(harmonic, dim))) coef $R \leftarrow$ R .coeff(harmonic, dim) coef $T \leftarrow$ T .coeff(harmonic, dim) coef \leftarrow coef T - coef R displace(dim) \leftarrow displace(dim) + coef $Y * \exp(\text{harmonic} * \sigma)$ **end for****end for****return** displace

4.7 Classification

4.7.1 Metric Computation

Each node of a target mesh is characterized with four statistical metrics. These metrics are the: Euclidean distance from the origin; Gaussian curvature; mean curvature; and normal surface curvature [239]. Statistical node-wise p -values between brain meshes for both control and autistic populations are computed using an unpaired t-test [240] at the 95% significance level.

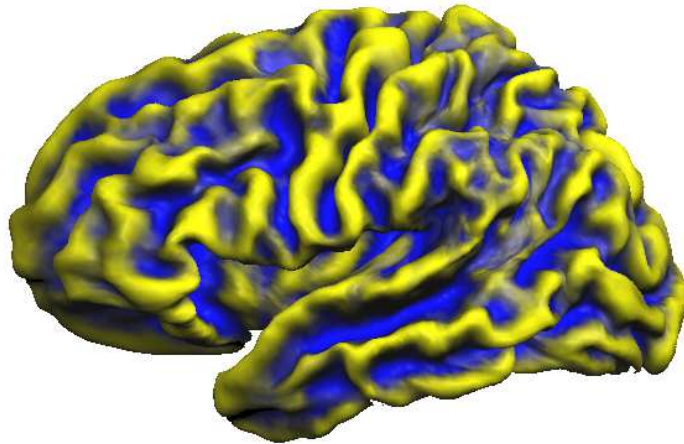


Figure 4.41: *High contrast representation of a brain mesh with the curvature highlighted for clarity.*

Three calculations are based on measurements of curvature in the brain. Each of these curvatures is calculated in a different way, and is sensitive to specific landscapes of the brain. Curvature calculations are primarily based on the computation of the principal curvatures of a node. The principal curvature is a measurement of how the surface of a shape bends in different directions in relation to a specific point. The curvature metrics are computed from surface distances on a mesh and are intrinsic calculations.

The normal curvature is used to determine the principal curvatures of a point. The normal

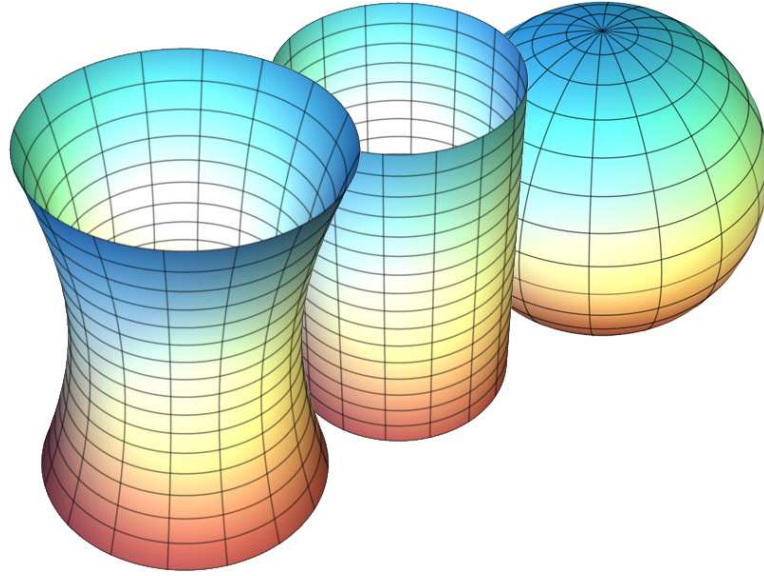


Figure 4.42: *Curvature on the surface of several 3-dimensional meshes.*

curvature is estimated at the vertices of triangular based mesh.

The Gaussian Curvature of a point is the product of the principal curvatures of that specific point [241]. The Gaussian curvature, K_G , is defined as:

$$K_G = \kappa_1 \kappa_2 \quad (4.23)$$

where κ_1 and κ_2 are the principal curvatures of a point. Similarly, the mean curvature, K_M , is related to the Gaussian curvature, but is a slight variation and is computed as the average of the principal curvatures:

$$K_M = \frac{(\kappa_1 + \kappa_2)}{2} \quad (4.24)$$

where again, κ_1 and κ_2 are the principal curvatures of a point.

The normal curvature is also related to the other two curvatures, and is defined as the maximum of the two principal curvatures.

$$K_N = \max(\kappa_1, \kappa_2) \quad (4.25)$$

4.7.2 Brodmann Areas

The principal understanding and classifications of brains as belonging to a neurotypical or autism spectrum disorder group are based on the understanding and comparison of the Brodmann areas. A Brodmann area is a region of the cerebral cortex defined by its cytoarchitecture, or the structure and organization of its cells. There are 52 Brodmann areas found in each hemisphere of the brains of mammals, resulting in the possibility that 104 Brodmann areas exist in a single brain [1, 4, 5]. This list is narrowed, due to the fact that human brains are missing several Brodmann areas, in comparison to primates. Not all Brodmann areas can be analyzed by looking at the surface of the human brain. Additional Brodmann areas can be found on the inner surface of the human brain, which at the time of publication has not been analyzed by the proposed framework.

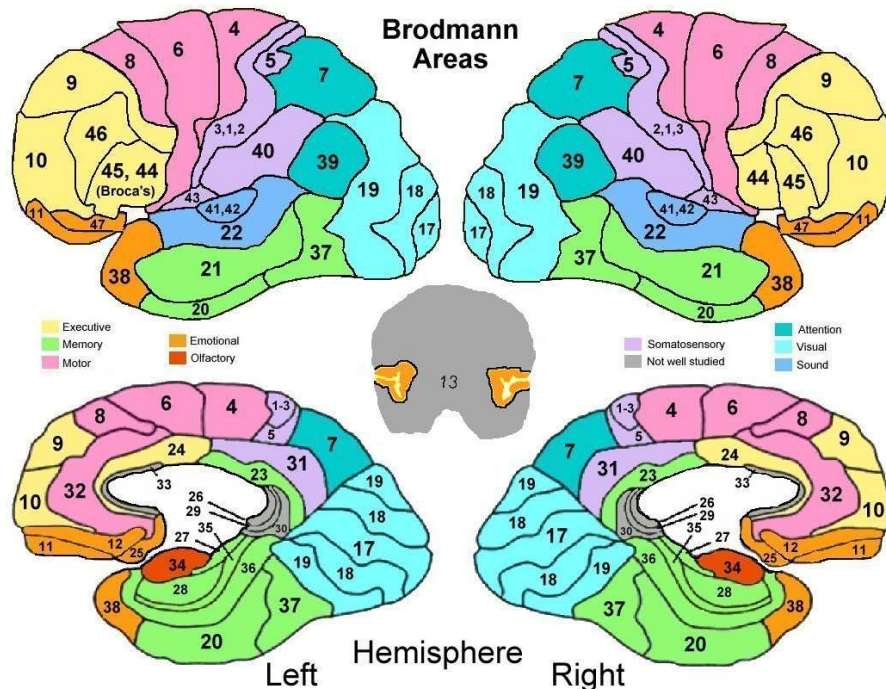


Figure 4.43: Visual map of the interior and exterior Brodmann areas of the brain.

4.7.3 *List of the Brodmann Areas*

Below is a list of all Brodmann areas for humans and other primates by area number and name. The Brodmann areas included in Sight processing are highlighted in bold and include brief explanations as to the function of each of these Brodmann areas.

- **Areas 1, 2, and 3 (also called 3, 1, 2)**

- *Primary somatosensory cortex*

- The primary somatosensory cortex is the main area of the brain involved in the sense of touch and fine motor control. The primary somatosensory cortex also plays a key role in identifying objects by touch. It also functions as a control center for day to day interactions. This region of the brain initiates actions and contributes to the understanding of language.

- **Area 4**

- *Primary motor cortex*

- The primary motor cortex plays a role in responding to commands. The primary motor cortex controls many of the body's physical actions. It is responsible for initiating physical action and constructing thoughts, such as moving body parts and focusing an individual's attention.

- **Area 5**

- *Somatosensory association cortex*

- The somatosensory association cortex primarily functions as a sensing location in the brain. It is involved in the processes regarding the senses of touch and feeling, such as pain. The SAC works in conjunction with area 3,1,2 and area 4, to allow human interaction with objects.

- **Area 6**

- *Pre-motor and supplementary motor cortex*
- The pre-motor and supplementary motor cortex occupies a large area of the frontal cortex. This area is primarily involved in planning complex and coordinated body movements. For example, the act of walking requires numerous muscles to function together simultaneously to make the body move forward without falling over.

- **Area 7**

- *Somatosensory association cortex*
- The somatosensory association cortex provides humans their understanding of the sense of space. This area of the brain, combines information from all of the human senses to estimate how far objects are from an individual, and determine where they lie in space. It also contributes to coordination, by allowing the motor cortex to understand where the limbs of the body are located in a spatial context. This allows the body to perform complex actions, such as eating with a fork.

- **Area 8**

- *Dorsolateral prefrontal cortex [Frontal eye field region]*
- The eye field dorsolateral prefrontal cortex is involved in managing the feeling of uncertainty and consciously controlling eye movement.

- **Area 9**

- *Dorsolateral prefrontal cortex*
- The dorsolateral prefrontal cortex is the area of the brain responsible for maintaining attention on a designated focal point. The area also contributes to the ability

to recall and utilize information from the working memory. The DPC is involved in inhibitive responses.

- **Area 10**

- *Anterior prefrontal cortex*

- The anterior prefrontal cortex is involved in retrieving memories and processing executive function. Executive function is the ability to connect past experiences while applying the knowledge to the present to make informed decisions.

- **Area 11**

- *Orbitofrontal area*

- The orbitofrontal area of the brain controls the ability to plan, reason, and make decisions. This area is linked to the hypothalamus of the brain, which is responsible for regulating a variety of the bodies naturally formed chemicals and stimuli.

- **Area 12**

- *Interior orbitofrontal area*

- The interior orbitofrontal area was previously considered part of Area 11. Specifically, it is located between the superior frontal gyrus and the inferior rostral sulcus of the brain. The interior orbitofrontal area plays an assistive role to the orbitofrontal area.

- **Area 13 and Area 14**

- *Insular cortex*

- **Area 15**

- *Anterior Temporal Lobe*

- Area 16
 - *Insular cortex*

- **Area 17**
 - *Primary visual cortex (V1)*
 - Visual cortex V1 is a specialized area of the brain used in processing information related to static and moving objects. The V1 area is heavily associated with pattern recognition and helps in determining between various objects.

- **Area 18**
 - *Secondary visual association cortex (V2)*
 - Visual cortex V2 is the largest of the three visual cortices. The V2 area process lexico-semantic associations. Lexico-semantic associations allows individuals to see and translate written words into mental associations. This region enables the visualization of text.

- **Area 19**
 - *Tertiary visual association cortex (V3)*
 - Visual cortex V3 processes feature extraction, shape recognition, and visual attention. The V3 area enables an individual to distinguish patterns and shapes helping recognize objects. For example, the process of distinguishing a computer keyboard from the other objects lying on a desk.

- **Area 20**
 - *Inferior Temporal gyrus*

- The inferior temporal gyrus is an area of the brain that is involved in high-level visual processing and recognition. The ITG is involved in understanding the concept of color. This area works with Area 19 to classify objects.

- **Area 21**

- *Middle Temporal gyrus*
- The middle temporal gyrus plays a role in auditory processing and understanding word meanings while reading. This area is responsible for processing facial recognition. In the brain, the middle temporal gyrus is much stronger in the left hemisphere than the right.

- **Area 22**

- *Superior Temporal Gyrus*
- The superior temporal gyrus generates an understanding of words, melody, pitch and sound intensity. Located in the back of the superior temporal gyrus is the well-known Wernicke's Area.

- **Area 23**

- *Ventral posterior cingulate cortex*

- **Area 24**

- *Ventral anterior cingulate cortex*

- **Area 25**

- *Subgenual area (part of the Ventromedial prefrontal cortex)*

- **Area 26**

- *Ectosplenial portion of the retrosplenial region of the cerebral cortex*
- Area 27
 - *Piriform cortex*
- Area 28
 - *Ventral entorhinal cortex*
- Area 29
 - *Retrosplenial cingulate cortex*
- Area 30
 - *Part of cingulate cortex*
- Area 31
 - *Dorsal Posterior cingulate cortex*
- Area 32
 - *Dorsal anterior cingulate cortex*
- Area 33
 - *Part of anterior cingulate cortex*
- Area 34
 - *Dorsal entorhinal cortex (on the Parahippocampal gyrus)*
- Area 35
 - *Perirhinal cortex (in the rhinal sulcus)*

- Area 36
 - *Ectorhinal area, now part of the perirhinal cortex (in the rhinal sulcus)*

- **Area 37**
 - *Fusiform gyrus*
 - The fusiform gyrus plays a key role in the process of understanding color, and the visual recognition of objects. This area enables the understanding of categories and words.

- **Area 38**
 - *Temporopolar area*
 - The temporopolar area of the brain is involved in the semantic and autobiographic representation of an individual's self-concept. The temporopolar area allows humans to discuss their experiences and history.

- **Area 39**
 - *Angular gyrus*
 - The angular gyrus is located in the Wernicke's area region of the brain. The angular gyrus processes sentence construction and reading. This area is responsible for associating written words with their phonetic sounds.

- **Area 40**
 - *Supramarginal gyrus*
 - The supramarginal gyrus is the last area located in the Wernicke's area. The supramarginal gyrus is responsible for determining the meaning of reading con-

cepts. It enables individuals to understand written words in their mind during the process of reading.

- **Area 41 and Area 42**

- *Primary and secondary auditory cortex*
- The primary and secondary auditory cortex contribute to the understanding and awareness of sounds.

- **Area 43**

- *Subcentral area*
- The subcentral area of the brain plays a minor role in the formation of spoken language. This area assists the Broca's area to produce speech.

- **Area 44**

- *Pars opercularis*
- The pars opercularis is the one of two areas of the brain that make up the Broca's Area. The pars opercularis is responsible for the production of speech.

- **Area 45**

- *Pars Triangularis*
- The pars triangularis is the second of two areas of the brain that make up the Broca's Area. The pars triangularis contributes to the production of speech. This area is responsible for understanding both abstract and concrete tasks.

- **Area 46**

- *Dorsolateral prefrontal cortex*

- The dorsolateral prefrontal cortex of the human brain allows humans to use and control memory. The dorsolateral prefrontal cortex enables humans to sort and organize memories.
- **Area 47**
 - *Inferior prefrontal gyrus*
 - The Inferior prefrontal gyrus is involved in the ability to process syntaxes and the inhibition of emotional responses.
- Area 48
 - *Retrosubicular area (a small part of the medial surface of the temporal lobe)*
- Area 49
 - *Parasubicular area in a rodent*
- Area 50 and Area 51
 - *These areas are only found in the brain of a monkey.*
- Area 52
 - *Parainsular area (at the junction of the temporal lobe and the insula)*

4.7.4 Ray-casting and Area Delineation

While the information provided by the Brodmann areas is useful, it is challenging to determine where the boundaries of these areas are located within a mesh of the human brain. Key difficulties include: (i) mesh points are not located sequentially next to one another (e.g. the mesh generation algorithm may place points 1 and 2 near one another, or it may place the

points on opposite sides of the brain mesh) ; and (ii) and initial point locations change every time a new mesh is created. The reason for this occurrence is because the mesh generation algorithm randomly assigns locations of nodes around the surface of a volume manifold. The nodes are evenly distributed, at random, in an attempt to not over saturate any single location.

The random node distribution problem is solved by performing a SPHARM based mesh alignment. This mesh alignment forces every node to have a static location (i.e. point 1 is on specific set of phi and theta angles in spherical space). The problem still remains that regions must be constructed to encompass the specific set of points that make up each Brodmann area. This concept can be simplified to a more commonly known problem entitled the *"Point in polygon"* problem. The solution is spherical ray-casting.

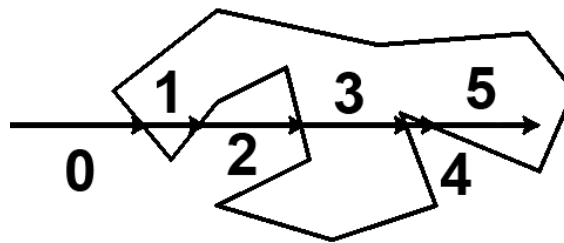


Figure 4.44: *The traditional Point in Polygon problem. Picking any of the five points, one can easily calculate how many intersections a ray that stretches from this point makes with the sides of the polygon.*

Ray-casting determines if a point lies within or outside a specific region. Ray-casting is more advanced than defining a traditional border, because this process allows any shaped object to act as a bounding region. This includes such difficult shapes as Us and Os where at some locations points are enclosed by a region, but are themselves not a part of the region. Ray-casting is, therefore, well suited to defining the Brodmann areas which are abnormal shaped regions. A ray-casting algorithm is not bound by a specific set of mathematical equations, but instead, is created based on a specific set of if-else determinations.

The ray-casting algorithm begins the region bounding process by defining the mathemat-

ical line equations that form the boundaries of the region. These line equations are used to establish whether a ray extending from a point passes through a boundary line. Each point in the mesh is examined iteratively. A ray is extended from each point along the horizontal axis at an angle of zero degrees. The ray is checked to determine if it passes through any of the boundary lines. Each time the ray intersects or breaks a boundary line, the algorithm tracks this collision. The total number of collisions determines the total number of boundary line intersections. If the number of collisions is zero, or an even integer, the point is determined to be outside of the bounded region. An odd number of collisions indicated that the point is located within the boundary region.

It is not necessary to use ray-casting to determine if every point in the mesh belongs to the bounded region. Points can be quickly excluded from this search by examining their locations relative to the minimum and maximum values of the boundary region. Points that fall outside of these extremes cannot be located inside the bounded region.

Ray-casting is effective on any shape or size of a bounded region. To clarify this point, consider the following example. If a point is located outside of the bounded region it must have zero or an even number of collisions. If this point is located to the right of the region, the ray extending from this point will never intersect a boundary. Conversely, if this point is located on the left, the ray must both enter and exit the bounded region. This results in a minimum of two boundary collisions. In a more complex shape, such as a region shaped like an O, the ray would make two or four collisions. For a given point that is located inside the bounded region, the number of collisions must be an odd number. A point on the right side of O, will have one collision, while a point on the left side will have three collisions. The assumption that a point with an odd number of collisions is inside the bounded region holds true for every possible shape that can be constructed.

To define the boundaries of the Brodmann areas, a set of points are manually placed at the corners of each area. The corner locations were determined by using 2D and 3D

Algorithm 7 Ray-Casting**INPUTS:** P = the point from which the ray starts A = the end-point of the segment with the smallest y coordinate. (A must be "below" B) B = the end-point of the segment with the greatest y coordinate. (B must be "above" A)**OUTPUTS:***True/False***if** $P_y = A_y$ or $P_y = B_y$ **then** $P_y \leftarrow P_y + \varepsilon$ **end if****if** $P_y < A_y$ or $P_y > B_y$ **then**return *false***else****if** $P_x > \max(A_x, B_x)$ **then**return *false***else****if** $P_x < \min(A_x, B_x)$ **then**return *true***else****if** $A_x \neq B_x$ **then** $red \leftarrow \frac{(B_y - A_y)}{(B_x - A_x)}$ **else** $red \leftarrow \infty$ **end if****if** $A_x \neq P_x$ **then** $blue \leftarrow \frac{(P_y - A_y)}{(P_x - A_x)}$ **else** $blue \leftarrow \infty$ **end if****if** $blue \geq red$ **then**return *true***else**return *false***end if****end if****end if** $i \leftarrow i + k$ **end if**

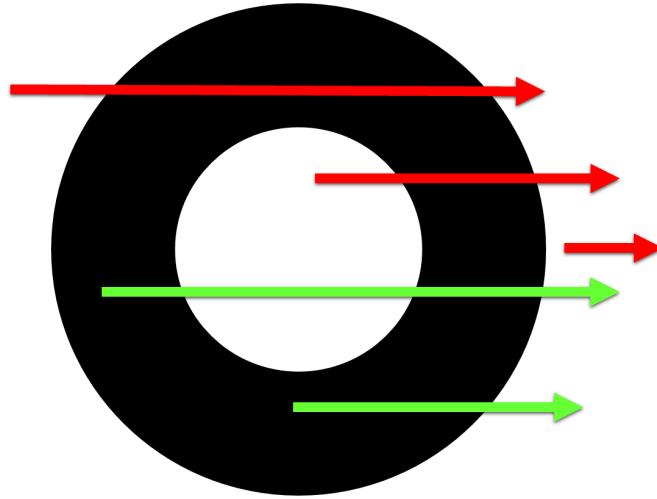


Figure 4.45: *Ray-casting demonstrated on a region shaped like an O. Red rays intersect an even number of times and fall outside of the region. Green rays intersect an odd number of times and fall within the region.*

reference maps of the Brodmann areas. A set of boundary mappings are associated with these points. The boundary mappings detail how specific points are located relative to one another in order to form the lines of the boundary region. There is a unique set of boundary mappings for each Brodmann area. Using these points and boundary mappings the borders of the Brodmann areas can be defined. This allows ray-casting to be used on each set of boundaries to determine if a point falls within a specified Brodmann area.

A unique feature of this Brodmann area ray-casting algorithm is the ability to flex the regions based on the shape and size of the brain. The technique of flexing can be used to stretch or shrink the boundaries of any given Brodmann area to dynamically examine the areas features. The technique can also be used to allow information along the borders of neighboring Brodmann areas to be shared. If the size of a brain is smaller or larger than the reference brains used in the Sight framework, this technique allows shrinking or expansions of the Brodmann areas. The shape of the Brodmann area remains consistent even when the size is altered. The regions are flexed by increasing or decreasing the locations of the edges,

relative to the centroid of each region.

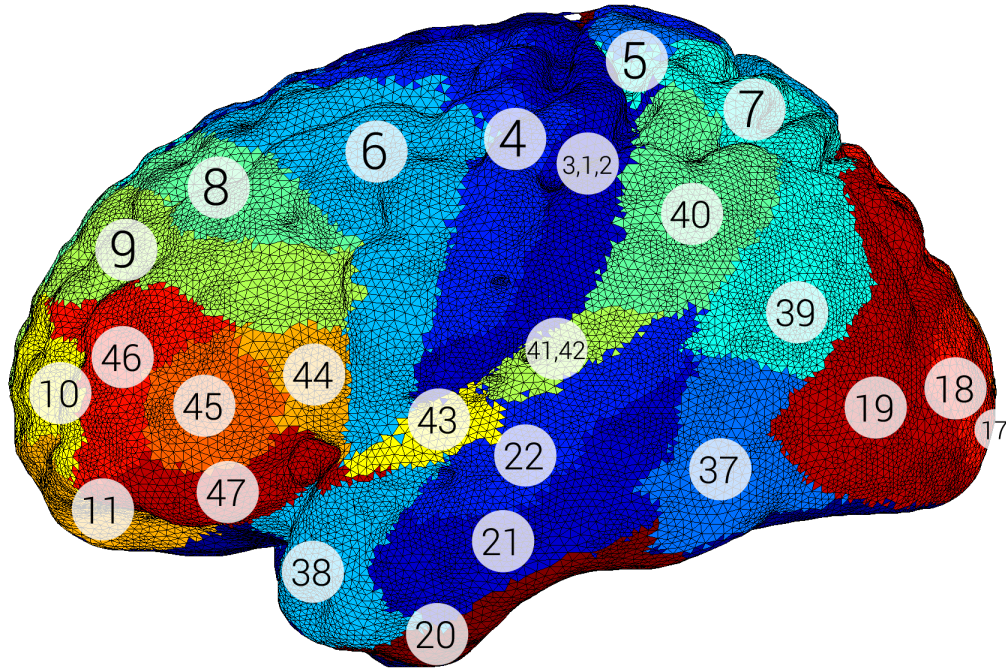


Figure 4.46: *The Brodmann areas can be identified and re-created on any brain using a ray-casting technique that has been optimized for these regions. The regions by the framework, along with numbers overlaying the identity of the region, are demonstrated.*

It is possible, with this ray-casting algorithm, to independently scale specific Brodmann areas to meet the requirements of the brain shape. This is beneficial because it allows the framework to dynamically adapt to unique localized changes and requirements in the shape of the brain. This process enables the accurate evaluation of any brain shape.

4.7.5 Constructing a Simple Classifier

A two part classifier is used for the analysis of the brain. This classifier constructs the diagnostic and risk assessment results for the Sight framework. The two parts of the classifier include the process of region validation and analysis.

The classifier is constructed using the Leave-One-Out (LOO) method. The LOO approach removes a single subject placing it in the test group. The remaining subjects are used to train the classifier. Each brain used to construct and test the classifier is iterated so that every subject serves as a test case when it is not included in the training set. This allows the maximum training group size to be utilized at all times. It also ensures that the training data set is never biased by including the test data within the training group. The LOO approach is a favorable method for testing the effectiveness of a system when test time is unimportant.

While there are a wide variety of complex and powerful black-box classifiers available, such as neural networks and support vector machines, the Sight classifier is based on the Nave Bayes approach. Naive Bayes classifiers have been used extensively throughout history, and were first used as a method of differentiating between text in the early 1960s. Currently, they serve as a good baseline method for determining the effectiveness of an approach involving two groups. Some of the advantages to a Naive Bayes classifier include excellent scalability and simple implementation. The ability to have simple and understandable implementation is the reason this method was selected. If the approach works using a simple classier, such as Nave Bayes, it will still be possible to use a more complex classifier on the same system to increase the accuracy. Simple classifiers are not at risk of overtraining. While complex classifiers could provide more accurate results, in this case understanding the basic process of the decision making tool increases demonstrates the validity of the Sight approach.

A simple probabilistic classifier is implemented for each metric of an instance and an instance is represented by a vector $x = (x_1, \dots, x_n)$ where n is the number of areas present for each instance. Each instance is assigned a probability such that $p(C_k | x_1, \dots, x_n)$ for each of K classes.

Using the Bayes' theorem the conditional probability can be described as:

$$p(C_k | x) = \frac{p(C_k)p(x | C_k)}{p(x)} \quad (4.26)$$

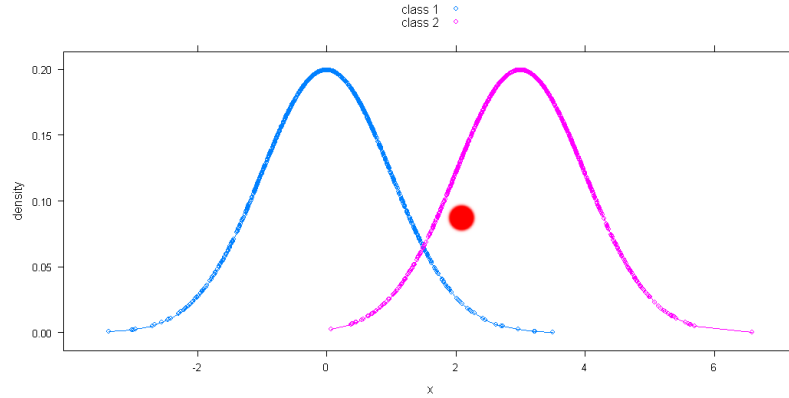


Figure 4.47: A simple Bayes classifier for two groups. The red point being classified can be seen to belong to class two.

This concept can be easily turned into a classifier where a class label $L = C_k$ for some class k is defined as:

$$L = \arg \max_{k \in \{1, \dots, K\}} p(C_k) \prod_{i=1}^n p(x_i | C_k) \quad (4.27)$$

NSIM Similarity Metric

The primary metric used for classification and examination of the data is the similarity metric (NSIM). The NSIM is mathematically defined between a reference and a target, for a single area, and a single metric, as:

$$NSIM = \sum_{i=0}^N (S_R < 0.1) \quad (4.28)$$

where $i = 1, \dots, N$ is the number of nodes within the Brodmann area, and S_R is defined as:

$$S_R = \left| \frac{S_{ref}}{\max(S_{ref})} - \frac{S_{tar}}{\max(S_{tar})} \right| \quad (4.29)$$

where S_{ref} is the median filtered reference array, and S_{tar} is the median filtered target array. The NSIM is the total number of nodes in the Brodmann area that have a similarity of greater than 90% with one another. Algorithmically, the NSIM is detailed in Algorithm 8.

Algorithm 8 NSIM Similarity Metric

INPUTS: Sr = Reference array of selected metric St = Target array of selected metric sim = Similarity threshold**OUTPUTS:** $nSim$ = NSIM Similarity Metric**for all** elements in R & T **do** $Sr(element) \leftarrow |Sr(element)|/max(R)$ $St(element) \leftarrow |St(element)|/max(T)$ **end for****for all** elements in R **do** $N(element) \leftarrow |Sr(element) - St(element)|$ **end for** $nSim \leftarrow 0$ **for all** elements in R **do****if** $N(element) < sim$ **then** $nSim \leftarrow nSim + 1$ **end if****end for** $nSim \leftarrow nSim/Size(R)$ **return** $nSim$

The NSIM is computed for a target brain using each metric and each Brodmann area. The NSIM is computed between the target and all brains in the reference, or training, data set. Each Brodmann region receives a unique NSIM similarity score for each brain mesh it is compared against. In this way, the top N NSIM values are determined for each Brodmann area in the brain being tested. This is used to determine which reference brains most closely match the target. The end result is that the target brain is represented by a composite of training database matches.

In more detail, the metric values for each Brodmann region are represented as 1-dimensional arrays. Initially, the NSIM value was determined by computing the cross-correlation of each 1-dimensional array. However, this approach suffered from difficulty in regions that have substantial likelihood of surface noise. To account for this, the NSIM is computed by filtering each signal using a median filter with a window size of five. Each signal is normalized between 0 and 1. The signals are subtracted from one another. The signals are rectified so that all values are positive. The NSIM is defined as the number of points in the signal below a threshold value, defined as 10% or 0.1. In this way, the NSIM represents the total number of nodes in a Brodmann region sufficiently similar to one another. The NSIM is not adversely affected by a small amount of erroneous data points because these are ignored. Using the NSIM, the classification of each region as neurotypical or autism spectrum disorder positive (ASD+) can be determined.

Brodmann Area Reduction

An interesting observation in the classification of the brain is related to the relevance of individual brain areas. Studies tend to focus on the brain as a whole, and classification is often performed using global measures (many examples are included in Chapter 3). However, through experimentation, including a lot of trial and error discovery, it was found that many areas of the brain contain noise when correlated with certain conditions. Logically, this would

make sense, although in the shape analysis of organs it is rarely done.

As an example, consider the condition dyslexia, which has a much more limited range of effects than autism. An individual diagnosed with dyslexia has difficulty understanding words because the brain has swapped the letters incorrectly. While there are a number of possible areas of the brain that may be implicated, there are additional areas that may be excluded. If an individual is able to correctly control the body and perform normal motor functions, is it reasonable to assume that these areas of the brain, which are largely unrelated to speech and language, play a significant role in the underlying causes of dyslexia? While all cases and conditions are different, it is reasonable to assume that there are brain locations that are not involved with a specific disorder. The concept of focusing on only the most important regions of the brain for specific conditions can help to narrow the search space when trying to classify a complex neurological condition.

The algorithm by which this search space is reduced is referred to as *Brodmann Area Reduction*, and can be thought of as a pre-processing stage, prior to making a classification. A summary of the algorithm can be found in Algorithm 9. Brodmann Area Reduction works by de-emphasizing Brodmann areas that have noisy classifications, and emphasizing areas that are more directly related to a specific neurological condition. To accomplish this an approach is applied to the training data set. Each subject in the training data set performs a classification using each Brodmann area for the metrics that have been selected. The number of correct classifications for each class are then identified. It is also necessary to handle the possibility of a blatantly incorrect area. If a specific Brodmann area classifies one class 100% of the time, and another class 0% of the time, the overall classification of that area is determined to be 0% accuracy, and not 50% accuracy, as the area will never provide a useful form of classification in practice.

After collecting the classification accuracies, each area is sorted based on its overall ability to correctly classify a subject. To ensure that the selection of the Brodmann areas is not

biased, the algorithm utilizes a Leave-One-Out approach for calculating the accuracy of each subject. While this approach is computationally inefficient, it must only be performed when a training database is first created or is updated. After a training database has been constructed, the Brodmann Area Reduction determinations are reloaded for examining new test cases. For possible commercial applications, this means that the actual implementation time of the algorithm is extremely fast for diagnosing new subjects.

Algorithm 9 Brodmann Area Reduction

INPUTS:

TRAINING = Training data set of subjects

OUTPUTS:

ACCURACY = Accuracy of each Brodmann Area

Repeat for each metric**for all** elements **in** TRAINING **do***C* ← *element*Remove *C* from TRAINING**for all** areas **in** *C* **do**

% Determine the classifications of each area

match ← 0*M* ← TRAINING(0)**for all** element *T* **in** TRAINING **do***temp* ← NSIM(*C*_{area}, *elementT*_{area})**if** *temp* > *match* **then***match* ← *temp**M* ← *elementT***end if****end for****if** *C*_{class} == *M*_{class} **then***ACCURACY*(*area*) ← *ACCURACY*(*area*) + 1**end if****end for**Add *C* to TRAINING**end for****for all** elements **in** ACCURACY **do***ACCURACY*(*elements*) ← *ACCURACY*(*elements*)/SIZE(TRAINING)**end for****SORT** ACCURACY**return** ACCURACY

Classification

The NSIM similarity metric is combined with the Brodmann Area Reduction to create a simple, but accurate classifier model. The following steps are required to classify a new subject, and are detailed in Algorithm 10. First, for each metric and each Brodmann area the subject identifies the closest matches in the training database. This step is similar to the step used in Brodmann Area reduction, except that only one test subject is being examined. Next, the impact of each Brodmann area is weighted by the Brodmann Area Reduction, such that areas that have shown a correlation with the neurological condition being examined are weighted more highly. Finally, the subject is classified using the top R areas of the brain. In practice, the majority of brain areas are not related to every condition, especially when considering that there are twice as many areas when examining both hemispheres of the brain. The number of areas, R , can be determined empirically, by exploring how many elements are used to maximize the classification probability. In many cases using an odd R near 9 or 11 is an effective solution. The total number of votes for each of these areas is tallied, and the final classification is determined. As an example, for $R = 9$, if 5 areas vote for Class 0, and 4 vote for Class 1, then the subject would be determined to be of class 0.

This approach can be slightly refined to improve upon the accuracy by accounting for the importance of the areas. Instead of making a division simply by using majority decision with an arbitrary number of areas, the winner based on the agreement of the most important areas can be used. Consider a theoretical example of $R = 4$, where, $(A_1 = 0.8, A_2 = 0.7, A_3 = 0.6, \text{ and } A_4 = 0.5)$, and corresponding classes of 0, 1, 0, 1. In this case, while there is an agreement of 2 for Class 0, and 2 for Class 1, the Brodmann weighting would provide a vote of 1.4 for Class 0, and 1.2 for Class 1. This is a trivial adaptation of the previous majority voting method, as the weighting has already been predetermined in Algorithm 9.

The actual number of top areas may also be refined by implementing a dynamic window for the classification. The window is determined by examining all adjacent Brodmann areas,

and selecting the window location and size based on the window location that maximizes the classification. This location and size can be computed by examining all possible starting locations and window sizes, and is a computationally simple task, even using a brute force algorithm. This final classification provides the most accurate results, and is the primary method of classification used by the Sight framework for identifying neurological, or other conditions.

4.7.6 Brodmann Risk Analysis

A more interesting aspect of the system is its use as a risk analysis tool. While this specific application is more difficult to determine the exact accuracy of, the risk analysis can provide a wealth of detailed information. An ongoing study, headed by Dan Lloyd of Trinity College focuses on the responsibilities of each Brodmann area [242, 243, 244]. Risk analysis can be determined directly from the classification information for a subject and a given neurological condition.

The Lloyd study is regularly updated and provides a comprehensive analysis of the latest research on the Brodmann areas. The Lloyd study contains results from Functional Magnetic Resonance Imaging scans (fMRIs) of more than 10,000 unique individuals, and is focused on 37 distinct behavioral domains. The study is also backed by peer-reviewed research published in more than 959 papers that comprises more than 4,221 different experiments. The primary focus of the study is determining what impact each Brodmann area has on a set of specific behavioral domains.

The Lloyd study is based on the determination of which Brodmann areas are associated with each human ability. This study is verified by a wealth of peer-reviewed research. As an example, regions 1, 2, 3, 4, and 6 are responsible for the execution of speech. The Lloyd study expands this information further to determine what level of impact each region plays.

Algorithm 10 Classification

INPUTS:

Subject to be classified

TRAINING = Training data set of subjects

OUTPUTS:

Class of subject

```

for all metrics do
  for all areas do
     $match \leftarrow 0$ 
     $M \leftarrow TRAINING(0)$ 
    for all elementT in TRAINING do
       $temp \leftarrow NSIM(C_{area}, elementT_{area})$ 
      if  $temp > match$  then
         $match \leftarrow temp$ 
         $M \leftarrow elementT$ 
      end if
    end for
    if  $M_{class} == 0$  then
       $class0 \leftarrow class0 + 1$ 
    else
       $class1 \leftarrow class1 + 1$ 
    end if
  end for
end for
if  $class0 == class1$  then
  return -1 % class is unsure
else
  if  $class0 > class1$  then
  return 0
  else
  return 1
  end if
end if

```

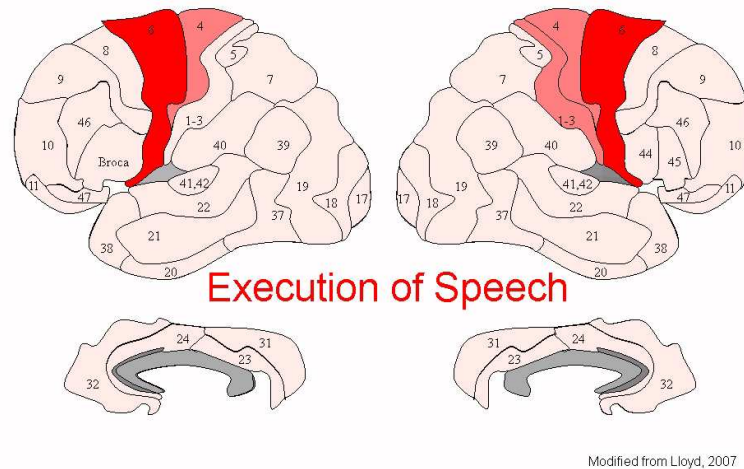


Figure 4.48: *The Brodmann areas of the human brain that play a role in the act of creating sounds and speech.*

While all of these regions play a role in the execution of speech, region 6 accounts for more than 50% of the ability.

This information is important for diagnostic imaging because it detects the likelihood of locating an abnormality in human processes that are difficult for individuals with autism. By associating the abnormalities in the brain with corresponding Brodmann areas it is possible to provide a risk assessment for specific abilities. Research has shown that indeed Brodmann area abnormalities correlate with clinical research on the behaviors of individuals diagnosed with autism spectrum disorders.

Using the work of Dan Lloyd, a table of percentage risk scores can be constructed. This table gives each Brodmann area an impact score for each characteristic trait. The characteristics explored include: Action - Execution, Action - Execution - Speech, Action - Imagination, Action - Inhibition, Action - Motor Learning, Action - Observation, Cognition, Cognition - Attention, Cognition - Language, Cognition - Language - Orthography, Cognition - Language - Phonology, Cognition - Language - Semantics, Cognition - Language - Speech, Cognition - Language - Syntax, Cognition - Memory - Explicit, Cognition - Memory - Working, Cognition

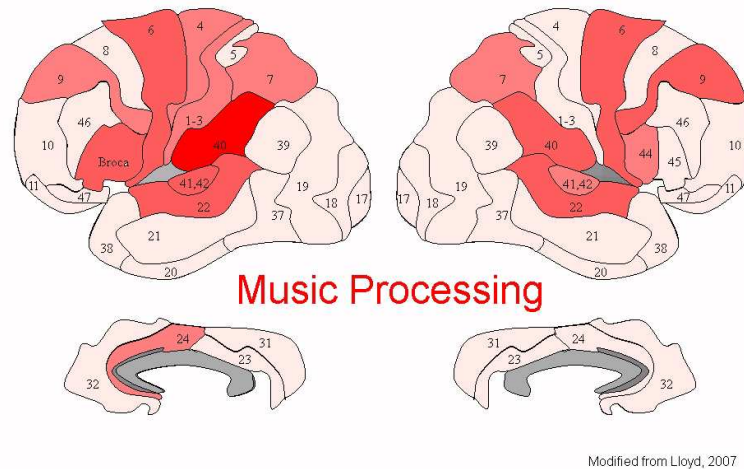


Figure 4.49: *The Brodmann areas of the human brain that play a role when listening to and processing music.*

- Music, Cognition - Reasoning, Cognition - Space, Cognition - Time, Emotion, Emotion - Anger, Emotion - Anxiety, Emotion - Disgust, Emotion - Fear, Emotion - Happiness, Emotion - Sadness, Interoception - Hunger, Interoception - Sexuality, Perception - Audition, Perception - Olfaction, Perception - Somesthesia, Perception - Somesthesia - Pain, Perception - Vision, Perception - Vision - Color, Perception - Vision - Motion, Perception - Vision - Shape.

Using this information a risk assessment, or likelihood of deviance, can be determined for each area. The risk of a characteristic is determined as follows. Following the classification of a subject, Brodmann area that are not classified as belonging to the typical group are weighted using the impact score for the chosen characteristic. It is not necessary to weight areas classified as typical, as these areas would not contribute to the possibility of deviance in a specific characteristic. The final percentage deviance for that characteristic is determined by the sum of the weighted areas. As an example, for the emotion "fear", if the sum of the impact scores of the Brodmann areas that are classified as non-typical is 0.8, than the individual would be 80% likely to exhibit some degree of deviance in their response to fear. This may mean that the individual is hyper- or hypo- responsive to fear, but is an indication that their

response would not be considered as "typical." This information can optionally be weighted by the Brodmann Area Reduction to further increase the accuracy.

While the algorithm is not able to determine if the individual will exhibit a hyper- or hypo-type response, this information is still exceptionally useful in the field of therapy. Discussions with therapists have indicated that many individuals diagnosed as falling on the autism spectrum show a wide range of physical responses to stimuli. It is often difficult to determine what exactly is the underlying reason for this response. While an individual may appear to be extremely angry, the response may be actually related to a combination of anxiety and the inability to process the commands that they are hearing. There are many examples where an observed response could be explained as a combination of other indirectly related characteristics.

By developing this risk analysis approach, the therapist, doctor, or parent, is able to gain a deeper understanding of the individual. This information can be used to help make more accurate inferences as to why an individual behaves with specific mannerisms, and can greatly improve the potential of implementing the correct therapy. The current alternative method to a detailed brain risk analysis, is to observe the trial over a series of months and years, and to try a multitude of different activities and observe the responses. This is a very time consuming approach, and can be dramatically sped up through by incorporating a modern risk analysis approach.

At this time, the the computation does not take into consideration the Brodmann regions on the internal surface of the brain. This study focuses solely on the exterior of the brain. At this time, due to the fact that the entire brain cannot be taken into account by the current Sight framework, it is not possible to obtain 100% accuracy in identifying the Brodmann areas. It is possible, in the future, to include interior regions of the brain by examining the cerebral white matter. Risk assessment provides early proof of concept for identifying individual trait abnormalities and can be expanded in the future. This approach may also be expanded

outside of the scope of a neurological condition such as autism, and could also be used for more recreational purposes. An interesting application is the use of the technology for identifying "unique" characteristics, and for discovering areas in which an individual is likely to excel in. This technology is still in the early stages, and there is an abundance of possibilities for applying this technology to many different tasks.

CHAPTER 5

RESULTS

The proposed shape analysis is applicable to a large number of different applications as it provides a generic framework for performing a detailed analysis on organs. The principle application of the technology is as a diagnostic and risk-assessment tool for individuals with autism spectrum disorders. Applications for dyslexia, Alzheimer's disease, and lung cancer are also presented.

5.1 Autism Spectrum Disorders

The primary focus of this dissertation is the applicability of the Sight framework to use the shape of the brain to classify autism spectrum disorders. Along with a demonstration of the risk assessment reports, results for classifying brains are computed on several multi-center databases. Data for validation comes from authoritative resources including the National Database of Autism Research (NDAR), The Autism Brain Imaging Data Exchange (ABIDE), and Infant Brain Imaging Symposium (IBIS).

The results include several indicators designed to simplify the understanding of the tables used for visualization. The tables contain numbered brain scans identified by the subject IDs, from their corresponding databases. In these tables, neurotypical individuals are denoted with a value of 1, and individuals diagnosed with autism spectrum disorder are represented as 0. In each table, the subject ID and ground truth diagnosis can be observed on the left of the table. The diagnostic determination of each classifier is presented, along with the cumulative sum of the classifier outputs. Classifiers representing the use of 7 through 14 significant Brodmann areas are used in the final classification. The final subject classification is presented on the right side of the table. Subjects are sorted and grouped for presentation by diagnosis. No subjects were excluded from the databases selected for testing. Due to the number of subjects, the result tables span multiple pages.

Three ABIDE databases were tested using the Sight framework. The global ABIDE database is divided by each of the participating centers. Each center's database contains a roughly even distribution of neurotypical and ASD+ individuals. The databases selected for analysis were the Kennedy Krieger Institute (KKI), University of California, Los Angeles (UCLA), and the University of Michigan (UM). These databases were selected from within the global database, because these sets offered the largest unique pools of individual brain scans available for testing. For this dissertation, a total of 238 individual subjects were analyzed and

classified from the ABIDE data exchange. Additional data from sources including the NDAR Tom Conturo/Vanderbilt University database and the IBIS database were also tested. These databases contain 46 and 36 subjects, respectively.

Classification results representing the use of 7 through 14 significant Brodmann areas were represented in the tables. Performance curves were graphed to illustrate the use of the top 30 significant Brodmann area classifiers. Using the range of 7 through 14 significant Brodmann areas, provided the optimal classification results during testing. Each classifier made a decision by polling the number of significant Brodmann areas used, as discussed in Section 4.7.5. The final subject classification was determined by the consensus of the classifiers using 7 through 14 significant Brodmann areas. The total number of neurotypical classifications was computed and a threshold determined to optimize the results. Subjects scoring equal to, or above the threshold, were classified as neurotypical. Subjects below the threshold were classified as being autism spectrum disorder positive.

5.1.1 Kennedy Krieger Institute Results

The results for analyzing the ABIDE Kennedy Krieger Institute (KKI) database are found in Table 5.1. The KKI database was collected from individuals between the ages of 7 to 12 years of age, with an average age of 10 years. Subjects were evaluated using the WISC, ADOS, and by medical professionals to determine a diagnosis. All scans were acquired using the MP RAGE, three-dimensional, T1-weighted, gradient-echo sequence. The results for the KKI database showed an overall accuracy of 88.89%. Assuming negative for diagnosing autism and positive for determining neurotypical, the test sensitivity (TPR) is 0.939, the specificity (SPC) is 0.810, the positive predictive value (PPV) is 0.886, and the negative predictive value (NPV) is 0.895.

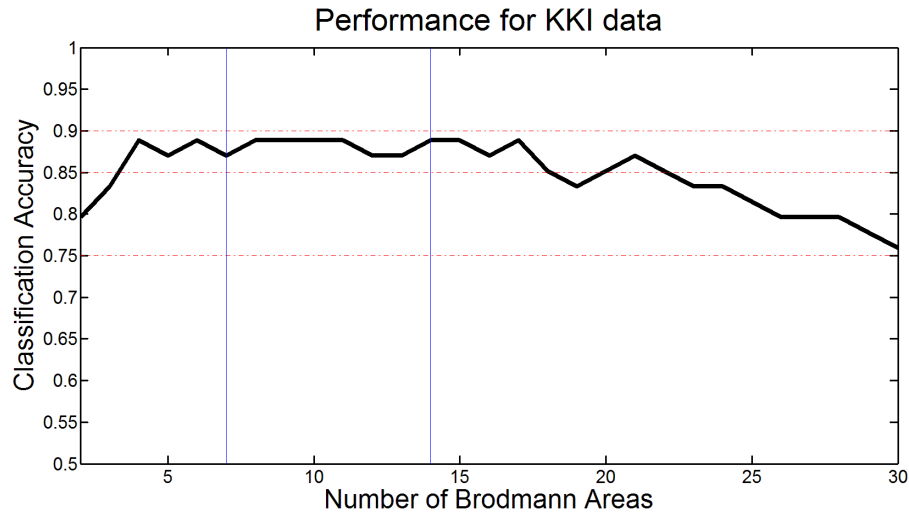


Figure 5.1: Performance using between 2 and 30 Brodmann areas for classification on the ABIDE KKI database. Horizontal accuracy guides are plotted at 7%, 85%, and 90% in red. Vertical blue lines border the Brodmann areas used for making a diagnosis. The individual results of these areas are presented in Table 5.1.

Table 5.1: Autism results for the ABIDE Kennedy Krieger Institute (KKI) database. Threshold = 4. *GT* is Ground Truth, *Sum* is the sum of the area cls, and *Class* is the Sigt Framework classification.

Subject ID	GT	Number of Brodmann Areas								Sum	Class
		7	8	9	10	11	12	13	14		
50791	0	0	0	0	0	0	0	0	0	0	0
50792	0	0	0	0	1	1	1	1	1	5	1
50793	0	0	0	0	0	0	0	0	0	0	0
50794	0	0	0	0	0	0	0	0	0	0	0
50795	0	0	0	1	1	1	1	1	1	6	1
50796	0	0	0	0	0	0	0	0	0	0	0
50797	0	0	0	0	0	0	0	0	0	0	0
50798	0	0	0	0	0	0	0	0	0	0	0

Continued on next page

Table 5.1 – continued from previous page

Subject ID	GT	7	8	9	10	11	12	13	14	Sum	Class
50799	0	1	1	1	1	1	1	1	1	8	1
50800	0	0	0	0	0	0	0	0	0	0	0
50801	0	0	0	0	0	0	0	0	0	0	0
50802	0	0	0	0	0	0	0	0	0	0	0
50803	0	0	0	0	0	0	0	0	0	0	0
50804	0	0	0	0	0	0	1	0	0	1	0
50805	0	0	0	0	0	0	0	0	0	0	0
50806	0	0	0	0	0	0	0	0	0	0	0
50807	0	0	0	0	0	0	0	0	0	0	0
50815	0	0	0	0	0	0	1	1	1	3	0
50823	0	0	0	0	0	0	0	0	0	0	0
50824	0	0	0	0	0	0	0	0	0	0	0
50826	0	0	1	0	1	1	1	1	1	6	1
50772	1	1	1	1	1	1	1	1	1	8	1
50773	1	0	1	1	1	1	1	1	1	7	1
50774	1	1	1	1	1	1	1	1	1	8	1
50775	1	1	1	1	1	1	1	1	1	8	1
50776	1	1	1	1	1	1	1	1	1	8	1
50777	1	1	1	1	1	1	1	1	1	8	1
50778	1	1	1	1	1	1	1	1	1	8	1
50779	1	0	0	0	0	0	1	0	0	1	0
50780	1	0	0	0	1	1	1	1	1	5	1
50781	1	1	1	1	1	1	1	1	1	8	1

Continued on next page

Table 5.1 – continued from previous page

Subject ID	GT	7	8	9	10	11	12	13	14	Sum	Class
50782	1	1	1	1	1	1	1	1	1	8	1
50783	1	0	0	0	1	1	1	1	1	5	1
50784	1	1	1	1	1	1	1	1	1	8	1
50785	1	1	1	1	1	1	1	1	1	8	1
50786	1	1	1	1	1	1	1	1	1	8	1
50787	1	1	1	1	1	1	1	1	1	8	1
50788	1	1	1	1	1	1	1	1	1	8	1
50789	1	1	1	1	1	1	1	1	1	8	1
50790	1	1	1	1	1	1	1	1	1	8	1
50808	1	1	1	1	1	1	1	1	1	8	1
50809	1	1	1	1	1	1	1	1	1	8	1
50810	1	1	1	1	1	1	1	1	1	8	1
50811	1	1	1	1	1	1	1	1	1	8	1
50812	1	1	1	1	1	1	1	1	1	8	1
50813	1	1	1	1	1	1	1	1	1	8	1
50814	1	1	1	1	1	1	1	1	1	8	1
50816	1	0	1	1	1	1	1	1	1	7	1
50817	1	1	1	1	1	1	1	1	1	8	1
50818	1	1	1	1	1	1	1	1	1	8	1
50819	1	1	1	1	1	1	1	1	1	8	1
50820	1	1	1	1	1	1	1	1	1	8	1
50821	1	1	1	1	1	1	1	1	1	8	1
50822	1	0	0	0	0	0	0	0	1	1	0

5.1.2 University of California, Los Angeles Results

The results for analyzing the ABIDE University of California, Los Angeles (UCLA) database are found in Table 5.2. The UCLA database was collected from individuals between the ages of 8 to 17 years of age, with an average age of 13 years. Subjects were evaluated using the WISC, ADOS, and by medical professionals to determine a diagnosis. All scans were acquired using the MP RAGE, three-dimensional, T1-weighted, gradient-echo sequence. The results for the UCLA database showed an overall accuracy of 94.36%. Assuming negative for diagnosing autism and positive for determining neurotypical, the test sensitivity (TPR) is 0.900, the specificity (SPC) is 0.976, the positive predictive value (PPV) is 0.964, and the negative predictive value (NPV) is 0.930.

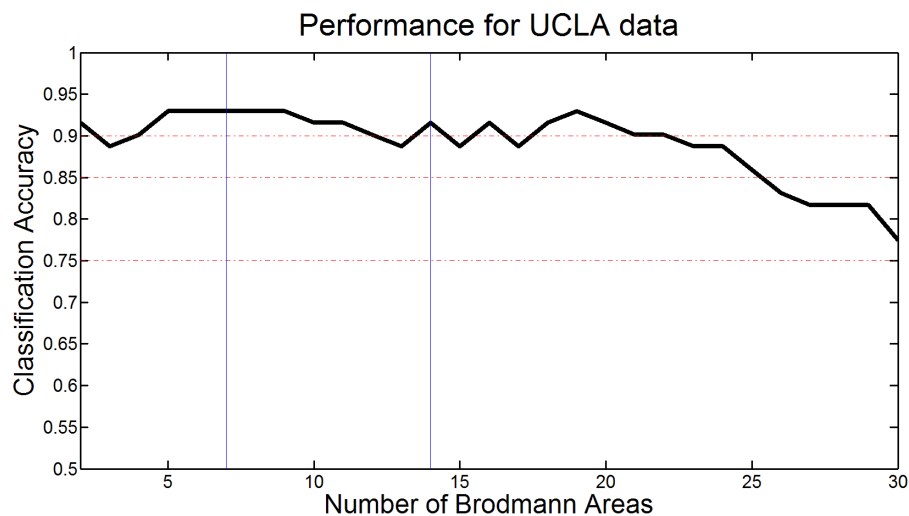


Figure 5.2: Performance using between 2 and 30 Brodmann areas for classification on the ABIDE UCLA database. Horizontal accuracy guides are plotted at 7%, 85%, and 90% in red. Vertical blue lines border the Brodmann areas used for making a diagnosis. The individual results of these areas are presented in Table 5.2.

Table 5.2: Autism results for the ABIDE University of California, Los Angeles (UCLA) database. Threshold = 4. *GT* is Ground Truth, *Sum* is the sum of the area cfs, and *Class* is the Sight Framework classification.

Subject ID	GT	Number of Brodmann Areas								Sum	Class
		7	8	9	10	11	12	13	14		
51201	0	0	0	0	0	0	0	0	0	0	0
51202	0	0	0	1	0	1	0	0	0	2	0
51203	0	0	0	0	0	1	0	1	1	3	0
51204	0	0	0	0	0	0	0	0	0	0	0
51205	0	0	0	0	0	0	0	0	0	0	0
51206	0	0	0	0	0	0	0	0	0	0	0
51207	0	0	0	0	0	0	0	0	0	0	0
51208	0	0	0	0	0	1	0	1	0	2	0
51209	0	0	0	0	0	0	0	0	0	0	0
51210	0	0	0	0	0	0	0	0	0	0	0
51211	0	0	0	0	0	0	0	0	0	0	0
51212	0	0	0	0	0	0	0	0	0	0	0
51213	0	1	1	1	1	0	0	1	0	5	1
51214	0	0	0	0	0	0	0	0	0	0	0
51215	0	0	0	0	0	0	0	0	0	0	0
51216	0	0	0	0	0	0	0	0	0	0	0
51217	0	0	0	1	0	0	0	0	0	1	0
51218	0	0	0	0	0	0	0	0	0	0	0
51219	0	0	0	0	0	0	0	0	0	0	0
51220	0	0	0	0	0	0	0	0	0	0	0

Continued on next page

Table 5.2 – continued from previous page

Subject ID	GT	7	8	9	10	11	12	13	14	Sum	Class
51221	0	0	0	0	0	0	0	0	0	0	0
51222	0	0	0	0	0	0	0	0	0	0	0
51223	0	1	0	0	0	0	0	0	0	1	0
51224	0	0	0	0	0	0	0	0	0	0	0
51225	0	0	0	0	0	0	0	0	0	0	0
51226	0	0	0	0	0	0	0	0	0	0	0
51227	0	0	0	0	0	0	0	0	0	0	0
51228	0	0	0	0	0	0	0	0	0	0	0
51229	0	0	0	0	0	0	0	0	0	0	0
51230	0	0	0	0	0	0	0	0	0	0	0
51231	0	0	0	0	0	0	0	0	0	0	0
51234	0	0	0	0	0	0	0	0	0	0	0
51235	0	0	0	0	0	0	0	0	0	0	0
51236	0	0	0	0	0	0	0	0	0	0	0
51237	0	0	0	0	0	0	0	0	0	0	0
51238	0	0	0	0	0	0	0	0	0	0	0
51239	0	0	0	0	0	0	0	0	0	0	0
51240	0	0	0	0	0	0	0	0	0	0	0
51241	0	0	0	0	0	0	0	1	1	2	0
51248	0	0	0	0	0	0	0	0	0	0	0
51249	0	0	0	0	0	0	0	1	1	2	0
51250	1	1	1	1	1	1	0	1	1	7	1
51251	1	1	1	1	1	1	1	1	1	8	1

Continued on next page

Table 5.2 – continued from previous page

Subject ID	GT	7	8	9	10	11	12	13	14	Sum	Class
51252	1	1	1	1	1	1	1	1	1	8	1
51253	1	1	1	1	1	1	0	1	1	7	1
51254	1	1	1	1	1	1	1	1	1	8	1
51256	1	0	0	0	0	0	0	0	0	0	0
51257	1	1	1	1	1	1	1	1	1	8	1
51258	1	1	1	1	0	1	1	1	1	7	1
51259	1	1	1	1	1	1	1	1	1	8	1
51260	1	1	1	1	1	1	1	1	1	8	1
51261	1	1	0	1	0	1	1	1	1	6	1
51262	1	0	0	0	0	0	0	0	0	0	0
51264	1	1	1	1	1	1	1	1	1	8	1
51265	1	1	1	1	1	1	1	1	1	8	1
51266	1	1	1	1	1	1	1	1	1	8	1
51267	1	1	1	1	1	1	1	1	1	8	1
51268	1	1	1	1	1	1	0	1	1	7	1
51269	1	1	1	1	1	1	1	1	1	8	1
51270	1	1	1	1	1	1	1	1	1	8	1
51271	1	1	1	1	1	1	1	1	1	8	1
51272	1	0	0	1	0	0	0	0	0	1	0
51273	1	1	1	1	1	1	1	1	1	8	1
51275	1	1	1	1	1	1	1	1	1	8	1
51276	1	1	1	1	1	1	0	1	1	7	1
51277	1	1	1	1	1	1	1	1	1	8	1

Continued on next page

Table 5.2 – continued from previous page

Subject ID	GT	7	8	9	10	11	12	13	14	Sum	Class
51278	1	1	1	1	1	1	1	1	1	8	1
51279	1	1	1	1	1	1	1	1	1	8	1
51280	1	1	1	1	1	1	1	1	1	8	1
51281	1	1	1	1	1	1	1	1	1	8	1
51282	1	1	1	1	1	1	1	1	1	8	1

5.1.3 University of Michigan Results

The results for analyzing the ABIDE University of Michigan (UM) database are found in Table 5.3. The UM database was collected from individuals between the ages of 8 to 18 years of age, with an average age of 13 years. Subjects were evaluated using the WISC, ADOS, and by medical professionals to determine a diagnosis. All scans were acquired using the MP RAGE, three-dimensional, T1-weighted, gradient-echo sequence. The results for the UM database showed an overall accuracy of 88.18%. Assuming negative for diagnosing autism and positive for determining neurotypical, the test sensitivity (TPR) is 0.872, the specificity (SPC) is 0.890, the positive predictive value (PPV) is 0.889, and the negative predictive value (NPV) is 0.875.

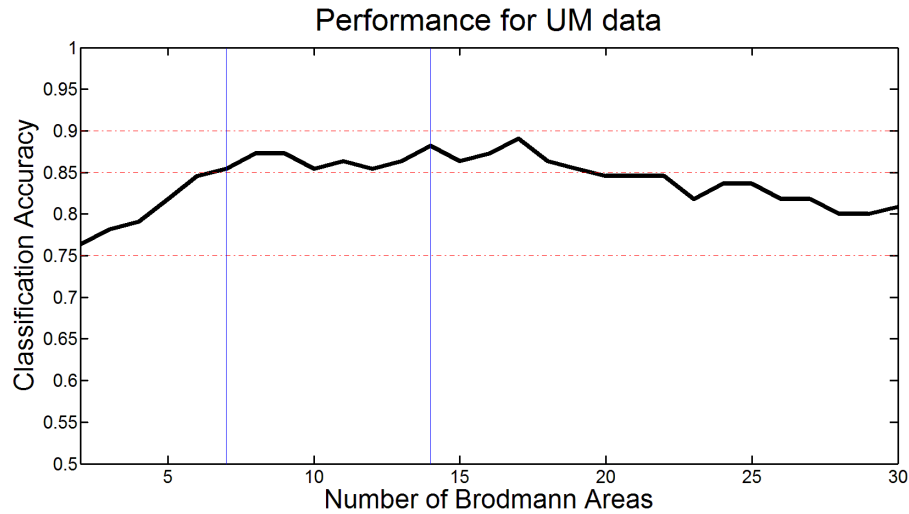


Figure 5.3: Performance using between 2 and 30 Brodmann areas for classification on the ABIDE UM database. Horizontal accuracy guides are plotted at 7%, 85%, and 90% in red. Vertical blue lines border the Brodmann areas used for making a diagnosis. The individual results of these areas are presented in Table 5.3.

Table 5.3: Autism results for the ABIDE University of Michigan (UM) database. Threshold = 4. GT is Ground Truth, Sum is the sum of the area cls, and Class is the Sigt Framework classification.

Subject ID	GT	Number of Brodmann Areas								Sum	Class
		7	8	9	10	11	12	13	14		
50272	0	0	0	0	0	0	0	0	0	0	0
50273	0	0	0	0	0	0	0	0	0	0	0
50274	0	0	0	0	0	0	0	0	0	0	0
50275	0	0	0	0	0	0	0	0	0	0	0
50276	0	0	0	0	0	0	0	0	0	0	0
50277	0	0	0	0	0	0	0	0	0	0	0
50278	0	1	0	0	0	0	0	0	0	1	0
50279	0	0	0	0	0	0	0	0	0	0	0

Continued on next page

Table 5.3 – continued from previous page

Subject ID	GT	7	8	9	10	11	12	13	14	Sum	Class
50280	0	0	0	0	0	0	0	0	0	0	0
50281	0	0	0	0	0	0	0	0	0	0	0
50282	0	0	0	0	1	0	1	1	0	3	0
50283	0	0	0	0	0	0	0	0	0	0	0
50284	0	1	1	1	1	1	1	1	1	8	1
50285	0	0	0	0	0	0	0	0	0	0	0
50286	0	0	0	0	0	0	0	0	0	0	0
50287	0	0	0	0	0	0	0	0	0	0	0
50288	0	0	0	0	0	0	0	0	0	0	0
50289	0	0	0	0	0	0	0	0	0	0	0
50290	0	0	0	0	0	0	0	0	0	0	0
50291	0	0	1	0	0	0	0	0	0	1	0
50292	0	0	0	0	0	0	0	0	0	0	0
50293	0	0	0	0	0	0	0	0	0	0	0
50294	0	0	0	0	0	0	0	1	0	1	0
50295	0	0	0	0	1	0	0	0	0	1	0
50296	0	0	0	0	0	0	0	0	0	0	0
50297	0	0	0	0	0	0	0	0	0	0	0
50298	0	0	0	0	0	0	0	0	0	0	0
50299	0	0	0	0	0	0	0	0	0	0	0
50300	0	0	0	0	0	0	0	0	0	0	0
50301	0	0	0	0	0	0	0	0	0	0	0
50302	0	0	0	1	0	0	0	0	0	1	0
Continued on next page											

Table 5.3 – continued from previous page

Subject ID	GT	7	8	9	10	11	12	13	14	Sum	Class
50303	0	0	0	0	0	0	0	0	0	0	0
50304	0	1	1	1	1	0	1	0	0	5	1
50305	0	1	1	1	1	0	0	0	0	4	1
50306	0	1	1	1	1	1	1	1	1	8	1
50307	0	0	0	0	0	0	0	0	0	0	0
50308	0	0	0	0	0	0	0	0	0	0	0
50309	0	0	0	0	0	0	0	0	0	0	0
50310	0	1	1	1	1	0	1	1	0	6	1
50311	0	0	0	0	0	0	0	0	0	0	0
50312	0	0	0	0	0	0	0	0	0	0	0
50313	0	0	0	0	0	0	0	0	0	0	0
50314	0	0	1	0	1	0	0	0	0	2	0
50315	0	0	0	0	0	0	0	0	0	0	0
50316	0	0	0	0	0	0	0	0	0	0	0
50317	0	0	0	0	0	0	0	0	0	0	0
50318	0	0	0	0	0	0	0	0	0	0	0
50319	0	0	0	0	1	0	0	0	0	1	0
50320	0	0	0	0	0	0	0	0	0	0	0
50321	0	0	0	0	0	0	0	0	0	0	0
50322	0	0	1	1	1	0	0	0	0	3	0
50323	0	0	0	0	0	0	0	0	0	0	0
50324	0	1	1	1	1	1	1	1	1	8	1
50325	0	0	0	0	0	0	0	0	0	0	0
Continued on next page											

Table 5.3 – continued from previous page

Subject ID	GT	7	8	9	10	11	12	13	14	Sum	Class
50326	0	0	0	0	0	0	0	0	0	0	0
50327	1	0	0	0	0	0	0	0	0	0	0
50328	1	1	1	1	1	1	1	1	1	8	1
50329	1	1	1	1	1	1	1	1	1	8	1
50330	1	0	1	1	1	1	1	1	1	7	1
50331	1	1	1	1	1	1	1	1	1	8	1
50332	1	1	1	1	1	1	1	1	1	8	1
50333	1	1	1	1	1	1	1	1	1	8	1
50334	1	1	1	1	1	1	1	1	1	8	1
50335	1	1	1	1	1	0	0	0	0	4	1
50336	1	1	1	1	1	1	1	1	1	8	1
50337	1	1	1	1	1	1	1	1	1	8	1
50338	1	1	1	1	1	1	1	1	1	8	1
50339	1	1	1	1	1	1	1	1	1	8	1
50340	1	1	1	1	1	1	1	1	1	8	1
50341	1	1	1	1	1	1	1	1	1	8	1
50342	1	1	1	1	1	1	1	1	1	8	1
50343	1	1	1	1	1	1	1	1	1	8	1
50344	1	1	1	1	1	1	1	1	1	8	1
50345	1	0	0	0	0	0	0	1	0	1	0
50346	1	1	1	1	1	1	1	1	1	8	1
50347	1	1	1	1	1	1	1	1	1	8	1
50348	1	0	0	1	1	0	0	1	1	4	1

Continued on next page

Table 5.3 – continued from previous page

Subject ID	GT	7	8	9	10	11	12	13	14	Sum	Class
50349	1	1	1	1	1	1	1	1	1	8	1
50350	1	1	1	1	1	1	1	1	1	8	1
50351	1	1	1	1	1	1	1	0	0	6	1
50352	1	1	1	1	1	1	1	1	1	8	1
50353	1	1	1	1	1	1	1	1	1	8	1
50354	1	1	1	1	1	1	1	1	1	8	1
50355	1	0	0	0	1	0	1	0	1	3	0
50356	1	1	1	1	1	1	1	1	1	8	1
50357	1	1	1	1	1	0	0	0	0	4	1
50358	1	1	1	1	1	1	1	1	1	8	1
50359	1	1	1	1	1	1	1	1	1	8	1
50360	1	1	1	1	1	1	1	1	1	8	1
50361	1	1	1	1	1	1	1	1	1	8	1
50362	1	0	1	1	1	0	0	0	0	3	0
50363	1	1	1	1	1	1	1	1	1	8	1
50364	1	1	1	1	1	0	0	0	0	4	1
50365	1	1	1	1	1	1	1	1	1	8	1
50366	1	1	1	1	1	1	1	1	1	8	1
50367	1	1	1	0	0	0	0	0	0	2	0
50368	1	1	1	1	1	1	1	1	1	8	1
50369	1	0	0	0	0	0	1	1	1	3	0
50370	1	1	1	1	1	1	1	1	1	8	1
50371	1	0	1	1	1	1	1	1	1	7	1
Continued on next page											

Table 5.3 – continued from previous page

Subject ID	GT	7	8	9	10	11	12	13	14	Sum	Class
50372	1	1	1	1	1	0	0	1	0	5	1
50373	1	1	1	1	1	1	1	1	1	8	1
50374	1	1	1	1	1	1	1	1	1	8	1
50375	1	1	1	1	1	1	1	1	1	8	1
50376	1	1	1	1	1	1	1	1	1	8	1
50377	1	1	1	1	1	1	1	1	1	8	1
50378	1	1	1	1	1	1	1	1	1	8	1
50379	1	1	1	1	1	1	1	1	1	8	1
50380	1	1	1	1	1	1	1	1	1	8	1
50381	1	0	1	0	0	0	0	0	0	1	0

5.1.4 NDAR Conturo Vanderbilt Results

The results for analyzing the NDAR Tom Conturo database from the Vanderbilt University School of Medicine database are found in Table 5.4. The Conturo database contains information from 46 subjects. The Conturo database was collected from individuals between the ages of 10 to 30 years of age, with an average age of 21 years. Subjects were evaluated using the ADI-R, ADOS, and by medical professionals to determine a diagnosis. All scans were acquired using a standard T1-weighted sagittal plane acquisition. Images were rotated to the axial plane for processing. The results for the Conturo database showed an overall accuracy of 95.65%. Assuming negative for diagnosing autism and positive for determining neurotypical, the test sensitivity (TPR) is 1.000, the specificity (SPC) is 0.920, the positive

predictive value (PPV) is 0.913, and the negative predictive value (NPV) is 1.000.

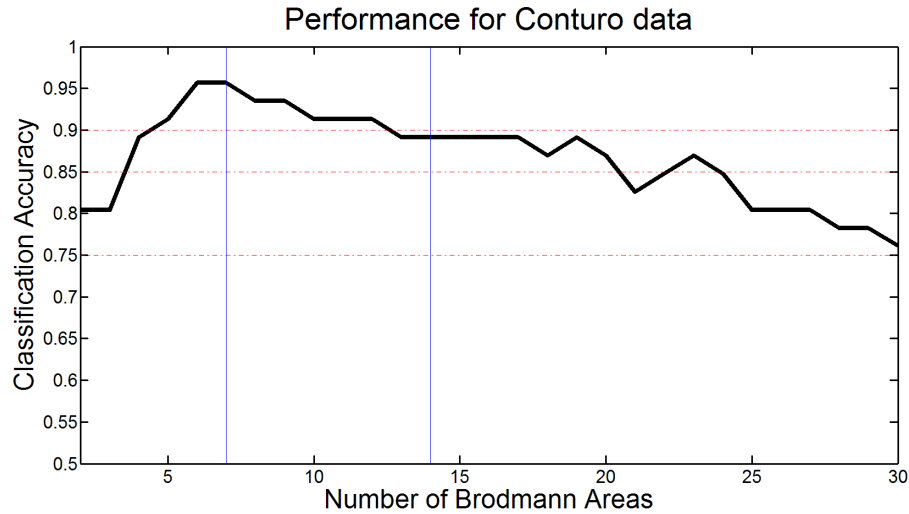


Figure 5.4: Performance using between 2 and 30 Brodmann areas for classification on the NDAR Tom Conturo database. Horizontal accuracy guides are plotted at 7%, 85%, and 90% in red. Vertical blue lines border the Brodmann areas used for making a diagnosis. The individual results of these areas are presented in Table 5.4.

Table 5.4: Autism results for the NDAR Tom Conturo database from the Vanderbilt University School of Medicine. Threshold = 3. *GT* is Ground Truth, *Sum* is the sum of the area classifiers, and *Class* is the Sight Framework classification.

Subject ID	GT	Number of Brodmann Areas								Sum	Class
		7	8	9	10	11	12	13	14		
2002_11_08_aut3	0	0	0	0	0	0	0	0	0	0	0
2004_04_20_aut5	0	0	0	0	0	0	0	0	0	0	0
2004_04_20_aut6	0	0	0	0	0	0	0	0	0	0	0
2004_05_30_aut8	0	0	0	0	0	0	0	0	0	0	0
2004_05_31_aut10	0	0	0	0	0	0	0	0	0	0	0
2004_07_31_aut14	0	0	0	0	0	0	0	0	0	0	0

Continued on next page

Table 5.4 – continued from previous page

Subject ID	GT	7	8	9	10	11	12	13	14	Sum	Class
2004_07_31_aut15	0	1	1	1	1	1	1	1	1	8	1
2004_08_01_aut16	0	1	0	0	0	0	0	1	0	2	0
2004_08_21_aut20	0	0	0	0	0	0	0	0	0	0	0
2004_08_21_aut21	0	0	0	0	0	0	0	0	0	0	0
2004_08_22_aut22	0	0	0	0	0	0	0	0	0	0	0
2004_08_22_aut23	0	0	0	0	0	0	0	0	0	0	0
2004_09_18_aut24_stl_1p5T	0	0	0	0	0	0	0	0	0	0	0
2004_10_23_aut25_stl_1p5T	0	0	0	0	0	0	0	0	0	0	0
2004_10_23_aut26_stl_1p5T	0	0	0	0	0	0	0	0	0	0	0
2004_12_19_aut27	0	0	0	0	0	0	0	0	0	0	0
2004_12_19_aut28	0	0	0	0	0	0	0	0	0	0	0
2004_12_20_aut29	0	0	0	0	0	0	0	0	1	1	0
2004_12_22_aut31	0	0	0	0	0	0	0	0	0	0	0
2005_03_11_aut32	0	0	0	0	0	0	0	0	0	0	0
2005_08_20_aut33	0	0	0	0	0	0	1	1	1	3	1
2006_01_14_aut35	0	0	0	0	0	0	0	0	0	0	0
2006_02_17_aut37	0	0	0	1	1	0	0	0	0	2	0
2006_02_18_aut39	0	0	0	0	0	0	0	0	0	0	0
2006_02_19_aut40	0	0	0	0	0	0	0	0	0	0	0
2004_07_02_vols31	1	1	1	1	0	0	0	0	0	3	1
2004_07_22_vols34	1	1	1	1	1	1	1	1	1	8	1
2004_07_31_vols38_shady	1	1	1	1	1	1	1	1	1	8	1
2004_08_21_vols40_shady	1	1	1	1	1	1	1	1	1	8	1

Continued on next page

Table 5.4 – continued from previous page

Subject ID	GT	7	8	9	10	11	12	13	14	Sum	Class
2005_03_17_vols44_shady	1	1	1	1	1	1	1	1	1	8	1
2005_03_19_vols46_shady	1	1	0	0	1	1	1	1	1	6	1
2005_03_19_vols47_shady	1	1	1	1	1	1	1	1	1	8	1
2005_08_18_vols49_shady	1	1	1	1	1	1	1	1	1	8	1
2005_08_21_vols53_shady	1	1	1	1	1	1	1	1	1	8	1
2005_08_22_vols54_shady	1	1	1	1	1	1	1	1	1	8	1
2005_08_23_vols55_shady	1	1	1	1	1	1	1	1	1	8	1
2005_08_24_vols56_shady	1	1	1	1	1	1	1	1	1	8	1
2005_08_25_vols57_shady	1	1	0	1	1	0	1	1	1	6	1
2005_08_27_vols58_shady	1	1	1	1	1	1	1	1	1	8	1
2005_08_27_vols59_shady	1	1	1	1	1	1	1	1	1	8	1
2006_01_11_vols66	1	1	1	1	0	0	0	0	0	3	1
2006_01_15_vols69_shady	1	1	1	1	1	1	1	1	1	8	1
2006_02_18_vols71_shady	1	1	1	1	1	1	1	1	1	8	1
2006_02_19_vols72_shady	1	1	1	1	1	1	1	1	1	8	1
2006_03_13_vols74	1	1	1	1	1	1	1	1	1	8	1
2006_03_17_vols75	1	1	1	1	1	1	1	1	1	8	1

5.1.5 Infant Brain Imaging Study Results

The results for analyzing the Infant Brain Imaging Study (IBIS) database are found in Table 5.5. A subset of the complete IBIS database was provided for evaluation purposes con-

sisting of 36 subjects. The IBIS database was collected from individuals between the ages of 6 to 9 months of age, with an average age of 7.5 months. Subjects were diagnosed as they grew older using the ADI-R, ADOS, and by medical professionals to determine a diagnosis. MRI brain scans were completed at the clinical sites on identical 3-T Siemens TIM Trio scanners (Siemens Medical Solutions, Malvern, Pa.) equipped with 12-channel head coils during natural sleep. The diffusion tensor imaging sequence was acquired as an ep2d_diff pulse sequence with a field of view of 190 mm, 7581 transversal slices, a slice thickness of 2 mm isotropic, 222-mm³ voxel resolution, a TR of 12,800/13,300 ms, a TE of 102 ms, variable b values between 0 and 1,000 s/mm^2 , 25 gradient directions, and a scan time of 56 minutes. The results for the IBIS database showed an overall accuracy of 97.29%. Assuming negative for diagnosing autism and positive for determining neurotypical, the test sensitivity (TPR) is 0.964, the specificity (SPC) is 1.000, the positive predictive value (PPV) is 1.000, and the negative predictive value (NPV) is 0.889.

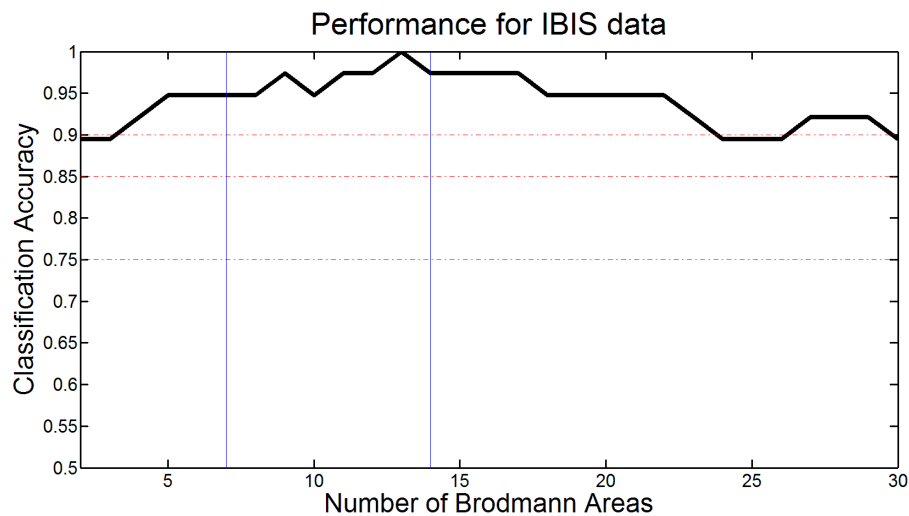


Figure 5.5: Performance using between 2 and 30 Brodmann areas for classification on the Infant Brain Imaging Study (IBIS) database. Horizontal accuracy guides are plotted at 7%, 85%, and 90% in red. Vertical blue lines border the Brodmann areas used for making a diagnosis. The individual results of these areas are presented in Table 5.5.

Table 5.5: Autism results for the Infant Brain Imaging Study (IBIS) database. Threshold = 4. *GT* is Ground Truth, *Sum* is the sum of the area classifiers, and *Class* is the Sigt Framework classification.

Subject ID	GT	Number of Brodmann Areas								Sum	Class
		7	8	9	10	11	12	13	14		
IBIS2118	0	0	0	0	0	0	0	0	0	0	0
IBIS2345	0	0	0	0	0	0	0	0	0	0	0
IBIS2938	0	0	0	0	0	0	0	0	0	0	0
IBIS3632	0	0	0	0	0	0	0	0	0	0	0
IBIS5907	0	0	0	0	0	0	0	0	0	0	0
IBIS6354	0	0	0	0	0	0	0	0	0	0	0
IBIS6685	0	0	0	0	0	0	0	0	0	0	0
IBIS7881	0	0	0	0	0	0	0	0	0	0	0
IBIS0079	1	1	1	1	1	1	1	1	1	8	1
IBIS0096	1	1	1	1	1	1	1	1	1	8	1
IBIS0198	1	1	1	1	1	1	1	1	1	8	1
IBIS0845	1	1	1	1	1	1	1	1	1	8	1
IBIS1127	1	1	1	1	1	1	1	1	1	8	1
IBIS1242	1	0	0	0	0	0	1	1	1	3	0
IBIS1818	1	1	1	1	1	1	1	1	1	8	1
IBIS2311	1	1	1	1	1	1	1	1	1	8	1
IBIS2325	1	1	1	1	1	1	1	1	1	8	1
IBIS2547	1	1	1	1	1	1	1	1	1	8	1
IBIS3704	1	1	1	1	1	1	1	1	1	8	1
IBIS4012	1	1	1	1	1	1	1	1	1	8	1

Continued on next page

Table 5.5 – continued from previous page

Subject ID	GT	7	8	9	10	11	12	13	14	Sum	Class
IBIS4272	1	1	1	1	1	1	1	1	1	8	1
IBIS4975	1	1	1	1	1	1	1	1	1	8	1
IBIS5293	1	1	1	1	1	1	1	1	1	8	1
IBIS6141	1	1	1	1	1	1	1	1	1	8	1
IBIS6332	1	1	1	1	1	1	1	1	1	8	1
IBIS6377	1	1	1	1	1	1	1	1	1	8	1
IBIS7324	1	1	1	1	1	1	1	1	1	8	1
IBIS7422	1	1	1	1	1	1	1	1	1	8	1
IBIS7653	1	1	1	1	1	1	1	1	1	8	1
IBIS7996	1	1	1	1	1	1	1	1	1	8	1
IBIS8368	1	1	1	1	1	1	1	1	1	8	1
IBIS8423	1	1	1	1	1	1	1	1	1	8	1
IBIS8470	1	1	1	1	1	1	1	1	1	8	1
IBIS8583	1	1	1	1	1	1	1	1	1	8	1
IBIS9360	1	1	1	1	1	1	1	1	1	8	1
IBIS9647	1	1	1	1	1	1	1	1	1	8	1

5.1.6 Risk Analysis Results

In order to report results to potential end-users, it was necessary to create a risk assessment tool. The initial diagnostic tool was intended for scientific purposes and to determine the efficacy of the proposed framework. Early stage risk assessment tools were constructed

to demonstrate the capability of the system for the purpose of displaying results in a readable manner. The first reports created by the Sight framework are for technical use only. An example report for a subject diagnosed with autism spectrum disorder can be found in Appendix 7. A comparative report for a neurotypical individual can be found in Appendix 7.

Providing useful reports for parents, therapists, and medical professional led to constructive feedback regarding improving the structure and layout of the reports. Reports constructed using simple, brightly colored visuals were preferred by end-users during A/B testing. Based on the feedback from more than 50 individuals, a mock-up of the revised report was constructed. An improved risk analysis report can be found in Appendix 7. The system will be improved based on user feedback as needed.

5.2 Other Applications

While the primary application of this dissertation is in the field of autism spectrum disorders. The approach includes different applications that require only minor modifications. The following section is a collection of other applications of the specific approach and the related results. The only differences between the primarily discussed application and these alternative applications are the end parameters examined, as these parameters are often specific to each individual application.

5.2.1 *Dyslexia*

The neurological disorder of dyslexia is difficult to diagnose and has a profound impact on a child's ability to fluently read and comprehend words despite the fact that they possess a normal intelligence level for their age and education [245]. Dyslexia is not uncommon, as it affects roughly 5-12% of the population [246]. However, it is often diagnosed only after a child's scholastic performance or lifestyle has already been impacted.

According to multiple studies, structural differences are found in the brains of subjects who have dyslexia. The earliest findings revealed a lack of the typical brain asymmetry and an increase in cortical anomalies [246]. According to Eliez et al. [247] and Casanova et al. [248], dyslexic subjects have smaller gyral indexes (the ratios between the pial contours and the convex hull of the brain surface) than normal subjects, suggesting that the dyslexic brains differ in folding. The recent comprehensive reviews by Richlan et al. [249] and Krafnick et al. [250] have demonstrated evidence of change in the bilateral temporoparietal and left occipitotemporal cortical regions of the brain's gray matter. Using voxel-based morphometry to examine in-vivo dyslexic brains, Eliez et al. [247] and Silani et al. [251] have indicated reduced gray matter volume in such brains. Klingberg et al. [252] and Niogi et al. [253]

also examined the cerebral white matter by using diffusion tensor imaging and found similar results. By analyzing MRIs, Elnakib et al. [254] and von Plessen et al. [255] discovered significant differences in the shapes and body length of the corpus callosum in key anatomical regions that help to identify dyslexia.

Results

The proposed framework has been examined using *in-vivo* data collected from 30 age-matched subjects (16 dyslexic and 14 control ones of age from 18 to 40 years in each group). The subjects were scanned with a 1.5 Tesla GE MRI system with voxel resolution of $0.9375 \times 0.9375 \times 1.5 \text{ mm}^3$ under a T1-weighted imaging sequence protocol. The reference brain was constructed from the Montreal Neurological Institute's ICBM 152 atlas [256, 257]. All results are displayed as overlays on the reference brain.

The training subsets, used for classification, were arbitrarily selected from the 30 subjects. The classification accuracy of the k -nearest classifier was then evaluated using a χ^2 -test at the three confidence levels, 85, 90, and 95%, in order to examine significant differences in the estimated SH index. As expected, the 85% and 90% confidence levels yielded the best results and correctly classified 16 out of 16 dyslexic subjects (a 100% accuracy) and 14 out of 14 control subjects (a 100% accuracy). The 95% confidence level accurately identifies 15 out of 16 dyslexic subjects (93.7%) and 12 out of 14 control subjects (85.7%). The accuracy of the traditional volumetric approach is 7 out of 16 dyslexic subjects (43.75%), and 9 out of 14 control subjects (64.29%) at the 85% confidence level. At a 95% confidence level our approach is more accurate than the traditional approach using an 85% confidence level. These results highlight the advantage of the proposed diagnostic tool.

The brain cortex can also be easily subdivided into four lobes: frontal, parietal, occipital, and temporal. To make the measurements more detailed, the frontal lobe can be subdivided into the pre-frontal and pre-motor areas. As shown in Table 5.6, the absolute numbers of the significantly different nodes or their relative numbers (percentages of the total brain nodes)

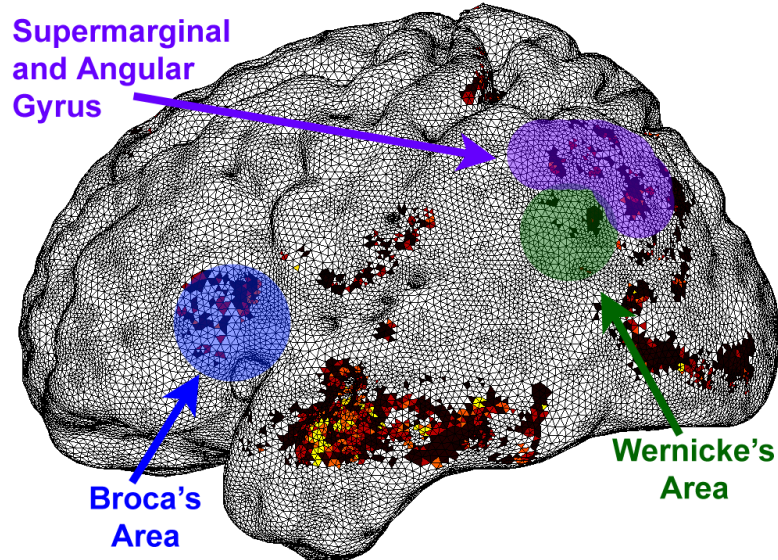


Figure 5.6: Differences discovered in brains of individuals diagnosed with dyslexia. The uniquely colored Broca's and Wernicke's areas, as well as the supermarginal and angular gyrus on the left brain hemisphere together with areas of significant difference in both distance and curvature measurements. Significantly different nodes are found in brain areas that correlate with phonological processing.

can easily be counted for each of these five brain areas. That the temporal and parietal lobes contain major areas of difference, possibly because the key areas associated with language processing reside in these brain lobes. Nonetheless, the proposed mapping provides potentially useful quantitative characteristics and more precise locations of the areas of the key dyslexic-to-normal brain differences. Furthermore, the approach has discovered significantly different areas that neighbor these key primary phonological processing areas. A potential reason for the occurrence of these differences may be related to migrations in brain function, where alternate parts of the brain work help to compensate in dyslexic individuals. This is a new theory proposed by Talan et al. [258].

Table 5.6: Numbers N_{sd} and relative numbers v_{sd} (% of the total nodes) of the significantly different nodes in the primary prefrontal, premotor, parietal, occipital, and temporal brain regions.

Brain Region	Left Hemisphere		Right Hemisphere	
	N_{sd}	$v_{sd}, \%$	N_{sd}	$v_{sd}, \%$
<i>Prefrontal</i>	0	0	0	0
<i>Premotor</i>	309	0.6	547	1.1
<i>Parietal</i>	939	1.8	1073	2.1
<i>Occipital</i>	706	1.4	185	0.3
<i>Temporal</i>	734	1.4	478	0.9
Totals	2688	5.3	2283	4.5

5.2.2 Alzheimer's Disease

Dementia brain diseases (e.g., Alzheimer, vascular dementia) are among the most interesting and challenging research areas in modern neuroscience. Alzheimers disease (AD) is the most common cause of a progressive dementia that accounts for 60-80% percent of cases [259]. AD is characterized by the decline in mental ability which severely affects the thinking and social abilities, which interfere with an adults' daily life [259]. Therefore, early diagnosis of dementia diseases is of great important to institute appropriate therapies. In this paper, we propose a a computer-aided diagnostic (CAD) system of dementia using structural T1- Weighted MRI data of the brain. Instead of examining the volumetric changes in individual brain structures, the proposed CAD system attempts to analyze and quantify differences between the whole 3D brain shapes for AD, mild cognitive impairment (MCI), and control subjects in order to discriminate between them more accurately.

Developing CAD system for the clinical diagnosis of dementia diseases essentially requires accurate delineation of the brain tissue, i.e., white and grey matters [260]. Thus, the first step of our framework performs skull stripping and brain segmentation. The proposed brain segmentation is based on the integration of statistical approaches (a probabilistic shape

prior, first-order intensity model, and second-order appearance model) that are integrated into a two-level joint Markov-Gibbs random field (MGRF) model of T1-MR brain images. Following brain segmentation, a 3D mesh model of a manifold of the brain surface is generated, mapped to a unit sphere, and approximated using spherical harmonic (SPHARM) analysis. The SPHARM reconstruction error and surface complexity of the manifold provide indexes to describe the overall complexity of the brain shape. These features are augmented into a k-nearest neighbor classifier to distinguish between Alzheimers disease (AD) mild cognitive impairment (MCI), and controls subjects.

Results

The framework was preliminarily evaluated on 30 subjects which were provided by the CADDementia challenge. The test data were collected from multicenter clinical-representative T1-weighted MRI data of patients with Alzheimers disease (AD), mild cognitive impairment (MCI) and healthy controls. To distinguish between the AD, MCI, and control subjects, a K-nearest neighbor classifier was used.

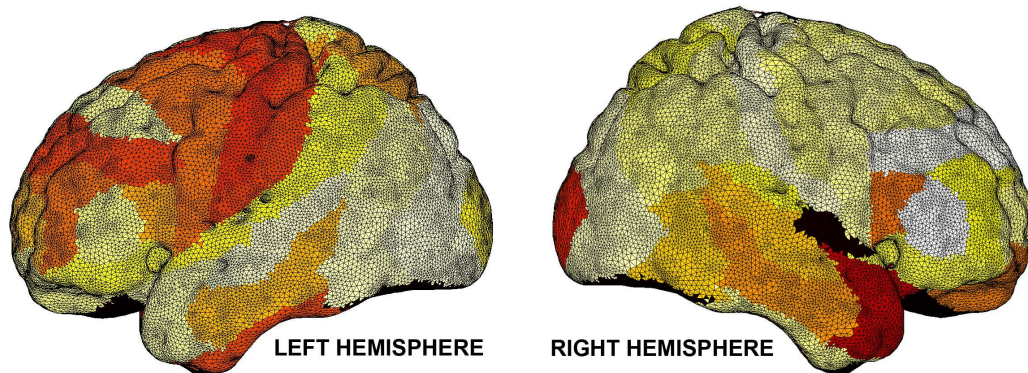


Figure 5.7: *Areas of change discovered in brains of individuals diagnosed with Alzheimer's Disease. The darker colored areas indicate a faster rate of brain degradation over time. Subjects were scanned in as part of a longitudinal study. The areas of greatest change were isolated and displayed on a brain map for visualization.*

Using this approach 10 out of 12 (an 83.3% accuracy) control subjects, 9 out of 10 (an 90.0% accuracy) AD subjects, and 5 out of 8 (an 62.5% accuracy) MCI subjects were iden-

tified. Some minor work was done in an effort to apply the technique to a larger data set, however difficulties in the data have made this an ongoing side-project.

5.2.3 Lung Cancer

Pulmonary nodules are the most common manifestation of lung cancer and are the principal cause of cancer-related deaths [261]. Fast and accurate classification of the nodules is of major importance for medical computer-aided diagnostic systems (CAD). A nodule is an approximately spherical volume of higher-density tissue visible in an X-ray lung image. Large malignant nodules (generally defined as greater than 1 cm in diameter) are easily detected with any traditional imaging equipment and are then diagnosed by needle biopsy or bronchoscopy. However, diagnostic options for small malignant nodules are limited, due to difficulties in accessing them, especially if they are located deep in the tissue or away from the large airways. Therefore, additional imaging and CAD techniques are needed. The popular direction of detecting small cancerous nodules is to analyze their growth rate over time.

Results

To justify the proposed methodology of analyzing the 3D shape of both malignant and benign nodules, the above proposed shape analysis framework was pilot-tested on a database of clinical multi-slice chest LDCT scans of 327 lung nodules (153 malignant and 174 benign). The CT data sets each have $0.7 \times 0.7 \times 2.0 \text{ mm}^3$ voxels, with nodule diameters ranging from 3 mm to 30 mm. Note that these 327 nodules were diagnosed using a biopsy (the ground truth).

The training subset for classification (15 malignant lung nodules and 15 benign lung nodules) was arbitrarily selected among all of the 327 lung nodules. The accuracy of classification based on using K-nearest classifier of both the training and test subjects was evaluated using the χ^2 -test at 95% confidence level. At the 95% confidence level, the correctly classified 143 out of 153 malignant nodules (a 93.5% accuracy), and 163 out of 174 control subjects (a

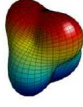
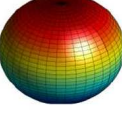
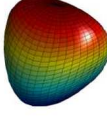
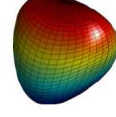
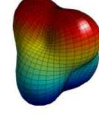
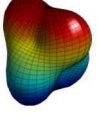
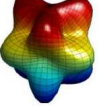

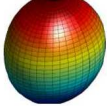
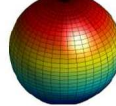
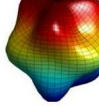
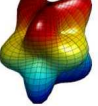
	Original mesh	1 SH	3 SHs	5 SHs	15 SHs	60 SHs
B						
M						

Figure 5.8: 3D shape approximation showing the differences between malignant (M) and benign (B) lung nodules.

93.7% accuracy). The overall accuracy using the proposed 3D shape-based CAD system for 95% confidence level is 93.6% in the first detection of lung nodules. The classification based on traditional growth rate approach [18] over one year is 87 out of 153 malignant nodules (a 56.9% accuracy), and 114 out of 174 benign nodules (a 65.7% accuracy) at a 95% confidence level, these results highlight the advantage of the proposed shape-based diagnostic approach.

Another way to measure and test the performance of the proposed diagnostic system is to compute the receiver operating characteristic (ROC). Each point on the graph is generated by using a different cut point (classification threshold). Figure 8 shows the ROC of the two approaches; the proposed shape index based diagnostic approach and the growth rate based diagnostic approach [262]. It is clear from Fig 8 that the area under ROC curve of our present approach is larger ($A_z = 0.9782$) than the area under the ROC curve of the growth rate based diagnostic approach [262] (A_z is 0.6757 for one year estimated growth rate). The high sensitivity and specificity results from using SPHARM to approximate the 3D shape of the detected lung nodule as a new discriminatory feature.

5.2.4 Summary

The aforementioned methods, help to illustrate the broad variety of applications for this approach. By uniquely modifying classifiers to account for specific differences, the framework is able to provide a tremendous amount of beneficial information for classifying different organs.

The results and methodology for the different stages of the Sight framework were published and tested in peer-reviewed conferences and journal articles. For more information and details regarding the results and validation of the individual stages please see the following citations [263, 264, 265, 266, 267, 268, 269, 270, 271, 272, 273, 274, 275, 276, 277, 278, 279, 280, 281].

CHAPTER 6

DISCUSSION

This study determined that features on the surface of the human brain provide essential information that can help categorize neurological conditions. The Sight framework was able to take 3-dimensional MRI scans of the human brain, remove non-brain information, and construct 3-dimensional meshes of the brain. Regions on the surface of the brain were able to be isolated. Metrics for each of these regions were successfully computed. The metrics and brain regions were able to be combined into a classifier for validating the hypothesis of the study.

The system has the ability to demonstrate the robustness of the algorithms by performing automated analyses on large neurological data sets. Processing of the brain scans were completed in a fully automated manner. The results of the processing enabled the construction of classifiers. The classifiers were used to determine locations within the brain that are important for distinguishing between neurotypical and atypical results. The classifiers were used to test the hypothesis that surface features of the brain can be used to distinguish unique characteristics and make diagnoses for individuals with neurological conditions.

Testing the algorithms developed in this study yielded positive results. Five databases were examined to evaluate subjects diagnosed with autism. In all of the databases, an accuracy of above 85% was achieved when using a simple classifier. In three of the five databases,

an accuracy above 90% was observed. These results clearly demonstrate the ability of the Sight framework to accurately distinguish the differences between the brains of neurotypical subjects and individuals who have autism. The algorithms were also used on subjects diagnosed with dyslexia, Alzheimer's disease, and Lung cancer. These tests yielded promising initial results for the expansion of the Sight framework to a wide variety of neurological and medical conditions. The results from the tests in this study prove that the Sight framework is successful in achieving the goals of the study, taking the field of medicine one step closer to definitively providing neurological diagnoses.

Using the Sight framework, the classification results were focused toward individual risk assessment reports based on the request of medical professionals and parents. These risk assessment reports provide information obtained by processing brain scans using the Sight framework. These results can serve as a targeted tool to improve diagnostic procedures and guide treatment therapies based on specific results. Medical professionals, therapists, and parents concur that knowing the areas of the brain on which to focus therapies is a crucial step toward improving patient outcomes. Professionals involved in early focus groups have agreed that early intervention, guided by risk assessment reports, would enhance current medical therapies.

Five software process patents have been filed around the individual procedures used in the Sight framework. These early software patent filings have been assigned to the University of Louisville. Two additional software copyright filings have been submitted regarding the source code used in the Sight framework. The submission of patents and copyrights around the technology helps to further validate that institutions, medical professionals, and engineering teams see the potential benefits of this technology. The patent and copyright filings have led to an increased market interest in the technology.

The results and capabilities of the Sight framework have been presented in national and international conferences. Presentation of the possibilities for enhanced understanding of

neurological conditions have generated interest from medical professionals, therapists, parents, and entrepreneurial ventures. Continued development and targeted results based on the feedback of stakeholders in autism diagnostics will continue to propel the technology forward.

6.1 Recommendations

The Sight framework has identified specific surface features that could be used to provide objective diagnosis distinguishing between the brains of neurotypical and individuals with other neurological conditions. The data and reports generated by this framework provide reliable information that can guide medical professionals, therapists, and parents as they implement therapies for patients having neurological disorders.

The Sight framework could serve as a reliable assisting tool to improve the outcomes of existing neurological testing. Improvements in the diagnostic reports that currently exist for autism could include visual and objective representations provided by the Sight framework to illuminate the inner functions of an individuals' brain. Patients suffering from dyslexia could be identified clearly by explaining which Brodmann areas are effected. Other conditions that could have improved diagnostic understanding include Alzheimers disease, ADHD, schizophrenia, bipolar disorder, concussions, and athletic head trauma. The technology could also be expanded to serve as a tool for individuals who desire to gain more insight into the general workings of their brains.

The technology has shown promise for examining other medical conditions, including lung cancer. Understanding that the framework can be applied to other organs of the body allows the future possibility of exploring non-invasive diagnoses and treatments for a wide variety of cancers and abnormalities within the human body.

Initial communication with potential entrepreneurial organizations has demonstrated

strong interest in developing this technology on a commercial scale. Continued exploration of the market viability of the technology should be explored. The future of the Sight framework is very bright, and there is a great potential for the software to improve the lives of countless patients.

6.2 Limitations

The limitations of the software center on the fact that the Sight framework was principally designed to explore the surface of shapes within the human body. Based on subject availability, the focus of the study was niched into the human brain. Further interest was targeted toward the study of the cerebral cortex. Information that cannot be inferred from examining the surface of a structure would require additional development. The capabilities of this software have not been tapped to the fullest extent with this application.

Access to large and targeted sets of data provided another limitation to the study. The quantity of MR brain scans available for individuals with autism is limited by data that has been previously collected. There are some larger study efforts, such as the ABIDE database, that proved a beneficial resource on which the Sight framework was tested. There are fewer data sets available for young children, and access is limited at this time.

The data was also limited by gender and social status restrictions. At present, only databases of Caucasian, middle to upper class individuals, have been collected. To be fair and equitable, scans of every ethnicity should be included for normalization purposes. At this time, large databases of other ethnicities have not been made available. Data for low income populations has not been created. While there are similarities between human brains, there is the potential to unearth differences. It would be beneficial to expand the framework to include a much broader population. There are financial difficulties with accomplishing this task.

The current speed and automation of the software provides another limitation. While

the majority of the framework has been fully automated, the software still requires manual initiation due to the process of operating in a command line environment. Completing a fully automated version of the software, including a user interface, would enable the software to test larger populations. Optimizations to further improve the speed of the algorithms used in the Sight framework would improve these outcomes.

Educating and changing the current diagnostic practices of physicians and other researchers is a challenging task. The current gold standard has been in effect since 1975, and while it is a cumbersome process, few changes have been made to help the process available to parents and patients with autism. Professionals frequently discuss the unfortunate nature of the diagnostic situation, but can be resistant to considering innovation in such a well-established field. They readily embrace the possibility that this type of technology could positively enhance their ability to provide accurate diagnoses in a timely manner. They have shown interest in this concept, but more targeted information must be made available to help them better understand the process. Parents are also hopeful that medical professionals will embrace the possibility of objective diagnoses for their children, because they feel that the current methods do not meet their needs.

6.3 Further Research

Further research into the possibilities of gathering additional data for other autistic populations and neurological conditions will enable the Sight framework to expand. Determining a method to expand the software to include the white matter and interior regions of the brain will give a more complete picture. This expansion would allow incorporation of Brodmann areas located in the interior of the brain. Combining the Sight framework with other modalities, including Diffusion Tensor Imaging (DTI), Functional Magnetic Resonance Imaging (fMRI), and genetic based research would allow for the construction of a complete map of the human brain. This

complete map will enable medical professionals to more fully understand the workings of the human body.

CHAPTER 7

CONCLUSION

Autism spectrum disorders are a large set of complex developmental disabilities with similar characteristics. Over the past decade, the prevalence of autism has dramatically increased. This has made a significant impact on the health and behavior of children and the modern health care system. While the subjective methods used to detect and diagnose autism have been debated in the medical community, there is a consensus that new technology must be developed to improve outcomes for children who have neurological conditions. Medical shape analysis provides the most promising body of research to guide the construction of technologies designed to understand neurological conditions. This dissertation was developed to aid in creating more accurate diagnostic assessment tools. The dissertation has been expanded to construct risk assessment tools for use in helping to guide targeted and effective treatment and intervention. Five patents have been filed regarding technology developed for this dissertation. The technology has also been proposed to the broader community, for integration with current autism diagnostic methods.

The primary aim of this work was to assess whether the shape of the human brain could be used as a reliable source of information for determining whether an individual was diagnosed with autism. To confirm this, a series of algorithms consisting of bias correction, skull stripping, multi-label brain segmentation, 3-dimensional mesh construction, spherical

harmonic decomposition, registration, and classification was constructed. The software algorithms were developed as an original contribution of this dissertation, in collaboration with the Bioluminescence laboratory at the University of Louisville Speed School of Engineering. The classification of each subject was used to construct both diagnoses and therapeutic risk assessments for each patient.

The method was tested on a large number of subjects spread across multi-center databases. The testing confirmed that the software was capable of accurately making a diagnosis of autism in a wide range of individuals. Results for the testing data sets achieved accuracies of 88.89% for the KKI database, 94.36% for the UCLA database, 88.18% for the UM database, 95.65% for the Conturo database, and 97.29% for the IBIS database. The sensitivity, specificity, PPV, and NPV values for every data set confirm the overall accuracy. Positive results demonstrated the possibility of expanding the framework into dyslexia, Alzheimer's disease, and lung cancer. These results confirm that the Sight framework is a reliable metric for making neurological diagnoses. The results were transformed from raw numbers into visual risk assessment reports. These risk assessment reports allow a wide range of individuals to understand and use the information to improve outcomes for patients who have neurological conditions.

The Sight framework is a reliable, understandable, and robust framework for the complete analysis of the human brain and its neurological conditions. Modern research and technology is capable of constructing bridges that allow humans to bridge the present with the future. The Sight framework can be a bridge that helps traverse the difficulties in understanding the complexities of the brain. The Sight framework can help medical professionals, therapists, and parents better understand the condition known as autism.

REFERENCES

- [1] M. B. Carpenter, J. Sutin, O. S. Strong, and A. Elwyn, *Human neuroanatomy*. Williams & Wilkins Baltimore, 1983.
- [2] M. Casanova, A. El-Baz, and J. Suri, *Imaging The Brain In Autism*. New York, NY: Springer, 2013.
- [3] G. Gerig, M. Styner, D. Jones, D. Weinberger, and J. Lieberman, "Shape analysis of brain ventricles using spharm," in *Mathematical Methods in Biomedical Image Analysis, 2001. MMBIA 2001. IEEE Workshop on*, pp. 171–178, IEEE, 2001.
- [4] P. L. Williams *et al.*, *Gray's Anatomy: The anatomical basis of medicine and surgery*. Churchill livingstone New York, 1995.
- [5] R. Carter, *The human brain book*. Penguin, 2014.
- [6] H. Y. Carr and E. M. Purcell, "Effects of diffusion on free precession in nuclear magnetic resonance experiments," *Physical Review*, vol. 94, no. 3, p. 630, 1954.
- [7] H. Y. Carr, "Field gradients in early MRI," *Physics Today*, vol. 57, no. 7, pp. 83–83, 2004.
- [8] P. Van Hecke, "P.a. rinck: Magnetic resonance in medicine (incl. CD-ROM). the basic textbook of the european magnetic resonance forum, 4th completely revised edition.," *European Radiology*, vol. 12, no. 3, pp. 712–712, 2002.

- [9] P. C. Lauterbur *et al.*, "Image formation by induced local interactions: examples employing nuclear magnetic resonance," *Nature*, vol. 242, no. 5394, pp. 190–191, 1973.
- [10] J. Sijbers, P. Scheunders, N. Bonnet, D. Van Dyck, and E. Raman, "Quantification and improvement of the signal-to-noise ratio in a magnetic resonance image acquisition procedure," *Magnetic resonance imaging*, vol. 14, no. 10, pp. 1157–1163, 1996.
- [11] W. McRobbie Donald, "MRI from picture to proton," 2007.
- [12] P. T. Callaghan, *Principles of nuclear magnetic resonance microscopy*, vol. 3. Clarendon Press Oxford, 1991.
- [13] D. L. Price, J. P. De Wilde, A. M. Papadaki, J. S. Curran, and R. I. Kitney, "Investigation of acoustic noise on 15 MRI scanners from 0.2 t to 3 t," *Journal of magnetic resonance imaging*, vol. 13, no. 2, pp. 288–293, 2001.
- [14] M. McJury, R. Stewart, D. Crawford, and E. Toma, "The use of active noise control (anc) to reduce acoustic noise generated during MRI scanning: some initial results," *Magnetic resonance imaging*, vol. 15, no. 3, pp. 319–322, 1997.
- [15] E. Bellon, E. Haacke, P. Coleman, D. Sacco, D. Steiger, and R. Gangarosa, "Mr artifacts: a review," *American Journal of Roentgenology*, vol. 147, no. 6, pp. 1271–1281, 1986.
- [16] E. M. Haacke, R. W. Brown, M. R. Thompson, and R. Venkatesan, "Magnetic resonance imaging," *Physical principles and sequence design*, 1999.
- [17] R. W. Brown, Y.-C. N. Cheng, E. M. Haacke, M. R. Thompson, and R. Venkatesan, *Magnetic resonance imaging: physical principles and sequence design*. John Wiley & Sons, 2014.

- [18] N. J. Tustison and J. C. Gee, "N4itk: Nicks n3 itk implementation for MRI bias field correction," *Insight Journal*, 2009.
- [19] N. J. Minshew and J. B. Payton, "New perspectives in autism, part i: The clinical spectrum of autism," *Current Problems in Pediatrics*, vol. 18, no. 10, pp. 567–610, 1988.
- [20] L. Kanner, *Child psychiatry*. Charles C. Thomas, 1948.
- [21] L. Kanner *et al.*, "Autistic disturbances of affective contact," *Nervous child*, vol. 2, no. 3, pp. 217–250, 1943.
- [22] T. Duong, H. Robinson, D. G. BA, and A. Ritvo, "Lower purkinje cell counts in the cerebella of four autistic subjects: initial findings of the ucla-nsac autopsy research report," *Am J Psychiatry*, vol. 143, no. 7, pp. 862–866, 1986.
- [23] S. H. Fatemi, A. R. Halt, G. Realmuto, J. Earle, D. A. Kist, P. Thuras, and A. Merz, "Purkinje cell size is reduced in cerebellum of patients with autism," *Cellular and molecular neurobiology*, vol. 22, no. 2, pp. 171–175, 2002.
- [24] T. L. Kemper and M. L. Bauman, "The contribution of neuropathologic studies to the understanding of autism.," *Neurologic clinics*, vol. 11, pp. 175–187, 1993.
- [25] M. Dapretto, M. S. Davies, J. H. Pfeifer, A. A. Scott, M. Sigman, S. Y. Bookheimer, and M. Iacoboni, "Understanding emotions in others: mirror neuron dysfunction in children with autism spectrum disorders," *Nature neuroscience*, vol. 9, no. 1, pp. 28–30, 2005.
- [26] E. Courchesne, "Brainstem, cerebellar and limbic neuroanatomical abnormalities in autism," *Current opinion in neurobiology*, vol. 7, no. 2, pp. 269–278, 1997.
- [27] L. Wing, "Asperger's syndrome: a clinical account," *Psychological medicine*, vol. 11, no. 01, pp. 115–129, 1981.

- [28] M. B. First, *Diagnostic and statistical manual of mental disorders*. Am Psychiatric Assoc, 1994.
- [29] A. P. Association *et al.*, *The Diagnostic and Statistical Manual of Mental Disorders: DSM 5*. bookpointUS, 2013.
- [30] M. A. Gernsbacher, M. Dawson, and H. H. Goldsmith, "Three reasons not to believe in an autism epidemic," *Current Directions in Psychological Science*, vol. 14, no. 2, pp. 55–58, 2005.
- [31] C. A. Molloy and P. Manning-Courtney, "Prevalence of chronic gastrointestinal symptoms in children with autism and autistic spectrum disorders," *Autism*, vol. 7, no. 2, pp. 165–171, 2003.
- [32] G. Baird, T. Charman, A. Pickles, S. Chandler, T. Loucas, D. Meldrum, I. Carcani-Rathwell, D. Serkana, and E. Simonoff, "Regression, developmental trajectory and associated problems in disorders in the autism spectrum: the snap study," *Journal of autism and developmental disorders*, vol. 38, no. 10, pp. 1827–1836, 2008.
- [33] S. Friedman, D. Shaw, A. Artru, T. Richards, J. Gardner, G. Dawson, S. Posse, and S. Dager, "Regional brain chemical alterations in young children with autism spectrum disorder," *Neurology*, vol. 60, no. 1, pp. 100–107, 2003.
- [34] E. London, "The environment as an etiologic factor in autism: a new direction for research.," *Environmental Health Perspectives*, vol. 108, no. Suppl 3, p. 401, 2000.
- [35] M. R. Herbert, "Contributions of the environment and environmentally vulnerable physiology to autism spectrum disorders," *Current opinion in neurology*, vol. 23, no. 2, pp. 103–110, 2010.

- [36] R. Warren, V. Singh, R. Averett, J. Odell, A. Maciulis, R. Burger, W. Daniels, and W. Warren, "Immunogenetic studies in autism and related disorders," *Molecular and chemical neuropathology*, vol. 28, no. 1-3, pp. 77–81, 1996.
- [37] A. J. Wakefield, S. H. Murch, A. Anthony, J. Linnell, D. Casson, M. Malik, M. Berelowitz, A. P. Dhillon, M. A. Thomson, P. Harvey, *et al.*, "Retracted: Ileal-lymphoid-nodular hyperplasia, non-specific colitis, and pervasive developmental disorder in children," *The Lancet*, vol. 351, no. 9103, pp. 637–641, 1998.
- [38] B. Taylor, E. Miller, C. Farrington, M.-C. Petropoulos, I. Favot-Mayaud, J. Li, and P. A. Waight, "Autism and measles, mumps, and rubella vaccine: no epidemiological evidence for a causal association," *The Lancet*, vol. 353, no. 9169, pp. 2026–2029, 1999.
- [39] I. Rapin and R. F. Tuchman, "Autism: definition, neurobiology, screening, diagnosis," *Pediatric Clinics of North America*, vol. 55, no. 5, pp. 1129–1146, 2008.
- [40] I. Rapin and R. F. Tuchman, "What is new in autism?," *Current opinion in neurology*, vol. 21, no. 2, pp. 143–149, 2008.
- [41] D. L. Robins, D. Fein, M. L. Barton, and J. A. Green, "The modified checklist for autism in toddlers: an initial study investigating the early detection of autism and pervasive developmental disorders," *Journal of autism and developmental disorders*, vol. 31, no. 2, pp. 131–144, 2001.
- [42] F. Abell, M. Krams, J. Ashburner, R. Passingham, K. Friston, R. Frackowiak, F. Happé, C. Frith, and U. Frith, "The neuroanatomy of autism: a voxel-based whole brain analysis of structural scans," *Neuroreport*, vol. 10, no. 8, pp. 1647–1651, 1999.
- [43] N. Boddaert, N. Chabane, H. Gervais, C. Good, M. Bourgeois, M. Plumet, C. Barthelemy, M. Mouren, E. Artiges, Y. Samson, *et al.*, "Superior temporal sulcus

- anatomical abnormalities in childhood autism: a voxel-based morphometry MRI study," *Neuroimage*, vol. 23, no. 1, pp. 364–369, 2004.
- [44] M. Herbert, D. Ziegler, C. Deutsch, L. O'Brien, N. Lange, A. Bakardjiev, J. Hodgson, K. Adrien, S. Steele, N. Makris, *et al.*, "Dissociations of cerebral cortex, subcortical and cerebral white matter volumes in autistic boys," *Brain*, vol. 126, no. 5, pp. 1182–1192, 2003.
- [45] B. Egaas, E. Courchesne, and O. Saitoh, "Reduced size of corpus callosum in autism," *Archives of Neurology*, vol. 52, no. 8, pp. 794–801, 1995.
- [46] C. M. Schumann, C. C. Barnes, C. Lord, and E. Courchesne, "Amygdala enlargement in toddlers with autism related to severity of social and communication impairments," *Biological psychiatry*, vol. 66, no. 10, pp. 942–949, 2009.
- [47] A. Elnakib, M. F. CasaNova, G. Gimel'farb, A. E. Switala, and A. El-Baz, "Autism Diagnostics By Centerline-Based Shape Analysis of The Corpus Callosum," in *Biomedical Imaging: From Nano to Macro, 2011 IEEE International Symposium on*, pp. 1843–1846, Apr. 2011.
- [48] E. Courchesne, G. Press, and R. Yeung-Courchesne, "Parietal lobe abnormalities detected with mr in patients with infantile autism.," *AJR. American journal of roentgenology*, vol. 160, no. 2, pp. 387–393, 1993.
- [49] C. M. Schumann, C. S. Bloss, C. C. Barnes, G. M. Wideman, R. A. Carper, N. Akshoomoff, K. Pierce, D. Hagler, N. Schork, C. Lord, *et al.*, "Longitudinal magnetic resonance imaging study of cortical development through early childhood in autism," *The Journal of Neuroscience*, vol. 30, no. 12, pp. 4419–4427, 2010.

- [50] D. P. Kennedy and E. Courchesne, "Functional abnormalities of the default network during self-and other-reflection in autism," *Social Cognitive and Affective Neuroscience*, vol. 3, no. 2, pp. 177–190, 2008.
- [51] C. for Disease Control, Prevention, *et al.*, "CDC estimates 1 in 68 children has been identified with autism spectrum disorder," *Press Release. Available at www.cdc.gov/media/releases/2014/p0327-autism-spectrum-disorder.html*, accessed on June, vol. 24, p. 2014, 2014.
- [52] E. B. Susan, *Epidemiology of autism: prevalence, associated characteristics, and implications for research and service delivery*. Routledge, 2013.
- [53] S. J. Blumberg, M. D. Bramlett, M. D. Kogan, L. A. Schieve, J. R. Jones, and M. C. Lu, "Changes in prevalence of parent-reported autism spectrum disorder in school-aged us children: 2007 to 2011–2012," *National health statistics reports*, vol. 65, no. 20, pp. 1–7, 2013.
- [54] M. Yeargin-Allsopp, C. Rice, T. Karapurkar, N. Doernberg, C. Boyle, and C. Murphy, "Prevalence of autism in a us metropolitan area," *Jama*, vol. 289, no. 1, pp. 49–55, 2003.
- [55] C. J. Newschaffer, M. D. Falb, and J. G. Gurney, "National autism prevalence trends from united states special education data," *Pediatrics*, vol. 115, no. 3, pp. e277–e282, 2005.
- [56] G. Dawson and J. Osterling, "Early intervention in autism," *The effectiveness of early intervention*, vol. n/a, pp. 307–326, 1997.
- [57] C. DiGuseppi, S. Hepburn, J. M. Davis, D. J. Fidler, S. Hartway, N. R. Lee, L. Miller, M. Rutenber, and C. Robinson, "Screening for autism spectrum disorders in children

- with down syndrome: population prevalence and screening test characteristics," *Journal of Developmental & Behavioral Pediatrics*, vol. 31, no. 3, pp. 181–191, 2010.
- [58] C. Gillberg, "Autism and pervasive developmental disorders," *Journal of Child Psychology and Psychiatry*, vol. 31, no. 1, pp. 99–119, 1990.
- [59] C. Lord, M. Rutter, P. DiLavore, and S. Risi, *ADOS: Autism Diagnostic Observation Schedule*. Western Psychological Services, 2008.
- [60] M. Rutter, A. Le Couteur, and C. Lord, *Autism diagnostic interview-revised*. Los Angeles, CA: Western Psychological Services, 2003.
- [61] A. D. Sandler, D. Brazduinas, W. Cooley, L. Gonzalez de Pijem, D. Hirsh, T. Kastner, M. Kummer, R. Quint, and E. Ruppert, "Developmental surveillance and screening of infants and young children," *Pediatrics*, vol. 108, no. 1, pp. 192–6, 2001.
- [62] D. Wechsler, *Manual for the Wechsler intelligence scale for children, revised*. Psychological Corporation, 1974.
- [63] A. Klin, D. J. Lin, P. Gorrindo, G. Ramsay, and W. Jones, "Two-year-olds with autism orient to non-social contingencies rather than biological motion," *Nature*, vol. 459, no. 7244, pp. 257–261, 2009.
- [64] P. J. Lombroso, M. P. Ogren, W. Jones, and A. Klin, "Heterogeneity and homogeneity across the autism spectrum: the role of development," *Journal of the American Academy of Child & Adolescent Psychiatry*, vol. 48, no. 5, pp. 471–473, 2009.
- [65] W. Jones, K. Carr, and A. Klin, "Absence of preferential looking to the eyes of approaching adults predicts level of social disability in 2-year-old toddlers with autism spectrum disorder," *Archives of General Psychiatry*, vol. 65, no. 8, pp. 946–954, 2008.

- [66] A. Klin, W. Jones, R. Schultz, F. Volkmar, and D. Cohen, "Visual fixation patterns during viewing of naturalistic social situations as predictors of social competence in individuals with autism," *Archives of general psychiatry*, vol. 59, no. 9, pp. 809–816, 2002.
- [67] Z. Boraston and S.-J. Blakemore, "The application of eye-tracking technology in the study of autism," *The Journal of Physiology*, vol. 581, no. 3, pp. 893–898, 2007.
- [68] D. Riby and P. J. Hancock, "Looking at movies and cartoons: eye-tracking evidence from williams syndrome and autism," *Journal of Intellectual Disability Research*, vol. 53, no. 2, pp. 169–181, 2009.
- [69] V. Barras, A. Simons III, and M. Arbib, "Synthetic Event-Related Potentials: A Computational Bridge Between Neurolinguistic Models And Experiments," *Neural Networks*, vol. 37, no. 0, pp. 66–92, 2013.
- [70] R. Lande, "Quantitative Genetic Analysis of Multivariate Evolution, Applied to Brain: Body Size Allometry," *Evolution*, vol. 33, no. 1, pp. 402–416, 1979.
- [71] R. Desimone, S. Schein, J. Moran, and L. Ungerleider, "Contour, Color And Shape Analysis Beyond The Striate Cortex," *Vision Research*, vol. 25, no. 3, pp. 441–452, 1985.
- [72] J. Martin, A. Pentland, and R. Kikinis, "Shape Analysis of Brain Structures Using Physical And Experimental Modes," in *Computer Vision and Pattern Recognition, 1994. Proceedings CVPR '94., 1994 IEEE Computer Society Conference on*, pp. 752–755, June 1994.
- [73] M. Delfour and J.-P. Zolsio, *Shapes and Geometries: Metrics, Analysis, Differential Calculus, and Optimization, Second Edition (Advances in Design and Control)*. SIAM-Society for Industrial and Applied Mathematics, 2nd ed., Dec. 2010.

- [74] H. Poincaré, *Analysis Situs*. Journal de l'Ecole polytechnique 11e sér, Gauthier-Villars, 1st ed., 1895.
- [75] L. de Floriani and M. Spagnuolo, *Shape Analysis and Structuring (Mathematics and Visualization)*. Springer, 1st ed., Nov. 2010.
- [76] D. Guliato and R. Rangayyan, *Modeling and Analysis of Shape: with Applications in Computer-Aided Diagnosis of Breast Cancer (Synthesis Lectures on Biomedical Engineering)*. Morgan and Claypool Publishers, 1st ed., Jan. 2011.
- [77] D. Attali, J.-d. Boissonnat, and H. Edelsbrunner, "Stability And Computation of Medial Axes A State-of-The-Art Report," in *Mathematical Foundations of Scientific Visualization, Computer Graphics, and Massive Data Exploration*, Springer, 2009.
- [78] H. Blum, "A Transformation For Extracting New Descriptors of Shape," *Models For The Perception of Speech And Visual Form*, vol. 19, no. 5, pp. 362–380, 1967.
- [79] H. Blum, "Biological Shape And Visual Science (Part I)," *Journal of Theoretical Biology*, vol. 38, no. 2, pp. 205–287, 1973.
- [80] M. Naf, O. Kubler, R. Kikinis, M. E. Shenton, and G. Szekeley, "Characterization And Recognition of 3D Organ Shape In Medical Image Analysis Using Skeletonization," in *Mathematical Methods in Biomedical Image Analysis, 1996., Proceedings of the Workshop on*, pp. 139–150, June 1996.
- [81] P. Golland, W. Grimson, and R. Kikinis, "Statistical Shape Analysis Using Fixed Topology Skeletons: Corpus Callosum Study," in *Information Processing in Medical Imaging*, pp. 382–387, Springer, 1999.

- [82] S. M. Pizer, D. S. Fritsch, P. A. Yushkevich, V. E. Johnson, and E. L. Chaney, "Segmentation, Registration, And Measurement of Shape Variation Via Image Object Shape," *IEEE Transactions on Medical Imaging*, vol. 18, pp. 851–865, Oct. 1999.
- [83] P. Golland, *Statistical Shape Analysis of Anatomical Structures*. PhD thesis, Department of Electrical Engineering and Computer Science, Massachusetts Institute of Technology, Aug. 2001.
- [84] M. Styner and G. Gerig, "Three-Dimensional Medial Shape Representation Incorporating Object Variability," in *Computer Vision and Pattern Recognition, 2001. CVPR 2001. Proceedings of the 2001 IEEE Computer Society Conference on*, vol. 2, pp. II–651 – II–656 vol.2, 2001.
- [85] K. Gorczowski, M. Styner, J.-Y. Jeong, J. S. Marron, J. Piven, H. C. Hazlett, S. M. Pizer, and G. Gerig, "Statistical Shape Analysis of Multi-Object Complexes," in *Computer Vision and Pattern Recognition, 2007. CVPR '07. IEEE Conference on*, pp. 1–8, June 2007.
- [86] B. Paniagua, A. Lyall, J. B. Berger, C. Vachet, R. M. Hamer, S. Woolson, W. Lin, J. Gilmore, and M. Styner, "Lateral Ventricle Morphology Analysis via Mean Latitude Axis," *Proc Soc Photo Opt Instrum Eng*, vol. 8672, Mar. 2013.
- [87] A. Elnakib, M. Casanova, G. Gimel'farb, A. El-Baz, and K. Suzuki, "Autism Diagnostics by 3D Shape Analysis of the Corpus Callosum," in *Machine Learning in Computer-Aided Diagnosis: Medical Imaging Intelligence and Analysis* (K. Suzuki, ed.), pp. 315–335, IGI Global, 2012.
- [88] A. Elnakib, M. Casanova, G. Gimel'farb, A. Switala, and A. El-Baz, "Dyslexia Diagnostics by 3D Shape Analysis of the Corpus Callosum," *Information Technology in Biomedicine, IEEE Transactions on*, vol. 16, no. 4, pp. 700–708, 2012.

- [89] A. Elnakib, A. El-Baz, M. Casanova, G. Gimel'farb, and A. Switala, "Image-Based Detection of Corpus Callosum Variability For More Accurate Discrimination Between Dyslexic And Normal Brains," in *Biomedical Imaging: From Nano to Macro, 2010 IEEE International Symposium on*, pp. 109–112, 2010.
- [90] A. Elnakib, A. El-Baz, M. Casanova, G. Gimel'farb, and A. Switala, "Image-Based Detection of Corpus Callosum Variability For More Accurate Discrimination Between Autistic And Normal Brains," in *Image Processing (ICIP), 2010 17th IEEE International Conference on*, pp. 4337–4340, 2010.
- [91] M. F. Casanova, A. El-Baz, A. Elnakib, J. Giedd, J. M. Rumsey, E. L. Williams, and A. E. Switala, "Corpus Callosum Shape Analysis with Application to Dyslexia," *Transl Neurosci*, vol. 1, pp. 124–130, June 2010.
- [92] M. F. Casanova, A. El-Baz, A. Elnakib, A. E. Switala, E. L. Williams, D. L. Williams, N. J. Minshew, and T. E. Conturo, "Quantitative Analysis of The Shape of The Corpus Callosum In Patients With Autism And Comparison Individuals," *Autism*, vol. 15, pp. 223–238, Mar. 2011.
- [93] A. El-Baz, A. Elnakib, M. Casanova, G. Gimelfarb, A. Switala, D. Jordan, and S. Rainey, "Accurate Automated Detection of Autism Related Corpus Callosum Abnormalities," *Journal of Medical Systems*, vol. 35, no. 5, pp. 929–939, 2011.
- [94] L. D. Griffin, "The Intrinsic Geometry of the Cerebral Cortex," *Journal of Theoretical Biology*, vol. 166, no. 3, pp. 261–273, 1994.
- [95] N. Khaneja, M. I. Miller, and U. Grenander, "Dynamic Programming Generation of Curves On Brain Surfaces," *IEEE Transactions on Pattern Analysis and Machine Intelligence*, vol. 20, pp. 1260–1265, Nov. 1998.

- [96] M. Berger and B. Gostiaux, *Differential Geometry: Manifolds and Curves and And Surfaces*. Graduate texts in mathematics, Springer-Verlag, 1988.
- [97] Y. Wang, B. S. Peterson, and L. H. Staib, "3D Brain Surface Matching Based On Geodesics And Local Geometry," *Computer Vision and Image Understanding*, vol. 89, no. 23, pp. 252 – 271, 2003.
- [98] J. Pastore, E. Moler, and V. Ballarin, "Segmentation of Brain Magnetic Resonance Images Through Morphological Operators And Geodesic Distance," *Digital Signal Processing*, vol. 15, no. 2, pp. 153–160, 2005.
- [99] A. Huang, R. Abugharbieh, R. Tam, and A. Trabousee, "MRI Brain Extraction with Combined Expectation Maximization and Geodesic Active Contours," in *Signal Processing and Information Technology, 2006 IEEE International Symposium on*, pp. 107–111, Aug. 2006.
- [100] W. Mio, J. C. Bowers, M. K. Hurdal, and X. Liu, "Modeling Brain Anatomy with 3D Arrangements of Curves," in *Computer Vision, 2007. ICCV 2007. IEEE 11th International Conference on*, pp. 1–8, Oct. 2007.
- [101] J. A. Butman and M. G. Linguraru, "Assessment of Ventricle Volume From Serial Mri Scans In Communicating Hydrocephalus," in *Biomedical Imaging: From Nano to Macro, 2008. ISBI 2008. 5th IEEE International Symposium on*, pp. 49–52, May 2008.
- [102] J. Hua, Z. Lai, M. Dong, X. Gu, and H. Qin, "Geodesic Distance-weighted Shape Vector Image Diffusion," *IEEE Transactions on Visualization and Computer Graphics*, vol. 14, pp. 1643–1650, Nov. 2008.
- [103] X. Liang and J. Zhang, "White Matter Integrity Analysis along Cingulum Paths in Mild Cognitive Impairment - A Geodesic Distance Approach," in *Bioinformatics and Biomed-*

- cal Engineering, 2008. ICBBE 2008. The 2nd International Conference on*, pp. 510–513, May 2008.
- [104] A. A. Joshi, D. W. Shattuck, H. Damasio, and R. M. Leahy, “Geodesic Curvature Flow On Surfaces For Automatic Sulcal Delineation,” in *Biomedical Imaging (ISBI), 2012 9th IEEE International Symposium on*, pp. 430–433, May 2012.
- [105] R. Kimmel and N. Kiryati, *Finding Shortest Paths On Surfaces By Fast Global Approximation And Precise Local Refinement*. Citeseer, 1994.
- [106] R. Kimmel, A. Amir, and A. M. Bruckstein, “Finding Shortest Paths On Surfaces Using Level Sets Propagation,” *IEEE Transactions on Pattern Analysis and Machine Intelligence*, vol. 17, no. 6, pp. 635–640, 1995.
- [107] R. Kimmel and J. A. Sethian, “Computing Geodesic Paths On Manifolds,” *Proceedings of the National Academy of Sciences*, vol. 95, no. 15, pp. 8431–8435, 1998.
- [108] E. Tripp, *The Meridian Handbook of Classical Mythology*. PENGUIN USA, 1974.
- [109] A. W. Toga and P. M. Thompson, “The Role of Image Registration In Brain Mapping,” *Image Vis Comput*, vol. 19, pp. 3–24, Jan 2001.
- [110] N. Duta, A. K. Jain, and M. P. Dubuisson-Jolly, “Learning 2D Shape Models,” in *Computer Vision and Pattern Recognition, 1999. IEEE Computer Society Conference on*, vol. 2, pp. 2 vol. (xxiii+637+663), 1999.
- [111] X. Penin, C. Berge, and M. Baylac, “Ontogenetic Study of The Skull In Modern Humans And The Common Chimpanzees: Neotenic Hypothesis Reconsidered With A Tridimensional Procrustes Analysis,” *American Journal of Physical Anthropology*, vol. 118, no. 1, pp. 50–62, 2002.

- [112] T. Bienvenu, F. Guy, W. Coudyzer, E. Gilissen, G. Roualdès, P. Vignaud, and M. Brunet, "Assessing Endocranial Variations In Great Apes And Humans Using 3D Data From Virtual Endocasts," *American Journal of Physical Anthropology*, vol. 145, no. 2, pp. 231–246, 2011.
- [113] N. Duta, A. K. Jain, and M. P. Dubuisson-Jolly, "Automatic Construction of 2D Shape Models," *IEEE Transactions on Pattern Analysis and Machine Intelligence*, vol. 23, no. 5, pp. 433–446, 2001.
- [114] T. McInerney and D. Terzopoulos, "Deformable Models In Medical Image Analysis," in *Mathematical Methods in Biomedical Image Analysis, 1996., Proceedings of the Workshop on*, pp. 171–180, June 1996.
- [115] C. Xu and J. L. Prince, "Snakes, Shapes, And Gradient Vector Flow," *Image Processing, IEEE Transactions on*, vol. 7, no. 3, pp. 359–369, 1998.
- [116] C. Xu and J. L. Prince, "Gradient Vector Flow Deformable Models," in *Handbook of Medical Imaging*, pp. 159–169, Academic Press: San Diego, CA, 2000.
- [117] C. Davatzikos, "Spatial Transformation and Registration of Brain Images Using Elastically Deformable Models," *Computer Vision and Image Understanding*, vol. 66, no. 2, pp. 207–222, 1997.
- [118] A. Dale, B. Fischl, and M. Sereno, "Cortical Surface-Based Analysis: I. Segmentation and Surface Reconstruction," *Neuroimage*, vol. 9, no. 2, pp. 179–194, 1999.
- [119] S. M. Smith, "Fast Robust Automated Brain Extraction," *Hum Brain Mapp*, vol. 17, pp. 143–155, Nov 2002.

- [120] A. H. Zhuang, D. J. Valentino, and A. W. Toga, "Skull-Stripping Magnetic Resonance Brain Images Using A Model-Based Level Set," *Neuroimage*, vol. 32, pp. 79–92, Aug 2006.
- [121] A. A. Joshi, D. W. Shattuck, P. M. Thompson, and R. M. Leahy, "Surface-Constrained Volumetric Brain Registration Using Harmonic Mappings," *Medical Imaging, IEEE Transactions on*, vol. 26, pp. 1657–1669, Dec. 2007.
- [122] Z. Tu, K. L. Narr, P. Dollar, I. DiNov, P. M. Thompson, and A. W. Toga, "Brain Anatomical Structure Segmentation by Hybrid Discriminative/Generative Models," *Medical Imaging, IEEE Transactions on*, vol. 27, pp. 495–508, April 2008.
- [123] A. Huang, R. Abugharbieh, and R. Tam, "A Hybrid Geometric Statistical Deformable Model for Automated 3D Segmentation in Brain MRI," *IEEE Transactions on Biomedical Engineering*, vol. 56, pp. 1838–1848, July 2009.
- [124] J. X. Liu, Y. S. Chen, and L. F. Chen, "Accurate And Robust Extraction of Brain Regions Using A Deformable Model Based On Radial Basis Functions," *Journal of Neuroscience Methods*, vol. 183, no. 2, pp. 255–266, 2009.
- [125] J. Li, X. Liu, J. Zhuo, R. P. Gullapalli, and J. M. Zara, "A Deformable Surface Model Based Automatic Rat Brain Extraction Method," in *Biomedical Imaging: From Nano to Macro, 2011 IEEE International Symposium on*, pp. 1741–1745, Apr. 2011.
- [126] A. Hashioka, S. Kobashi, K. Kuramoto, Y. Wakata, K. Ando, R. Ishikura, T. Ishikawa, S. Hirota, and Y. Hata, "Shape And Appearance Knowledge Based Brain Segmentation For Neonatal MR Images," in *World Automation Congress (WAC), 2012*, pp. 1–6, June 2012.

- [127] R. P. Woods, S. T. Grafton, C. J. Holmes, S. R. Cherry, and J. C. Mazziotta, "Automated image registration: I. General methods and intrasubject, intramodality validation," *J Comput Assist Tomogr*, vol. 22, no. 1, pp. 139–152, 1998.
- [128] R. P. Woods, S. T. Grafton, J. D. Watson, N. L. Sicotte, and J. C. Mazziotta, "Automated image registration: II. Intersubject validation of linear and nonlinear models," *J Comput Assist Tomogr*, vol. 22, no. 1, pp. 153–165, 1998.
- [129] D. Shen and C. Davatzikos, "HAMMER: Hierarchical Attribute Matching Mechanism For Elastic Registration," in *Mathematical Methods in Biomedical Image Analysis, 2001. MMBIA 2001. IEEE Workshop on*, pp. 29–36, 2001.
- [130] T. Liu, D. Shen, and C. Davatzikos, "Deformable Registration of Cortical Structures via Hybrid Volumetric And Surface Warping," *Neuroimage*, vol. 22, pp. 1790–1801, Aug. 2004.
- [131] G. Gerig, M. Styner, D. Jones, D. Weinberger, and J. Lieberman, "Shape Analysis of Brain Ventricles Using SPHARM," in *Mathematical Methods in Biomedical Image Analysis, 2001. MMBIA 2001 IEEE Workshop on*, pp. 171–178, 2001.
- [132] M. K. Chung, K. M. Dalton, and R. J. Davidson, "Encoding Neuroanatomical Information using Weighted Spherical Harmonic Representation," in *Statistical Signal Processing, 2007. SSP '07. IEEE/SP 14th Workshop on*, pp. 146–150, Aug. 2007.
- [133] A. Kelemen, G. Székely, and G. Gerig, "Elastic Model-Based Segmentation of 3D Neuroradiological Data Sets," *IEEE Transactions on Medical Imaging*, vol. 18, no. 10, pp. 828–839, 1999.
- [134] A. Uthama, R. Abugharbieh, A. Traboulsee, and M. J. McKeown, "Invariant SPHARM Shape Descriptors for Complex Geometry in MR Region of Interest Analysis," in *Engi-*

- neering in Medicine and Biology Society, 2007. EMBS 2007. 29th Annual International Conference of the IEEE*, pp. 1322–1325, Aug 2007.
- [135] A. Ben Abdallah, F. Ghorbel, H. Essabbah, and M. H. Bedoui, “Chapter 9: Shape Analysis of Left Ventricle Using Invariant 3D Spherical Harmonics Shape Descriptors,” in *Geometric Modeling and Imaging, 2008. GMAI 2008. 3rd International Conference on*, pp. 53–58, July 2008.
- [136] M. K. Chung, K. M. Dalton, and R. J. Davidson, “Tensor-Based Cortical Surface Morphometry via Weighted Spherical Harmonic Representation,” *Medical Imaging, IEEE Transactions on*, vol. 27, pp. 1143–1151, Aug. 2008.
- [137] A. Uthama, R. Abugharbieh, S. J. Palmer, A. Traboulsee, and M. J. McKeown, “SPHARM-Based Spatial fMRI Characterization With Intersubject Anatomical Variability Reduction,” *Selected Topics in Signal Processing, IEEE Journal of*, vol. 2, pp. 907–918, Dec 2008.
- [138] M. Esmail-Zadeh, H. Soltanian-Zadeh, and K. Jafari-Khouzani, “SPHARM-based Shape Analysis of Hippocampus For Lateralization In Mesial Temporal Lobe Epilepsy,” in *Electrical Engineering (ICEE), 2010 18th Iranian Conference on*, pp. 39–44, May 2010.
- [139] M. Nitzken, M. F. Casanova, G. Gimel’farb, F. Khalifa, A. Elnakib, A. E. Switala, and A. El-Baz, “3D Shape Analysis of The Brain Cortex With Application To Autism,” in *Biomedical Imaging: From Nano to Macro, 2011 IEEE International Symposium on*, pp. 1847–1850, Apr. 2011.
- [140] M. Nitzken, M. F. Casanova, G. Gimel’farb, A. Elnakib, F. Khalifa, A. Switala, and A. El-Baz, “3D Shape Analysis of The Brain Cortex With Application To Dyslexia,” in *Image*

- Processing (ICIP), 2011 18th IEEE International Conference on*, pp. 2657–2660, Sept. 2011.
- [141] X. Geng, T. J. Ross, H. Gu, W. Shin, W. Zhan, Y.-P. Chao, C.-P. Lin, N. Schuff, and Y. Yang, “Diffeomorphic Image Registration of Diffusion MRI Using Spherical Harmonics,” *Medical Imaging, IEEE Transactions on*, vol. 30, pp. 747–758, Mar. 2011.
- [142] H. Kim, T. Mansi, A. Bernasconi, and N. Bernasconi, “Vertex-Wise Shape Analysis of The Hippocampus: Disentangling Positional Differences From Volume Changes,” *Med Image Comput Comput Assist Interv*, vol. 14, no. Pt 2, pp. 352–359, 2011.
- [143] A. Hosseinbor, M. K. Chung, S. Schaefer, C. van Reekum, L. Peschke-Schmitz, M. Sutterer, A. L. Alexander, and R. J. Davidson, “4D Hyperspherical Harmonic (HyperSPHARM) Representation of Multiple Disconnected Brain Subcortical Structures,” in *Medical Image Computing and Computer Assisted Intervention (MICCAI), 2013 16th International Conference on*, Sept. 2013.
- [144] C. H. Brechbuhler, G. Gerig, and O. Kbler, “Parametrization of Closed Surfaces for 3D Shape Description,” *Computer Vision and Image Understanding*, vol. 61, no. 2, pp. 154–170, 1995.
- [145] M. Styner, I. Oguz, S. Xu, C. Brechbuhler, D. Pantazis, J. J. Levitt, M. E. Shenton, and G. Gerig, “Framework for the Statistical Shape Analysis of Brain Structures using SPHARM-PDM,” *Insight Journal*, vol. 1071, no. 1071, pp. 242–250, 2006.
- [146] M. Nitzken, M. Casanova, F. Khalifa, G. Sokhadze, and A. El-Baz, “Shape-Based Detection of Cortex Variability for More Accurate Discrimination Between Autistic and Normal Brains,” in *Multi Modality State-of-the-Art Medical Image Segmentation and Registration Methodologies* (A. S. El-Baz, R. Acharya U, A. F. Laine, and J. S. Suri, eds.), pp. 161–185, Springer New York, 2011.

- [147] A. Elnakib, M. Nitzken, M. Casanova, H. Park, G. Gimel'farb, and A. El-Baz, "Quantification of Age-Related Brain Cortex Change Using 3D Shape Analysis," in *Pattern Recognition (ICPR), 2012 21st International Conference on*, pp. 41–44, 2012.
- [148] E. L. Williams, A. El-Baz, M. Nitzken, A. E. Switala, and M. F. Casanova, "Spherical Harmonic Analysis of Cortical Complexity In Autism And Dyslexia," *Transl Neurosci*, vol. 3, pp. 36–40, Mar. 2012.
- [149] F. L. Bookstein, "'Voxel-based morphometry' should not be used with imperfectly registered images," *Neuroimage*, vol. 14, pp. 1454–1462, Dec. 2001.
- [150] U. Grenander and M. I. Miller, "Computational Anatomy: An Emerging Discipline," *Quarterly of Applied Mathematics*, vol. 56, no. 4, pp. 617–694, 1998.
- [151] M. Afzali and H. Soltanian-Zadeh, "Comparison of Voxel-Based Morphometry (VBM) And Tractography of Diffusion Tensor MRI (DT-MRI) In Temporal Lobe Epilepsy," in *Electrical Engineering (ICEE), 2010 18th Iranian Conference on*, pp. 18–23, 2010.
- [152] M. K. Chung, K. J. Worsley, and A. C. Evans, "Tensor-Based Brain Surface Modeling And Analysis," in *Computer Vision and Pattern Recognition, 2003. Proceedings. 2003 IEEE Computer Society Conference on*, vol. 1, pp. I–467–I–473 vol.1, 2003.
- [153] A. D. Leow, A. D. Klunder, C. R. Jack Jr, A. Toga, A. Dale, M. A. Bernstein, P. J. Britson, *et al.*, "Longitudinal Stability of MRI For Mapping Brain Change Using Tensor-Based Morphometry," *NeuroImage*, vol. 31, no. 2, pp. 627–640, 2006.
- [154] N. Lepore, C. Brun, Y. Y. Chou, M. C. Chiang, R. A. Dutton, K. M. Hayashi, E. Luders, O. L. Lopez, H. J. Aizenstein, A. W. Toga, J. T. Becker, and P. M. Thompson, "Generalized Tensor-Based Morphometry of HIV/AIDS Using Multivariate Statistics On Deformation Tensors," *IEEE Trans Med Imaging*, vol. 27, pp. 129–141, Jan. 2008.

- [155] Y. Wang, T. F. Chan, A. W. Toga, and P. M. Thompson, "Shape Analysis With Multivariate Tensor-Based Morphometry And Holomorphic Differentials," in *Computer Vision, 2009 IEEE 12th International Conference on*, pp. 2349–2356, 2009.
- [156] H. Yang, W. Liu, H. Xia, Z. Zhou, and L. Tong, "Longitudinal change of the grey matter of mild cognitive impairment patients over 3 years by using voxel-based morphometry," in *Biomedical Engineering and Informatics (BMEI), 2012 5th International Conference on*, pp. 304–308, 2012.
- [157] E. Fletcher, A. Knaack, B. Singh, E. Lloyd, E. Wu, O. Carmichael, and C. DeCarli, "Combining Boundary-Based Methods With Tensor-Based Morphometry in the Measurement of Longitudinal Brain Change," *Medical Imaging, IEEE Transactions on*, vol. 32, no. 2, pp. 223–236, 2013.
- [158] J. Shi, Y. Wang, R. Ceschin, X. An, M. D. Nelson, A. Panigrahy, and N. Lepore, "Surface Fluid Registration And Multivariate Tensor-Based Morphometry In Newborns - The Effects of Prematurity On The Putamen," in *Signal Information Processing Association Annual Summit and Conference (APSIPA ASC), 2012 Asia-Pacific*, pp. 1–8, 2012.
- [159] J. Ashburner and K. J. Friston, "Why Voxel-Based Morphometry Should Be Used," *NeuroImage*, vol. 14, no. 6, pp. 1238–1243, 2001.
- [160] Q. He, Y. Duan, J. Miles, and N. Takahashi, "Statistical Shape Analysis of the Corpus Callosum in Subtypes of Autism," in *Bioinformatics and Bioengineering, 2007. BIBE 2007. Proceedings of the 7th IEEE International Conference on*, pp. 1087–1091, Oct. 2007.
- [161] A. El-Baz, M. F. Casanova, G. Gimel'farb, M. Mott, and A. E. Switala, "Autism Diagnostics By 3D Texture Analysis of Cerebral White Matter Gyrifications," *Med Image Comput Comput Assist Interv*, vol. 10, no. Pt 2, pp. 882–890, 2007.

- [162] J. Cates, P. T. Fletcher, M. Styner, M. Shenton, and R. Whitaker, "Shape Modeling And Analysis With Entropy-Based Particle Systems," *Inf Process Med Imaging*, vol. 20, pp. 333–345, 2007.
- [163] T. Geraud, J. . F. Mangin, I. Bloch, and H. Maitre, "Segmenting Internal Structures In 3D MR Images of The Brain By Markovian Relaxation On A Watershed Based Adjacency Graph," in *Image Processing, 1995. Proceedings., International Conference on*, vol. 3, pp. 548–551vol.3, Oct. 1995.
- [164] F. Yang and F. Kruggel, "Optimization Algorithms for Labeling Brain Sulci Based on Graph Matching," in *Computer Vision, 2007. ICCV 2007. IEEE 11th International Conference on*, pp. 1–7, Oct. 2007.
- [165] S. S. Long and L. B. Holder, "Graph Based MRI Brain Scan Classification And Correlation Discovery," in *Computational Intelligence in Bioinformatics and Computational Biology (CIBCB), 2012 IEEE Symposium on*, pp. 335–342, May 2012.
- [166] K. Yamaguchi, S. Kobashi, I. Mohri, S. Imawaki, M. Taniike, and Y. Hata, "Brain Shape Homologous Modeling Using Sulcal-Distribution Index In MR Images," in *Systems, Man and Cybernetics, 2009. SMC 2009. IEEE International Conference on*, pp. 1102–1106, Oct 2009.
- [167] K. Yamaguchi, S. Kobashi, K. Kuramoto, Y. T. Kitamura, S. Imawaki, and Y. Hata, "Statistical Quantification of Brain Shape Deformation With Homologous Brain Shape Modeling," in *World Automation Congress (WAC), 2010*, pp. 1–6, Sept 2010.
- [168] S. Angenent, S. Haker, A. Tannenbaum, and R. Kikinis, "On the Laplace-Beltrami Operator And Brain Surface Flattening," *Medical Imaging, IEEE Transactions on*, vol. 18, pp. 700–711, Aug. 1999.

- [169] R. Lai, Y. Shi, N. Sicotte, and A. W. Toga, "Automated Corpus Callosum Extraction via Laplace-Beltrami Nodal Parcellation And Intrinsic Geodesic Curvature Flows On Surfaces," in *Computer Vision (ICCV), 2011 IEEE International Conference on*, pp. 2034–2040, Nov. 2011.
- [170] R. Shishegar, H. Soltanian-Zadeh, and S. R. Moghadasi, "Hippocampal Shape Analysis In Epilepsy Using Laplace-Beltrami Spectrum," in *Electrical Engineering (ICEE), 2011 19th Iranian Conference on*, p. 1, May 2011.
- [171] D. Germanaud, J. Lefevre, R. Toro, C. Fischer, J. Dubois, L. Hertz-Pannier, and J. F. Mangin, "Larger is twistier: spectral analysis of gyrification (SPANGY) applied to adult brain size polymorphism," *Neuroimage*, vol. 63, pp. 1257–1272, Nov. 2012.
- [172] M. Makram, H. Kamel, and M. Emna, "3D Elastic Registration Using A Balanced Multi Resolution Reeb Graph : Application For A Detection of A Maxilla Facial Malformation," in *Computer and Communication Engineering, 2008. ICCCE 2008. International Conference on*, pp. 1063–1071, May 2008.
- [173] Y. Shi, R. Lai, and A. Toga, "Cortical Surface Reconstruction via Unified Reeb Analysis of Geometric and Topological Outliers in Magnetic Resonance Images," *Medical Imaging, IEEE Transactions on*, vol. PP, no. 99, p. 1, 2012.
- [174] H. Lombaert, L. Grady, J. R. Polimeni, and F. Chriet, "Fast Brain Matching With Spectral Correspondence," *Inf Process Med Imaging*, vol. 22, pp. 660–673, 2011.
- [175] H. Lombaert, L. Grady, J. R. Polimeni, and F. Chriet, "FOCUSR: Feature Oriented Correspondence Using Spectral Regularization—A Method for Precise Surface Matching," *IEEE Trans Pattern Anal Mach Intell*, vol. 35, pp. 2143–2160, Sept. 2013.

- [176] S. Prima, S. Ourselin, and N. Ayache, "Computation of The Mid-Sagittal Plane In 3D Brain Images," *Medical Imaging, IEEE Transactions on*, vol. 21, pp. 122–138, Feb. 2002.
- [177] S. Gefen, Y. Fan, L. Bertrand, and J. Nissano, "Symmetry-based 3D Brain Reconstruction," in *Biomedical Imaging: Nano to Macro, 2004. IEEE International Symposium on*, pp. 744–747 Vol. 1, Apr. 2004.
- [178] X. Liu, C. Imielinska, A. F. Laine, and A. D'Ambrosio, "Symmetry Based Multi-modality Registration of the Brain Imagery," in *Signal Processing and Information Technology, 2007 IEEE International Symposium on*, pp. 807–812, Dec. 2007.
- [179] J. Feng, F. Desheng, and B. Shuoben, "Brain Image Segmentation Based on Bilateral Symmetry Information," in *Bioinformatics and Biomedical Engineering, 2008. ICBBE 2008. The 2nd International Conference on*, pp. 1951–1954, May 2008.
- [180] M. Fournier, B. Combes, N. Roberts, S. Keller, T. J. Crow, W. D. Hopkins, and S. Prima, "Surface-Based Method To Evaluate Global Brain Shape Asymmetries In Human And Chimpanzee Brains," in *Biomedical Imaging: From Nano to Macro, 2011 IEEE International Symposium on*, pp. 310–316, 30 2011-April 2 2011.
- [181] G. T. Herman, M. I. Kohn, and R. E. Gur, "Computerized Three-Dimensional Volume Analysis From Magnetic Resonance Images For Characterization of Brain Disorders," in *Biomedical Engineering., Proceedings of a Special Symposium on Maturing Technologies and Emerging Horizons in*, pp. 65–67, Nov. 1988.
- [182] G. Wagenknecht and S. Winter, "Volume-of-Interest Segmentation of Cortical Regions For Multimodal Brain Analysis," in *Nuclear Science Symposium Conference Record, 2008. NSS '08. IEEE*, pp. 4368–4372, Oct. 2008.

- [183] M. F. Casanova, A. El-Baz, M. Mott, G. Mannheim, H. Hassan, R. Fahmi, J. Giedd, J. M. Rumsey, A. E. Switala, and A. Farag, "Reduced Gyral Window And Corpus Callosum Size In Autism: Possible Macroscopic Correlates of A Minicolumnopathy," *J Autism Dev Disord*, vol. 39, pp. 751–764, May 2009.
- [184] M. F. Casanova, A. S. El-Baz, J. Giedd, J. M. Rumsey, and A. E. Switala, "Increased White Matter Gyral Depth In Dyslexia: Implications For Corticocortical Connectivity," *J Autism Dev Disord*, vol. 40, pp. 21–29, Jan. 2010.
- [185] A. El-Baz, M. Casanova, G. Gimel'farb, M. Mott, A. Switala, E. Vanbogaert, and R. McCracken, "A New CAD System For Early Diagnosis of Dyslexic Brains," in *Image Processing, 2008. ICIP 2008. 15th IEEE International Conference on*, pp. 1820–1823, 2008.
- [186] A. El-Baz, M. Casanova, G. Gimel'farb, M. Mott, A. Switala, E. Vanbogaert, and R. McCracken, "Dyslexia Diagnostics By 3D Texture Analysis of Cerebral White Matter Gyri-fications," in *Pattern Recognition, 2008. ICPR 2008. 19th International Conference on*, pp. 1–4, 2008.
- [187] A. El-Baz, M. Casanova, G. Gimel'farb, M. Mott, and A. Switwala, "A New Image Analysis Approach For Automatic Classification of Autistic Brains," in *Biomedical Imaging: From Nano to Macro, 2007. ISBI 2007. 4th IEEE International Symposium on*, pp. 352–355, 2007.
- [188] A. El-Baz, M. Casanova, G. Gimelfarb, M. Mott, and A. Switala, "An MRI-Based Diagnostic Framework For Early Diagnosis of Dyslexia," *International Journal of Computer Assisted Radiology and Surgery*, vol. 3, no. 3-4, pp. 181–189, 2008.
- [189] R. Fahmi, A. El-Baz, H. Abd El Munim, A. Farag, and M. Casanova, "Classification Techniques For Autistic Vs. Typically Developing Brain Using MRI Data," in *Biomedical*

- Imaging: From Nano to Macro, 2007. ISBI 2007. 4th IEEE International Symposium on*, pp. 1348–1351, 2007.
- [190] H. Doraiswamy and V. Natarajan, “Efficient algorithms for computing Reeb graphs,” *Computational Geometry*, vol. 42, no. 67, pp. 606–616, 2009.
- [191] M. Reuter, F.-E. Wolter, and N. Peinecke, “Laplace-Spectra As Fingerprints For Shape Matching,” in *Proceedings of the 2005 ACM symposium on Solid and physical modeling*, SPM '05, (New York, NY, USA), pp. 101–106, ACM, 2005.
- [192] M. Reuter, F.-E. Wolter, and N. Peinecke, “Laplace-Beltrami Spectra as Shape-DNA of Surfaces And Solids,” *Computer-Aided Design*, vol. 38, no. 4, pp. 342–366, 2006.
- [193] R. M. Rustomov, “Laplace-Beltrami Eigenfunctions For Deformation Invariant Shape Representation,” in *Proceedings of the fifth Eurographics symposium on Geometry processing*, SGP '07, (Aire-la-Ville, Switzerland, Switzerland), pp. 225–233, Eurographics Association, 2007.
- [194] C. Bouman and K. Sauer, “A generalized Gaussian image model for edge-preserving MAP estimation,” *IEEE Transactions on Image Processing*, vol. 2, no. 3, pp. 296–310, 1993.
- [195] N. J. Tustison, B. B. Avants, *et al.*, “N4ITK: improved N3 bias correction,” *IEEE Transactions on Medical Imaging*, vol. 29, no. 6, pp. 1310–1320, 2010.
- [196] J. Besag, “On the statistical analysis of dirty pictures,” *Journal of the Royal Statistical Society. Series B (Methodological)*, pp. 259–302, 1986.
- [197] M. Jenkinson, C. F. Beckmann, T. E. Behrens, M. W. Woolrich, and S. M. Smith, “FSL,” *Neuroimage*, vol. 62, pp. 782–790, Aug. 2012.

- [198] S. M. Smith, M. Jenkinson, M. W. Woolrich, C. F. Beckmann, T. E. Behrens, H. Johansen-Berg, P. R. Bannister, M. De Luca, I. Drobnjak, D. E. Flitney, R. K. Niazzy, J. Saunders, J. Vickers, Y. Zhang, N. De Stefano, J. M. Brady, and P. M. Matthews, "Advances in functional and structural MR image analysis and implementation as FSL," *Neuroimage*, vol. 23 Suppl 1, pp. S208–219, 2004.
- [199] M. W. Woolrich, S. Jbabdi, B. Patenaude, M. Chappell, S. Makni, T. Behrens, C. Beckmann, M. Jenkinson, and S. M. Smith, "Bayesian analysis of neuroimaging data in FSL," *Neuroimage*, vol. 45, pp. S173–186, Mar. 2009.
- [200] D. Adalsteinsson, *A fast level set method for propagating interfaces*. PhD thesis, Cite-seer, 1994.
- [201] A. El-Baz, A. Elnakib, F. Khalifa, M. A. El-Ghar, P. McClure, A. Soliman, and G. Gimelfarb, "Precise segmentation of 3-D magnetic resonance angiography," *IEEE Transactions on Biomedical Engineering*, vol. 59, no. 7, pp. 2019–2029, 2012.
- [202] A. Farag, A. El-Baz, and G. Gimelfarb, "Precise segmentation of multimodal images," *IEEE Transactions on Image Processing*, vol. 15, no. 4, pp. 952–968, 2006.
- [203] A. El-Baz, *Novel stochastic models for medical image analysis*. PhD thesis, University of Louisville, Louisville, KY, USA, 2006.
- [204] D. W. Shattuck and R. M. Leahy, "Brainsuite: an automated cortical surface identification tool," *Medical image analysis*, vol. 6, no. 2, pp. 129–142, 2002.
- [205] D. W. Shattuck and R. M. Leahy, "Automated graph-based analysis and correction of cortical volume topology," *Medical Imaging, IEEE Transactions on*, vol. 20, no. 11, pp. 1167–1177, 2001.

- [206] D. W. Shattuck, S. R. Sandor-Leahy, K. A. Schaper, D. A. Rottenberg, and R. M. Leahy, "Magnetic resonance image tissue classification using a partial volume model," *NeuroImage*, vol. 13, no. 5, pp. 856–876, 2001.
- [207] S. Sandor and R. Leahy, "Surface-based labeling of cortical anatomy using a deformable atlas," *IEEE Trans Med Imaging*, vol. 16, pp. 41–54, Feb. 1997.
- [208] R. P. Woods, S. T. Grafton, J. D. Watson, N. L. Sicotte, and J. C. Mazziotta, "Automated image registration: II. intersubject validation of linear and nonlinear models," *Journal of computer assisted tomography*, vol. 22, no. 1, pp. 153–165, 1998.
- [209] R. P. Woods, S. T. Grafton, C. J. Holmes, S. R. Cherry, and J. C. Mazziotta, "Automated image registration: I. general methods and intrasubject, intramodality validation," *Journal of computer assisted tomography*, vol. 22, no. 1, pp. 139–152, 1998.
- [210] S. Geman and D. Geman, "Stochastic relaxation, gibbs distributions, and the Bayesian restoration of images," *Pattern Analysis and Machine Intelligence, IEEE Transactions on*, vol. PAMI-6, no. 6, pp. 721–741, 1984.
- [211] T. Poggio, V. Torre, and C. Koch, "Computational vision and regularization theory," *Nature*, vol. 317, no. 6035, pp. 314–319, 1985.
- [212] J. Besag, "On the Statistical Analysis of Dirty Pictures," *Journal of the Royal Statistical Society. Series B (Methodological)*, vol. 48, no. 3, pp. 259–302, 1986.
- [213] R. Chellappa, *Markov random fields : theory and application*. Boston: Academic Press, 1993.
- [214] S. Z. Li, *Markov Random Field Modeling in Computer Vision*. Secaucus, NJ, USA: Springer-Verlag New York, Inc., 1995.

- [215] G. Gimel'farb, *Image Textures and Gibbs Random Fields*. Kluwer Academic Publishers, 1999.
- [216] G.-H. Shi, "Manifold method of material analysis," tech. rep., DTIC Document, 1992.
- [217] Y.-L. Yang, Y.-J. Yang, H. Pottmann, and N. J. Mitra, "Shape space exploration of constrained meshes," *ACM Trans. Graph.*, vol. 30, no. 6, p. 124, 2011.
- [218] M. H. Freedman and F. Quinn, "Topology of 4-manifolds, volume 39 of princeton mathematical series," 1990.
- [219] V. Guillemin and A. Pollack, *Differential topology*, vol. 370. American Mathematical Soc., 2010.
- [220] R. Fisher, S. Perkins, A. Walker, and E. Wolfart, "Connected component labeling," *website: <http://homepages.inf.ed.ac.uk/rbf/HIPR2/label.htm>*, 2003.
- [221] Q. Fang and D. A. Boas, "Tetrahedral mesh generation from volumetric binary and grayscale images," in *Biomedical Imaging: From Nano to Macro, 2009. ISBI'09. IEEE International Symposium on*, pp. 1142–1145, IEEE, 2009.
- [222] Q. Fang, S. A. Carp, J. Selb, R. Moore, D. B. Kopans, E. L. Miller, D. H. Brooks, and D. A. Boas, "A multi-modality image reconstruction platform for diffuse optical tomography," in *Biomedical optics*, p. BMD24, Optical Society of America, 2008.
- [223] "CGAL, Computational Geometry Algorithms Library." <http://www.cgal.org>.
- [224] J. Murray and W. Van Ryper, "Wavefront obj file format summary," 2005.
- [225] G. A. Hansen, R. W. Douglass, and A. Zardecki, *Mesh enhancement: selected elliptic methods, foundations and applications*. Imperial College Press, 2005.

- [226] M. Desbrun, M. Meyer, P. Schröder, and A. H. Barr, "Implicit fairing of irregular meshes using diffusion and curvature flow," in *Proceedings of the 26th annual conference on Computer graphics and interactive techniques*, pp. 317–324, ACM Press/Addison-Wesley Publishing Co., 1999.
- [227] S. Rusinkiewicz, "Estimating curvatures and their derivatives on triangle meshes," in *3D Data Processing, Visualization and Transmission, 2004. 3DPVT 2004. Proceedings. 2nd International Symposium on*, pp. 486–493, IEEE, 2004.
- [228] Y. Ohtake, A. Belyaev, and H.-P. Seidel, "Ridge-valley lines on meshes via implicit surface fitting," in *ACM Transactions on Graphics (TOG)*, vol. 23, pp. 609–612, ACM, 2004.
- [229] M. K. Chung, K. M. Dalton, and R. J. Davidson, "Tensor-based cortical surface morphology via weighted spherical harmonic representation," *Medical Imaging, IEEE Transactions on*, vol. 27, no. 8, pp. 1143–1151, 2008.
- [230] M. K. Chung, K. M. Dalton, L. Shen, A. C. Evans, and R. J. Davidson, "Weighted fourier series representation and its application to quantifying the amount of gray matter," *Medical Imaging, IEEE Transactions on*, vol. 26, no. 4, pp. 566–581, 2007.
- [231] R. Courant and D. Hilbert, *Methods of Mathematical Physics*, vol. 63. Interscience, New York, 1953.
- [232] W. M. Wells III, P. Viola, H. Atsumi, S. Nakajima, and R. Kikinis, "Multi-modal volume registration by maximization of mutual information," *Medical image analysis*, vol. 1, no. 1, pp. 35–51, 1996.
- [233] O. Bottema and B. Roth, *Theoretical kinematics*. Courier Dover Publications, 2011.
- [234] J. M. McCarthy, *Introduction to theoretical kinematics*. MIT press, 1990.

- [235] C. E. Shannon, "A mathematical theory of communication," *ACM SIGMOBILE Mobile Computing and Communications Review*, vol. 5, no. 1, pp. 3–55, 2001.
- [236] M. S. Hassouna and A. A. Farag, "Multistencils fast marching methods: A highly accurate solution to the eikonal equation on cartesian domains," *IEEE Transactions on Pattern Analysis and Machine Intelligence*, vol. 29, no. 9, pp. 1563–1574, 2007.
- [237] L. Shen, H. Huang, F. Makedon, and A. J. Saykin, "Efficient registration of 3d spharm surfaces," in *Computer and Robot Vision, 2007. CRV'07. Fourth Canadian Conference on*, pp. 81–88, IEEE, 2007.
- [238] M. K. Chung, R. Hartley, K. Dalton, and R. J. Davidson, "Encoding cortical surface by spherical harmonics," *Statistica Sinica*, vol. 18, no. 4, p. 1269, 2008.
- [239] E. Abbena, S. Salamon, and A. Gray, *Modern Differential Geometry of Curves and Surfaces with Mathematica*. CRC press, 2006.
- [240] E. S. Pearson, W. S. Gosset, R. L. Plackett, and G. A. Barnard, *Student: a statistical biography of William Sealy Gosset*. Oxford University Press, USA, 1990.
- [241] I. R. Porteous, *Geometric differentiation: for the intelligence of curves and surfaces*. Cambridge University Press, 2001.
- [242] D. Lloyd, "Terra cognita: From functional neuroimaging to the map of the mind," *Brain and Mind*, vol. 1, no. 1, pp. 93–116, 2000.
- [243] D. Lloyd, "Functional mri and the study of human consciousness," *Journal of Cognitive Neuroscience*, vol. 14, no. 6, pp. 818–831, 2002.
- [244] D. Lloyd, "Through a glass darkly: Schizophrenia and functional brain imaging," *Philosophy, Psychiatry, & Psychology*, vol. 18, no. 4, pp. 257–274, 2011.

- [245] K. R. Pugh, W. E. Mencl, A. R. Jenner, L. Katz, S. J. Frost, J. R. Lee, S. E. Shaywitz, and B. A. Shaywitz, "Functional neuroimaging studies of reading and reading disability(developmental dyslexia)," *Mental Retardation and Developmental Disabilities Research Reviews*, vol. 6, no. 3, pp. 207–213, 2000.
- [246] G. Lyon, S. Shaywitz, and B. Shaywitz, "A definition of dyslexia," *Annals of Dyslexia*, vol. 53, no. 1, pp. 1–14, 2003.
- [247] S. Eliez, J. M. Rumsey, J. N. Giedd, J. E. Schmitt, A. J. Patwardhan, and A. L. Reiss, "Morphological alteration of temporal lobe gray matter in dyslexia: an MRI study," *Journal of Child Psychology and Psychiatry*, vol. 41, no. 5, pp. 637–644, 2000.
- [248] M. F. Casanova, J. Araque, J. Giedd, and J. M. Rumsey, "Reduced brain size and gyrification in the brains of dyslexic patients," *Journal of Child Neurology*, vol. 19, no. 4, pp. 275–281, 2004.
- [249] F. Richlan, M. Kronbichler, and H. Wimmer, "Structural abnormalities in the dyslexic brain: A meta-analysis of voxel-based morphometry studies," *Human Brain Mapping*, vol. 34, no. 11, pp. 3055–3065, 2013.
- [250] A. J. Krafnick, D. L. Flowers, M. M. Luetje, E. M. Napoliello, and G. F. Eden, "An investigation into the origin of anatomical differences in dyslexia," *The Journal of Neuroscience*, vol. 34, no. 3, pp. 901–908, 2014.
- [251] G. Silani, U. Frith, J.-F. Demonet, F. Fazio, D. Perani, C. Price, C. Frith, and E. Paulesu, "Brain abnormalities underlying altered activation in dyslexia: a voxel based morphometry study," *Brain*, vol. 128, no. 10, pp. 2453–2461, 2005.
- [252] T. Klingberg, M. Hedehus, E. Temple, T. Salz, J. D. Gabrieli, M. E. Moseley, and R. A. Poldrack, "Microstructure of temporo-parietal white matter as a basis for reading ability:

- evidence from diffusion tensor magnetic resonance imaging,” *Neuron*, vol. 25, no. 2, pp. 493–500, 2000.
- [253] S. N. Niogi and B. D. McCandliss, “Left lateralized white matter microstructure accounts for individual differences in reading ability and disability,” *Neuropsychologia*, vol. 44, no. 11, pp. 2178–2188, 2006.
- [254] A. Elnakib, A. El-Baz, M. F. Casanova, G. Gimel’farb, and A. E. Switala, “Image-based detection of corpus callosum variability for more accurate discrimination between dyslexic and normal brains,” in *2010 IEEE International Symposium on Biomedical Imaging: From Nano to Macro (ISBI’10)*, pp. 109–112, IEEE, 2010.
- [255] K. von Plessen, A. Lundervold, N. Duta, E. Heiervang, F. Klauschen, A. I. Smievoll, L. Ersland, and K. Hugdahl, “Less developed corpus callosum in dyslexic subjects: a structural MRI study,” *Neuropsychologia*, vol. 40, no. 7, pp. 1035–1044, 2002.
- [256] V. S. Fonov, A. C. Evans, K. Botteron, C. R. Almli, R. C. McKinstry, and D. L. Collins, “Unbiased average age-appropriate atlases for pediatric studies,” *NeuroImage*, vol. 54, no. 1, pp. 313–327, 2011.
- [257] V. S. Fonov, A. C. Evans, R. McKinstry, C. Almli, and D. Collins, “Unbiased nonlinear average age-appropriate brain templates from birth to adulthood,” *NeuroImage*, vol. 47, p. S102, 2009.
- [258] J. Talan, “A new theory and brain areas implicated to explain dyslexia,” *Neurology Today*, vol. 14, no. 3, pp. 12–13, 2014.
- [259] A. Association *et al.*, “2014 alzheimer’s disease facts and figures,” *Alzheimer’s & Dementia*, vol. 10, no. 2, pp. e47–e92, 2014.

- [260] M. A. Balafar, A. R. Ramli, M. I. Saripan, and S. Mashohor, "Review of brain mri image segmentation methods," *Artificial Intelligence Review*, vol. 33, no. 3, pp. 261–274, 2010.
- [261] H. K. Weir, M. J. Thun, B. F. Hankey, L. A. Ries, H. L. Howe, P. A. Wingo, A. Jemal, E. Ward, R. N. Anderson, and B. K. Edwards, "Annual report to the nation on the status of cancer, 1975–2000, featuring the uses of surveillance data for cancer prevention and control," *Journal of the National Cancer Institute*, vol. 95, no. 17, pp. 1276–1299, 2003.
- [262] A. P. Reeves, A. B. Chan, D. F. Yankelevitz, C. I. Henschke, B. Kressler, and W. J. Kostis, "On measuring the change in size of pulmonary nodules," *Medical Imaging, IEEE Transactions on*, vol. 25, no. 4, pp. 435–450, 2006.
- [263] A. Alansary, A. Soliman, M. Nitzken, F. Khalifa, A. Elnakib, M. Mostapha, M. Casanova, and A. El-Baz, "An integrated geometrical and stochastic approach for accurate infant brain extraction," in *Image Processing (ICIP), 2014 IEEE International Conference on*, pp. 3542–3546, IEEE, 2014.
- [264] B. Dombroski, M. Nitzken, A. Elnakib, F. Khalifa, A. El-Baz, and M. F. Casanova, "Cortical surface complexity in a population-based normative sample," *Translational Neuroscience*, vol. 5, no. 1, pp. 17–24, 2014.
- [265] A. Elnakib, A. Soliman, M. Nitzken, M. F. Casanova, G. Gimel'farb, and A. El-Baz, "Magnetic resonance imaging findings for dyslexia: A review," *Journal of Biomedical Nanotechnology*, vol. 10, no. 10, pp. 2778–2805, 2014.
- [266] M. Mostapha, A. Alansary, A. Soliman, F. Khalifa, M. Nitzken, R. Khodeir, M. F. Casanova, and A. El-Baz, "Atlas-based approach for the segmentation of infant dti mr brain images," in *Biomedical Imaging (ISBI), 2014 IEEE 11th International Symposium on*, pp. 1255–1258, IEEE, 2014.

- [267] M. Mostapha, A. Soliman, F. Khalifa, A. Elnakib, A. Alansary, M. Nitzken, M. F. Casanova, and A. El-Baz, "A statistical framework for the classification of infant dt images," in *Image Processing (ICIP), 2014 IEEE International Conference on*, pp. 2222–2226, IEEE, 2014.
- [268] M. J. Nitzken, M. F. Casanova, and A. El-Baz, "Spharm analysis of the brain cortex for diagnosing dyslexia," in *Biomedical Imaging (ISBI), 2014 IEEE 11th International Symposium on*, (Beijing, China), IEEE, Apr. 2014.
- [269] M. J. Nitzken, M. F. Casanova, G. Gimelfarb, T. Inanc, J. M. Zurada, and A. El-Baz, "Shape analysis of the human brain: a brief survey.," *IEEE journal of biomedical and health informatics*, vol. 18, no. 4, pp. 1337–1354, 2014.
- [270] A. Alansary, A. Soliman, F. Khalifa, A. Elnakib, M. Mostapha, M. Nitzken, M. Casanova, and A. El-Baz, "MAP-based framework for segmentation of mr brain images based on visual appearance and prior shape," *MIDAS J*, vol. 1, p. 1, 2013.
- [271] M. Nitzken, N. Bajaj, S. Aslan, G. Gimel'farb, A. El-Baz, and A. Ovechkin, "Local wavelet-based filtering of electromyographic signals to eliminate the electrocardiographic-induced artifacts in patients with spinal cord injury," *Journal of biomedical science and engineering*, vol. 6, no. 7B, pp. 1–10, 2013.
- [272] A. Elnakib, M. Nitzken, M. Casanova, H. Park, G. Gimel'farb, and A. El-Baz, "Quantification of age-related brain cortex change using 3D shape analysis," in *Pattern Recognition (ICPR), 2012 21st International Conference on*, pp. 41–44, IEEE, 2012.
- [273] E. L. Williams, A. El-Baz, M. Nitzken, A. E. Switala, and M. F. Casanova, "Spherical harmonic analysis of cortical complexity in autism and dyslexia," *Translational Neuroscience*, vol. 3, no. 1, pp. 36–40, 2012.

- [274] A. El-Baz, M. Nitzken, A. Elnakib, F. Khalifa, G. Gimel'farb, R. Falk, and M. A. El-Ghar, "3D shape analysis for early diagnosis of malignant lung nodules," in *Proceedings of International Conference Medical Image Computing and Computer-Assisted Intervention, (MICCAI'11)*, (Toronto, Canada, September 18–22), pp. 175–182, 2011.
- [275] A. El-Baz, M. Nitzken, G. Gimelfarb, E. Van Bogaert, R. Falk, M. A. El-Ghar, and J. Suri, "Three-dimensional shape analysis using spherical harmonics for early assessment of detected lung nodules," in *Lung Imaging and Computer Aided Diagnosis*, ch. 19, pp. 421–438, chapter, 2011.
- [276] A. El-Baz, M. Nitzken, F. Khalifa, A. Elnakib, G. Gimel'farb, R. Falk, and M. A. El-Ghar, "3D shape analysis for early diagnosis of malignant lung nodules," in *Proceedings of International Conference on Information Processing in Medical Imaging, (IPMI'11)*, (Monastery Irsee, Germany (Bavaria), July 3–8), pp. 772–783, 2011.
- [277] A. El-Baz, M. Nitzken, E. Vanbogaert, G. Gimel'Farb, R. Falk, and M. Abo El-Ghar, "A novel shape-based diagnostic approach for early diagnosis of lung nodules," in *Biomedical Imaging: From Nano to Macro, 2011 IEEE International Symposium on*, pp. 137–140, IEEE, 2011.
- [278] M. Kondapaneni, M. Nitzken, E. Bogaert, G. Gimelfarb, R. Falk, M. A. El-Ghar, and A. El-Baz, "A novel shape-based diagnostic approach for early diagnosis of lung nodules," *CHEST Journal*, vol. 140, no. 4_MeetingAbstracts, pp. 655A–655A, 2011.
- [279] M. Nitzken, M. Casanova, G. Gimel'farb, A. Elnakib, F. Khalifa, A. Switala, and A. El-Baz, "3D shape analysis of the brain cortex with application to dyslexia," in *Image Processing (ICIP), 2011 18th IEEE International Conference on*, (Brussels, Belgium), pp. 2657–2660, IEEE, Sept. 2011. (Selected for oral presentation. Oral acceptance rate is 10 percent and the overall acceptance rate is 35 percent).

- [280] M. Nitzken, M. Casanova, G. Gimel'farb, F. Khalifa, A. Elnakib, A. E. Switala, and A. El-Baz, "3D shape analysis of the brain cortex with application to autism," in *Biomedical Imaging: From Nano to Macro, 2011 IEEE International Symposium on*, (Chicago, Illinois, USA), pp. 1847–1850, IEEE, Mar. 2011.
- [281] M. Nitzken, M. F. Casanova, F. Khalifa, G. Sokhadze, and A. El-Baz, "Shape-based detection of cortex variability for more accurate discrimination between autistic and normal brains," in *Handbook of Multi-Modality State-of-the-Art Medical Image Segmentation and Registration Methodologies* (A. El-Baz, R. Acharya, A. Laine, and J. Suri, eds.), vol. 2, ch. 7, pp. 161–185, New York: Springer Verlag, Mar. 2011.

APPENDICES

Appendix 1 - ASD+ Example Risk Analysis Report

Example risk analysis report constructed for an individual diagnosed with autism spectrum disorder.



Breakthrough Medical Diagnostics for a Modern World

Analysis Report

Report Summary

Generated on: 20-May-2014

(c) NeuroAtlas, LLC. 2014

Name: Demo Subject - ASD

Age: 8 months

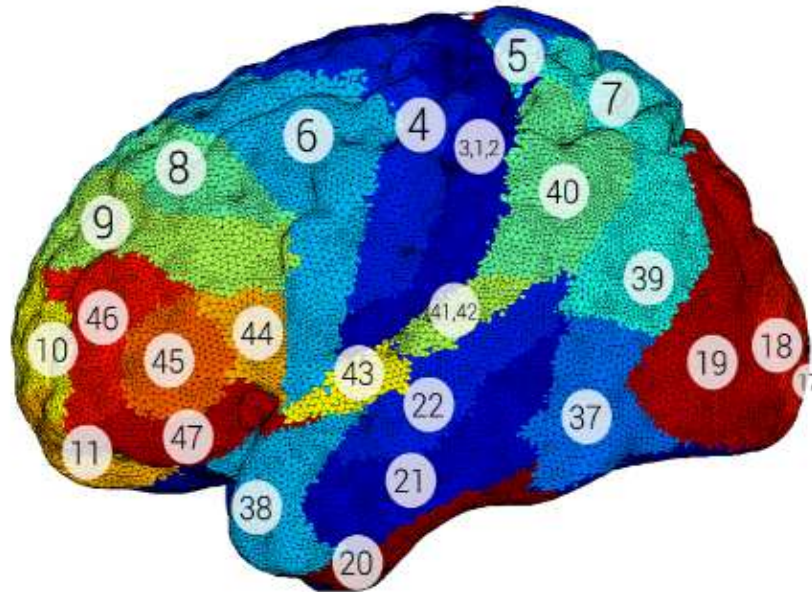
Physician: Dr. J. Doe

Overall Trend



Disclaimer: The medical information in this report is provided as an information resource only, and is not to be used or relied on for any diagnostic or treatment purposes. This information is intended solely for patient education and should not be used as a substitute for professional diagnosis and treatment.

Regional Analysis



Areas 1, 2 & 3 (also called 3, 1, 2)
Primary Somatosensory Cortex

The primary somatosensory cortex is the main sensory receptive area for the sense of touch. Like other sensory Area, there is a map of sensory space in this location, called the sensory homunculus. Homunculus representation: legs and trunk fold over midline; arms and hands (most tissue dedicated) are along middle of strip; face (with much tissue dedicated to lips) near bottom.

Area 4
Primary Motor Cortex

Motor homunculus. Because Brodmann area 4 is in the same general location as primary motor cortex, the homunculus here is called the motor homunculus.

Area 5
Somatosensory Association Cortex

Area 5 is involved in somatosensory processing and association.

Area 19
Tertiary visual association cortex (V3)

With area 18, involved in feature-extraction, shape recognition, and visual attention.

Area 20
Inferior Temporal gyrus

High-level visual processes and recognition.

Area 21
Middle Temporal gyrus

Auditory processing and language, notably left side.

Area 22
Superior Temporal Gyrus

Includes Wernickes area in its posterior. Left side involved in generation and understanding of words. Right side, melody, pitch, and sound intensity.

Area 37
Fusiform gyrus

Area 6
Pre-Motor and Supplementary Motor Cortex
Secondary Motor Cortex, Supplementary motor Area. This large area of the frontal cortex is believed to play a role in the planning of complex, coordinated movements.

Area 7
Somatosensory Association Cortex
Involved in locating objects in space; where vision and proprioception converge, enabling us to determine where objects are in relation to parts of the body. Generally, use in visuo-motor coordination such as in reaching to grasp an object.

Area 8
Dorsolateral prefrontal cortex [Frontal eye fields]
Involved in management of uncertainty (increasing uncertainty increases activation here in fMRI). Hope occurs here, a high-order expectation positively correlated with uncertainty. This area also includes frontal eye fields where conscious control of eyes is believed to take place.

Area 9
Dorsolateral prefrontal cortex
Sustaining attention and working memory. Lesions cause difficulty in inhibiting responses.

Area 10
Anterior prefrontal cortex
Frontopolar area is involved in strategic processes of memory retrieval and executive function.

Area 11
Orbitofrontal area
Orbital and rectus gyri, plus part of the rostral part of the superior frontal gyrus. Involved in planning, reasoning, and decision making. Perhaps the only cortical constraint of the hypothalamus.

Area 17
Primary Visual Cortex (V1)
Highly specialized for processing information about static and moving objects and is excellent in pattern recognition.

Area 18
Secondary visual Association Cortex (V2)
Bulk of the volume of the occipital lobe.

Involved in lexico-semantic associations (i.e., associated words with visual percepts).

Area 38
Temporopolar area
Important area in self representation, semantic (left) and autobiographic (right).

Area 39
Angular gyrus
A part of Wernickes area - reading, on left side grapheme-phoneme conversion, and general semantic involvement.

Area 40
Supramarginal gyrus part of Wernickes area
Involved in reading, both in regards to meaning and phonology.

Areas 41 and 42
Primary and Secondary Auditory Cortex
Conscious awareness of sound.

Area 43
Subcentral Area
Associated with spoken language.

Area 44
Pars Opercularis
Part of Brocas area on left hemisphere. Functions of to speech production.

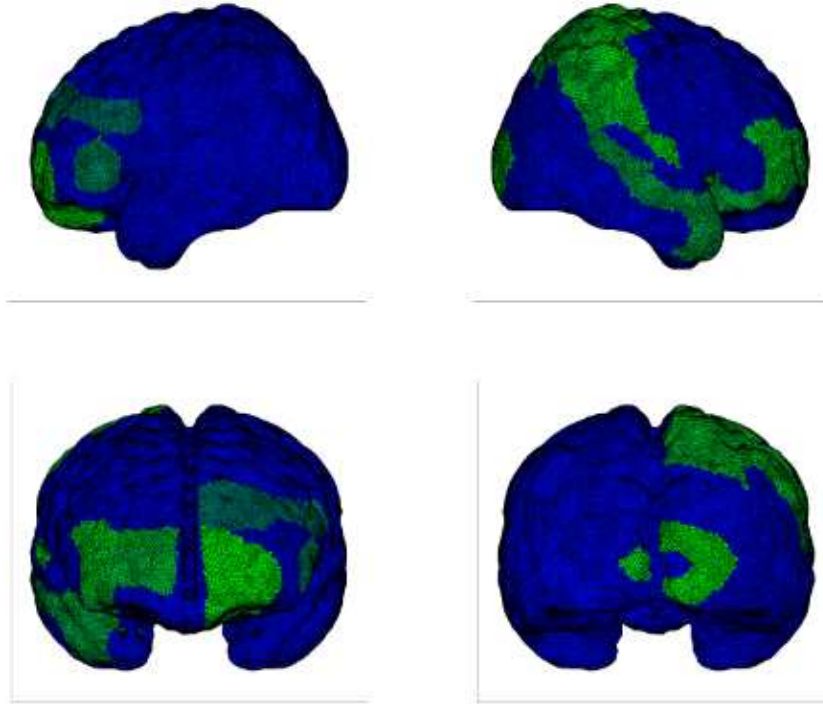
Area 45
Pars Triangularis
Part of Brocas area on left hemisphere. Functions of to speech production.

Area 46
Dorsolateral prefrontal cortex
Involved in memory, particularly working memory and memory control and organization.

Area 47
Inferior prefrontal gyrus
Involved in syntactical processing and emotional inhibition.

GAUSSIAN CURVATURE

3D Visualization



Left Hemisphere

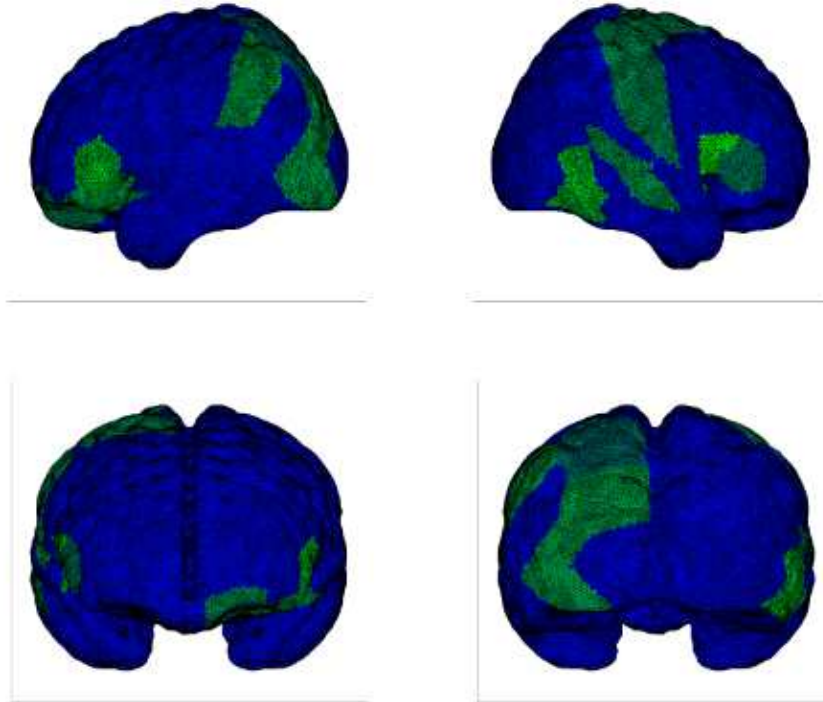
REGION	5	7	9	10	11	17	18	20	22	38	39	4142	44	45
CLASS	0	0	1	1	1	1	0	0	0	0	0	0	0	1
CONFIDENCE	0.93	0.89	0.51	1.00	0.94	0.87	0.95	0.92	0.51	0.76	0.94	0.79	0.45	0.59

Right Hemisphere

REGION	123	4	5	6	7	10	17	18	22	38	39	40	43	46	47
CLASS	1	0	1	0	1	1	0	1	1	1	0	1	0	1	1
CONFIDENCE	0.92	0.85	0.97	0.89	0.81	0.78	0.65	0.97	0.67	0.71	0.97	0.81	0.96	0.87	0.73

MEAN CURVATURE

3D Visualization



Left Hemisphere

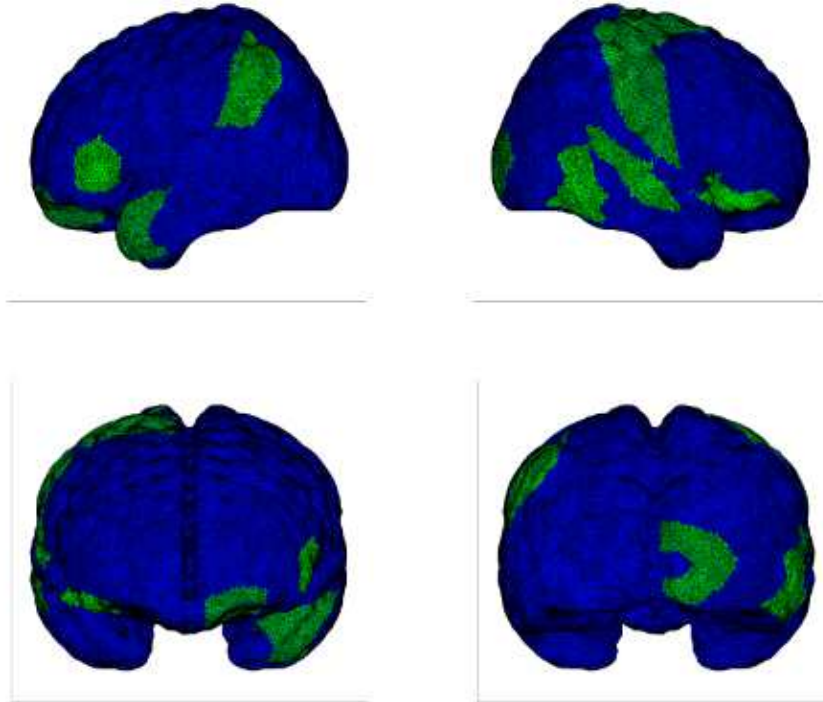
REGION	4	7	8	9	11	17	19	20	22	39	40	45	47
CLASS	0	1	0	0	1	0	1	0	0	0	1	1	1
CONFIDENCE	0.43	0.30	0.48	0.32	0.38	0.53	0.42	0.45	0.44	0.33	0.43	0.51	0.44

Right Hemisphere

REGION	123	4	9	11	17	18	22	37	39	44	45
CLASS	1	1	0	0	0	0	1	1	0	1	1
CONFIDENCE	0.40	0.39	0.33	0.39	0.23	0.45	0.41	0.52	0.44	0.62	0.36

NORMAL CURVATURE

3D Visualization



Left Hemisphere

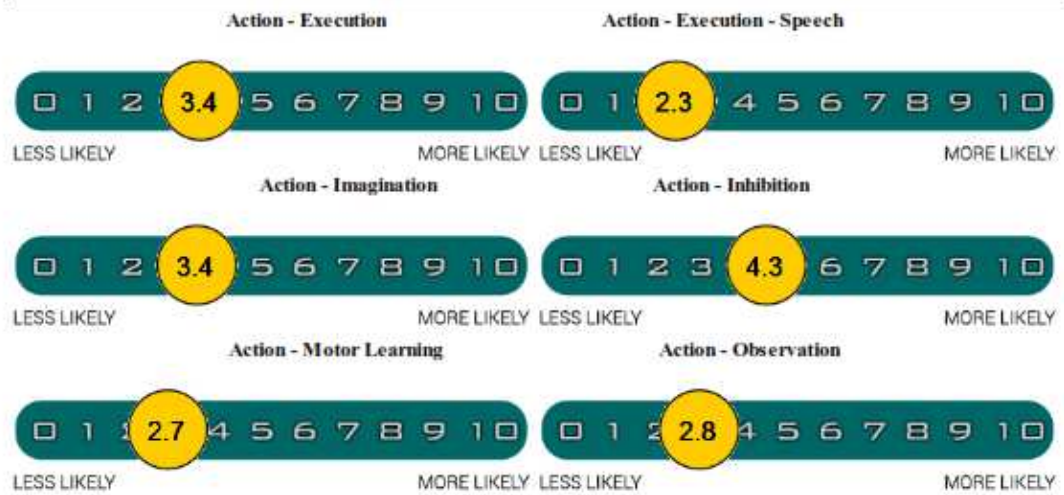
REGION	4	6	8	11	17	19	22	38	39	40	45
CLASS	0	0	0	1	0	0	0	1	0	1	1
CONFIDENCE	0.55	0.50	0.59	0.51	0.68	0.58	0.56	0.53	0.51	0.59	0.66

Right Hemisphere

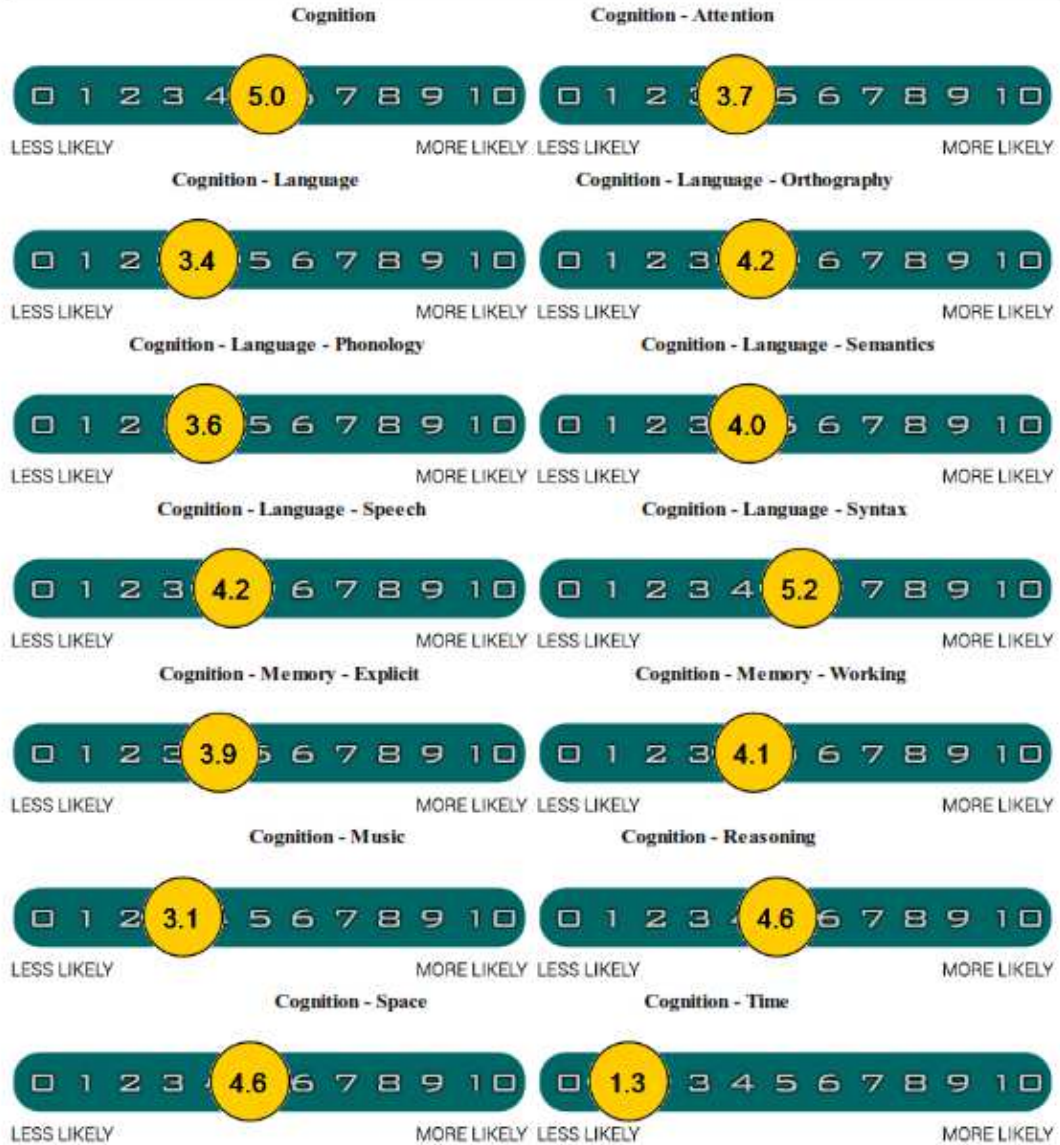
REGION	123	4	10	18	20	22	37	43	47
CLASS	1	1	0	1	0	1	1	0	1
CONFIDENCE	0.55	0.53	0.60	0.56	0.58	0.61	0.64	0.67	0.67

Neurocracy Analysis

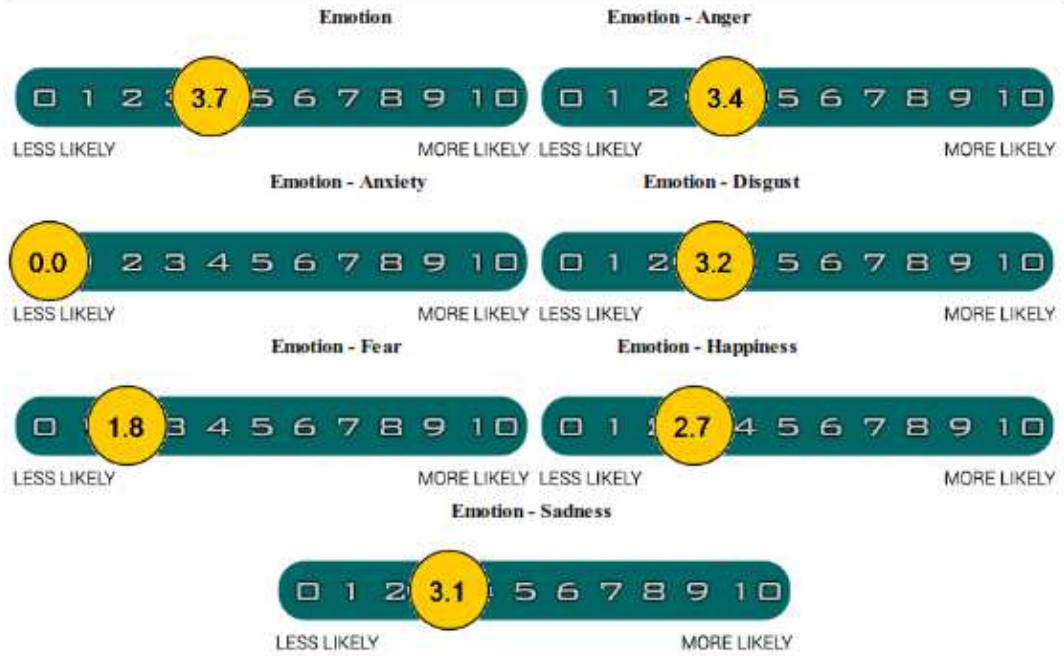
Action



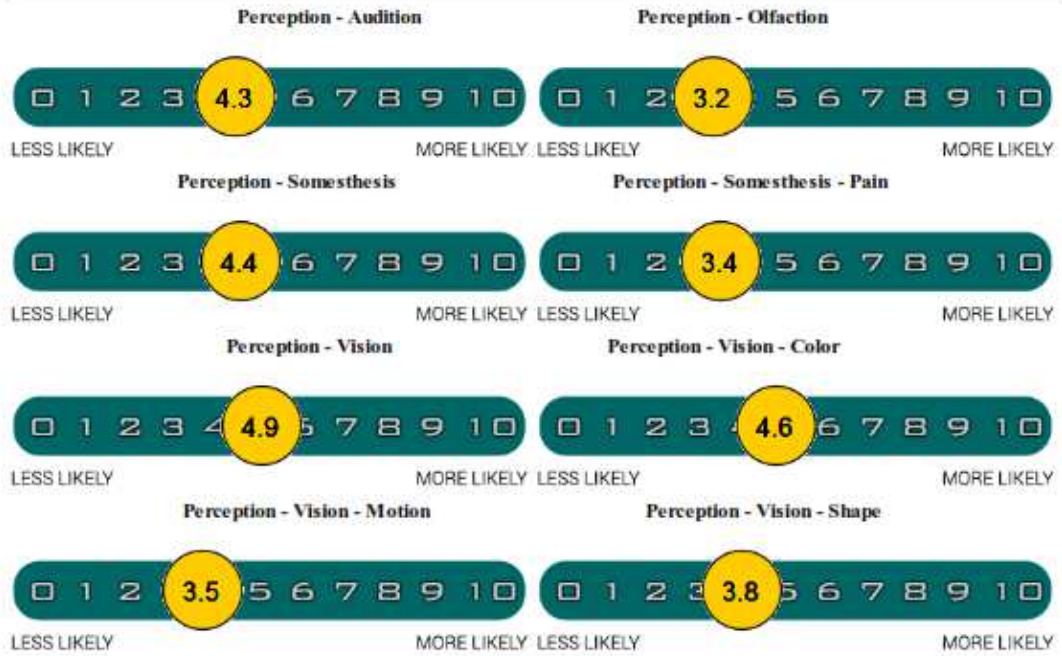
Cognition



Emotion



Perception



Appendix 2 - NT Example Risk Analysis Report

Example risk analysis report constructed for a neurotypical individual.



Breakthrough Medical Diagnostics for a Modern World

Analysis Report

Report Summary

Generated on: 20-May-2014

(c) NeuroAtlas, LLC. 2014

Name: Demo Subject - NT

Age: 8 months

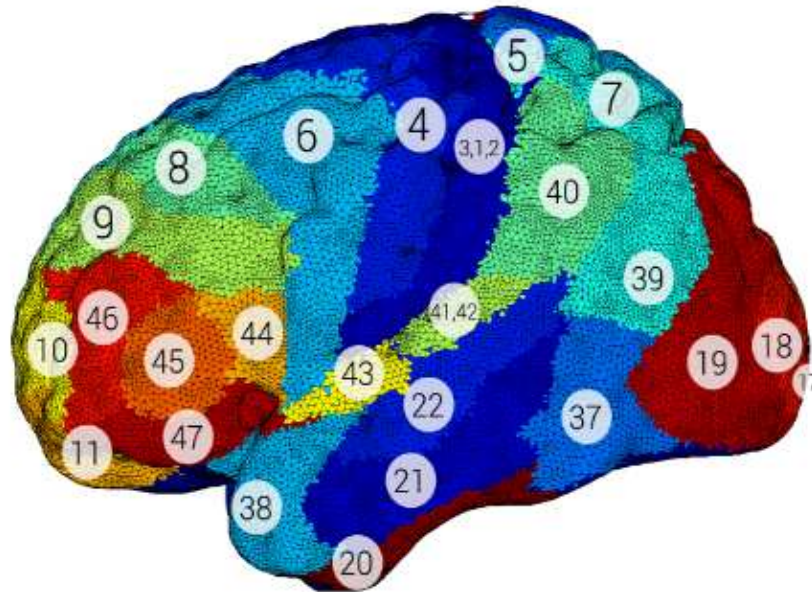
Physician: Dr. J. Doe

Overall Trend



Disclaimer: The medical information in this report is provided as an information resource only, and is not to be used or relied on for any diagnostic or treatment purposes. This information is intended solely for patient education and should not be used as a substitute for professional diagnosis and treatment.

Regional Analysis



Areas 1, 2 & 3 (also called 3, 1, 2)
Primary Somatosensory Cortex

The primary somatosensory cortex is the main sensory receptive area for the sense of touch. Like other sensory Area, there is a map of sensory space in this location, called the sensory homunculus. Homunculus representation: legs and trunk fold over midline; arms and hands (most tissue dedicated) are along middle of strip; face (with much tissue dedicated to lips) near bottom.

Area 4
Primary Motor Cortex

Motor homunculus. Because Brodmann area 4 is in the same general location as primary motor cortex, the homunculus here is called the motor homunculus.

Area 5
Somatosensory Association Cortex

Area 5 is involved in somatosensory processing and association.

Area 19
Tertiary visual association cortex (V3)

With area 18, involved in feature-extraction, shape recognition, and visual attention.

Area 20
Inferior Temporal gyrus

High-level visual processes and recognition.

Area 21
Middle Temporal gyrus

Auditory processing and language, notably left side.

Area 22
Superior Temporal Gyrus

Includes Wernickes area in its posterior. Left side involved in generation and understanding of words. Right side, melody, pitch, and sound intensity.

Area 37
Fusiform gyrus

Area 6
Pre-Motor and Supplementary Motor Cortex
Secondary Motor Cortex, Supplementary motor Area. This large area of the frontal cortex is believed to play a role in the planning of complex, coordinated movements.

Area 7
Somatosensory Association Cortex
Involved in locating objects in space; where vision and proprioception converge, enabling us to determine where objects are in relation to parts of the body. Generally, use in visuo-motor coordination such as in reaching to grasp an object.

Area 8
Dorsolateral prefrontal cortex [Frontal eye fields]
Involved in management of uncertainty (increasing uncertainty increases activation here in fMRI). Hope occurs here, a high-order expectation positively correlated with uncertainty. This area also includes frontal eye fields where conscious control of eyes is believed to take place.

Area 9
Dorsolateral prefrontal cortex
Sustaining attention and working memory. Lesions cause difficulty in inhibiting responses.

Area 10
Anterior prefrontal cortex
Frontopolar area is involved in strategic processes of memory retrieval and executive function.

Area 11
Orbitofrontal area
Orbital and rectus gyri, plus part of the rostral part of the superior frontal gyrus. Involved in planning, reasoning, and decision making. Perhaps the only cortical constraint of the hypothalamus.

Area 17
Primary Visual Cortex (V1)
Highly specialized for processing information about static and moving objects and is excellent in pattern recognition.

Area 18
Secondary visual Association Cortex (V2)
Bulk of the volume of the occipital lobe.

Involved in lexico-semantic associations (i.e., associated words with visual percepts).

Area 38
Temporopolar area
Important area in self representation, semantic (left) and autobiographic (right).

Area 39
Angular gyrus
A part of Wernickes area - reading, on left side grapheme-phoneme conversion, and general semantic involvement.

Area 40
Supramarginal gyrus part of Wernickes area
Involved in reading, both in regards to meaning and phonology.

Areas 41 and 42
Primary and Secondary Auditory Cortex
Conscious awareness of sound.

Area 43
Subcentral Area
Associated with spoken language.

Area 44
Pars Opercularis
Part of Brocas area on left hemisphere. Functions of to speech production.

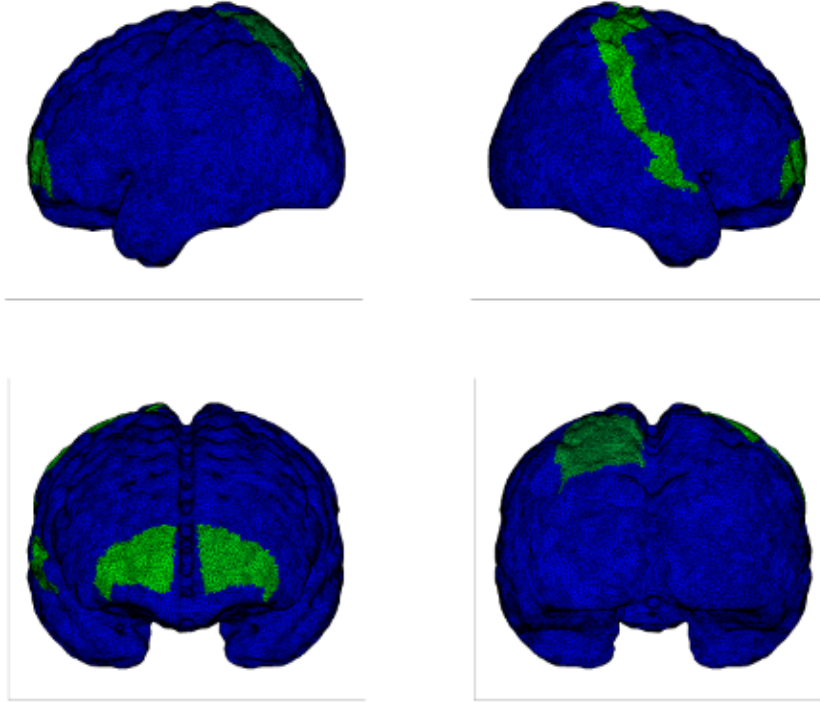
Area 45
Pars Triangularis
Part of Brocas area on left hemisphere. Functions of to speech production.

Area 46
Dorsolateral prefrontal cortex
Involved in memory, particularly working memory and memory control and organization.

Area 47
Inferior prefrontal gyrus
Involved in syntactical processing and emotional inhibition.

GAUSSIAN CURVATURE

3D Visualization



Left Hemisphere

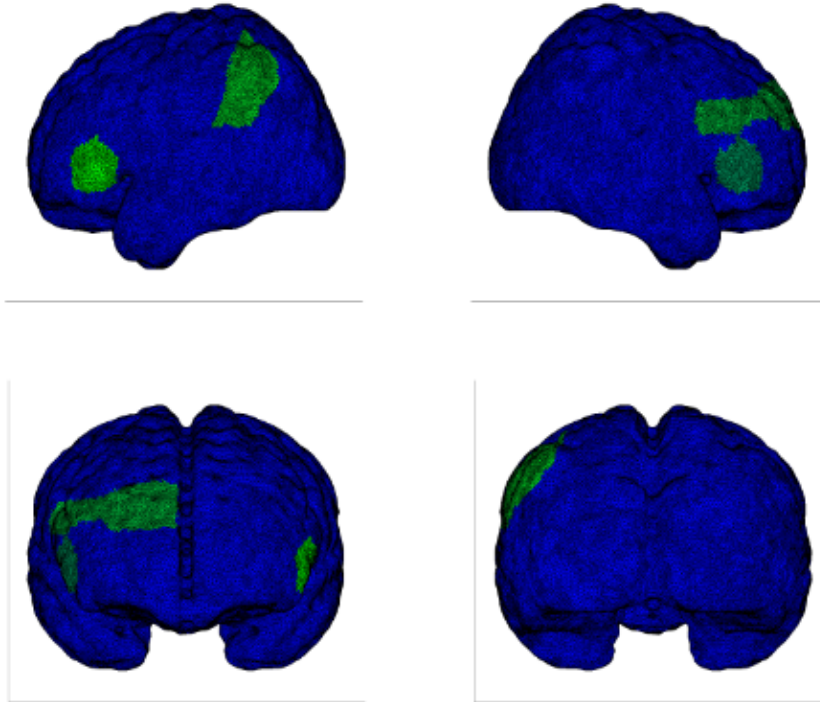
REGION	5	7	9	10	11	17	18	20	22	38	39	4142	44	45
CLASS	0	1	0	1	0	0	0	0	0	0	0	0	0	0
CONFIDENCE	0.94	0.71	0.93	0.88	0.88	0.76	0.99	0.99	0.59	0.81	0.98	0.78	1.00	0.46

Right Hemisphere

REGION	123	4	5	6	7	10	17	18	22	38	39	40	43	46	47
CLASS	1	0	0	0	0	1	0	0	0	0	0	0	1	0	0
CONFIDENCE	0.99	0.74	0.85	0.80	0.92	0.93	0.90	0.84	0.81	0.83	0.74	0.94	0.92	0.89	0.73

MEAN CURVATURE

3D Visualization



Left Hemisphere

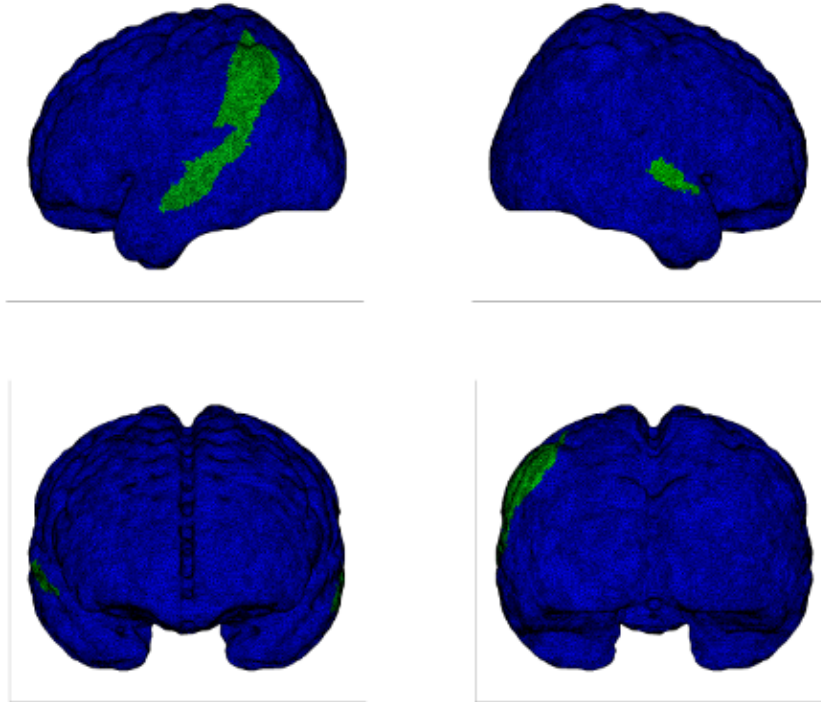
REGION	4	7	8	9	11	17	19	20	22	39	40	45	47
CLASS	0	0	0	0	0	0	0	0	0	0	1	1	0
CONFIDENCE	0.36	0.36	0.38	0.34	0.47	0.69	0.43	0.45	0.39	0.57	0.41	0.49	0.35

Right Hemisphere

REGION	123	4	9	11	17	18	22	37	39	44	45
CLASS	0	0	1	0	0	0	0	0	0	0	1
CONFIDENCE	0.41	0.38	0.36	0.44	0.69	0.51	0.41	0.42	0.41	0.46	0.30

NORMAL CURVATURE

3D Visualization



Left Hemisphere

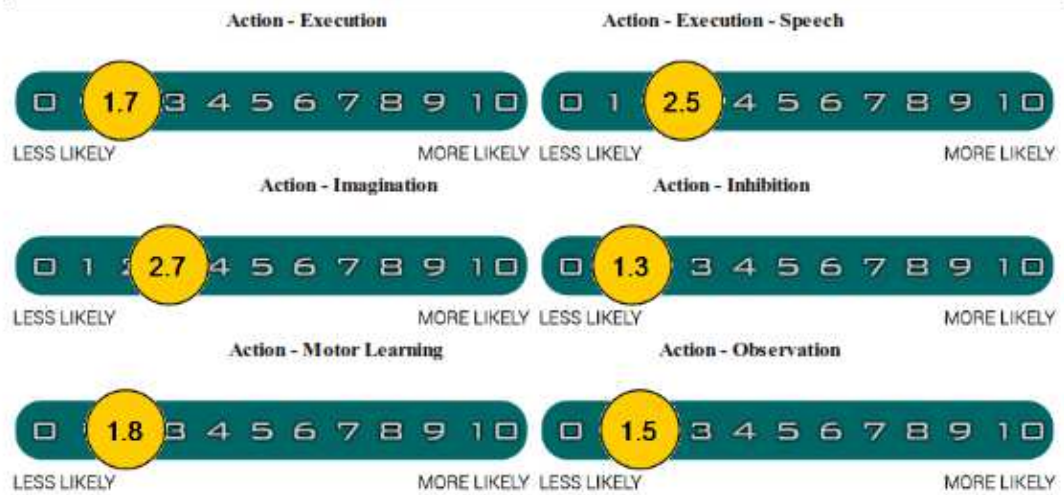
REGION	4	6	8	11	17	19	22	38	39	40	45
CLASS	0	0	0	0	0	0	1	0	0	1	0
CONFIDENCE	0.53	0.48	0.50	0.54	0.74	0.58	0.58	0.55	0.64	0.60	0.59

Right Hemisphere

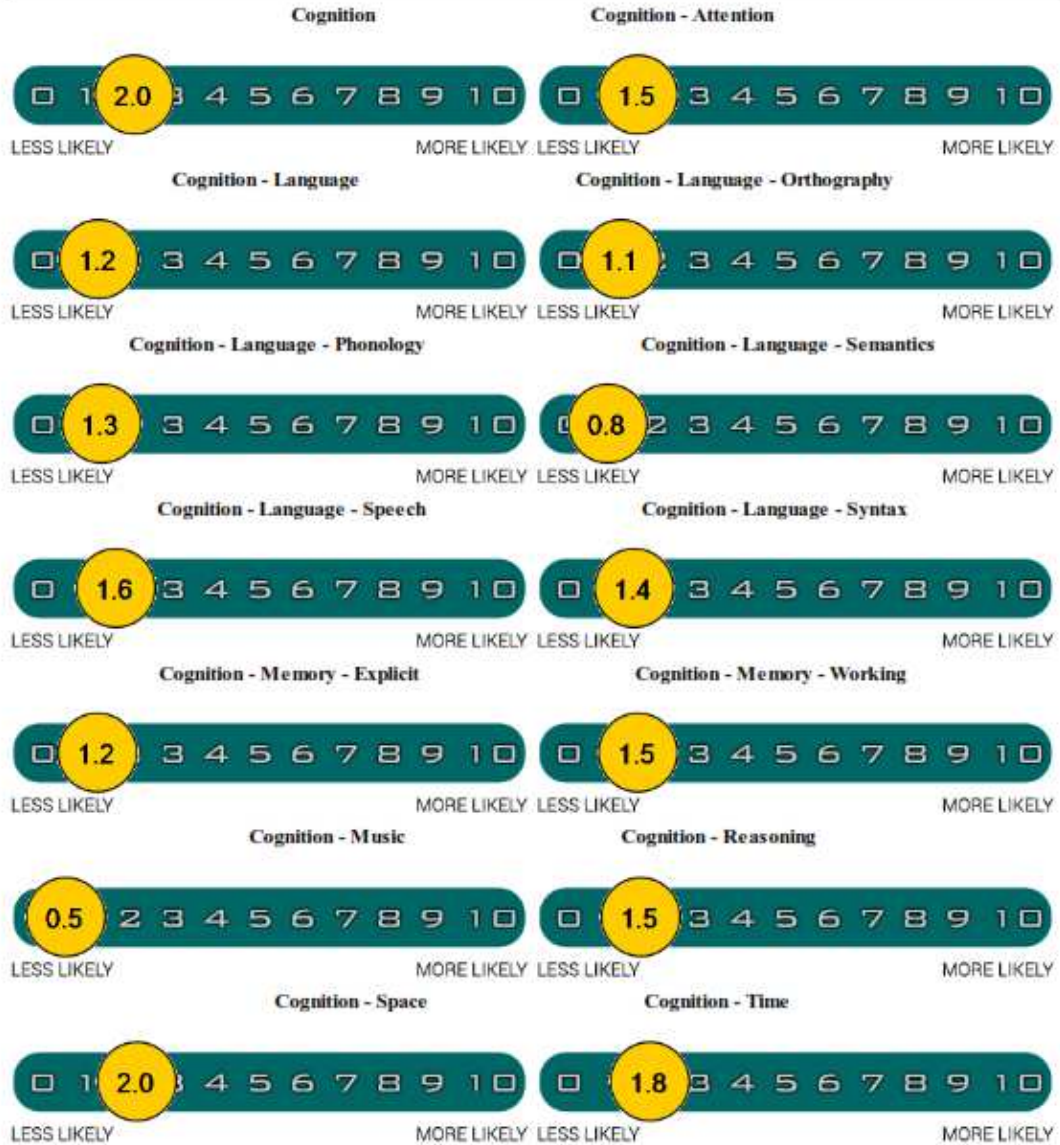
REGION	123	4	10	18	20	22	37	43	47
CLASS	0	0	0	0	0	0	0	1	0
CONFIDENCE	0.50	0.52	0.52	0.60	0.51	0.53	0.53	0.66	0.69

Neurocracy Analysis

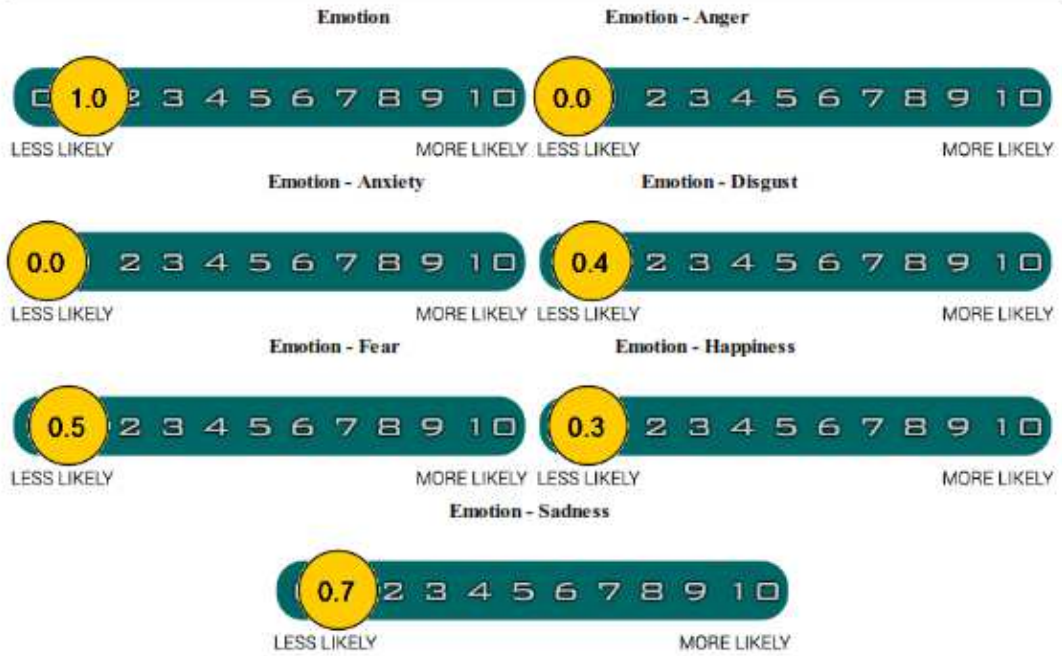
Action



Cognition



Emotion



Perception

Perception - Audition



LESS LIKELY

MORE LIKELY

Perception - Olfaction



LESS LIKELY

MORE LIKELY

Perception - Somesthesia



LESS LIKELY

MORE LIKELY

Perception - Somesthesia - Pain



LESS LIKELY

MORE LIKELY

Perception - Vision



LESS LIKELY

MORE LIKELY

Perception - Vision - Color



LESS LIKELY

MORE LIKELY

Perception - Vision - Motion



LESS LIKELY

MORE LIKELY

Perception - Vision - Shape



LESS LIKELY

MORE LIKELY

Appendix 3 - Revised Risk Analysis Report

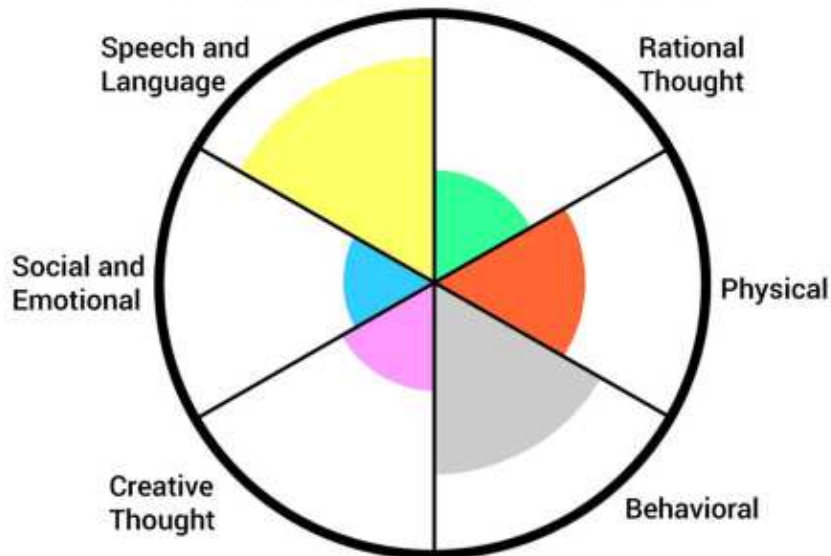
Example of the revised mock risk analysis report constructed from feedback.



Brain Mapping Technology

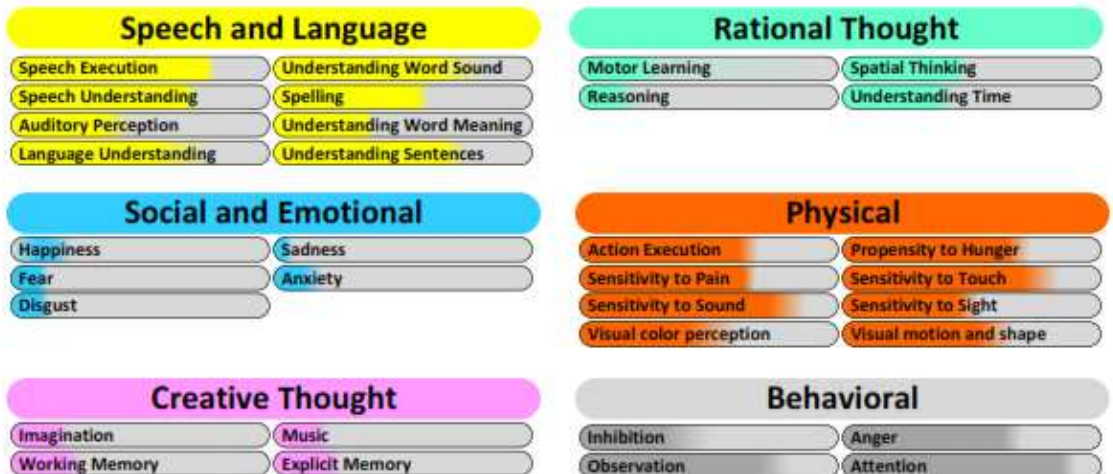
SAMPLE REPORT

YOUR BRAIN AS A WHOLE



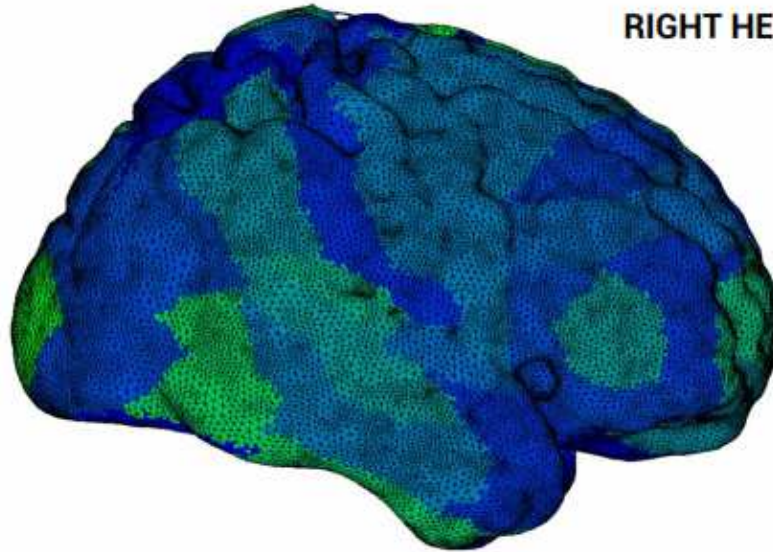
Ever wondered what areas of your brain are similar or unique to an average brain? The BrainGraph shows you how similar each area of your brain is to an average brain!

A DETAILED LOOK AT YOUR AREAS

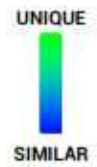
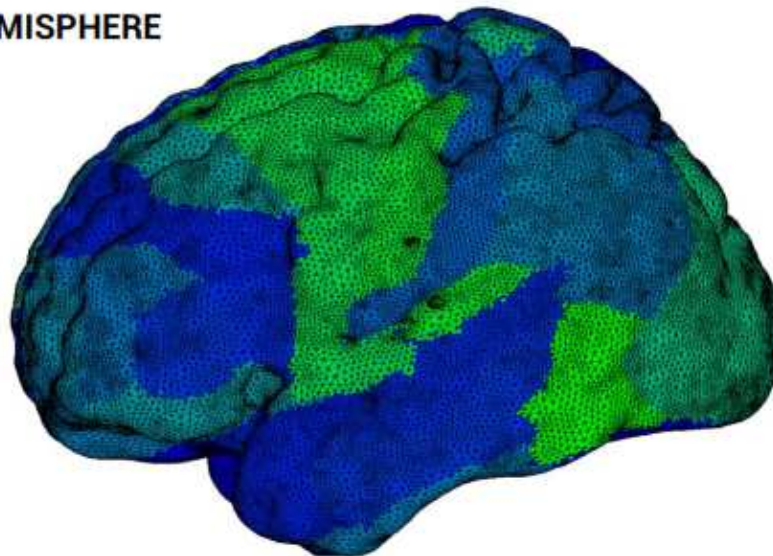


SEEING IS UNDERSTANDING

RIGHT HEMISPHERE



LEFT HEMISPHERE



Now that you have a brain map you are probably wondering what to do next? We've divided suggestions into areas of continued enrichment and areas to work on your unique skills!

Areas of Continued Enrichment

Areas of enrichment help you get the most out of your brain. We target enrichment suggestions to areas where your brain is similar to a collection of normative brains!

Social and Emotional

A well-established, highly effective, and lasting treatment is called cognitive-behavioral therapy, or CBT. It focuses on identifying, understanding, and changing thinking and behavior patterns. Benefits are usually seen in 12 to 16 weeks, depending on the individual. Patients learn skills during therapy sessions.

Creative Thought

You might think of creativity as something clever marketers or copywriters whip out when they need to, but according to Keith Sawyer, research psychologist and author of "Zig Zag: The Surprising Path to Greater Creativity," everyone can be more creative just by taking eight incremental steps.

Physical

Because the body is primarily composed of water, staying hydrated is crucial to your physical health. Water is the purest form of hydration and comes right out of your faucet at home. Staying properly hydrated helps the body's cells to function more efficiently. Cutting back on sugary drinks is good for your dental health, your weight, and your budget.

Behavioral

It will all boil down to understanding the acronym A-B-C. This stands for antecedent, behavior, and consequence. This three-term pattern comes from the science of Applied Behavior Analysis (ABA). Understanding this concept is very important, because it will help you identify what triggered the child's behavior and also what is positively reinforcing the behavior.

Areas to Build Your Unique Skills

Areas to build additional skills targets the areas where your brain is unique! These are areas that may excel or need additional focus, and we have some suggestions to help you get started.

Speech and Language

The components of speech production include: phonation, producing sound; resonance; fluency; intonation, variance of pitch; and voice, including aeromechanical components of respiration. The components of language include: phonology, manipulating sound according to the rules of a language; morphology, understanding and using minimal units of meaning; syntax, constructing sentences by using languages' grammar rules; semantics, interpreting signs or symbols of communication to construct meaning; and pragmatics, social aspects of communication.

Rational Thought

Determining optimality for rational behavior requires a quantifiable formulation of the problem, and making several key assumptions. When the goal or problem involves making a decision, rationality factors in how much information is available (e.g. complete or incomplete knowledge). Collectively, the formulation and background assumptions are the model within which rationality applies.

Finding Support Groups and Providers

Based on your location and unique characteristics we wanted to provide you with some information that can connect you with local providers that may be useful for you!

General Information

Anderson Behavioral Consulting, LLC

Meghan Anderson
310 Codell Dr. #1
Lexington, KY 40509
(937) 974-6176
Email: andersonbehavioralconsulting@yahoo.com
Web: <http://www.andersonbehavioralconsulting.com>

The Arc of Kentucky

833 East Main
Frankfort, KY 40601
(502) 875-5225; (800) 281-1272
Email: arcofky@aol.com

Autism Society of Kentuckiana

Web: <http://www.ask-lou.org/>

Autism Society of the Bluegrass

Sara Spragens
453 Rookwood Pky
Lexington, KY 40505
(859) 299-9000
Email: sspragens@insightbb.com
Web: <http://asbg.org/>

Autism Society of Western Kentucky

PO Box 1647 230 Second Street, Suite 206
Henderson, Kentucky
(270) 826-0510

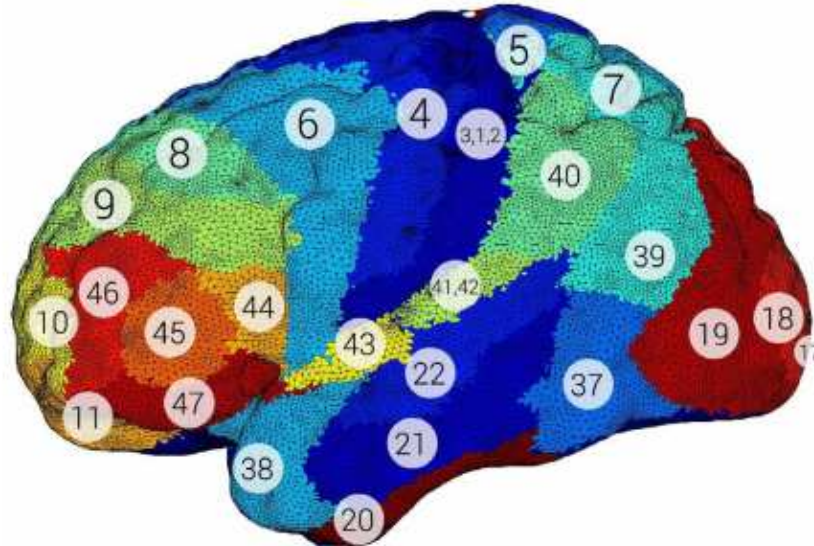
Brain Injury Association of Kentucky

Margaret Millner
7410 New LaGrange Road, Ste. 100
Louisville, KY 40222
(502) 493-0609; (800) 592-1117; (502) 426-2993 (fax)
Email: eddie.reynolds@biak.us
Web: <http://www.biak.us>

Children and Youth Services Branch

NIMH
100 Fair Oaks Lane, 4W-C
Frankfort, KY 40621-0001
(502) 564-7610; (800) 374-9146
Email: Randy.Oliver@mail.state.ky.us
Web: <http://mhmr.ky.gov/kdmhmrs/default.asp>

Understanding Areas of the Brain



The Brodmann Areas

Areas 1, 2 & 3 (also called 3, 1, 2)

Primary Somatosensory Cortex

The primary somatosensory cortex is the main area of the brain for the sense of touch and fine motor control. It also plays a key role in helping us identify objects by touch and interact day to day. This region of the brain mainly plays a role in our ability to make actions and also contributes some to our understanding of language.

Area 4

Primary Motor Cortex

This is the primary motor cortex and plays a role in our body responding to our commands. Because the primary cortex plays a large role in control of many of the bodies actions it has some degree of input in many of our actions and thoughts including moving a body part and focusing our attention.

Area 5

Somatosensory Association Cortex

The somatosensory association cortex primarily functions as a sensing location in the brain. It is very involved in our sense of touch and feelings such as pain. It works alongside area 3,1,2 and area 4 to help us interact with objects.

Area 6

Pre-Motor and Supplementary Motor Cortex

This area of the brain occupies a large area of the frontal cortex on your brain and is primarily involved in helping you plan complex and coordinated movements of your body. Take walking as a simple example where many muscles have to move together to make your body move forward without falling over!

Area 7

Somatosensory Association Cortex

The somatosensory association cortex gives us our sense of space. When we see an object we combine all of our different senses to estimate how far and where around us that object lies. It also helps us to figure out where our body is so that when we reach for our fork we are able to pick it up and use it.

Area 8

Dorsolateral prefrontal cortex [Frontal eye fields]

The dorsolateral prefrontal cortex is involved in managing our feeling of uncertainty and consciously controlling our eyes. So when you are feeling unsure its this area of your brain that is firing!

Area 9

Dorsolateral prefrontal cortex

This area of our brain is responsible for helping us keep our attention on our target and contributes to our ability to use our working memory. It is also involved in helping us inhibit our responses to a variety of events.

Area 10

Anterior prefrontal cortex

The anterior prefrontal cortex is involved in retrieving our memories and processing executive function. Executive function is our ability to connect past experiences with what is going on in the present to help make good decisions.

Understanding Areas of the Brain

Area 11

Orbitofrontal area

The orbitofrontal area of the brain plays a large role in our ability to plan, reason, and make decisions. It is also linked to the hypothalamus of the brain which is responsible for regulating a variety of the bodies naturally formed chemicals and stimuli.

Area 17

Primary Visual Cortex (V1)

Visual Cortex V1 is a specialized area of the brain for processing information related to static and moving objects around us. It is also heavily associated with pattern recognition and helps us to determine what the objects around us are.

Area 18

Secondary visual Association Cortex (V2)

The second visual cortex is the largest and is involved in lexico-semantic associations. This allows us to see and translate written words into associations. So when we read tree in our minds we visualize a picture of a tree!

Area 19

Tertiary visual association cortex (V3)

The last visual cortex, V3, is involved in feature extraction, shape recognition and visual attention. For example, it enables us to look inside the refrigerator and figure out what object is the container of milk.

Area 20

Inferior Temporal gyrus

The inferior temporal gyrus is an area of the brain that is involved in high-level visual processing and recognition. It is also involved in our understanding of the concept of color and it works alongside Area 19 to help us understand objects.

Area 21

Middle Temporal gyrus

The middle temporal gyrus plays a role in auditory (sound) processing and our understanding word meanings while reading. It also plays a role in recognizing faces of people we know. The left side of the brain plays a notably stronger role than the right.

Area 22

Superior Temporal Gyrus

The superior temporal gyrus is involved in the generation and understanding of words and our understanding of melody, pitch and sound intensity. This area of the brain contains the well-known Wernickes Area in the rear.

Area 37

Fusiform gyrus

The fusiform gyrus plays a key role in processing our understanding of color and our ability to visually recognize things. It is also involved in understanding categories and words.

Area 38

Temporopolar area

The temporopolar area of the brain is involved in our semantic and autobiographic representation of our concept of self and allows us to talk about our experiences.

Area 39

Angular gyrus

The angular gyrus also contributes to the Wernickes area region of the brain and is involved in general sentence construction, reading, and associates written pieces of words with their phonetic sounds.

Area 40

Supramarginal gyrus

The last major part of the brain involved in Wernickes area. This area is responsible for determining the meaning of what we read and helps us to hear written words in our minds.

Areas 41 and 42

Primary and Secondary Auditory Cortex

The primary and secondary auditory cortex contribute to our understanding and awareness of sounds.

Area 43

Subcentral Area

The subcentral area of the brain plays a minor role in helping us form and speak language. It helps contribute along with Broca's Area.

Area 44

Pars Opercularis

The Pars Opercularis is the first part of the brain that is involved in the Broca's Area. This part of the brain is heavily responsible for our production of speech.

Area 45

Pars Triangularis

The Pars Triangularis is the second major part of the brain that is involved in the Broca's Area. This part of the brain is heavily responsible for our production of speech and understanding of abstract and concrete tasks.

Area 46

Dorsolateral prefrontal cortex

Area 46 of the brain is heavily involved in our ability to use and control our memory. It is also involved in our ability to organize our own memories.

Area 47

Inferior prefrontal gyrus

The Inferior Prefrontal Gyrus is involved in our ability to process a variety of syntaxes and our ability to inhibit our emotional responses.

Appendix 4 - Wavefront OBJ Format

Format Specification

Lines beginning with a hash character (#) are comments.

```
# this is a comment
```

An OBJ file contains several types of definition:

```
# List of Vertices, with (x,y,z) coordinates.
```

```
v 0.123 0.234 0.345
```

```
v ...
```

```
...
```

```
# Texture coordinates, in (u,v) coordinates.
```

```
vt 0.500 -1.352
```

```
vt ...
```

```
...
```

```
# Normals in (x,y,z) form; normals might not be unit.
```

```
vn 0.707 0.000 0.707
```

```
vn ...
```

```
..
```

Face Definitions

Faces are defined using lists of vertex, texture and normal indices. Polygons such as quadrilaterals can be defined by using more than three vertex/texture/normal indices. OBJ files also

support free form curved surface objects such as NURB surfaces. There are several way to define a face, but each face line definition starts with "f" character.

Vertex

A valid vertex index starts from 1 and match first vertex element of vertex list previously defined. Each face can contain more than three elements.

f v1 v2 v3 v4 ...

Vertex/Texture-coordinate

Each texture coordinate index must follow with no space the first slash. Texture coordinates index are optional. A valid texture coordinate index starts from 1 and match first texture coordinate element of texture coordinate list previously defined. Each face can contain more than three elements.

f v1/vt1 v2/vt2 v3/vt3 ...

Vertex/Texture-coordinate/Normal

Each normal index must follow with no space the second slash. Normals index are optional. A valid normal index starts from 1 and match first normal element of normal list previously defined. Each face can contain more than three elements.

f v1/vt1/vn1 v2/vt2/vn2 v3/vt3/vn3 ...

Vertex/Normal

As texture coordinates are optional, one can define geometry without them, but one must put normal index after second slash.

f v1//vn1 v2//vn2 v3//vn3 ...

CURRICULUM VITA

NAME: Matthew Joseph Nitzken

ADDRESS: 9907 Winged Foot Drive
Louisville, KY 40223

DOB: Woodbridge, VA - September 16, 1987

EDUCATION: B.S., Bioengineering
University of Louisville
2005 - 09

M.Eng., Bioengineering
University of Louisville
2009 - 10

Ph.D., Electrical & Computer Engineering
University of Louisville
2010 - 15

AWARDS: Graduate Dean's Citation
University of Louisville, Louisville, KY
2015

First Place Entrepreneurial Award
KSTC State Tech. Competition
2014

Second Place in Engineering
Research Louisville, Louisville, KY
2014

Outstanding Student in Electrical Engineering
University of Louisville, Louisville, KY
2014

Theobald Excellence Scholarship
University of Louisville, Louisville, KY
2014

First Place MRBrainS Imaging Competition
MICCAI, Nagoya, Japan
2013

Outstanding Student in Electrical Engineering
University of Louisville, Louisville, KY
2013

Novel Research Innovation Option
University of Louisville, Louisville, KY
2013

Novel Research Innovation License
University of Louisville, Louisville, KY
2013

First Place Entrepreneurial Award
OVALS Entrepreneurial Competition
2012

First Place and Best in Bioengineering
Engineering Exposition, Louisville, KY
2012

Third Place and Best in Bioengineering
Engineering Exposition, Louisville, KY
2011

Second Place
Research Louisville, Louisville, KY
2011

High Honors
University of Louisville, Louisville, KY
2010

Mickey R. Wilhelm Achievement Award
University of Louisville, Louisville, KY
2009

Wilburn-Shipman Scholarship
University of Louisville, Louisville, KY
2005

John Caddy Memorial Scholarship

American Air Filter, Louisville, KY
2005

Century Scholarship
University of Cincinnati, Cincinnati, OH
2005

Cincinnati Scholarship
University of Cincinnati, Cincinnati, OH
2005

PROFESSIONAL SOCIETIES:

Institute of Electrical and Electronics Engineers
Biomedical Engineering Society
Medical Image Computing and Computer Assisted Intervention Society
XLerate Health - National Medical Healthcare Accelerator
LaunchIT - Greater Louisville Inc. Entrepreneurial Accelerator
IEEE Communications Society
Society for Cardiovascular Magnetic Resonance
American Society of Heating, Refrigerating and Air-Conditioning

PUBLICATIONS IN PEER-REVIEWED JOURNALS:

Cortical surface complexity in a population-based normative sample. Brynn A Dombroski, M J Nitzken, A A Elnakib, F Khalifa, A E Switala, A S El-Baz, M F Casanova. *Translational Neuroscience* 5.1 (2014) pp. 17–24. Springer, 2014.

Magnetic Resonance Imaging Findings for Dyslexia: A Review. A Elnakib, A Soliman, M Nitzken, M F Casanova, G Gimel'farb, A El-Baz. *Journal of Biomedical Nanotechnology* 10.10 (2014) pp. 2778–2805. American Scientific Publishers, 2014.

Shape analysis of the human brain: a brief survey. M J Nitzken, M F Casanova, G Gimel'farb, T Inanc, J M Zurada, A El-Baz. *IEEE journal of biomedical and health informatics* 18.4 (2014) pp. 1337–1354. 2014.

MAP-based framework for segmentation of MR brain images based on visual appearance and prior shape. A Alansary, A Soliman, F Khalifa, A Elnakib, M Mostapha, M Nitzken, M Casanova, A El-Baz. *MIDAS J* 1 (2013) p. 1. 2013.

Local wavelet-based filtering of electromyographic signals to eliminate the electrocardiographic-induced artifacts in patients with spinal cord injury. M Nitzken, N Bajaj, S Aslan, G Gimel'farb, A El-Baz, A Ovechkin. *Journal of biomedical science and engineering* 6.7B (2013) pp. 1–10. NIH Public Access, 2013.

Markov-Gibbs Random Field Model for Improved Full-Cardiac Cycle Strain Estimation from Tagged CMR. M J Nitzken, A S El-Baz, G M Beache. *Journal of Cardiovascular Magnetic Resonance* 14.1 (2012) pp. 1–2. Springer, 2012.

Spherical harmonic analysis of cortical complexity in autism and dyslexia. E L Williams, A El-Baz, M Nitzken, A E Switala, M F Casanova. *Translational neuroscience* 3.1 (2012) pp. 36–40. Springer, 2012.

Three-dimensional shape analysis using spherical harmonics for early assessment of detected lung nodules. A El-Baz, M Nitzken, G Gimel'farb, E Van Bogaert, R Falk, M A El-Ghar, J Suri. *Lung Imaging and Computer Aided Diagnosis* 19 (2011) pp. 421–438. 2011.

A novel shape-based diagnostic approach for early diagnosis of lung nodules. M Kondapaneni, M Nitzken, E Bogaert, G Gimel'farb, R Falk, M Au El-Ghar, A El-Baz. *CHEST Journal* 140.4 Meeting Abstracts (2011) 655A–655A. American College of Chest Physicians, 2011.

PUBLICATIONS IN PEER-REVIEWED CONFERENCE PROCEEDINGS:

An integrated geometrical and stochastic approach for accurate infant brain extraction. A Alansary, A Soliman, M Nitzken, F Khalifa, A Elnakib, M Mostapha, MF Casanova, A El-Baz. *Image Processing (ICIP), 2014 IEEE International Conference on, 2014, Paris, France.*

A Statistical Framework For The Classification of Infant DT Images. M Mostapha, A Soliman, F Khalifa, A Elnakib, A Alansary, M Nitzken, M Casanova, A El-Baz. *Image Processing (ICIP), 2014 IEEE International Conference on, 2014, Paris, France.*

Atlas-based approach for the segmentation of infant DTI MR brain images. M Mostapha, A Alansary, A Soliman, F Khalifa, M Nitzken, R Khodeir, M F Casanova, A El-Baz. *Biomedical Imaging (ISBI), 2014 IEEE 11th International Symposium on, 2014, Beijing, China.*

SPHARM Analysis of the Brain Cortex for Diagnosing Dyslexia. M J Nitzken, M F Casanova, A El-Baz. *Biomedical Imaging (ISBI), 2014 IEEE 11th International Symposium on, 2014, Beijing, China.*

Quantification of age-related brain cortex change using 3D shape analysis. A Elnakib, M Nitzken, MF Casanova, H Park, G Gimel'farb, A El-Baz. *Pattern Recognition (ICPR), 2012 21st International Conference on, 2012, Tsukuba, Japan.*

A novel approach for global lung registration using 3D Markov-Gibbs appearance model. A El-Baz, F Khalifa, A Elnakib, M Nitzken, A Soliman, Patrick McClure, M Au El-Ghar, G Gimel'Farb. *Medical Image Computing and Computer-Assisted Intervention–MICCAI 2012, 2012, Nice, France.*

Accurate modeling of tagged CMR 3D image appearance characteristics to improve cardiac cycle strain estimation. M Nitzken, G Beache, A Elnakib, F Khalifa, G

Gimel'farb, A El-Baz. Image Processing (ICIP), 2012 19th IEEE International Conference on, 2012, Orlando, Florida, USA.

A Cerebral Spectrum From Autism to Dyslexia: Determining Cortical Surface Complexity Utilizing Spherical Harmonics. M F Casanova, M Nitzken, E L Williams, A E Switala, A El-Baz. IMFAR Program Booklet & Abstracts, 2012, Toronto, Canada.

Improving full-cardiac cycle strain estimation from tagged CMR by accurate modeling of 3D image appearance characteristics. M Nitzken, G Beache, A Elnakib, F Khalifa, G Gimel'farb, A El-Baz. Biomedical Imaging (ISBI), 2012 9th IEEE International Symposium on, 2012, Barcelona, Spain.

3D shape analysis for early diagnosis of malignant lung nodules. A El-Baz, M Nitzken, F Khalifa, A Elnakib, G Gimel'farb, R Falk, M A El-Ghar. Medical Image Computing and Computer-Assisted Intervention—MICCAI 2011, 2011, Toronto, Canada.

3D shape analysis of the brain cortex with application to dyslexia. M Nitzken, MF Casanova, G Gimel'farb, A Elnakib, F Khalifa, A Switala, A El-Baz. Image Processing (ICIP), 2011 18th IEEE International Conference on, 2011, Brussels, Belgium.

3D shape analysis for early diagnosis of malignant lung nodules. A El-Baz, M Nitzken, F Khalifa, A Elnakib, G Gimel'farb, R Falk, M A El-Ghar. Information Processing in Medical Imaging, 2011, Monastery Irsee, Germany.

A novel shape-based diagnostic approach for early diagnosis of lung nodules. A El-Baz, M Nitzken, E Vanbogaert, G Gimel'Farb, R Falk, M Abo El-Ghar. Biomedical Imaging: From Nano to Macro, 2011 IEEE International Symposium on, 2011, Chicago Illinois, USA.

A new framework for automated identification of pathological tissues in contrast enhanced cardiac magnetic resonance images. A Elnakib, G M Beache, M Nitzken, G Gimel'farb, A El-Baz. Biomedical Imaging: From Nano to Macro, 2011 IEEE International Symposium on, 2011, Chicago, Illinois, USA.

Automatic analysis of left ventricle wall thickness using short-axis cine CMR images. F Khalifa, G M Beache, M Nitzken, G Gimel'farb, G Giridharan, A El-Baz. Biomedical Imaging: From Nano to Macro, 2011 IEEE International Symposium on, 2011, Chicago Illinois, USA.

3D shape analysis of the brain cortex with application to autism. M Nitzken, MF Casanova, G Gimel'farb, F Khalifa, A Elnakib, A E Switala, A El-Baz. Biomedical Imaging: From Nano to Macro, 2011 IEEE International Symposium on, 2011, Chicago, Illinois, USA.

BOOKS AND SYMPOSIA:

A El-Baz, M Nitzken, G Gimel'Farb, E. Van Bogaert, R. Falk, M Abo El-Ghar, J. Suri. "3D Shape Analysis Using Spherical Harmonics for Early Assessment of Detected

Lung Nodules". In: Handbook of Lung Imaging and Computer Aided Diagnosis. Ed. by A. El-Baz and J. Suri. Vol. 1. 1. United Kingdom: Taylor & Francis, Oct. 2011. Chap. 19. ISBN: 978-1-4398-4557-8.

M Nitzken, M F Casanova, F Khalifa, G Sokhadze, A El-Baz. "Shape-Based Detection of Cortex Variability for More Accurate Discrimination Between Autistic and Normal Brains". In: Handbook of Multi-Modality State-of-the-Art Medical Image Segmentation and Registration Methodologies. Ed. by A. El-Baz, R. Acharya, A. Laine, and J. Suri. Vol. 2. New York: Springer Verlag, Mar. 2011. Chap. 7, pp. 161–185. ISBN: 978-1-4419-8203-2.

PATENTS:

M Nitzken, A El-Baz. "Computer Aided Diagnostic System Incorporating Shape Analysis for Diagnosing Malignant Lung Nodules". English. Provisional 61-617,865. -.

M Nitzken, A El-Baz, A Alansary, A Soliman, M Casanova. "Brain Segmentation Method for Young Children and Adults". English. Provisional -. -.

M Nitzken, A El-Baz, N. Bajaj, A. Ovechkin. "Localized ECG Removal from EMG Signals Using Wavelet Analysis". English. Disclosure disclosure. -.

M Nitzken, A El-Baz, G. Beache. "Improved Spatial-Spectral Analysis by Augmented Modeling of 3D Image Appearance Characteristics with Application to Radio Frequency Tagged Cardiovascular Magnetic Resonance (CMR)". English. Non Provisional 61-617,871. -.

M Nitzken, A El-Baz, M Casanova. "Computer Aided Diagnostic System Incorporating 3D Shape Analysis of the Brain for Identifying Autism/or Dyslexia". English. Non Provisional 61-617,869. -.

SOFTWARE COPYRIGHTS:

3D Image Enhancement for Improvements in Spectral Tracking (No. TX 7-546-226). M Nitzken, A El-Baz. 2014.

Shape Analysis for Early Diagnosis of Autism and Lung Cancer (No. TX 7-520- 124). M Nitzken, A El-Baz. 2013.